

**Photovoltaic Windows
Theories, Devices and Applications**

Gao, Yuan

DOI

[10.4233/uuid:7aa8438c-6106-4c0f-a33f-0ceb8782ad23](https://doi.org/10.4233/uuid:7aa8438c-6106-4c0f-a33f-0ceb8782ad23)

Publication date

2019

Document Version

Final published version

Citation (APA)

Gao, Y. (2019). *Photovoltaic Windows: Theories, Devices and Applications*. [Dissertation (TU Delft), Delft University of Technology]. <https://doi.org/10.4233/uuid:7aa8438c-6106-4c0f-a33f-0ceb8782ad23>

Important note

To cite this publication, please use the final published version (if applicable).
Please check the document version above.

Copyright

Other than for strictly personal use, it is not permitted to download, forward or distribute the text or part of it, without the consent of the author(s) and/or copyright holder(s), unless the work is under an open content license such as Creative Commons.

Takedown policy

Please contact us and provide details if you believe this document breaches copyrights.
We will remove access to the work immediately and investigate your claim.

PHOTOVOLTAIC WINDOWS

THEORIES, DEVICES AND APPLICATIONS

Yuan GAO

高源

PHOTOVOLTAIC WINDOWS

THEORIES, DEVICES AND APPLICATIONS

Proefschrift

ter verkrijging van de graad van doctor
aan de Technische Universiteit Delft,
op gezag van de Rector Magnificus prof. dr. ir. T.H.J.J. van der Hagen,
voorzitter van het College voor Promoties,
in het openbaar te verdedigen op dinsdag 25 juni 2019 om 10:00 uur

door

Yuan GAO

Master of Science in Electronics Science and Technology, Fudan University, China
geboren te Jinzhou, China.

Dit proefschrift is goedgekeurd door de

promotor: prof. dr. M. Zeman
promotor: prof. dr. G.Q. Zhang
copromotor: dr. O. Isabella

Samenstelling promotiecommissie:

Rector magnificus,	voorzitter
Prof. dr. M. Zeman,	Technische Universiteit Delft
Prof. dr. G.Q. Zhang,	Technische Universiteit Delft
Dr. O. Isabella,	Technische Universiteit Delft

Onafhankelijke leden:

Prof. dr. A.H.M.E. Reinders,	Technische Universiteit Eindhoven
Prof. dr. ing. T. Klein,	Technische Universiteit Delft
Prof. dr. A. Weeber,	Technische Universiteit Delft
Prof. dr. ir. W.D. van Driel,	Technische Universiteit Delft



Keywords: photovoltaic windows, building-integrated photovoltaic, building energy, algrivoltaic, thin-film solar cells, smart windows

Printed by: IPSKAMP Printing

Front & Back: *Window of Energy*, designed by Y. Gao, inspired by the *Church of the Light*, an elegant design of Japanese architect Tadao Ando.

Copyright © 2019 by Y. Gao
All rights reserved.

No part of this material may be reproduced, stored in a retrieval system, nor transmitted in any form or by any means without the prior written permission of the copyright owner.

ISBN 978-94-6366-175-1

An electronic version of this dissertation is available at
<http://repository.tudelft.nl/>.

To my parents
Wanjun Gao, Lixia Qi

献给我的父母
高万军 齐丽霞

CONTENTS

1	Introduction	1
1.1	Solar energy and photovoltaics	2
1.2	Building-integrated photovoltaic windows	5
1.3	More than power generation	7
1.4	Aim and scope of this dissertation	9
1.5	Outline of this dissertation	10
1.6	Contribution to the research field	12
	References	12
2	One-axis photovoltaic window blinds	15
2.1	Introduction	16
2.1.1	Literature review on photovoltaic window blinds	16
2.1.2	Motivations and objectives.	17
2.2	Methods	18
2.2.1	Model of solar irradiance.	19
2.2.2	Models of $G_{t,global}$ and shadows on PV blinds	21
2.2.3	Model of solar cell and PV module	23
2.2.4	Model of equivalent irradiance for partial shading	23
2.2.5	Glare model	24
2.3	Results	25
2.3.1	Photovoltaic performance under (partial) shading.	26
2.3.2	Optimal design of cell layouts	28
2.3.3	Annual photovoltaic performance	29
2.3.4	Glare protection	31
2.4	Discussion	31
2.5	Conclusions.	32
	References	32
3	Multi-axis photovoltaic window shades	35
3.1	Literature review on multi-axis photovoltaic window shades	36
3.2	Two-DOF sun tracking	36
3.2.1	Model of two-DOF rotation	36
3.2.2	Derivative and calculation of S_b and P_{in}	37
3.2.3	Two-DOF results and analysis	42
3.3	Three-DOF sun tracking	43
3.3.1	Model of three-DOF rotation.	43
3.3.2	Three-DOF results and analysis	44
3.3.3	VP-3-DOF sun tracking	48

3.4	Results	50
3.4.1	Photovoltaic performance	50
3.4.2	Glare protection	51
3.5	Discussion	53
3.5.1	VP-3-DOF sun tracking	53
3.5.2	Limitations of the current work	54
3.6	Conclusions.	55
	References	55
4	Energy performance of buildings with photovoltaic window shades	57
4.1	Introduction	58
4.2	Methods	60
4.2.1	3D model of an office room	61
4.2.2	Models of solar cell and PV module	63
4.2.3	Input parameters	63
4.2.4	Tilt angles and sun-tracking methods	64
4.2.5	Daylighting and artificial lighting	65
4.2.6	Heating and cooling system	67
4.3	Results	68
4.3.1	PV electricity generation	68
4.3.2	Energy consumption by artificial lighting	68
4.3.3	Energy consumption by heating and cooling.	70
4.3.4	Overall energy generation and consumption.	73
4.4	Discussion	74
4.5	Conclusions.	75
	References	75
5	Photovoltaic windows of agricultural greenhouses	79
5.1	Introduction to agrivoltaics	80
5.2	Methods	84
5.2.1	Greenhouse model.	85
5.2.2	Solar irradiance model.	88
5.2.3	Equivalent irradiance under partial diffuse shadows.	88
5.2.4	Model of the PV module	93
5.2.5	Model of the PV greenhouse array	95
5.2.6	Methods of annual accumulative and average calculation	97
5.3	Results	97
5.3.1	Partial shading effects on PV modules	97
5.3.2	PV performance at a given time instant	98
5.3.3	Interior irradiance at a given time instant	103
5.3.4	Daily results in hourly time step	105
5.3.5	Annual accumulative and average results	105

5.4	Discussion	110
5.4.1	Balancing interior illuminance and PV generation	110
5.4.2	Other impact factors	110
5.4.3	Ideal simulation results	111
5.4.4	Restrictions of the current work	111
5.5	Conclusions.	111
	References	112
6	Transparency-tunable photovoltaic windows	115
6.1	Introduction to semi-transparent solar cell	116
6.2	Semi-transparent amorphous silicon solar cell	117
6.2.1	Design and optimization.	117
6.2.2	Experimental process and results	119
6.3	PDLC film.	121
6.3.1	Working principle	121
6.3.2	Experimental performance	122
6.4	Prototype	123
6.5	Discussion and conclusion	125
	References	126
7	Conclusions and perspectives	129
7.1	Answer the questions	129
7.2	Conclusions.	130
7.3	Perspectives.	131
	Nomenclature	135
	Appendix A	143
	Appendix B	145
	Appendix C	149
	Appendix D	151
	Summary	153
	Samenvatting	155
	Acknowledgements	157
	List of Publications	161
	Curriculum Vitæ	165

1

INTRODUCTION

*Burning oil is like taking furniture from your house
and setting it on fire for heat.*

Elon Musk

*We shape our buildings;
Thereafter they shape us.*

Winston Churchill

*Some facts about **time***

*It takes about **eight minutes**, for a photon to travel 93 million miles from the sun to the earth.*

*It takes **decades to hundreds of years**, for a tree to reach full maturity, by capturing photons from the sun through photosynthesis day after day.*

*It then needs **millions of years**, and every proper condition, for a tree to become fossil fuels.*

*However, burning out those fuels might only take **seconds**.*

Fortunately, we have found a time-saving and environment-friendly approach to capture photons and utilize the solar energy by photovoltaic technologies.

*It will take you couples of **minutes** (most likely) or **hours** (my honor) to explore the most recent development in photovoltaic windows in this dissertation, which took the author more than **four years** to accomplish.*

Parts of this chapter have been published in Applied Energy **228**, 1454 (2018) [1].

Current photovoltaic (PV) industrial chain mainly serves the conventional utility-scale PV power stations. Rigid and opaque silicon-based PV modules domain the market so far. As distributed PV capacities expand, PV modules tend to be integrated with existing infrastructures (mostly, buildings). To adapt with the building environment, innovative design is required from the cell level to the system level. This dissertation specially deals with the window-integrated photovoltaics. In this introduction, the global energy situation and the concise history of photovoltaic technologies are presented as background knowledge. The major topic, building-integrated PV windows, is then briefly introduced and explained in detail regarding the distinct features from conventional PV stations. The aim, scope, and outline of this dissertation is finally addressed.

1.1. SOLAR ENERGY AND PHOTOVOLTAICS

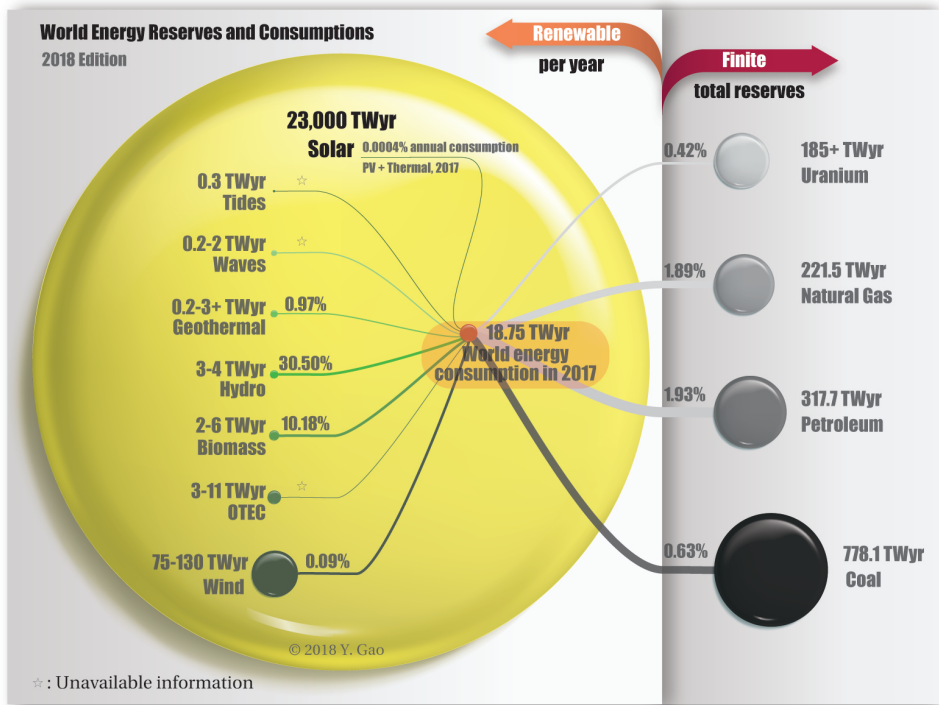


Figure 1.1: The world energy reserves and consumptions in 2017. The area of discs represents the energy reserves. Above the lines are annual consumptions in 2017 as a percentage of reserves [2–4].

HUMAN beings consume 18.75 TWyr^1 energy worldwide in 2017 [4]. This figure has increased by 41.04% since 2000 [4], and is predicted to reach 23.87 TWyr in 2040 [5]. The continuous increase of global energy demand is challenging the limited energy resources on this planet. As of press time, traditional fossil fuels are still the primary

¹TWyr is the abbreviation of terawatt-year. 1 TWyr is equal to 8.76×10^{12} kilowatt hour (kWh).

energy sources of humankind. However, the shares of fossil fuels in total power generation are projected to decrease from now to 2040 [5]. The decline of fossil-fuel proportions stems from not only the depleting resources, but also the severe air pollution and carbon dioxide emission from fossil-fuel combustion [6]. According to the Paris Agreement, the world shall unite to deal with the global climate change due to greenhouse-gas emissions [7]. In this case, renewable alternatives to fossil fuels are in urgent need. Among all available energy resources on this planet, land-received solar energy is the most abundant one, even richer than the combination of all the other forms, as shown in Figure 1.1. Ideally, only a small fraction (1/1200) of land-received solar energy is sufficient to supply the worldwide energy consumption [8]. Therefore, huge efforts have been made to develop cost-efficient technologies to harvest solar energy.

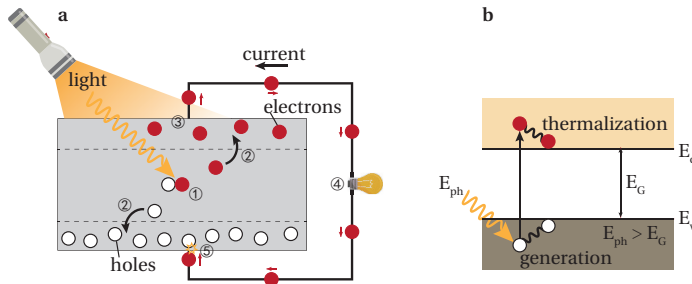


Figure 1.2: Solar cell's operating principles based on the photovoltaic effect. **a**, Flow of charge carriers in a simple model of solar cell: ① generation of electron-hole pairs, ② separation of charge carriers, ③ collection of charge carriers at the terminals, ④ extraction of electrons through the external circuit, and ⑤ recombination of electron-hole pairs. **b**, Band diagram of charge carriers. Figure is adapted from [9].

In fact, most of the commonly-used energy sources by human beings come indirectly from the sun, e.g., fossil fuels, wind energy, biomass, etc. They usually form naturally in a low conversion efficiency and through a long cycle. In 1839, the French physicist Alexandre-Edmond Becquerel discovered the photovoltaic effect, which is a phenomenon that a voltage is generated in response to radiant energy (mostly, light). Later in 1905, Albert Einstein explained the photoelectric effect² in his paper, which earned him the Nobel Prize in 1921 because of the novel concept of wave-particle duality in the nature of light. As our knowledge of light and semiconductors grows, various PV technologies have been developed based on the most fundamental mechanism of photovoltaic effect, which is illustrated in Figure 1.2. Firstly, three steps occur within the photovoltaic materials to generate voltage between electrodes from light radiation. ① An electron is excited to a higher energy level by a photon, simultaneously creating a hole, which behaves as a positively-charged particle. In quantum theories, the energy state of an electron in the semiconductor material is not continuous, meaning that no energy state is allowed to exist between the valence band edge (E_v) and the conduction band edge (E_c), as shown in Figure 1.2b. Therefore, in the light beam containing photons

²Photoelectric effect is a phenomenon discovered by the German physicist Heinrich Hertz in 1887 that free electrons are emitted from a metal surface when light strikes it. The major difference from photovoltaic effect is that electrons are emitted to the space, not directly enter a new material.

with various energies (E_{ph}), only those with E_{ph} larger than the bandgap ($E_g = E_c - E_v$) of the ideal semiconductor materials can create electron-hole pairs. ② Charge carriers (electrons and holes) are separated based on certain mechanisms depending on the photovoltaic technologies. ③ Charge carriers are collected at the terminals, where a potential difference is created in between. Till now, a voltage is formed between two electrodes and the mechanism of photovoltaic effect has been briefly explained. Secondly, two further steps are taken to generate electricity in the external circuit. ④ Electrons are extracted from the electrode and used to drive an electric circuit. ⑤ Passing through the loads, electrons combine with holes at the other electrode. Together, five steps have explained the working principle of solar cells based on photovoltaic effects.

In 1954, the first modern solar cell was developed in the Bell Laboratories in the United States. The silicon-based solar cell showed an power conversion efficiency (PCE) of about 6% [10]. In 1985, the PCE of crystalline silicon (c-Si) solar cells had exceeded 20%, which was demonstrated at the University of New South Wales. As of press time, the most efficient non-concentrator single-junction solar cell was fabricated with thin-film crystal gallium arsenide (GaAs), which holds the record PCE of 29.1% [11]. However, GaAs is an expensive material, which is also carcinogenic for humans. Therefore, it is mostly used in space technologies or military applications. Nowadays, c-Si solar cells dominate the PV market, representing more than 90% market share. Among them, the most efficient type (non-concentrator, and single-junction) is the silicon-based hetero-junction solar cell, with a record PCE of 26.6% [11]. As the PCE improves and the module costs reduce, photovoltaic prices have fallen from \$76.67 per watt in 1977 to \$0.23 per watt in 2017 [12]. In some regions, the LCOE³ of photovoltaic solar energy is already cheaper than the price of grid electricity [13].

In general, current photovoltaic technologies fall into three categories. They are listed below with the record efficiency⁴ (non-concentrator, and single-junction) to date marked in subsequent brackets.

- Wafer-based cells, including traditional *crystalline silicon (c-Si, 26.6%)* and *gallium arsenide (GaAs, 29.1%)*, which is a thin film of GaAs separated from a GaAs wafer.
- Commercial thin-film cells, including *amorphous silicon (a-Si, 14.0%)*, *cadmium telluride (CdTe, 22.1%)*, and *copper indium gallium (di)selenide (CIGS, 22.9%)*.
- Emerging thin-film cells, including *perovskite (24.2%)*, *organic (15.6%)*, and *quantum dot (QD, 16.6%)*.

In 2017, cumulative PV capacity reached almost 398 GW and generated over 460 TWh, accounting for about 2% of global power output. As predicted by the International Energy Agency (IEA), those numbers will keep going up in the next five years, as shown in Figure 1.3. Till 2023, the cumulative PV capacity and annual generation will both be around 2.8 times that of 2017, according to the optimistic estimates [2]. In the future, photovoltaic will be one of the most promising renewable energy resources, as boosted by the policies and the market.

³Levelized Cost of Electricity (LCOE), representing the total cost to build and operate an energy producing source over its anticipated lifetime divided by the total amount of electricity produced.

⁴See Appendix A “Best Research-Cell Efficiencies” for detail.

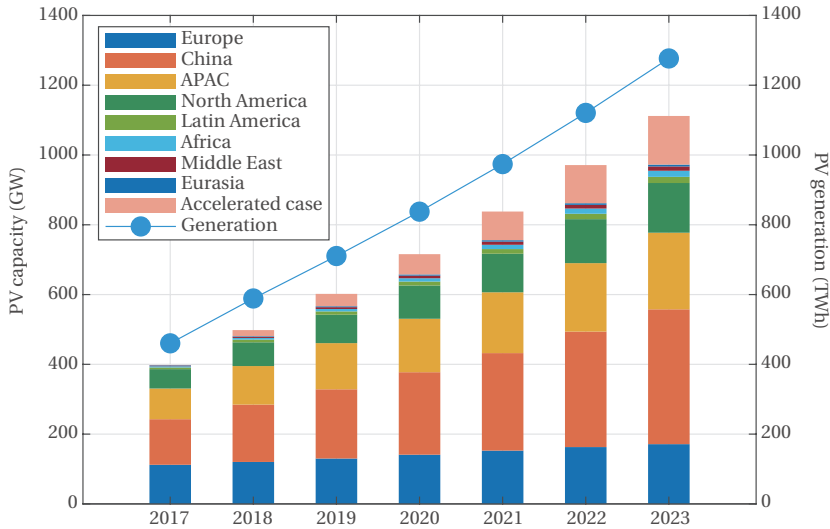


Figure 1.3: Diagram of cumulative PV capacity (bar) and annual PV generation (dot) from 2017 to 2023, main and accelerated cases [2].

1.2. BUILDING-INTEGRATED PHOTOVOLTAIC WINDOWS

As estimated, the world's entire primary energy demand can theoretically be met by installing today's photovoltaic products in less than a tenth of the area of the Sahara [14]. However, large-scale photovoltaic coverages could lead to regional and global climate change, in terms of temperature, precipitation, atmospheric circulation, etc. [15]. In contrast, a more decentralized installation of PV panels in urban areas will result in less impact on the regional and global climate [15]. Commonly, but not universally, distributed photovoltaics refer to electricity-generating PV systems with a rated capacity of 100 kW or less [16]. It is projected by IEA that the net additions of distributed PV capacity will increase fast in the next five years, as shown in Figure 1.4. Compared with utility-scale types, distributed PVs can reduce the transmission losses and allow for flexible installations integrated with existing infrastructures. In urban areas, buildings provide not only convenient environment for photovoltaic installation, but also local loads for power consumption. Therefore, building-integrated photovoltaics (BIPVs) have been considered to be a promising form of distributed PVs. Note that a building in this dissertation refers to a structure which serves not just limited to humans, but also plants or animals.

Globally, more than a third of energy consumption is attributable to the building sector [17]. In developed regions, those numbers are even higher (39% for U.S. and 40% for Europe) [18]. Reducing the consumption of building energy generated from fossil fuels helps alleviate the air pollution and global warming. Some European countries even regulate that all new buildings shall be nearly zero energy buildings (ZEBs) by the end

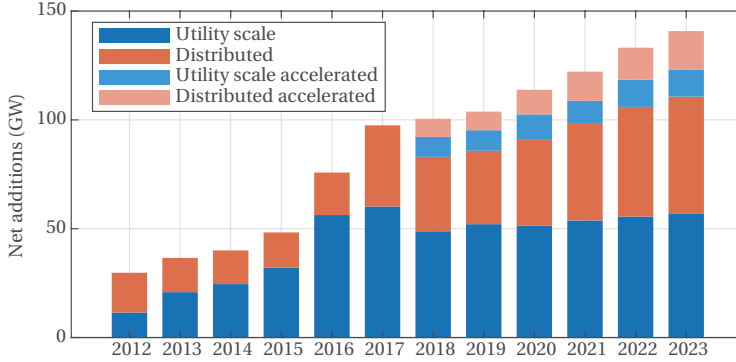


Figure 1.4: Net additions of solar PV capacity from 2012 to 2023, main and accelerated cases [2].

of 2020 [19]. Apparently, local energy harvesting is required to realize this goal. Among all realistic strategies, BIPV is an obvious choice for those regions with adequate solar radiation.

According to the mounting positions of buildings, BIPV can be classified into roof, wall, and glass-attached types. As predicted, the global market of BIPV will reach nearly \$7 billion in 2026 [17]. By then, the glass-attached PV accounts for the largest proportion among the three categories, as shown in Figure 1.5. It means that the potential BIPV market in the window areas of the buildings is huge. In this dissertation, a photovoltaic window refers to a daylight-management apparatus with photovoltaic solar cells, modules, or systems embedded on, in, or around a window of the building [20, 21].

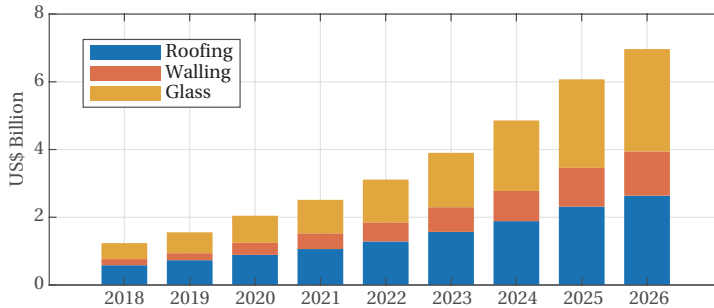


Figure 1.5: Predicted worldwide BIPV market revenue. Figure is adapted from [17].

PV windows take full advantage of vertical space in congested urban areas, where available horizontal lands are scarce, and local energy consumptions are tremendous. To evaluate the equivalent horizontal area (EHA) of available vertical surfaces of buildings, we define $R_{v/h}$ as the ratio of the annual solar energy received on the sunward (e.g. equator-facing for temperate zones) vertical unit area to that received on the horizontal

Table 1.1: $R_{v/h}$ of nine selected cities around the world

City	$R_{v/h}$
Shanghai	0.8717
New York City	0.9128
Tokyo	0.9345
Beijing	0.9629
London	1.0233
Los Angeles	0.7799
Toronto	0.9289
Paris	0.9669
Berlin	1.0181

unit area, i.e.,

$$R_{v/h} = \frac{\int G_{v,global}(t) dt}{\int G_{h,global}(t) dt}, \quad (1.1)$$

where $G_{v,global}$ indicates the global irradiance on a sunward vertical plane; and $G_{h,global}$ indicates the global irradiance on a horizontal plane. The integration time here is an entire year (365 days). According to reliable climate data [22], the calculated value of $R_{v/h}$ for Shanghai is 0.8717. More specifically, the EHA of the highest skyscraper (632 m) in Shanghai equals to the area of 3.5 standard football fields, which occupy 15.6-fold horizontal areas as the building does [1]. $R_{v/h}$ for nine selected cities is calculated and shown in Table 1.1. Considering all the urban high-rise buildings around the world, vertical area holds enormous potential for the utilization of solar energy, especially the window area, which is relatively large in modern buildings.

The nature of PV windows is to manipulate photons in order to turn incident light partially into electricity and partially into transmitted light. Most reported approaches are implemented by integrating opaque PV with window treatments⁵; or by integrating transparent [23], semi-transparent [24], regionally transparent PV [25], or light-directed materials [26] with window glazing. As shown in Figure 1.6, diverse possibilities of PV windows are illustrated by existing products, demonstrations, and devices. This dissertation mainly focuses on the discussion of opaque PV window shading elements and semi-transparent PV window glazing.

1.3. MORE THAN POWER GENERATION

UNLIKE traditional centralized PV power plants, PV windows serve as a multifunctional fraction of buildings. From the architectural point of view, power generation is just one aspect of the initial consideration of architectural design. Architects mainly consider the appearance, practicality, and user demand of the building. Therefore, the optimal design of PV windows is not limited to maximizing the power generation, but also aims to balance the dynamic built environment from the aspects of energy, photo-

⁵A window treatment is a decorating element placed on, in, around, or over a window, to achieve the function of anti-glare, heat insulation, privacy protection, aesthetics, etc.



Figure 1.6: Existing PV-window demonstrations. **a**, Smart solar blinds from SolarGaps. **b**, Adaptive solar façade at the House of Natural Resources [27]. **c**, PV greenhouse with reflective aluminum mirrors [28]. **d**, Transparent PV solar device [29].

biology⁶ and aesthetics.

Energy. Heating is one of the most direct impact of sunlight on buildings in terms of energy. The long-wavelength (infrared) portion of the solar radiation contributes to the majority of heating, which is favorable to buildings in cold winter. However, solar heating increases the cooling loads of buildings in hot summer. Such heating can be regulated by adjusting the penetration of sunlight into buildings from PV windows. PV windows can also control the amount of incident visible light. If PV windows absorbed excessive sunlight and consequently resulted in inadequate daylighting for illumination (e.g. < 500 lux for office), artificial lighting will be required to compensate the illuminance level, consuming extra electric energy. Additionally, furniture ages with excessive irradiation of short-wavelength (ultraviolet) portion of sunlight. Renovation can be considered as a special form of energy waste.

Photobiology. Solar radiation not only acts on building energy, but also affects the creatures in buildings. As for human beings, light acts on retina triggering not only vision but also circadian rhythm [30]. The ultraviolet B rays of sunlight falling on skin catalyze the production of Vitamin D [31]. Regarding most of plants, light energy transfers electrons from water to carbon dioxide, to produce carbohydrates during oxygenic photosynthesis [32]. According to the degree of user demand and light quality, there are mainly three levels of light requirements in architectural design. The most basic level is to avoid damage to humans (such as blue-light hazard [33]) and to keep plants alive. This is attainable by providing adequate, natural, and healthy light. The next level of light design would

⁶Photobiology is broadly defined to include all biological phenomena involving non-ionizing radiation.

be to provide suitable light and thermal environment for occupants (including plants). Specifically, direct sun irradiance would cause disability glare for observers [33]; and inappropriate color temperature might affect the human moods [30]. An even higher level, which requires customized light input, can improve the working efficiency [30] of users and boost the growth of plants [34]. Therefore, the living conditions of creatures in buildings are affected by PV windows, which can control the quantity and quality of incident sunlight.

Aesthetics. Rigid, rectangular, either black or blue appearance, is the primary impression of people on photovoltaic solar modules. Such conventional standard products are designed to enhance light absorption and module robustness. However, this is far from enough for architects, who expect diverse options of PV modules in terms of color, shape, transmittance, flexibility, etc. It requires interdisciplinary collaboration at the beginning of the cell development and module design. Currently, novel BIPV products have emerged in the market, such as colorful, image-printable, and even white PV modules from CSEM [35], solar tiles from Tesla [36] and Hanergy [37], etc. Those products open a new paradigm for BIPV. Since aesthetics vary from person to person, this issue will not be discussed as an academic issue in the dissertation. However, the absence of such discussions does not reduce the significance of the aesthetic issue, especially for the PV market.

Aforementioned three aspects should be considered comprehensively in the initial stages of the development of PV windows, from the semiconductor material, to solar cell, to PV module, and lastly to system levels. Those aspects are highly interconnected with respect to the overall performance of PV windows. For instance, enlarging the absorption of sunlight by PV windows may possibly reduce the incident solar irradiation, leading to the changes of energy consumption by artificial lighting, heating and cooling, meanwhile affecting the visual comfort of human or the photosynthesis of plants. Therefore, this dissertation is essentially intended to balance the contribution of solar photons to different architectural aspects.

1.4. AIM AND SCOPE OF THIS DISSERTATION

WITHIN this dissertation, scientific research has been conducted around the topic of PV windows. The aim of this dissertation is to answer the following research questions:

1. How to generate electricity in the window area of buildings by integrating photovoltaic applications?
2. What is the optimal sun-tracking position for the interior PV shading elements to achieve the maximum power generation and non-glare daylighting, and what is the optimal layout of solar cells on the slat of PV blinds?
3. How to balance the overall annual energy performance of buildings integrated with PV blinds in terms of PV power generation, artificial lighting, heating and cooling?
4. How is the PV performance across the full range of rotation angles in the greenhouses with high-density and low-density PV layouts, and how is the corresponding interior irradiance distribution?

5. How to fabricate semi-transparent thin-film amorphous silicon solar cell, and how to control the transmittance of the semi-transparent PV window?

In order to answer aforementioned questions, the following scope has been determined for this dissertation:

1. Among all categories of buildings, two types of them, high-rise buildings and glass greenhouses, are mainly studied in this dissertation. For existing high-rise buildings, we focus on the interior PV windows since exterior installations would increase the initial cost, have high requirements on wind and snow loads, and affect the appearance of the buildings. In terms of PV windows on greenhouse roofs, exterior installations are considered in our study based on the fact that greenhouses are usually not very tall buildings. Exterior roof PV installations for greenhouses are easier than vertical installations for skyscrapers. Additionally, exterior PV modules receives more solar irradiance, resulting in more electricity generation.
2. Among current available PV technologies, thin-film solar cells are envisioned as suitable candidates for interior PV windows due to their intrinsic properties, such as light-weighted, flexible, etc. This dissertation has been limited to a few thin-film PV technologies, i.e. amorphous silicon (Chapter 2, 3, and 6) and cadmium telluride (Chapter 4).
3. As for greenhouse PV application, suitable commercial products have been available in the market. In this dissertation, we choose a ultra-thin high-performance PV module, which uses the PV technology of crystalline silicon (Chapter 5).
4. To form a PV window, one or more PV technologies are integrated with conventional window treatments, e.g. blinds, shutters, shades, curtains, films, awning, etc. This dissertation mainly focuses on window blinds and films, in academic words, opaque PV shading elements and semi-transparent PV glazing.
5. It is unrealistic to include all optimization objectives in the aforementioned three aspects with respect to the performance of PV windows. Several selected critical parameters are presented in this dissertation, i.e. PV power generation, glare index, incident irradiance, incident illuminance, thermal effects, and transmitted spectrum. In each independent task, one specific parameter or a combination of them has been implemented to optimize the intended performance.
6. Modeling and simulation are the major methodologies in module-level and system-level studies. Verification experiments could be expected in further study, but not in this dissertation. As to semi-transparent solar cells, only small-area devices have been fabricated in our laboratory to demonstrate the concept.

1.5. OUTLINE OF THIS DISSERTATION

THIS dissertation is structured in seven distinct chapters, as illustrated in Figure 1.7. In this chapter, a brief introduction to solar energy, photovoltaics, and building-integrated PV windows in general is given. This chapter leads the following Chapters 2-6, each containing an independent research topic.

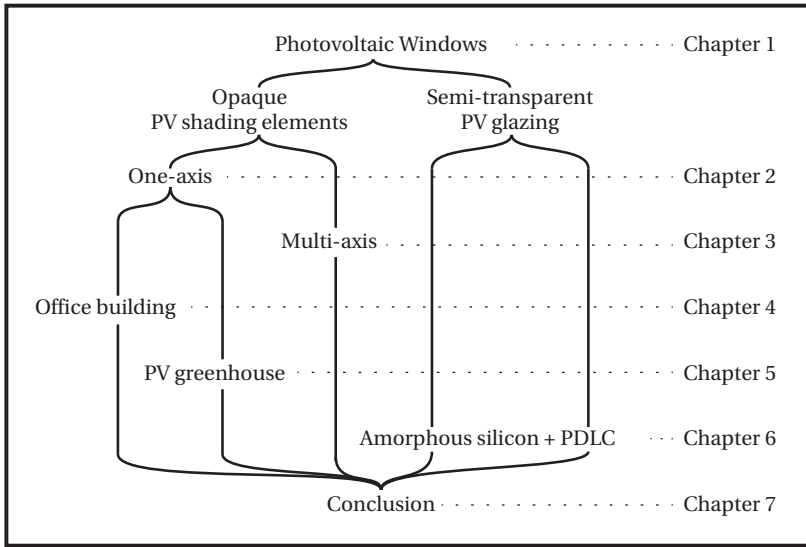


Figure 1.7: Outline of this dissertation in logical and structural sequence.

In **Chapter 2**, a mathematical model of solar irradiance and a geometrical model of a reference office are built, which are also useful in Chapter 3 and 4. Additionally, one-axis PV blinds and the total input power are modeled and analyzed in regard to annual power generation and glare protection. An optimal sun-tracking angle has been found to achieve both maximum power generation and non-glare daylighting. Optimal design of cell layout is also proposed to avoid shading from window frames.

In **Chapter 3**, PV shading elements with extra degree of freedoms (DOFs) have been modeled and analyzed in a similar way as in Chapter 2. Two-DOF PV shading elements have been proved to be the same as one-axis PV blinds in respect to optimal sun-tracking positions. PV shading elements with three-DOF sun-tracking abilities are demonstrated capable to meet all the requirements, i.e. gaining the maximum power generation, protecting from glare, and avoid shadows from the window frame. A corresponding variable-pivot three DOF (VP-3-DOF) sun-tracking algorithm is given in the form of an analytical solution.

In **Chapter 4**, the overall energy performance of the reference office with one-axis PV blinds is analyzed over an entire year. Photovoltaic power generation and power consumption by artificial lighting, heating and cooling have been fully considered.

In **Chapter 5**, PV windows are applied to the skylight in Dutch greenhouses. Unlike vertically-mounted PV windows mentioned above, the greenhouse PV panels are installed on a pitched roof to regulate the sunlight for plants, instead of humankind. PV layouts in high and low densities are evaluated under four special sun-tracking positions with regard to power generation and interior irradiance. Simulation results provide guidelines to balance the PV power generation and food production in greenhouses.

In **Chapter 6**, semi-transparent devices are fabricated to demonstrate the PV win-

dows. The incident sunlight can be tuned with PDLC films to form self-powered photo-electrochromic devices.

Chapter 7 concludes the insights throughout the dissertation. In addition, an outlook is given on PV windows.

1.6. CONTRIBUTION TO THE RESEARCH FIELD

THIS project has contributed to the developments of building-integrated PV windows in the following aspects:

- A comprehensive methodology to evaluate the annual performance of BIPV considering the PV partial shading effects.
- Optimum one-DOF sun-tracking algorithms for PV blinds with improved layout of horizontal-stripe cells.
- Optimum VP-3-DOF sun-tracking algorithms for three-DOF PV shading elements.
- Design guidance as to how to balance the power generation and interior irradiance of PV greenhouse.
- A simulation-based method to fabricate semi-transparent solar cells.

REFERENCES

- [1] Y. Gao, J. Dong, O. Isabella, R. Santbergen, H. Tan, M. Zeman, and G. Zhang, *A photovoltaic window with sun-tracking shading elements towards maximum power generation and non-glare daylighting*, *Applied Energy* **228**, 1454 (2018).
- [2] *Market Report Series: Renewables 2018, Analysis and Forecasts to 2023*, Tech. Rep. (IEA).
- [3] R. Perez and M. Perez, *A fundamental look at energy reserves for the planet*, The IEA SHC Solar Update **50** (2009).
- [4] *Global Energy Statistical Yearbook 2018*, <https://yearbook.enerdata.net/#energy-consumption-data.html>.
- [5] *BP Energy Outlook 2018 Edition*, Tech. Rep. (BP Energy Economics).
- [6] B. Obama, *The irreversible momentum of clean energy*, *Science* **355**, 126 (2017).
- [7] J. Rogelj, M. Den Elzen, N. Höhne, T. Fransen, H. Fekete, H. Winkler, R. Schaeffer, F. Sha, K. Riahi, and M. Meinshausen, *Paris Agreement climate proposals need a boost to keep warming well below 2 °c*, *Nature* **534**, 631 (2016).
- [8] F. Creutzig, P. Agoston, J. C. Goldschmidt, G. Luderer, G. Nemet, and R. C. Pietzcker, *The underestimated potential of solar energy to mitigate climate change*, *Nature Energy* **2** (2017), 10.1038/nenergy.2017.140, 1710.05957.

- [9] A. Smets, K. Jäger, O. Isabella, R. van Swaaij, and M. Zeman, *Solar Energy: The Physics and Engineering of Photovoltaic Conversion, Technologies and Systems* (UIT Cambridge, 2016) p. 488.
- [10] D. M. Chapin, C. S. Fuller, and G. L. Pearson, *A new silicon p-n junction photocell for converting solar radiation into electrical power*, *Journal of Applied Physics* **25**, 676 (1954).
- [11] *Best research-cell efficiencies*, <https://www.nrel.gov/pv/assets/pdfs/best-research-cell-efficiencies-190416.pdf> (accessed: May 2019) .
- [12] L. T. Lam, L. Branstetter, and I. L. Azevedo, *A sunny future: Expert elicitation of China's solar photovoltaic technologies*, *Environmental Research Letters* **13** (2018), 10.1088/1748-9326/aaab70.
- [13] S. Chu, Y. Cui, and N. Liu, *The path towards sustainable energy*, *Nature Materials* **16**, 16 (2016).
- [14] Q. Schiermeier, J. Tollefson, T. Scully, A. Witze, and O. Morton, *Energy alternatives: Electricity without carbon*, *Nature* **454**, 816 (2008).
- [15] A. Hu, S. Levis, G. A. Meehl, W. Han, W. M. Washington, K. W. Oleson, B. J. Van Ruijven, M. He, and W. G. Strand, *Impact of solar panels on global climate*, *Nature Climate Change* **6**, 290 (2016).
- [16] P. Komor and T. Molnar, *Prepared for TEC-UNFCCC, Bonn, Germany*, Tech. Rep. February 2015 (2015).
- [17] C. Ballif, L. E. Perret-Aebi, S. Lufkin, and E. Rey, *Integrated thinking for photovoltaics in buildings*, *Nature Energy* **3**, 438 (2018).
- [18] K. Amasyali and N. M. El-Gohary, *A review of data-driven building energy consumption prediction studies*, *Renewable and Sustainable Energy Reviews* **81**, 1192 (2018).
- [19] I. Sartori, A. Napolitano, and K. Voss, *Net zero energy buildings: A consistent definition framework*, *Energy and Buildings* **48**, 220 (2012).
- [20] N. Skandalos and D. Karamanis, *PV glazing technologies*, *Renewable and Sustainable Energy Reviews* **49**, 306 (2015).
- [21] Y. T. Chae, J. Kim, H. Park, and B. Shin, *Building energy performance evaluation of building integrated photovoltaic (BIPV) window with semi-transparent solar cells*, *Applied Energy* **129**, 217 (2014).
- [22] J. Remund and S. Kunz, *METEONORM: Global meteorological database for solar energy and applied climatology* (Meteotest, 1997).
- [23] R. R. Lunt and V. Bulovic, *Transparent, near-infrared organic photovoltaic solar cells for window and energy-scavenging applications*, *Applied Physics Letters* **98** (2011), 10.1063/1.3567516.

- [24] K.-S. Chen, J.-F. Salinas, H.-L. Yip, L. Huo, J. Hou, and A. K.-Y. Jen, *Semi-transparent polymer solar cells with 6% PCE, 25% average visible transmittance and a color rendering index close to 100 for power generating window applications*, *Energy & Environmental Science* **5**, 9551 (2012).
- [25] N. Sellami and T. K. Mallick, *Optical characterisation and optimisation of a static Window Integrated Concentrating Photovoltaic system*, *Solar Energy* **91**, 273 (2013).
- [26] H. Li, K. Wu, J. Lim, H.-J. Song, and V. I. Klimov, *Doctor-blade deposition of quantum dots onto standard window glass for low-loss large-area luminescent solar concentrators*, *Nature Energy* **1**, 16157 (2016).
- [27] P. Jayathissa, M. Luzzatto, J. Schmidli, J. Hofer, Z. Nagy, and A. Schlueter, *Optimising building net energy demand with dynamic BIPV shading*, *Applied Energy* **202**, 726 (2017).
- [28] A. Marucci and A. Cappuccini, *Dynamic photovoltaic greenhouse: Energy efficiency in clear sky conditions*, *Applied Energy* **170**, 362 (2016).
- [29] D. Liu, C. Yang, and R. R. Lunt, *Halide Perovskites for Selective Ultraviolet-Harvesting Transparent Photovoltaics*, *Joule*, 1827 (2018).
- [30] P. R. Boyce, *Human factors in lighting* (Crc Press, 2014).
- [31] W. B. Grant and M. F. Holick, *Benefits and requirements of vitamin D for optimal health: A review*, *Alternative Medicine Review* **10**, 94 (2005).
- [32] H. Lambers, F. S. Chapin, and T. L. Pons, *Photosynthesis*, in *Plant physiological ecology* (Springer, 2008) pp. 11–99.
- [33] J. D. Bullough, *The blue-light hazard: A review*, *Journal of the Illuminating Engineering Society* **29**, 6 (2000).
- [34] X. li Chen, Q. chang Yang, W. pin Song, L. chun Wang, W. zhong Guo, and X. zhang Xue, *Growth and nutritional properties of lettuce affected by different alternating intervals of red and blue LED irradiation*, *Scientia Horticulturae* **223**, 44 (2017).
- [35] *White solar modules*, <https://www.csem.ch/Page.aspx?pid=36617> .
- [36] *Tesla solar roof*, <https://www.tesla.com/solarroof> .
- [37] *HanTile: solar roof tile*, <https://www.hanergyamerica.com/hantile/> .

2

ONE-AXIS PHOTOVOLTAIC WINDOW BLINDS

Abstract

Vertical space bears great potential of solar energy especially for congested urban areas, where photovoltaic (PV) windows in high-rise buildings can contribute to both power generation and daylight harvest. Previous studies on sun-tracking PV windows strayed into the trade-off between tracking performance and mutual shading, failing to achieve the maximum energy generation. In this chapter, we first build integrated models which couple the performance of one-axis sun-tracking PV windows to the rotation angles. Secondly, one-axis sun tracking are mathematically proven to be not able to gain either maximum power generation or non-glare daylighting under reasonable assumptions. When the restriction of the proposed model is relaxed, however, the aforementioned goals can be achieved by the optimum one-axis sun tracking with extended PV slats and particular design of cell layout. The proposed optimum sun-tracking method also reveals great protection against sun glare.

2.1. INTRODUCTION

PV windows have been invented in varied forms, among which one of the most basic combinations is to integrate opaque solar cells with window blinds. Power generation and incident sunlight can be regulated by controlling the tilt angle of the slats covered with solar cells. In this chapter, PV shading effects have been considered through building mathematical models. Reasonable design of cell layout on the slat has been given, and optimum sun-tracking algorithms have been derived.

2.1.1. LITERATURE REVIEW ON PHOTOVOLTAIC WINDOW BLINDS

Due to the obvious feasibility of PV blinds, there exist many relevant studies, which range from simulations to field experiments. Kang et al. analyzed several parameters of a PV blind. Among a series of inclined angles (from 0° to 90° in 15° intervals), the maximum electricity production was obtained in the inclined angle of 75° . The optimal width of the PV module was half of the width of the blind to avoid PV shading effects. Moreover, the ventilation in the double-layer window façade decreased the temperature of the cavity, consequently improved the electricity production by 8.3% [2].

Kim et al. studied a combined system of a PV blind and dimmable LED lights. The PV modules (6% PCE) were attached to the blind slats. In the reference room, the slat angle was kept at 0° . Meanwhile, in the adjacent test room, the slat angle was hourly controlled to be orthogonal to the profile angle of the sunlight. The LED lighting in both rooms was automatically controlled with the feedback of photosensors in order to maintain the illuminance level of the target working plane. Experimental results showed that the PV power generation in the test room was 32% more than that in the reference room; but the energy saving of LED lighting in the test room was 35% less than that in the reference room. Due to the low efficiency of PV modules used in this study, the overall energy performance was inconclusive [3].

Bahr et al. assessed the design parameters of a PV-blind system based on a costs-benefits analysis. Two variables were considered: the ratio between the installation distance of adjacent slats to the module depth (1, 2, and 3), and the tilt angle (0° , 25° , and 60°). The profit rate of the PV blind system was calculated by considering heating and cooling loads, PV power generation with partial shading effects, daylighting and artificial lighting. Simulation results showed that the highest profit rate was obtained when the ratio was 2; and the tilt angle was 0° [4].

Mandalaki et al. investigated various typologies of PV shading systems in terms of energy efficiency and visual comfort conditions. The Brise-Soleil system was proved to be the most suitable typology to integrate PV modules. However, all typologies were assessed in a fixed position; and the tilt angle of blinds was not given [5].

Luo et al. compared the thermal performance of PV blind within a double skin façade (DSF) with that of conventional DSFs with and without shading blinds. Experimental results showed that the DSF PV blind can save 12.16% and 25.57% respectively in summer compared with those two counterparts [6].

Hu et al. conducted comparative studies on the BIPV Trombe wall systems in regard of electricity production and heating/cooling load reduction. Results showed that the PV blind-integrated Trombe wall system was superior to the glass-attached and mass wall-attached PV Trombe wall systems in terms of electricity saving and CO₂ emission

reduction [7, 8].

Hong et al. investigated the design parameters of the PV blind by nonlinearity analysis. Three design variables were mainly considered, i.e. the orientation, the width of the PV panel (from 10 mm to 50 mm in 10 mm intervals), and the season. Results showed that the PV blind with 10 mm-width PV panels revealed the best performance in terms of electricity generation and saving-to-investment ratio at year 25 because the relatively smaller width alleviated the PV partial shading effects [9].

Park et al. developed a four-node-based finite element model (FEM_{4-node}) to predict the electricity generation of the PV blind. By this means, the economic performance of the PV blind can be comprehensively analyzed for practical applications [10]. Based on FEM_{4-node}, Oh and Koo et al. improved the prediction accuracy of the model by developing a nine-node-based finite element model (FEM_{9-node}) [11, 12].

Hong et al. proposed the bi-directional control method, which eliminated the partial shading problem of PV blinds. Compared with the uni-directional control method (PV panel remained as orthogonal to the profile angle of the sunlight), the bi-directional control improved the average illuminance of the room and generated comparative electricity [13]. In a following study, Hong et al. further evaluated the bi-directional control method in regard of lighting and thermal performance. Results showed that the energy consumption of lighting and heating system were reduced, but the cooling system consumed more energy, compared with the uni-directional control method [14].

2.1.2. MOTIVATIONS AND OBJECTIVES

A common misconception is that BIPV sun tracking is to orient the PV surface perpendicular to the sun rays. This misconception stems from the sun-tracking method commonly found in conventional PV power stations, where sun trackers (or solar trackers) are used to orient flat PV panels towards the sun in order to increase the energy collection. During daylight hours, the PV panels are kept in an optimum position perpendicular to the direction of the solar radiation [15]. Theoretical explanation of ubiquitous perpendicular-sun-tracking methods resides in the basic model of the global irradiance on a tilt plane ($G_{t,global}$) [16], i.e.,

$$G_{t,global} = I_e^{dir} \cos \gamma + G_{h,d} R_d + G_{t,ground}, \quad (2.1)$$

where I_e^{dir} is the direct normal (or direct beam) irradiance (DNI) of the sunlight; γ is the angle between the PV surface normal and the incident direction of the sunlight; $G_{h,d}$ is the diffuse horizontal irradiance; R_d is the diffuse transposition factor; $G_{t,ground}$ is the ground-reflected irradiance. The product $I_e^{dir} \cos \gamma$ represents the direct irradiance on the tilt plane, i.e. $G_{t,beam}$, which is a dominant component contributing more than 90% of the global irradiance in a cloudless day [17]. The other two components, diffuse ($G_{t,d} = G_{h,d} R_d$) and ground-reflected irradiance, contribute a small proportion to the clear-sky $G_{t,global}$, and vary with the orientation of the plane. If we ignore the variations of those two components caused by the orientation and take such components as orientation-independent constants because of their small contribution, we can conclude that the maximum $G_{t,global}$ is achieved when γ equals to zero, i.e. the PV surface is perpendicular to the incident sun rays. The maximum $G_{t,global}$ leads to the maximum

incident energy per unit time, i.e. the maximum input power P_{in} , because the direct-beam-illuminated PV area S_b remains as a constant; i.e.

$$P_{in} = G_{t,global} S_b. \quad (2.2)$$

However, the perpendicular-sun-tracking method is not necessarily applicable to BIPV due to complicated building environment and multiple sun-tracking purposes. Compared with conventional sun-tracking PVs, building integrated sun-tracking PVs make a profound difference because S_b shrinks when shadows appear on the PV surface caused by adjacent elements. In this circumstance, the product of a maximum $G_{t,global}$ with a reduced S_b cannot guarantee a maximum P_{in} any more. The shadows on the PV surface not only lead to a diminished S_b , but also result in PV partial shading problems, which affect the PV performance, especially the module efficiency η_m . η_m drops dramatically when uneven shadows are found on series-connected solar cells. PV module performs the best when no shadow casts upon it. To maximize P_{out} at a given time, a straightforward way is keeping the PV surface towards the optimal orientation, where it receives the maximum P_{in} ; and no shadow appears on it, resulting in the maximum η_m (Eq. (2.3)). Therefore, one of the purposes of sun tracking is to preserve the maximum P_{out} at every tracking moment, so that the PV module generates the maximum energy E , which is the integral of P_{out} over a certain period of time t (Eq. (2.4)).

$$P_{out} = P_{in} \eta_m. \quad (2.3)$$

$$E = \int P_{out}(t) dt. \quad (2.4)$$

As to BIPV, sun tracking is not only aiming at the maximum E , but also the capability to fulfill building functions. For window treatments, two main functions are daylighting and glare protection. In a nutshell, the objectives of building-integrated solar tracking for PV windows are to receive the maximum P_{in} , to avoid shadows on the PV surface, and to enable daylighting without glare. This work focuses on the solutions to meet these objectives.

2.2. METHODS

UNLIKE the method of case study in most aforementioned literatures, in this study, a general theory of BIPV sun tracking method is developed based on modeling and simulation. Simplifications and assumptions are properly applied to the models and simulations to achieve general sun-tracking solutions in complex architectural environment. The solar irradiance model is built based on typical conditions of building windows and window treatments. The shadow position on PV shading elements is derived from basic three-dimensional rotation matrices using the knowledge of solid analytical geometry. Shadows on shading elements and inside the room are simulated and observed by SketchUp, a three-dimensional modeling software which can present realtime shadows [18]. Taking the partial shading effects into consideration, the annual energy generation is then calculated in the simulation model built by MATLAB SimuLink, using the climate database from Meteonorm, which generates accurate climate data for any place in the world [19]. Point-in-time glare is simulated in the Rhinoceros model

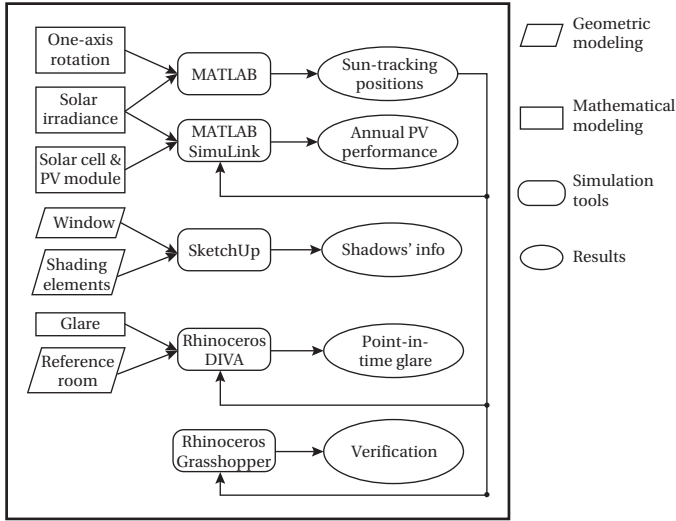


Figure 2.1: Simulation tools that have been used in this chapter.

of a reference room by DIVA and Grasshopper [20]. Rhinoceros is an accurate three-dimensional modeling tool, which contains accessible development tools and plug-ins, such as Grasshopper and DIVA. In this study, DIVA is used to simulate the point-in-time glare using various sun-tracking methods [21]. Grasshopper, a graphical algorithm editor, is used to link the movements of shading elements with the solar position [22]. The simulation tools are illustrated in relation to the models and results in this study (Figure 2.1).

2.2.1. MODEL OF SOLAR IRRADIANCE

Firstly, an equator-facing window in the sunward side of a high-rise building is defined, which is rarely shaded by surrounding objects from the sun (Fig. 2.2a). We only consider the buildings located in the temperate zone (between 23.5° and 66.5° for both north and south latitude) to ensure the sun stays the same side of the building during the PV-functioning hours for an entire year. Usually, the solar position is defined by the solar altitude α_s and the solar azimuth A_s in the horizontal coordinate system. Here, we denote the solar position by a unit vector $\mathbf{n}_s(x_s, y_s, z_s)$ in corresponding Cartesian coordinate system (Fig. 2.2b). Eq. (5.6) transforms the spherical coordinates into the Cartesian coordinates.

$$\mathbf{n}_s = \begin{bmatrix} x_s \\ y_s \\ z_s \end{bmatrix} = \begin{bmatrix} -\cos \alpha_s \cos A_s \\ \cos \alpha_s \sin A_s \\ \sin \alpha_s \end{bmatrix}. \quad (2.5)$$

Analogously, the orientation of the PV surface on the shading element is denoted by the altitude α_{PV} and the azimuth A_{PV} of the normal of the PV surface in the horizontal coordinate system, and $\mathbf{n}_{PV}(x_n, y_n, z_n)$ in the Cartesian coordinate system (Fig. 2.2d). By the aforementioned definitions, we succeed in including \mathbf{n}_{PV} and \mathbf{n}_s in the same three-

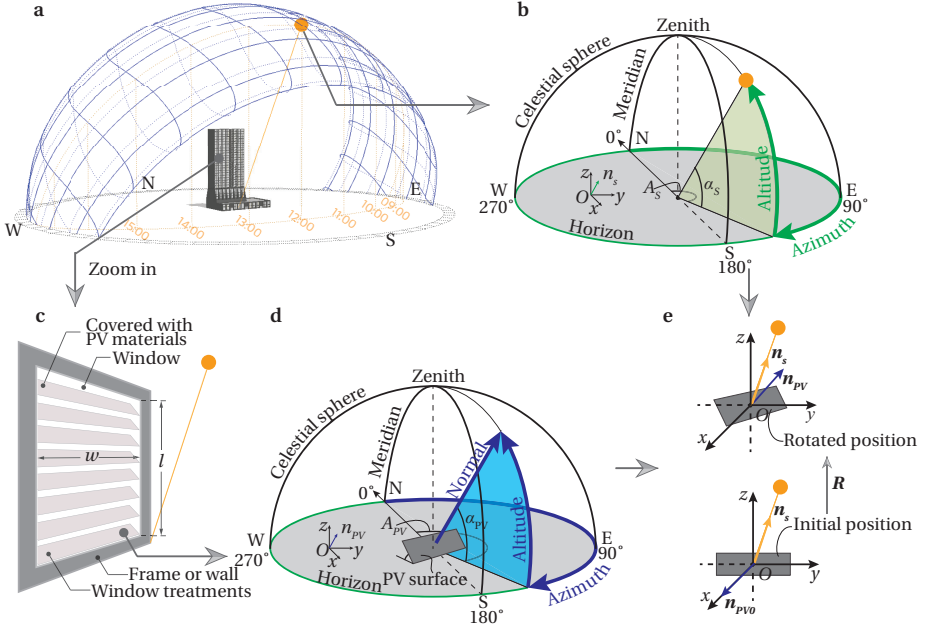


Figure 2.2: Definitions for the irradiance model.

dimensional Cartesian coordinate system (Fig. 2.2e). Since \mathbf{n}_{PV} only indicates the orientation of the PV surface instead of the exact position of the shading element, here we define the initial position of the shading element (a rectangular PV module) as a vertical plane facing equator ($\mathbf{n}_{PV0}(1, 0, 0)$), and let one side of the rectangle be parallel with the horizontal plane. An arbitrary position can be achieved from the initial position by a series of rotations, which is mathematically expressed as a rotation matrix, denoted as \mathbf{R} (Figure 2.2e). \mathbf{n}_{PV} can be derived by

$$\mathbf{n}_{PV} = \mathbf{R} \cdot \mathbf{n}_{PV0}. \quad (2.6)$$

Based on above definitions, the following assumptions are made to simplify the physical building structures and the solar radiation models. These assumptions are commonly found in similar studies [16, 23], and are not restrictive as compared with the real scenario.

1. The window is an equator-facing rectangle perpendicular to the horizontal plane. The dimensions of the window and window shading elements are given, whose thicknesses are ignored to simplify the analyses. Window shading elements are mounted interiorly behind the window glass, or within the double-pane window. The transmittance of the outer glass is high, i.e. the absorption and reflection of sunlight can be ignored. The PV window shading elements are just able to cover the whole window area for the sake of daylight control and privacy protection, i.e. the total area of PV material S_{PV} equals to wl (Figure 2.2c).

2. The shading elements in the window treatments rotate simultaneously so that they receive identical solar irradiance, which benefits the performance of series-connected mini modules. Therefore, the position of an individual shading element can be obtained from one target shading element by a simple translation.
3. The total diffuse irradiance on the PV surface from the sky, ground, and interior reflection is isotropic. In other words, the surface receives identical diffuse irradiance from any direction. The ground-reflected irradiance $G_{t,ground}$ is ignored here. We also simply take the irradiance on the shading area as the isotropic diffuse irradiance, i.e. $G_{h,d}$.

According to aforementioned definitions and assumptions, we can build an isotropic solar irradiance model for the sun-tracking PV window. Since $\cos \gamma$ equals to $\mathbf{n}_{PV}^T \cdot \mathbf{n}_s$, where the symbol T indicates the transpose operator, referring Eqs. (2.1) and (2.6), the global irradiance on the tilt PV shading element $G_{t,global}$ is derived as

$$G_{t,global} = I_e^{dir} \mathbf{n}_{PV}^T \cdot \mathbf{n}_s + G_{h,d} = I_e^{dir} (\mathbf{R} \cdot \mathbf{n}_{PV0})^T \cdot \mathbf{n}_s + G_{h,d}. \quad (2.7)$$

According to Assumption 3, the irradiance on the shading area of the PV surface is $G_{h,d}$. Therefore, the solar input power on a diffuse partially-shaded plane is derived as

$$P_{in} = G_{t,global} S_b + G_{h,d} (S_{PV} - S_b) = I_e^{dir} S_b (\mathbf{R} \cdot \mathbf{n}_{PV0})^T \cdot \mathbf{n}_s + G_{h,d} S_{PV}, \quad (2.8)$$

where S_{PV} indicates the entire PV area. In this model, the solar position (\mathbf{n}_s) of a specific date and time is predictable with the given longitude and latitude [24]; I_e^{dir} and $G_{h,d}$ are accessible climate data [19]; \mathbf{n}_{PV0} and S_{PV} are constants; S_b can be treated as a function of \mathbf{R} for certain geometrical structures of shading elements. Therefore, an optimum \mathbf{R} is the key solution to meet aforementioned objectives.

Notably, we consider that the shading elements are covered with lightweight thin-film PV materials. In industry, thin film PV modules contain series-connected solar cells formed by laser scribing technology, which makes it difficult to integrate bypass diodes. Therefore, PV modules in shadows are possible to suffer from the partial shading effects. Also, we assume the shape of solar cells is rectangular, which is the standard shape for industrial PV cells and modules, though other geometric design is possible [25].

2.2.2. MODELS OF $G_{t,global}$ AND SHADOWS ON PV BLINDS

According to Eq. (2.8), the global irradiance on the tilt PV shading element $G_{t,global}$ and shadows on PV shading elements are two key models to derive the input power P_{in} . Furthermore, shadows also affect the module efficiency η_m , then consequently affect the output power P_{out} of the PV module (Eq. (2.3)). Here, $G_{t,global}$ and shadows are studied under specific sun-tracking conditions.

The most common one-axis window treatment is a Venetian blind, which usually contains several identical rectangular slats (Figure 2.3a). In the following description of the mathematic model, one degree of freedom (DOF) refers to the rotation of the rigid PV plane around a single horizontal axis. Mathematically, we use the rotation matrix $\mathbf{R}_y(\theta_y)$ to describe such rotations (Figure 2.3b), i.e.,

$$\mathbf{R}_y(\theta_y) = \begin{bmatrix} \cos\theta_y & 0 & -\sin\theta_y \\ 0 & 1 & 0 \\ \sin\theta_y & 0 & \cos\theta_y \end{bmatrix}, \quad (2.9)$$

where the rotation is around y -axis; θ_y equals to α_{PV} . According to Eq. (2.7), $G_{t,global}$ can be derived as

$$G_{t,global} = I_e^{dir} (x_s \cos\theta_y + z_s \sin\theta_y) + G_{h,d}. \quad (2.10)$$

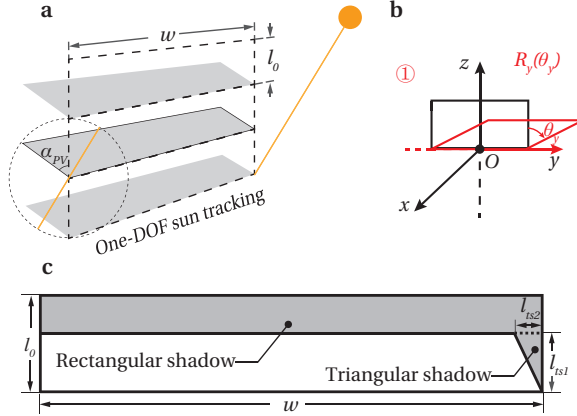


Figure 2.3: One-DOF sun tracking with a horizontal axis. **a**, A schematic of a PV blind with horizontal slats. **b**, Definition of rotation angle θ_y . **c**, A schematic of two types of shadows on the slat.

Typical shadows on the individual slat are observed as shown in Fig 2.3c. The rectangular shadow comes from the upper slat and only exists in a certain range of θ_y . The triangular shadow is cast by the window frame or wall. Here, shadows are basically determined by two parameters, l_{ts1} and l_{ts2} , as labeled in Fig 2.3c. Using the basic knowledge of solid analytical geometry, l_{ts1} and l_{ts2} are derived as shown in Eq. (2.11) and Eq. (2.12) respectively.

$$l_{ts1} = \begin{cases} l_0, & \arctan \frac{z_s}{x_s} - \frac{\pi}{2} \leq \theta_y < 0; \\ \frac{l_0 x_s}{x_s \cos\theta_y + z_s \sin\theta_y}, & 0 \leq \theta_y \leq 2 \arctan \frac{z_s}{x_s}; \\ l_0, & 2 \arctan \frac{z_s}{x_s} < \theta_y \leq \arctan \frac{z_s}{x_s} + \frac{\pi}{2}. \end{cases} \quad (2.11)$$

$$l_{ts2} = \left| \frac{l_0 y_s \sin\theta_y}{x_s \cos\theta_y + z_s \sin\theta_y} \right|. \quad (2.12)$$

The direct-beam-illuminated PV area on the individual slat S_{b0} in this model is then derived as

$$S_{b0} = l_{ts1} w - \frac{1}{2} l_{ts1} l_{ts2}. \quad (2.13)$$

2.2.3. MODEL OF SOLAR CELL AND PV MODULE

The two-diode model of the solar cell is used to simulate the PV power generation in certain conditions of irradiance. The equivalent circuit is shown in Figure 4.4, where the output current is described as

$$I = I_{ph} - I_{o1} \left[\exp\left(\frac{V + IR_s}{a_1 V_{T1}}\right) - 1 \right] - I_{o2} \left[\exp\left(\frac{V + IR_s}{a_2 V_{T2}}\right) - 1 \right] - \frac{V + IR_s}{R_p}, \quad (2.14)$$

where I_{ph} is the light-induced current. I_{o1} and I_{o2} are the reverse saturation currents of diode 1 and diode 2 respectively. V is the voltage across the solar cell electrical ports. R_s and R_p are the series and parallel resistances respectively. a_1 and a_2 are the quality factors (or called diode emission coefficients) of diode 1 and diode 2 respectively. $V_{T1,2}$ denotes the thermal voltage of the PV module having N_s cells connected in series, defined as,

$$V_{T1,2} = N_s \frac{kT}{q} \quad (2.15)$$

where k is the Boltzmann constant ($1.3806503 \times 10^{-23} \text{ J/K}$), T is the temperature of the p-n junction, and q is the electron charge ($1.60217646 \times 10^{-19} \text{ C}$). Detailed model description can be found in [26]. The solar cell model in MATLAB Simulink is simplified by 5 parameters. In this study, the model is parameterized according to the data sheet of a commercially available thin film Silicon PV module. Note that the parameters vary according to the dimensions of the target solar cell. Following simulation results are based on those parameters.

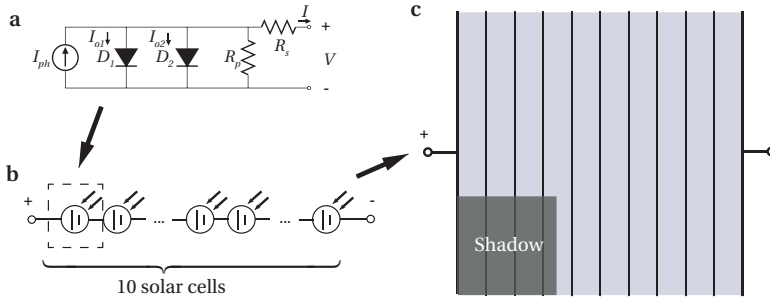


Figure 2.4: Model of solar cell and PV module in shadows **a**, An equivalent circuit diagram of the two-diode model of solar cells and **b**, A one-dimensional circuit diagram of the PV module with ten series-connected solar cells without by-pass diode. **c**, A two-dimensional circuit diagram of the PV module under shadows.

2.2.4. MODEL OF EQUIVALENT IRRADIANCE FOR PARTIAL SHADING

In reality, two types of shading conditions are commonly observed, complete and diffuse shading conditions. As shown in Figure 2.5a, the irradiance of the shading area is zero when it comes to the complete shading condition, e.g. a leaf on the PV panel. As to the diffuse shading condition, the shading area still receives the solar irradiance, e.g. the shadow of a tree on the PV panel. As shown in Figure 2.5b, we simply take the horizontal diffuse irradiance $G_{h,d}$ as the solar irradiance on the diffuse shading area.

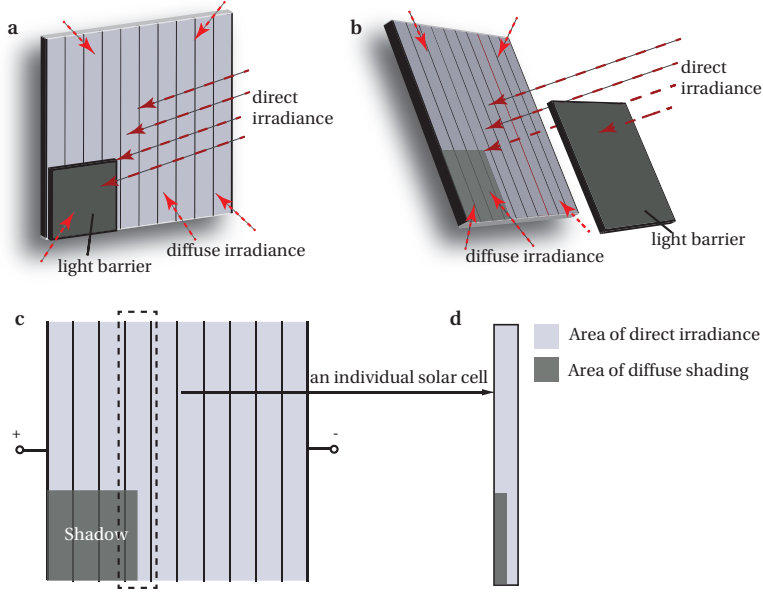


Figure 2.5: Partial shading on the PV module **a**, Complete shading condition. **b**, Diffuse shading condition, where the irradiance of shading area equals to the diffuse irradiance. **c**, PV module under the diffuse shading condition, as illustrated in **b**. **d**, Direct illuminated and diffuse shading area on an individual solar cell.

To simulate the partial shading effects, the equivalent global irradiance $G_{t,global}^{eq}$ of an individual solar cell is derived as

$$G_{t,global}^{eq} = \frac{I_e^{dir} \mathbf{n}_{PV}^T \cdot \mathbf{n}_s S_b^i + G_{h,d} S_{PV}^i}{S_{PV}^i} = \frac{S_b^i}{S_{PV}^i} I_e^{dir} \mathbf{n}_{PV}^T \cdot \mathbf{n}_s + G_{h,d} \quad (2.16)$$

where S_b^i is the direct-beam-illuminated area on the individual solar cell (Figure 2.5c & d). S_{PV}^i is the total area of the individual solar cell. $G_{t,global}^{eq}$ is a critical input of the partial-shading simulation. S_b^i can be derived by the aforementioned models of shadows under different sun-tracking methods.

2.2.5. GLARE MODEL

To evaluate the visual comfort under different sun-tracking methods, the Rhinoceros model of a reference room is used in this study [20]. In this model, point-in-time glare are calculated by DIVA, a highly optimized daylighting and energy modeling plug-in for Rhinoceros [21].

Currently, there is a number of different indices for assessing visual comfort [27]. In this study, we use Unified Glare Rating (UGR) and Discomfort Glare Probability (DGP) to evaluate the level of glare.

CIE's Unified Glare Rating (UGR) is defined as

$$UGR = 8 \log_{10} \left[\frac{0.25}{L_b} \sum_{i=1}^N \left(\frac{L_{s,t}^2 \omega_{s,t}}{P_i^2} \right) \right]. \quad (2.17)$$

subject to $\omega_s \in [3 \times 10^{-4}, 10^{-1}]_{sr}$

where the subscript s is used for those quantities depending on the observer position and i for those quantities depending on the light sources. L_b is the background luminance. $L_{s,t}$ is the luminance in the direction connecting the observer with each source. $\omega_{s,t}$ is the solid angle subtending the source i from the position of the observer. P is the Guth position index, expressing the dependence of perceived discomfort glare on the position of the source i with respect to the observer. UGR ranges between 10 (imperceptible) to 34 (intolerable) with a three-unit step [27].

Discomfort Glare Probability (DGP) is defined as

$$DGP = 5.87 \times 10^{-5} E_v + 0.0918 \log_{10} \left[1 + \sum_{i=1}^N \left(\frac{L_{s,t}^2 \omega_{s,t}}{E_v^{1.87} P_i^2} \right) \right] + 0.16, \quad (2.18)$$

where E_v is the vertical eye illuminance. DGP reveals a strong correlation with the user's response regarding glare perception [27].

2.3. RESULTS

Table 2.1: Typical climate data used for calculation and simulation

Parameters	Data
Location	31.17°N, 121.43°E (Shanghai)
Time	11:00 (local time, UTC + 8)
Date	20th March (March equinox)
Year	2017
α_s	55.63°
A_s	152.72°
I_e^{dir}	1000 W/m ²
$G_{h,d}$	100 W/m ²
l	1 m
w	1 m
l_0^*	0.1 m

* l_0 indicates the length of the one-DOF slat in Figure 2.3a.

TO give the optimum sun-tracking solutions, a typical set of climate data of Shanghai (see Table 2.1) is used for the calculation and simulation of $G_{t,global}$, S_b , P_{in} , and point-in-time glare under all possible sun-tracking positions. Then, accumulated power generation (E_a) and average efficiency ($\bar{\eta}_m$) over the year under conventional and the proposed optimum sun-tracking methods are simulated and compared. Lastly, results of nine global cities are obtained to conclude a general improvement of E_a and $\bar{\eta}_m$ by using the proposed method.

2.3.1. PHOTOVOLTAIC PERFORMANCE UNDER (PARTIAL) SHADING

Based on the aforementioned partial shading model and example data set, the output power of the mini PV module is simulated under various conditions of shadows. As shown in Figure 2.6, the results show that the PV module performs the best when no shadow casts upon it. Note that the real geometry of the mini PV module on the slat is not necessarily like this. Besides, η_m drops dramatically when uneven shadows are found on series-connected solar cells. The performance of PV power generation is less affected by diffuse shadows than that by complete shadows with the same dimensions.

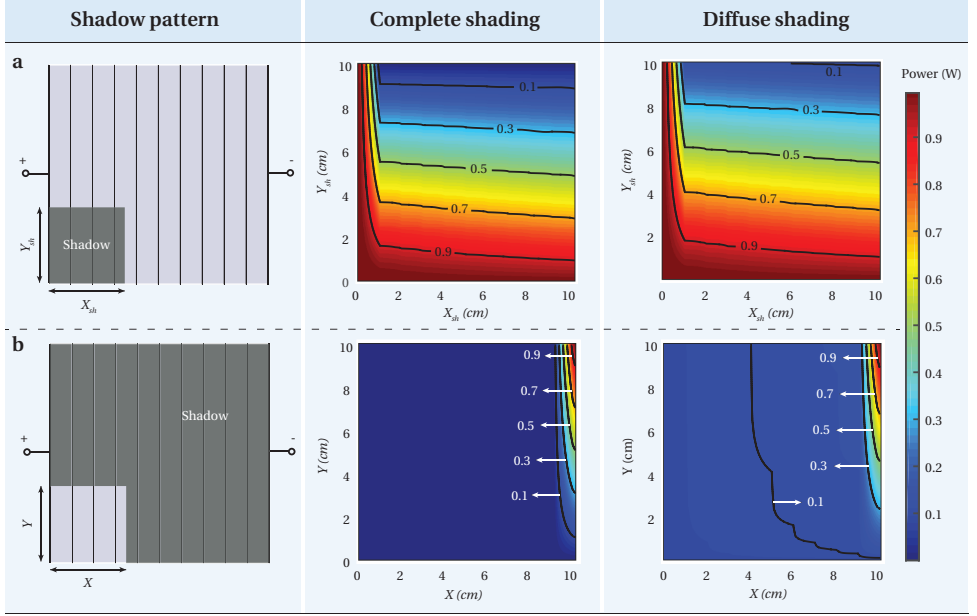


Figure 2.6: Simulation results of PV partial shading effects. **a**, PV module under a rectangular shadow with dimension of X_{sh} and Y_{sh} , and corresponding color maps of PV power generation under two different shading conditions. **b**, PV module under a rectangular illuminated area with dimension of X and Y , and corresponding color maps of PV power generation under two different shading conditions.

As discussed in the model of one-DOF PV blind, rectangular and triangular shadows are observed in the typical shading conditions. Usually, the area of triangular shadow on a long narrow slat is negligible due to its relatively small size. Therefore, Eq. (2.13) is simplified as

$$S_{b0} = l_{ts1} w. \quad (2.19)$$

In this case, according to Eq. (2.8), the input power P_{in} for all slats in the PV blind is derived as

$$P_{in} = \begin{cases} I_e^{dir} l w (x_s \cos \theta_y + z_s \sin \theta_y) + G_{h,d} l w, & \arctan \frac{z_s}{x_s} - \frac{\pi}{2} \leq \theta_y < 0; \\ I_e^{dir} l w x_s + G_{h,d} l w, & 0 \leq \theta_y \leq 2 \arctan \frac{z_s}{x_s}; \\ I_e^{dir} l w (x_s \cos \theta_y + z_s \sin \theta_y) + G_{h,d} l w, & 2 \arctan \frac{z_s}{x_s} < \theta_y \leq \arctan \frac{z_s}{x_s} + \frac{\pi}{2}. \end{cases} \quad (2.20)$$

We notice that P_{in} is independent of l_0 , the length of the individual slat. It means that the number of slats does not affect P_{in} as long as the dimension of the window is given and the triangular shadows are ignored. We also notice that P_{in} remains maximum when $\theta_y \in [0, 2 \arctan(z_s/x_s)]$, which means the quasi-perpendicular position ($\theta_y = \arctan(z_s/x_s)$) where $G_{t,global}$ reaches the peak is not the only option for the maximum P_{in} . To better illustrate $G_{t,global}$, S_b , and P_{in} in different tilt positions, a set of example data is introduced (see Table 2.1) to draw the semicircular color maps (Figure 2.7b, c, d).

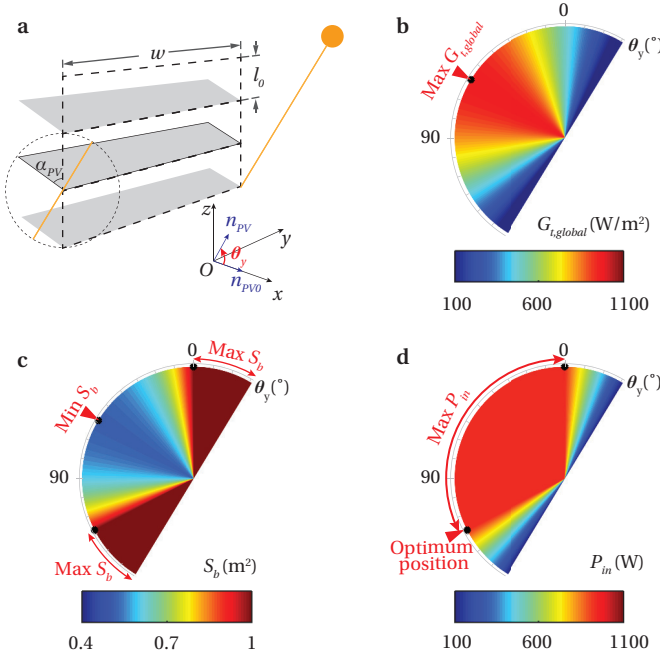


Figure 2.7: Simulation results of all possible one-DOF sun tracking positions. **a**, A schematic of a PV blind with rotation angle θ_y . **b**, A semicircular color map of $G_{t,global}$ as a function of θ_y . **c**, A semicircular color map of S_b as a function of θ_y . **d**, A semicircular color map of P_{in} as a function of θ_y .

Referring to Eq. (2.3), the maximum P_{out} is gained with the maximum P_{in} and η_m , i.e. no shadow on the PV plane ($S_b = S_{PV}$). In regard to this one-DOF PV blind, the optimum position is located where θ_y equals to 0 or $2 \arctan(z_s/x_s)$. However, $\theta_y = 0$ means the blind stays in the closed position forever, which is not appropriate, because it turns the window into a PV wall and disables the function of daylighting. Therefore, the only feasible option of the optimum θ_y is $2 \arctan(z_s/x_s)$.

Shadow simulation in a SketchUp [18] model (Figure 2.8) demonstrates that this optimum θ_y can effectively avoid rectangular shadows from upper slats. However, it cannot eliminate triangular shadows from window frames. Such triangular shadows are ignored when we estimate P_{in} because of the small area. But they cannot be ignored regarding η_m due to partial shading effects of PV modules. What is worse, on the other side of the blind, incident sunlight forms glare zones in the interior space. We have also tested the PV blind with vertical slats, whose optimum position ($\theta_z = 2(\pi - A_s)$) cannot avoid tri-

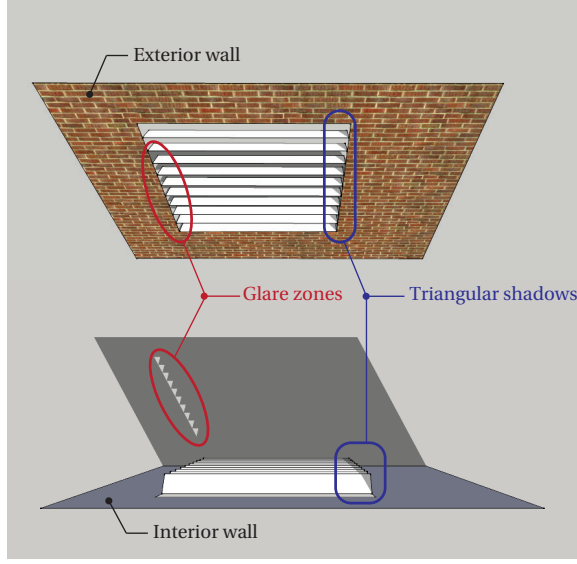


Figure 2.8: Shadow simulation of the optimum position of one-DOF shading elements by SketchUp [18]. Interior glare zones (red) and triangular shadows (blue) on the slats are marked.

angular shadows and glare zones either. Therefore, we conclude that PV window treatments with one DOF are not able to achieve the maximum P_{out} and not able to avoid glare in the optimum position in the proposed model. Despite the restrictions of this model, improved design of the one-DOF PV blind will be discussed in the next section.

2.3.2. OPTIMAL DESIGN OF CELL LAYOUTS

When inevitable shadows are cast on the PV modules, the layout of solar cells determines how serious the PV module suffers from the partial shading effects. In terms of the one-DOF sun tracking, triangular shadows caused by walls and window frames are inevitable. In this case, the cell layouts of vertical stripes (Fig 2.9a) and horizontal stripes (Fig 2.9c) are affected by partial shading effects. Obviously, vertical stripes suffers more since the series current is limited by the most shaded cell. To alleviate the decrease of PV module efficiency, optimal layouts are applicable if the restriction in Assumption 1 (PV area equals to wl) is relaxed. In regards to vertical stripes, we can leave the shading area blank, i.e. without covering the solar cells (Fig 2.9b). The length of blank area is $2l_{tri}$, where the side length of the triangular shadow l_{tri} is derived as

$$l_{tri} = \left| \frac{y_s}{x_s} \sin \theta_y \right| l_0. \quad (2.21)$$

To avoid shadows, the actual l_{tri} shall be the maximum value among all possible l_{tri} over the entire year. As to horizontal stripes, we can extend the width of the slats to w' (Fig 2.9d), where

$$w' = w + 2l_{tri}. \quad (2.22)$$

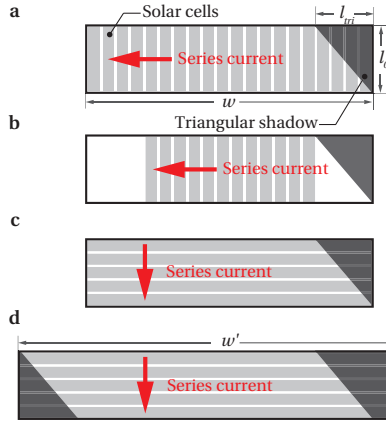


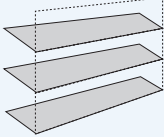
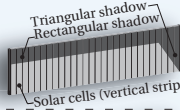
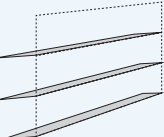
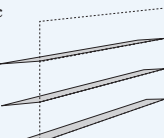
Figure 2.9: Optimization of cell layouts for one-DOF sun tracking. **a**, A PV slat with vertical stripes, suffering from the partial shading effects caused by the triangular shadow. **b**, An improved PV slat with vertical stripes, avoiding the influence by the triangular shadow. **c**, A PV slat with horizontal stripes, suffering from the partial shading effects caused by the triangular shadow. **d**, An improved PV slat with horizontal stripes, avoiding the influence by the triangular shadow and able to achieve the maximum power generation without causing glare interior, but consuming more PV materials.

Theoretically, the improved layout of horizontal stripes is able to achieve the maximum power generation and non-glare daylighting with one-DOF sun tracking ($\theta_y = 2\arctan(z_s/x_s)$). However, the extension of slats costs more PV material, whose area is $2l_{tri}l$ for the window.

2.3.3. ANNUAL PHOTOVOLTAIC PERFORMANCE

To evaluate the performance of different sun-tracking methods and cell layouts, the annual energy generation and average module efficiency are calculated using the climate database from Meteonorm. By inputting a set of $G_{t,global}^{eq}$ for each solar cell in the PV module, the simulation models generate hourly output power and module efficiency. Then the annual energy generation per unit area (E_a) and the annual average efficiency ($\bar{\eta}_m$) of the PV module can be calculated. The simulation results of two sun-tracking methods and two cell layouts are obtained by using the climate data of Shanghai, as shown in Figure 2.10. It is obvious that the improved layout with optimum sun-tracking method performs better than others in all the aspects of annual energy generation, annual average efficiency, and glare protection. Compared with conventional perpendicular sun tracking, the proposed sun tracking methods improve the annual energy generation by 12.00% and the annual average efficiency by 8.52%. Though the optimum one-DOF sun tracking with unextended horizontal stripes shows competitive results in aspect of E_a and $\bar{\eta}_m$, it cannot protect glare from the sun properly. Besides, the PV performance of the optimum one-DOF sun tracking with unextended horizontal stripes depends on the ratio of the width (w) to the side length (l_0) of the slat, i.e. R_{w/l_0} (Figure 2.11). E_a and $\bar{\eta}_m$ drop dramatically with the decrease of R_{w/l_0} , and they cannot reach the max value. Note that here we ignore the power generation by the extended shading

area due to the low diffuse irradiance. Therefore, we conclude that the improved layout design with optimum one-DOF sun tracking is capable to gain the maximum annual energy generation and annual average efficiency, and also capable to protect glare from the sun.

Sun-tracking method	Formula	Cell layout & shadow pattern on an individual shading element *	Annual energy generation (kWh/m ²) Annual average efficiency (%)	Glare
a  Quasi-perpendicular one-DOF sun tracking	$\begin{cases} \theta_y = \arctan \frac{z_s}{x_s} \\ \theta_z = 0 \\ \theta_n = 0 \end{cases}$	 Triangular shadow Rectangular shadow Solar cells (vertical strips)	62.33 8.80	Yes
		 Solar cells (horizontal strips)	56.51 8.30	
b  Optimum one-DOF sun tracking	$\begin{cases} \theta_y = 2 \arctan \frac{z_s}{x_s} \\ \theta_z = 0 \\ \theta_n = 0 \end{cases}$	 Triangular shadow Solar cells (vertical strips)	59.02 7.72	Yes
		 Solar cells (horizontal strips)	69.37 9.54	
c  Optimum one-DOF sun tracking	$\begin{cases} \theta_y = 2 \arctan \frac{z_s}{x_s} \\ \theta_z = 0 \\ \theta_n = 0 \end{cases}$	 Triangular shadow **	69.81 9.55	No

* Note that the number of solar cells on the individual shading element for illustration is not necessarily the same as that for simulation.

** The performance of the optimum one-DOF sun tracking with slats covered by horizontal solar cells is depending on the ratio of the width (w) to the side length (l_0) of the slat.

Figure 2.10: Simulation results of four sun-tracking methods and two cell layouts using irradiation data of Shanghai. **a**, Quasi-perpendicular one-DOF sun tracking. **b**, Optimum One-DOF sun tracking. **c**, Optimum One-DOF sun tracking with improved design of cell layouts. Note that in **c** we ignore contribution of diffuse irradiance to the extended area for simplified calculation. Therefore, the actual values of E_a and η_m in **c** shall be even more than that presented here.

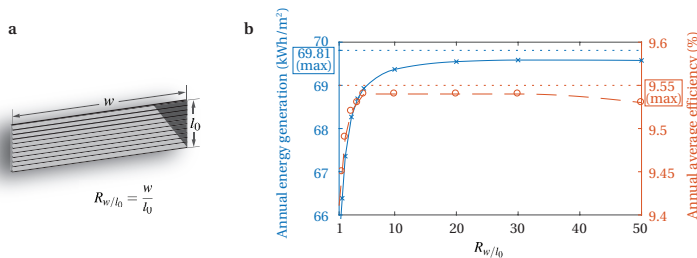
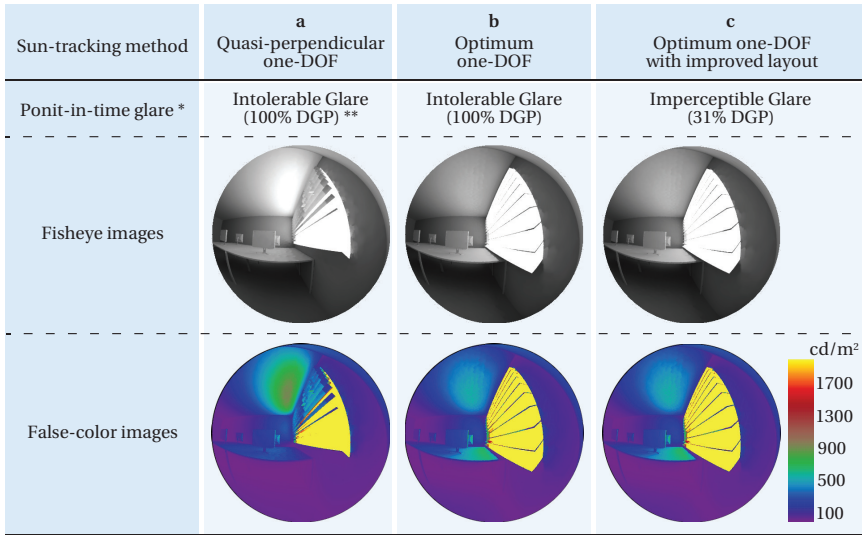


Figure 2.11: Definition and influence of R_w/l_0 . **a**, Definition of R_w/l_0 , i.e. the ratio of the width (w) to the side length (l_0) of the slat with horizontal stripes. **b**, Plots of E_a and η_m in the function of R_w/l_0 .

2.3.4. GLARE PROTECTION

The glare simulations are conducted in the position near the window of the reference office [20]. Figure 2.12 quantitatively and visually shows the simulation results based on the glare model mentioned above. Particularly, the proposed optimum solution reveals imperceptible glare and 31% DGP, which is the best among all the solutions. The results of point-in-time glare coincide with the theoretical derivations and the shadow simulations by SketchUp. Specifically, triangular direct-illuminated zones were observed in the optimum one-DOF sun tracking (Figure 2.8). It means that human eyes are possible to be exposed under the direct sunlight. Among the candidate solutions, only the improved layout with the optimum one-DOF sun tracking is capable to completely block the direct sunlight, resulting in comfortable diffuse daylighting environment inside the room.



* Simulation conditions: 11:00 AM, 20th March, 2017, clear sky, in the reference office, in Shanghai.

** Point-in-time glare is evaluated by discomfort glare rating (DGR) and daylight glare probability (DGP).

Figure 2.12: Simulation results of point-in-time glare by three possible solutions.

2.4. DISCUSSION

IN reality, the PV shading elements in our models could be PV blinds (one DOF). The PV shading system can be installed within the cavity of a double-pane window in new buildings, or simply mounted in the interior window area of existing buildings, just like the installation of conventional window blinds. The size of the PV slats should be customized according to the dimensions of windows. The optimum sun-tracking position can be obtained by $\theta_y = \arctan(z_s/x_s)$ (one DOF) with the given solar position. The real-time solar position can be calculated through the solar position algorithms [24] by preset information, i.e. date, time, longitude and latitude of the building, and azimuth of the window. A sun sensor can alternatively provide the solar position by realtime monitoring. The flowchart of calculating the optimum sun-tracking position illustrates how to

implement the sun-tracking algorithm in practical applications (Figure 2.13).

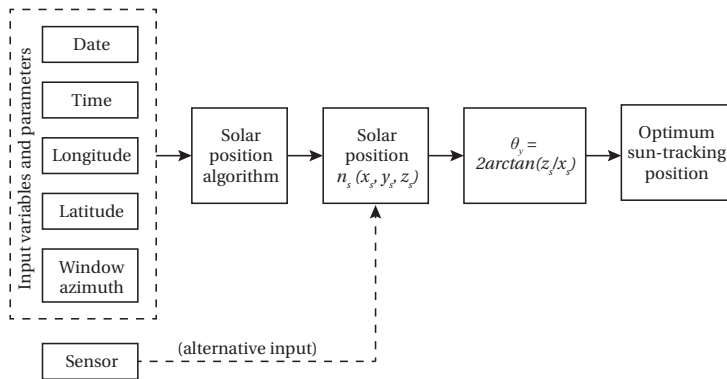


Figure 2.13: Flowchart of determining the one-DOF optimum sun-tracking position.

The PV-generated electricity can be supplied to direct-current (DC) appliances by a charge controller or alternating-current (AC) appliances by an inverter. The surplus electricity generation can be stored in local battery banks or be sold to the grid. The PV shading system can also be coupled with artificial lighting, heating and cooling systems. Besides the automatic sun-tracking mode, occupants also have demands for manual control of the PV shading elements. For example, PV shading elements should stay closed (the initial position) when occupants intend to dim the light or when privacy is required. Also, open positions are in need when occupants desire the sunshine or the outside view. Once manual control is involved, the PV power generation is no longer the primary goal of the PV shading system.

2.5. CONCLUSIONS

IN this chapter, we have investigated the performance of the one-degree-of-freedom (one-DOF) sun tracking using our proposed irradiance model. The optimum one-DOF sun tracking with the improved layout of horizontal stripes enables the sun-tracking PV window to achieve the maximum power generation and non-glare daylighting at the same time. Compared with conventional quasi-perpendicular sun tracking, the proposed sun-tracking methods improve the annual energy generation by 12.00% and the annual average efficiency by 8.52%. Such module-level improvements are more pronounced than that triggered by new materials and process in most studies. The PV blinds with optimum one-DOF rotation require a simple mechanical structure, but cost more PV materials.

REFERENCES

- [1] Y. Gao, J. Dong, O. Isabella, R. Santbergen, H. Tan, M. Zeman, and G. Zhang, *A photovoltaic window with sun-tracking shading elements towards maximum power generation and non-glare daylighting*, *Applied Energy* **228**, 1454 (2018).

- [2] S. Kang, T. Hwang, and J. T. Kim, *Theoretical analysis of the blinds integrated photovoltaic modules*, in *Energy and Buildings*, Vol. 46 (2012) pp. 86–91.
- [3] S. H. Kim, I. T. Kim, A. S. Choi, and M. Sung, *Evaluation of optimized PV power generation and electrical lighting energy savings from the PV blind-integrated daylight responsive dimming system using LED lighting*, *Solar Energy* **107**, 746 (2014).
- [4] W. Bahr, *A comprehensive assessment methodology of the building integrated photovoltaic blind system*, *Energy and Buildings* **82**, 703 (2014).
- [5] M. Mandalaki, T. Tsoutsos, and N. Papamanolis, *Integrated PV in shading systems for Mediterranean countries: Balance between energy production and visual comfort*, *Energy and Buildings* **77**, 445 (2014).
- [6] Y. Luo, L. Zhang, X. Wang, L. Xie, Z. Liu, J. Wu, Y. Zhang, and X. He, *A comparative study on thermal performance evaluation of a new double skin façade system integrated with photovoltaic blinds*, *Applied Energy* **199**, 281 (2017).
- [7] Z. Hu, W. He, J. Ji, D. Hu, S. Lv, H. Chen, and Z. Shen, *Comparative study on the annual performance of three types of building integrated photovoltaic (BIPV) Trombe wall system*, *Applied Energy* **194**, 81 (2017).
- [8] Z. Hu, W. He, D. Hu, S. Lv, L. Wang, J. Ji, H. Chen, and J. Ma, *Design, construction and performance testing of a PV blind-integrated Trombe wall module*, *Applied Energy* **203**, 643 (2017).
- [9] T. Hong, C. Koo, J. Oh, and K. Jeong, *Nonlinearity analysis of the shading effect on the technical–economic performance of the building-integrated photovoltaic blind*, *Applied Energy* **194**, 467 (2017).
- [10] H. S. Park, C. Koo, T. Hong, J. Oh, and K. Jeong, *A finite element model for estimating the techno-economic performance of the building-integrated photovoltaic blind*, *Applied Energy* **179**, 211 (2016).
- [11] J. Oh, C. Koo, T. Hong, K. Jeong, and M. Lee, *An economic impact analysis of residential progressive electricity tariffs in implementing the building-integrated photovoltaic blind using an advanced finite element model*, *Applied Energy* **202**, 259 (2017).
- [12] C. Koo, T. Hong, J. Oh, and J.-K. Choi, *Improving the prediction performance of the finite element model for estimating the technical performance of the distributed generation of solar power system in a building façade*, *Applied Energy* **215**, 41 (2018).
- [13] S. Hong, A. S. Choi, and M. Sung, *Development and verification of a slat control method for a bi-directional PV blind*, *Applied Energy* **206**, 1321 (2017).
- [14] S. Hong, A. Choi, and M. Sung, *Impact of bi-directional PV blind control method on lighting, heating and cooling energy consumption in mock-up rooms*, *Energy and Buildings* **176**, 1 (2018).

- [15] H. Mousazadeh, A. Keyhani, A. Javadi, H. Mobli, K. Abrinia, and A. Sharifi, *A review of principle and sun-tracking methods for maximizing solar systems output*, Renewable and Sustainable Energy Reviews **13**, 1800 (2009).
- [16] C. A. Gueymard, *Direct and indirect uncertainties in the prediction of tilted irradiance for solar engineering applications*, Solar Energy **83**, 432 (2009).
- [17] A. Smets, K. Jäger, O. Isabella, R. van Swaaij, and M. Zeman, *Solar Energy: The Physics and Engineering of Photovoltaic Conversion, Technologies and Systems* (UIT Cambridge, 2016) p. 488.
- [18] A. Chopra, *Introduction to google sketchup* (John Wiley & Sons, 2012).
- [19] J. Remund and S. Kunz, *METEONORM: Global meteorological database for solar energy and applied climatology* (Meteotest, 1997).
- [20] Y. Gao, J. Dong, O. Isabella, M. Zeman, and G. Q. Zhang, *Daylighting simulation and analysis of buildings with dynamic photovoltaic window shading elements*, in *Solid State Lighting: International Forum on Wide Bandgap Semiconductors China (SSLChina: IFWS), 2017 14th China International Forum on* (IEEE, 2017) pp. 52–55.
- [21] J. A. Jakubiec and C. F. Reinhart, *DIVA 2.0: Integrating daylight and thermal simulations using rhinoceros 3D, DAYSIM and EnergyPlus*, Proceedings of Building Simulation 2011: 12th Conference of International Building Performance Simulation Association, 2202 (2011), arXiv:arXiv:1011.1669v3.
- [22] K. Lagios, J. Niemasz, and C. F. Reinhart, *Animated Building Performance Simulation (ABPS) - Linking Rhinoceros/Grasshopper With Radiance/Daysim*, SimBuild 2010, 321 (2010).
- [23] J. Hofer, A. Groenewolt, P. Jayathissa, Z. Nagy, and A. Schlueter, *Parametric analysis and systems design of dynamic photovoltaic shading modules*, Energy Science & Engineering, 134 (2016).
- [24] I. Reda and A. Andreas, *Solar position algorithm for solar radiation applications*, Solar energy **76**, 577 (2004).
- [25] S. Dongaonkar and M. A. Alam, *Geometrical design of thin film photovoltaic modules for improved shade tolerance and performance*, Progress in Photovoltaics: Research and Applications **23**, 170 (2015), arXiv:1303.4604.
- [26] K. Ishaque, Z. Salam, and Syafaruddin, *A comprehensive MATLAB Simulink PV system simulator with partial shading capability based on two-diode model*, Solar Energy **85**, 2217 (2011).
- [27] I. Konstantzos and A. Tzempelikos, *Daylight Glare Probability Measurements And Correlation With Indoor Illuminances In A Full- Scale Office With Dynamic Shading Controls*, International High Performance Buildings Conference, 147 (2014).

3

MULTI-AXIS PHOTOVOLTAIC WINDOW SHADES

Abstract

In the previous chapter, the frame-shading problem of PV blinds was solved by extending the PV slats. Alternatively, this issue was addressed by adding extra degree of freedoms (DOFs) in this chapter. As organized previously, models of two-DOF and three-DOF rotations are at first built. Secondly, two-DOF sun tracking is mathematically proven to be not able to gain either maximum power generation or non-glare daylighting under the strict assumptions, just like the one-DOF counterpart. Then we derive the optimum rotation angles of the variable-pivot-three-degree-of-freedom (VP-3-DOF) sun-tracking elements and demonstrate that the optimum VP-3-DOF sun tracking can achieve the aforementioned goals. Simulation results of nine global cities show that the annual energy generation and average module efficiency are improved respectively by 27.40% and 19.17% via the optimum VP-3-DOF sun tracking over the conventional perpendicular sun tracking. The proposed optimum sun-tracking method can also protect against sun glare. Additionally, the optimum VP-3-DOF sun tracking has been demonstrated to be applicable to horizontal PV windows.

Parts of this chapter have been published in Applied Energy **228**, 1454 (2018) [1].

3.1. LITERATURE REVIEW ON MULTI-AXIS PHOTOVOLTAIC WINDOW SHADES

COMPARED with one-axis PV window blinds, only a handful of literatures have been found regarding PV windows with two-DOF shading elements due to the complex structure. Those with three-DOF sun-tracking functions are rarely reported.

Most of the studies on two-DOF sun-tracking PV shading devices were based on a prototype of an adaptive solar envelope (ASE) at the ETH House of Natural Resources [2], as shown in Figure 3.1. Hofer et al. tackled the partial shading problem by adjusting the size of PV panel on the square and the distance between squares, without considering to use other sun-tracking method [3]. Jayathissa et al. chose the optimal sun-tracking method by exploring all possible dynamic PV orientations [4]. However, for simplicity, all PV panels moved simultaneously with discrete angles (15°). Therefore, it can not achieve a continuous sun tracking according to the solar position.

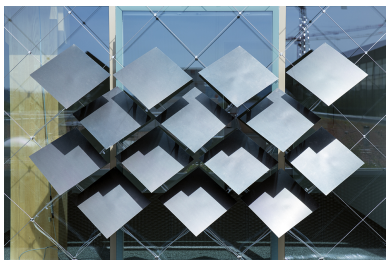


Figure 3.1: Adaptive solar panels attached to the façade of the House of Natural Resources (Copyright © ETH Zurich / Marco Carocari).

Hong et al. conducted a preliminary study on the two-axis PV blind. The slope of the PV panel ranged from 0° to 90° ; and the azimuth of the PV panel was limited in the range of -9° to 9° , as shown in Figure 3.2a. The electricity generation of the two-axis PV blind was not evaluated in this study [5]. Based on a similar setup, Koo et al. compared four types of PV blinds, i.e. amorphous silicon (a-Si) PV panels embedded in fixed blind, a-Si PV panels embedded in two-axis sun-tracking blind, copper-indium-gallium-selenide (CIGS) PV panels embedded in fixed blind, and CIGS PV panels embedded in two-axis sun-tracking blind. The conceptual diagram is illustrated in Figure 3.2b. Simulation and analysis results showed that the two-axis CIGS PV blind performed better than other alternatives in terms of energy self-sufficiency rate and net present value at year 25 [6].

3.2. TWO-DOF SUN TRACKING

3.2.1. MODEL OF TWO-DOF ROTATION

THE methodology in this chapter is basically the same as that in Chapter 2 (see Section 2.2). The multi-DOF rotation models in this work are similar to the ASE at ETH, but with no limitation of rotation angles. Dual-axis sun tracking is commonly used in PV power stations since it can maximize P_{in} by positioning PV panels perpendicular to the sunbeam [7]. In this model, two-DOF refers to free rotations of the PV shading

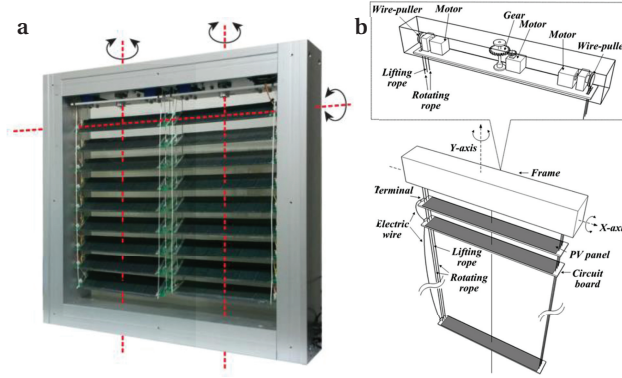


Figure 3.2: **a**, Prototype model of two-axis PV blinds (figure adapted from [5]). **b**, Conceptual diagram of the two-axis PV-blind prototype (figure adapted from [6]).

element around two axes (Figure 3.3a). To achieve free rotations around both axes, we define that shading elements are identical squares; and the centre of each square is its pivot, i.e. the cross point of two axes. According to Assumption 2 in Section 2.2, we only need to study the rotation of an individual shading element regarding solar irradiance because the positions of other squares can be obtained by simple translations due to fixed pivots. Therefore, we define the centre of the target square as the origin of the Cartesian coordinates. The altitude of the target PV square α_{PV} varies with the rotation around y -axis, denoted by the rotation matrix $\mathbf{R}_y(\theta_y)$ (see Eq. (3.3)). The azimuth of the target PV square A_{PV} is changed by the rotation around z -axis, denoted by the rotation matrix $\mathbf{R}_z(\theta_z)$, i.e.,

$$\mathbf{R}_z(\theta_z) = \begin{bmatrix} \cos\theta_z & -\sin\theta_z & 0 \\ \sin\theta_z & \cos\theta_z & 0 \\ 0 & 0 & 1 \end{bmatrix}. \quad (3.1)$$

The orientations of θ_y and θ_z are illustrated in Figure 3.3b. According to Eq. (2.7), $G_{t,global}$ can be further derived as

$$\begin{aligned} G_{t,global} &= I_e^{dir} (\mathbf{R}_z(\theta_z) \cdot \mathbf{R}_y(\theta_y) \cdot \mathbf{n}_{PV0})^T \cdot \mathbf{n}_s + G_{h,d} \\ &= I_e^{dir} (x_s \cos\theta_y \cos\theta_z + y_s \cos\theta_y \sin\theta_z + z_s \sin\theta_y) + G_{h,d}. \end{aligned} \quad (3.2)$$

It's interesting to notice that the one-DOF sun tracking can be regarded as a special case of the two-DOF sun tracking. Compared with the one-DOF case, the PV shading elements with two DOFs produce more complicated patterns of shadows, whose area has no closed-form solution.

3.2.2. DERIVATIVE AND CALCULATION OF S_b AND P_{in}

In order to calculate the direct-beam-illuminated PV area S_b with arbitrary θ_y and θ_z , we firstly study that area on a typical single element S_{b0} , and assume all elements have the same patterns of shadows. It means that we ignore the shadows from walls and window frames, and treat them as if they came from surrounding elements. In this way, we will

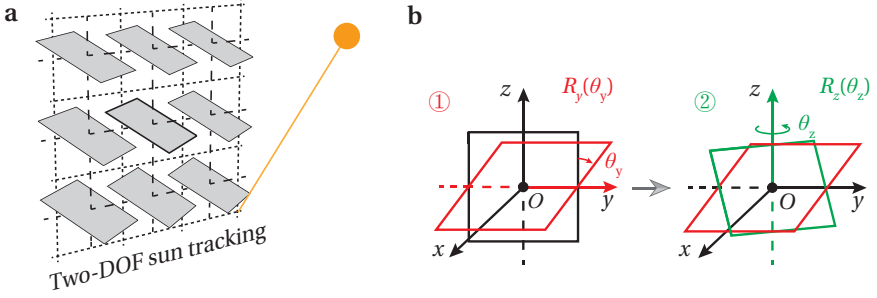


Figure 3.3: Two-DOF sun tracking and definition of rotation angles **a**, A schematic of the rotated two-DOF PV squares. **b**, Definition of rotation angles θ_y and θ_z .

obtain a slightly smaller S_b than that containing shadows from walls and window frames. Also, we assume that the PV shading elements are identical squares with the side length of l_0 ($l_0 = w_0$). As to the window ($l = n_l l_0$ and $w = n_w l_0$), we need $n_l n_w$ squares to cover up the window area. Since the position of axes will not affect the relative position of rotated squares, thus will not affect S_b , we choose the centre of the square to position two axes for convenience.

Let Q_{ij} denote No. ij square, which can be taken as a set of all the points on the square; let $O_{ij}(x_{Oij}, y_{Oij}, z_{Oij})$ denote the centre of Q_{ij} ; let Q_{Aij} , Q_{Bij} , Q_{Cij} , and Q_{Dij} denote the four corners of Q_{ij} (Figure 3.4a). We define the origin of the Cartesian coordinates $O(0, 0, 0)$ as the centre of the target square Q_{00} , then the centre O_{ij} of Q_{ij} can be written as $(0, il_0, jl_0)$. The position of the centre O_{ij} does not change when the square rotates around it since we choose it as the pivot. A tilt position of Q_{ij} be can achieved by a twice-rotation procedure from the initial position. Firstly, Q_{ij} rotates θ_y around the axis ($x = 0$ & $z = l_0 j$) clockwise (viewing from the positive y -axis). Secondly, Q_{ij} rotates θ_z around the axis ($x = 0$ & $y = l_0 i$) anti-clockwise (viewing from the positive z -axis). Since all squares rotate the same angle simultaneously, an arbitrary point on Q_{ij} can be derived from Q_{00} . So here we mainly discuss the rotation of Q_{00} . In the original coordinate $Oxyz$, rotation matrices $R_y(\theta_y)$ and $R_z(\theta_z)$ can be expressed as

$$\mathbf{R}_y(\theta_y) = \begin{bmatrix} \cos\theta_y & 0 & -\sin\theta_y \\ 0 & 1 & 0 \\ \sin\theta_y & 0 & \cos\theta_y \end{bmatrix}, \quad (3.3)$$

$$\mathbf{R}_z(\theta_z) = \begin{bmatrix} \cos\theta_z & -\sin\theta_z & 0 \\ \sin\theta_z & \cos\theta_z & 0 \\ 0 & 0 & 1 \end{bmatrix}. \quad (3.4)$$

Note that $R_y(\theta_y)$ is different from the rotation matrix $R_{y,C-C'}$ as mentioned in the previous section.

For rotated squares, imagine that point O_{ij} casts a shadow point $O_{sij}(x_{Osj}, y_{Osj}, z_{Osj})$ on the surface of target square Q_{00} (Figure 3.4b). Then we have $\overrightarrow{O_{sij}O_{ij}} \parallel \mathbf{n}_s$.

Similarly, in order to study the area of shadows, we build new coordinates $Ox'y'z'$ based on the rotated square Q_{00} (Figure 3.4c & d). From coordinates $Oxyz$ to coordinates

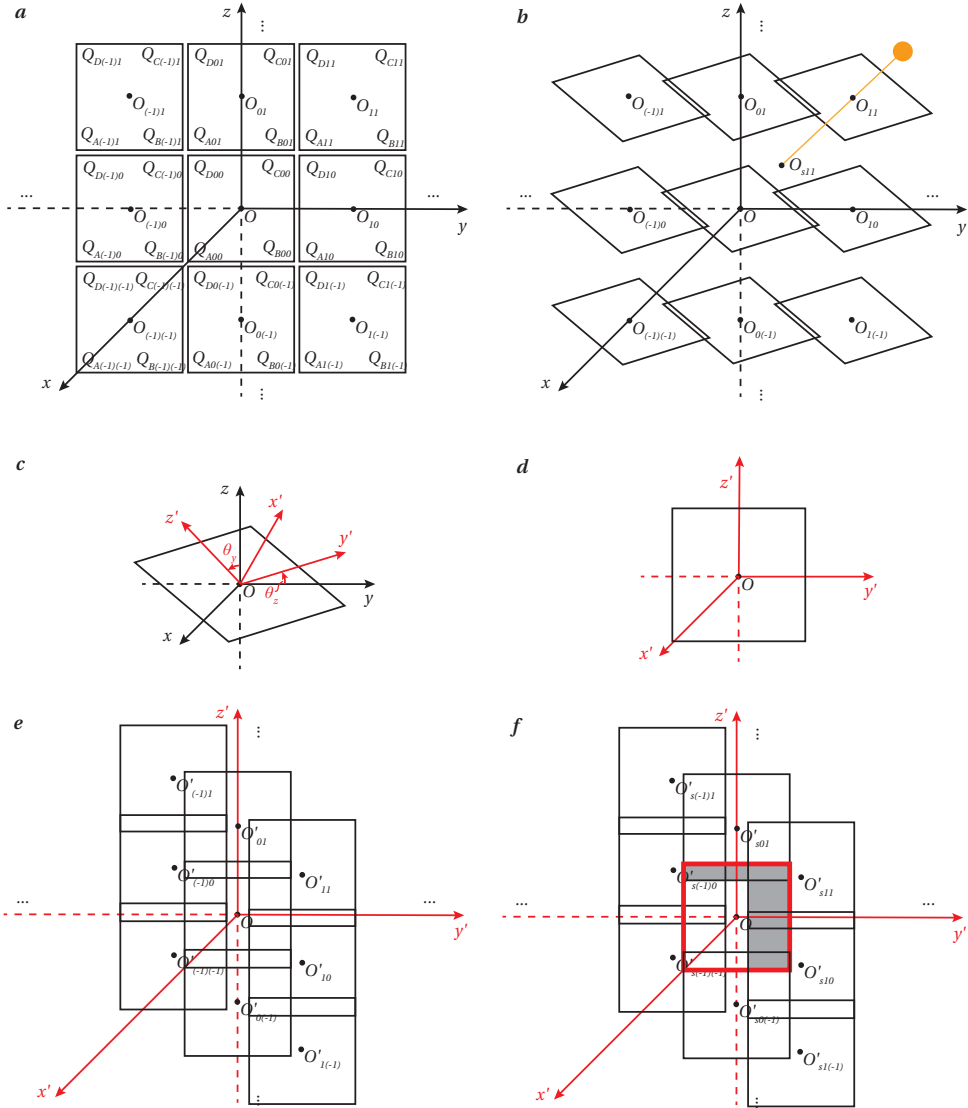


Figure 3.4: Definitions in two-DOF model in the Cartesian coordinates. **a**, Two-DOF square Q_{ij} in the initial position in the original Cartesian coordinates $Oxyz$. Point O_{ij} denotes the centre of Q_{ij} ; points Q_{Aij} , Q_{Bij} , Q_{Cij} , and Q_{Dij} denote the four corners of Q_{ij} . **b**, Two-DOF square Q_{ij} in the rotated position in the original Cartesian coordinates $Oxyz$. Point O_{s11} denotes the shadow point on the surface of the target square Q_{00} casted by O_{11} . **c**, Target Two-DOF square Q_{00} in the rotated position in the original Cartesian coordinates $Oxyz$ and the new Cartesian coordinates $Ox'y'z'$. **d**, Target Two-DOF square Q_{00} in the rotated position in the new Cartesian coordinates $Ox'y'z'$. **e**, Two-DOF square Q_{ij} in the rotated position in the new Cartesian coordinates $Ox'y'z'$. **f**, Shadows on the surface of target square Q_{00} casted by Q_{ij} in the new Cartesian coordinates $Ox'y'z'$. Grey parts are the real shadows on the target square Q_{00} .

$Ox'y'z'$, a rotation matrix $\mathbf{R}_{zy,C-C'}(\theta_z, \theta_y)$ is required to achieve transformation, i.e.

$$\begin{aligned} \mathbf{R}_{zy,C-C'}(\theta_z, \theta_y) &= \mathbf{R}_y(-\theta_y) \cdot \mathbf{R}_z(-\theta_z) \\ &= \begin{bmatrix} \cos\theta_y & 0 & \sin\theta_y \\ 0 & 1 & 0 \\ -\sin\theta_y & 0 & \cos\theta_y \end{bmatrix} \cdot \begin{bmatrix} \cos\theta_z & \sin\theta_z & 0 \\ -\sin\theta_z & \cos\theta_z & 0 \\ 0 & 0 & 1 \end{bmatrix} \\ &= \begin{bmatrix} \cos\theta_z \cos\theta_y & \sin\theta_z \cos\theta_y & \sin\theta_y \\ -\sin\theta_z & \cos\theta_z & 0 \\ -\cos\theta_z \sin\theta_y & -\sin\theta_z \sin\theta_y & \cos\theta_y \end{bmatrix}. \end{aligned} \quad (3.5)$$

In the new coordinates $Ox'y'z'$, the normal vector of the square is $\mathbf{n}'_{PV}(1, 0, 0)$. The solar position $\mathbf{n}'_s(x'_s, y'_s, z'_s)$ and the centre $O'_{ij}(x'_{Oij}, y'_{Oij}, z'_{Oij})$ of the square can be calculated by

$$\mathbf{n}'_s = \begin{bmatrix} x'_s \\ y'_s \\ z'_s \end{bmatrix} = \mathbf{R}_{zy,C-C'}(\theta_z, \theta_y) \cdot \mathbf{n}_s = \begin{bmatrix} \cos\theta_z \cos\theta_y & \sin\theta_z \cos\theta_y & \sin\theta_y \\ -\sin\theta_z & \cos\theta_z & 0 \\ -\cos\theta_z \sin\theta_y & -\sin\theta_z \sin\theta_y & \cos\theta_y \end{bmatrix} \cdot \begin{bmatrix} x_s \\ y_s \\ z_s \end{bmatrix}, \quad (3.6)$$

$$\begin{bmatrix} x'_{Oij} \\ y'_{Oij} \\ z'_{Oij} \end{bmatrix} = \mathbf{R}_{zy,C-C'}(\theta_z, \theta_y) \cdot \begin{bmatrix} x_{Oij} \\ y_{Oij} \\ z_{Oij} \end{bmatrix} = \begin{bmatrix} \cos\theta_z \cos\theta_y & \sin\theta_z \cos\theta_y & \sin\theta_y \\ -\sin\theta_z & \cos\theta_z & 0 \\ -\cos\theta_z \sin\theta_y & -\sin\theta_z \sin\theta_y & \cos\theta_y \end{bmatrix} \cdot \begin{bmatrix} 0 \\ l_0 i \\ l_0 j \end{bmatrix}. \quad (3.7)$$

In the new coordinates $Ox'y'z'$, we also have $\overrightarrow{O'_{sij}O'_{ij}} \parallel \mathbf{n}'_s$. The surface of the target square \mathbb{Q}_{00} is $x' = 0$, and the line $O'_{ij}O'_{sij}$ can be expressed as

$$\frac{x' - x'_{Oij}}{x'_s} = \frac{y' - y'_{Oij}}{y'_s} = \frac{z' - z'_{Oij}}{z'_s} = \lambda_{ij}. \quad (3.8)$$

Since the shadow point $O'_{sij}(x'_{Osj}, y'_{Osj}, z'_{Osj})$ is both on the surface of the target square ($x' = 0$) and on the the line $O'_{ij}O'_{sij}$, the equation to obtain O'_{sij} is given by

$$\begin{cases} x'_{Osj} = 0 \\ \frac{x'_{Osj} - x'_{Oij}}{x'_s} = \frac{y'_{Osj} - y'_{Oij}}{y'_s} = \frac{z'_{Osj} - z'_{Oij}}{z'_s} = \lambda_{ij} \end{cases}, \quad (3.9)$$

where the solution of $O'_{sij}(x'_{Osj}, y'_{Osj}, z'_{Osj})$ is derived as

$$\begin{cases} x'_{Osj} = 0 \\ y'_{Osj} = -\frac{y'_s}{x'_s} x'_{Oij} + y'_{Oij} \\ z'_{Osj} = -\frac{z'_s}{x'_s} x'_{Oij} + z'_{Oij} \end{cases}. \quad (3.10)$$

By obtaining $O'_{sij}(x'_{O_{sij}}, y'_{O_{sij}}, z'_{O_{sij}})$, the 3D problem ends up as a 2D problem. The shadow area on the target square Q_{00} casted by Q_{ij} is determined by the relative position between O'_{sij} and $O(0, 0, 0)$ on the condition that Q_{ij} is in front of Q_{00} in the direction of sunlight, i.e., $x'_{O_{ij}} > 0$ (Figure 3.4e & f). Since the surfaces of squares are parallel to each other, the shadows on the target surface are also squares with the same dimensions.

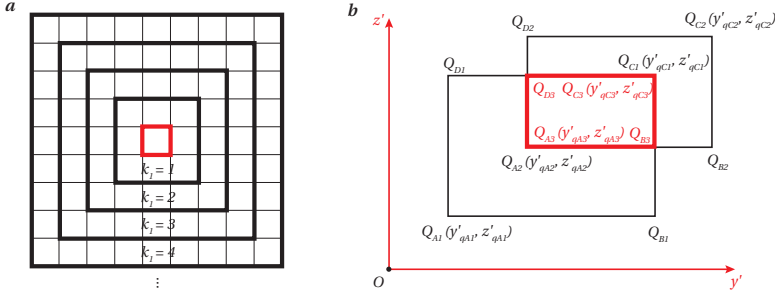


Figure 3.5: Definitions for the calculation of S_b on the target square. **a**, Definition of the set $\mathbb{T}_{sur}^{k_1}$, which is grouped and numbered as illustrated. **b**, Definitions of the rectangle $Q_{rec}(y'_{qA}, z'_{qA}, y'_{qC}, z'_{qC})$, and the overlapped rectangle Q_{rec3} (red) of two rectangles Q_{rec1} and Q_{rec2} .

In order to find out the surrounding squares contributing to the shadows on the target square, we group the surrounding squares by the sequence number of i and j . Each group is defined as a set, which is denoted as $\mathbb{T}_{sur}^{k_1}\{Q_{ij} \mid |i| \leq k_1, |j| \leq k_1, Q_{ij} \notin \mathbb{T}_{sur}^{k_{temp}}, k_{temp} < k_1, k_{temp} \in \mathbb{N}_0, k_1 \in \mathbb{N}_1\}$ (Figure 3.5a). The set of Q_{ij} contributing to the shadows on Q_{00} within $\mathbb{T}_{sur}^{k_1}$ is denoted as $\mathbb{T}_{sqsh}^{k_1}$. The union of total $\mathbb{T}_{sqsh}^{k_1}$ is denoted as \mathbb{T}_{sqsh} . The number of squares contributing to the shadows on the target square is denoted as k_2 . \mathbb{T}_{sqsh} and k_2 can be obtained by the function of f_{sqsh} , which is defined and explained in Algorithm 1 (see Appendix B).

Since it's quite difficult to predict the shape of shadows on the target square, we developed algorithms which are applicable to the calculation of such shadows by defining a few functions. The nature of those algorithms is to derive the overlapping rectangle of two rectangles which have parallel sides. Due to the way we define the coordinates $Ox'y'z'$, the sides of rectangles are parallel with the coordinates. Therefore, we can define a rectangle $Q_AQ_BQ_CQ_D$ as Q_{rec} , whose sides are parallel with the coordinates (Figure 3.5b). The coordinates of two corners $Q_A(y'_{qA}, z'_{qA})$ and $Q_C(y'_{qC}, z'_{qC})$ can represent the size and shape of Q_{rec} . Therefore, we denote the rectangle $Q_AQ_BQ_CQ_D$ as $Q_{rec}(y'_{qA}, z'_{qA}, y'_{qC}, z'_{qC})$. The function f_{ov}^2 is developed to find Q_{rec3} , the overlapped rectangle of Q_{rec1} and Q_{rec2} (Figure 3.5b). Further, $f_{ov}^{k_3}$ is developed to find the overlapped rectangle of k_3 rectangles (see Algorithm 2 in Appendix B). When there's no overlapped area among rectangles, we denoted the overlapped rectangle as $Q_{rec0}(0, 0, 0, 0)$. We also develop f_s to calculate the area of rectangle $Q_{rec}(y'_{qA}, z'_{qA}, y'_{qC}, z'_{qC})$ in Algorithm 3 (see Appendix B).

The reason we have to find the overlapped rectangle is that we cannot simply add up the areas of two rectangular shadows as the total area. We have to eliminate the extra area caused by overlap. As to the calculation of more than three rectangles, we also have

to consider the area of overlapped rectangles of the overlapped rectangles because we eliminate them twice and have to add them again. This algorithm is described more clearly in Algorithm 4 (see Appendix B). By obtaining the area of shadows S_{sh0} on the target square, S_{b0} can be calculated by

$$S_{b0} = S_{PV0} - S_{sh0}, \quad (3.11)$$

where S_{PV0} denotes the area of an individual PV shading element.

Using the example data in Table 2.1, we can calculate S_{b0} and P_{in0} in all conditions of θ_y and θ_z . In terms of all PV shading elements, S_b and P_{in} can be calculated by

$$S_b = n_l n_w S_{b0}, \quad (3.12)$$

$$P_{in} = n_l n_w P_{in0}. \quad (3.13)$$

3.2.3. TWO-DOF RESULTS AND ANALYSIS

By using the same data set in Table 2.1, $G_{t,global}$, S_b and P_{in} are calculated under a full range of conditions of θ_y and θ_z . As before, we ignore the shadows from walls and window frames at first.

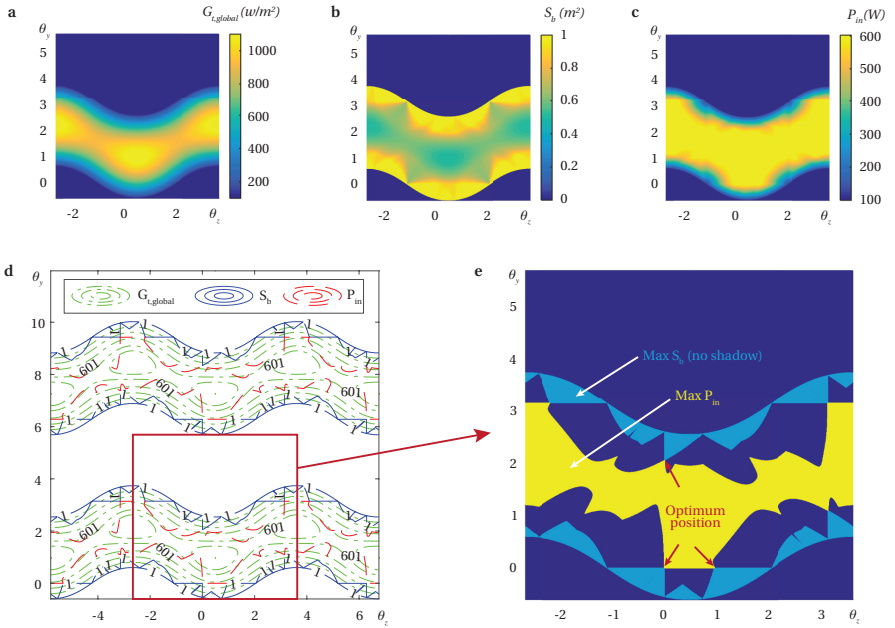


Figure 3.6: Simulation results of all possible two-DOF sun tracking positions. **a-c**, Color maps of $G_{t,global}$, S_b , and P_{in} on the squares as a function of θ_y and θ_z . **d**, A periodic contour map of $G_{t,global}$ (green), S_b (blue), and P_{in} (red) on the squares as a function of θ_y and θ_z . **e**, A color map of the maximum P_{in} (yellow) and the maximum S_b (light blue) on the squares as a function of θ_y and θ_z with three optimum positions marked. Note that the unit of angles θ_y and θ_z is radian.

Apparently, $G_{t,global}$ hits the peak when the PV plane is perpendicular to the sun-beam (Figure 3.6a). However, S_b reaches its minimum value at the very same position (Figure 3.6b). As their product, P_{in} remains the maximum within a certain range, instead of a single point (Figure 3.6c). This conclusion is similar to that under the one-DOF conditions (Figure 2.7d). To have the maximum P_{out} , the optimum position should be located where P_{in} and S_b climb to the peak simultaneously.

To illustrate this issue clearly, two-dimensional maps of the three parameters are drawn together as shown in Figure 3.6d. If the optimum position exists, theoretically, there are infinitely many such positions since periodic patterns are observed for $G_{t,global}$, S_b , and P_{in} . Therefore, we only focus on the period nearest to the initial position, where three eligible positions are found (Figure 3.6e). However, such three positions are located at either $\theta_y = 0$ or $\theta_z = 0$, i.e., they are equivalent to the one-DOF sun tracking. Specifically, among the three optimum positions in the θ_z - θ_y coordinates (Figure 3.6e), $(0,0)$ indicates the closed position, which is meaningless for windows as discussed before; $(0, 2\arctan(z_s/x_s))$ and $(2(\pi - A_s), 0)$ represent the optimum positions of the one-DOF sun tracking with horizontal axes and vertical axes respectively. Therefore, in terms of the optimum position of sun tracking, the PV shading elements with two DOFs perform exactly the same as that with one DOF. Triangular shadows caused by walls and window frames affect the module efficiency the same way as discussed in one-DOF sun tracking. Therefore, we can draw a similar conclusion that PV window treatments with two DOFs are not able to achieve the maximum P_{out} and not able to avoid glare in the optimum position in the proposed model.

3.3. THREE-DOF SUN TRACKING

3.3.1. MODEL OF THREE-DOF ROTATION

As proved previously, PV shading elements with two DOFs cannot lead to a perfect solution. Therefore, one more DOF is added to the rotation of the PV shading elements in order to achieve the optimization objective. As before, the centre of the target PV square is defined as its pivot, i.e. the cross point of the three axes. Note that the position of the pivot does not change the relative positions of all squares. Thus, the centre can be used as the pivot, when we study the shadows on the target square from its surrounding neighbors. The three-DOF sun tracking can be taken as three-step rotations and mathematically defined using three rotation matrices (Figure 3.7). The first and second rotations can be mathematically denoted by the rotation matrices $\mathbf{R}_y(\theta_y)$ and $\mathbf{R}_z(\theta_z)$, which are exactly the same as those in the two-DOF model. The third rotation is denoted as $\mathbf{R}_n(\theta_n)$, which means that the target square rotates θ_n around its normal \mathbf{n}_{PV} clockwise (viewing from the positive direction of \mathbf{n}_{PV}). After the first and second rotations, \mathbf{n}_{PV} is derived from the initial PV orientation $\mathbf{n}_{PV0}(1, 0, 0)$ as

$$\mathbf{n}_{PV} = \begin{bmatrix} x_n \\ y_n \\ z_n \end{bmatrix} = \mathbf{R}_z(\theta_z) \cdot \mathbf{R}_y(\theta_y) \cdot \mathbf{n}_{PV0} = \begin{bmatrix} \cos\theta_y \cos\theta_z \\ \cos\theta_y \sin\theta_z \\ \sin\theta_y \end{bmatrix}. \quad (3.14)$$

The third rotation matrix $\mathbf{R}_n(\theta_n)$ can be expressed as

$$\mathbf{R}_n(\theta_n) = \hat{\mathbf{n}}_{PV} + \cos\theta_n(\mathbf{I} - \hat{\mathbf{n}}_{PV}) - \sin\theta_n \mathbf{n}_{PV}^*, \quad (3.15)$$

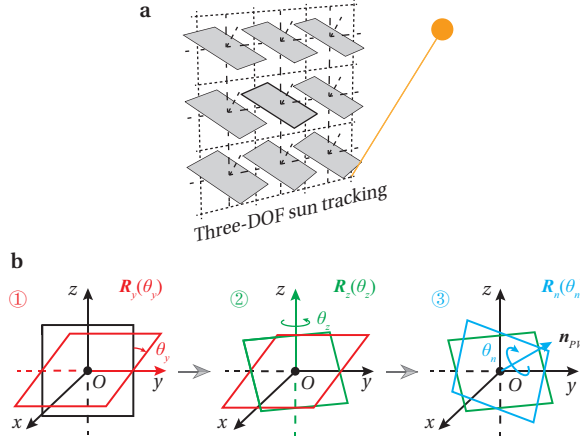


Figure 3.7: Three-DOF sun tracking and definition of rotation angles **a**, A schematic of the rotated three-DOF PV squares. **b**, Definition of rotation angles θ_y , θ_z , and θ_n .

where $\hat{\mathbf{n}}_{PV}$ and \mathbf{n}_{PV}^* can be obtained by Eqs. (3.16) and (3.17), i.e.

$$\hat{\mathbf{n}}_{PV} = \mathbf{n}_{PV} \cdot \mathbf{n}_{PV}^T = \begin{bmatrix} x_n^2 & x_n y_n & x_n z_n \\ x_n y_n & y_n^2 & y_n z_n \\ x_n z_n & y_n z_n & z_n^2 \end{bmatrix}, \quad (3.16)$$

$$\mathbf{n}_{PV}^* = \begin{bmatrix} 0 & -z_n & y_n \\ z_n & 0 & -x_n \\ -y_n & x_n & 0 \end{bmatrix}, \quad (3.17)$$

where $\mathbf{n}_{PV}(x_n, y_n, z_n)$ is given by Eq. (3.14).

The overall rotation matrix for the target square with three DOF can be expressed as

$$\mathbf{R}_{yzn}(\theta_y, \theta_z, \theta_n) = \mathbf{R}_n(\theta_n) \cdot \mathbf{R}_z(\theta_z) \cdot \mathbf{R}_y(\theta_y). \quad (3.18)$$

Since the third rotation does not change the normal of the PV square, $G_{t,global}$ in this three-DOF model is the same as that in the two-DOF model (see Eq 3.2). The aforementioned algorithms (see Section 3.2.2) are also applicable to the calculation of S_b on the three-DOF PV squares.

3.3.2. THREE-DOF RESULTS AND ANALYSIS

Compared with the two-DOF rotations, the three-DOF sun tracking requires one more dimension to illustrate the results of $G_{t,global}$, S_b , and P_{in} as shown in Figure 3.8. Apparently, θ_n does not affect $G_{t,global}$ at all because it does not change α_{PV} and A_{PV} (Figure 3.8a). However, it changes the shadows on the squares, and thus influences S_b (Figure 3.8b). Therefore, P_{in} varies with θ_n , θ_z , and θ_y (Figure 3.8c). From the 3D color maps, it is difficult to determine the optimum positions by only visual observation.

According to Eq. (3.18), an optimum $\mathbf{R}_{yzn}(\theta_y, \theta_z, \theta_n)$ corresponds to an optimum sun-tracking position, where the maximum P_{in} and η_m are observed. Therefore, theoretically, the optimum $\mathbf{R}_{yzn}(\theta_y, \theta_z, \theta_n)$ can be derived based on the following two main

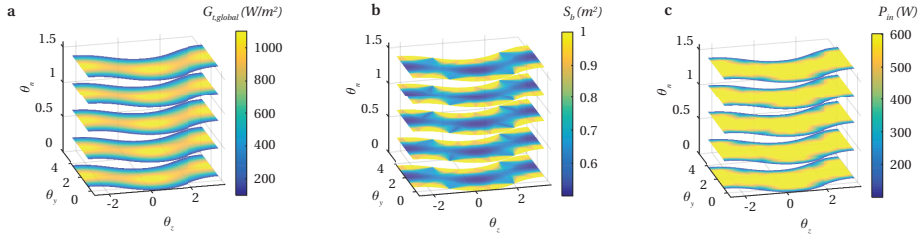


Figure 3.8: Simulation results of all possible three-DOF sun tracking positions. **a**, A 3D color map of $G_{t,global}$ on the squares as a function of θ_y , θ_z , and θ_n . **b**, A 3D color map of S_b on the squares as a function of θ_y , θ_z , and θ_n . **c**, A 3D color map of P_{in} on the squares as a function of θ_y , θ_z , and θ_n .

conditions. First, there shall be no shadow on the target square from surrounding squares. Second, the input power P_{in} shall stay the maximum, which is the same as that in the initial position.

Since the position of the centre O_{ij} does not change when the square rotates around it, we can use $O_{sij}(x_{O_{sij}}, y_{O_{sij}}, z_{O_{sij}})$, a hypothetical shadow point on the surface of target square Q_{00} casted by O_{ij} , to determine the shadows on Q_{00} (Figure 3.9a). In order to study the area of shadows, we build new coordinates $Ox'y'z'$ based on the rotated Q_{00} . From coordinates $Oxyz$ to $Ox'y'z'$, a rotation matrix $R_{nzy,C-C'}(\theta_n, \theta_z, \theta_y)$ is required to achieve the transformation, which can be taken as a reverse procedure of the rotation within the original coordinates $Oxyz$. $R_{nzy,C-C'}(\theta_n, \theta_z, \theta_y)$ can be expressed as

$$R_{nzy,C-C'}(\theta_n, \theta_z, \theta_y) = R_y(-\theta_y) \cdot R_z(-\theta_z) \cdot R_n(-\theta_n). \quad (3.19)$$

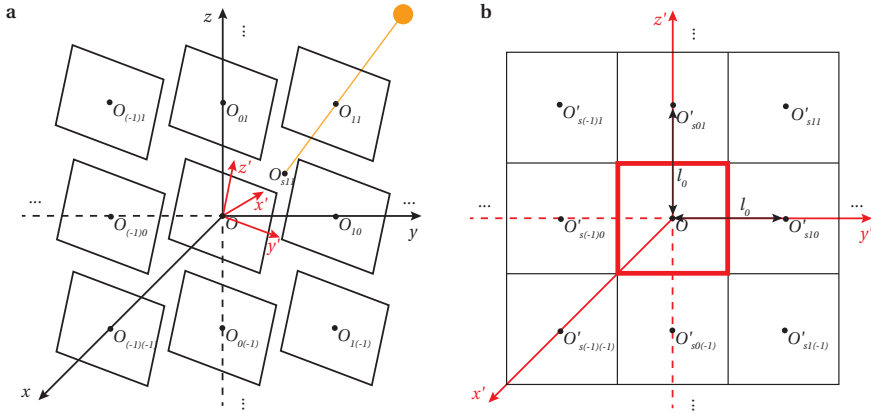


Figure 3.9: Definitions of three-DOF sun tracking. **a**, A schematic of the hypothetical shadow point O_{sij} , rotated squares, and the new Cartesian coordinates (red) built based on the target square. **b**, A schematic of the ideal shadow pattern and geometrical conditions in the new Cartesian coordinates.

By $R_{nzy,C-C'}$, a 3-D problem is converted into a 2-D problem (Figure 3.9b). In the new coordinates $Ox'y'z'$, in order to obtain the maximum S_b and P_{in} , $O'_{...}$ shall be in

such positions that no shadow appears on \mathbb{Q}'_{00} and no sunlight “leak” away, which means the solar power is fully received by the target square without wasted. As illustrated in Figure 3.9b, O'_{s01} and O'_{s10} shall appear where conditions are fulfilled as follows,

$$\left| \overrightarrow{OO'_{s10}} \right| = \left| \overrightarrow{OO'_{s01}} \right| = l_0. \quad (3.20)$$

To attain the optimum rotation angles θ_y , θ_z , and θ_n , following derivations are conducted based on the original coordinates $Oxyz$. With $\mathbf{R}_{yzn}(\theta_y, \theta_z, \theta_n)$, \mathbf{n}_{PV} is obtained by Eq. (3.14). Since $\overrightarrow{O_{ij}O_{sij}} \parallel \mathbf{n}_s$, O_{sij} is on the line $O_{ij}O_{sij}$, i.e.,

$$\frac{x_{O_{sij}} - x_{O_{ij}}}{x_s} = \frac{y_{O_{sij}} - y_{O_{ij}}}{y_s} = \frac{z_{O_{sij}} - z_{O_{ij}}}{z_s} = \lambda_{ij}. \quad (3.21)$$

For \mathbb{Q}_{10} and \mathbb{Q}_{01} , O_{s10} and O_{s01} should be on the line $O_{10}O_{s10}$ and $O_{01}O_{s01}$ respectively. Referring to Eq. (3.20), O_{s10} and O_{s01} should also be in such position that $\left| \overrightarrow{OO_{s10}} \right| = \left| \overrightarrow{OO_{s01}} \right| = l_0$. Therefore, equations are derived as follows,

$$\begin{cases} |OO_{s10}|^2 = x_{O_{s10}}^2 + y_{O_{s10}}^2 + z_{O_{s10}}^2 = l_0^2 \\ |OO_{s01}|^2 = x_{O_{s01}}^2 + y_{O_{s01}}^2 + z_{O_{s01}}^2 = l_0^2 \\ \frac{x_{O_{s10}}}{x_s} = \frac{y_{O_{s10}} - l_0}{y_s} = \frac{z_{O_{s10}}}{z_s} = \lambda_{10} \\ \frac{x_{O_{s01}}}{x_s} = \frac{y_{O_{s01}}}{y_s} = \frac{z_{O_{s01}} - l_0}{z_s} = \lambda_{01} \end{cases}. \quad (3.22)$$

Considering $x_s^2 + y_s^2 + z_s^2 = 1$, it's easy to derive

$$\begin{cases} \lambda_{01} = 0 & \text{or} & \lambda_{01} = -2z_s l_0 \\ \lambda_{10} = 0 & \text{or} & \lambda_{10} = -2y_s l_0 \end{cases}. \quad (3.23)$$

When $\lambda_{ij} = 0$, O_{sij} is overlapped with O_{ij} , which means that the square is either in the closed state or under 1-DOF rotation. Therefore, with $\lambda_{ij} = 0$ left out, we have the only solution as follows,

$$\begin{cases} \lambda_{01} = -2z_s l_0 \\ \lambda_{10} = -2y_s l_0 \end{cases}. \quad (3.24)$$

Then the coordinates of O_{s01} and O_{s10} are obtained.

$$\begin{cases} x_{O_{s01}} = -2x_s z_s l_0 \\ y_{O_{s01}} = -2y_s z_s l_0 \\ z_{O_{s01}} = (1 - 2z_s^2) l_0 \end{cases}, \quad (3.25)$$

$$\begin{cases} x_{O_{s10}} = -2x_s y_s l_0 \\ y_{O_{s10}} = (1 - 2y_s^2) l_0 \\ z_{O_{s10}} = -2y_s z_s l_0 \end{cases}. \quad (3.26)$$

To derive $\mathbf{n}_{PV}(x_n, y_n, z_n)$, we first consider that O_{sij} is on the surface of \mathbb{Q}_{00} , i.e.,

$$x_n x + y_n y + z_n z = 0. \quad (3.27)$$

Then, we consider that $\mathbf{n}_{PV}(x_n, y_n, z_n)$ should enable \mathbb{Q}_{00} to have the maximum P_{in} . From previous results we know that P_{in} hits the peak when squares are in the initial position. Therefore, we let P_{in} with $\mathbf{n}_{PV}(x_n, y_n, z_n)$ equal to that with $\mathbf{n}_{PV0}(1, 0, 0)$, i.e.

$$(I_e^{dir} \mathbf{n}_{PV}^\top \cdot \mathbf{n}_s + G_{h,d}) S_{PV0} = (I_e^{dir} \mathbf{n}_{PV0}^\top \cdot \mathbf{n}_s + G_{h,d}) S_{PV0}, \quad (3.28)$$

i.e.

$$x_n x_s + y_n y_s + z_n z_s = x_s. \quad (3.29)$$

Referring to Eq. (3.27) and 3.29, we have

$$\begin{cases} x_n x_s + y_n y_s + z_n z_s = x_s \\ x_n x_{Os01} + y_n y_{Os01} + z_n z_{Os01} = 0 \\ x_n x_{Os10} + y_n y_{Os10} + z_n z_{Os10} = 0 \end{cases} \quad (3.30)$$

With Eq. (3.25) and 3.26, equations are solved and \mathbf{n}_{PV} is obtained, i.e.

$$\begin{cases} x_n = 2x_s^2 - 1 \\ y_n = 2x_s y_s \\ z_n = 2x_s z_s \end{cases} \quad (3.31)$$

Combined with Eq. (3.14), θ_y and θ_z are obtained by

$$\begin{cases} \theta_y = (-1)^{(k_y)} \arcsin(2x_s z_s) + k_y \pi, k_y \in \mathbb{Z} \\ \theta_z = \pm \arccos\left(\frac{2x_s^2 - 1}{\cos \theta_y}\right) + 2k_z \pi, k_z \in \mathbb{Z} \end{cases}, \quad (3.32)$$

where k_y and k_z are two arbitrary integers.

To derive θ_n , according to Eq. (3.26), $\overrightarrow{OO_{s10}}$, which is $\overrightarrow{OO_{10}^*}(0, l_0, 0)$ after three-step rotations, can be expressed as,

$$\overrightarrow{OO_{s10}} = \mathbf{R}_n(\theta_n) \cdot \mathbf{R}_z(\theta_z) \cdot \mathbf{R}_y(\theta_y) \cdot \begin{bmatrix} 0 \\ l_0 \\ 0 \end{bmatrix} = \begin{bmatrix} -2x_s y_s l_0 \\ (1 - 2y_s^2) l_0 \\ -2y_s z_s l_0 \end{bmatrix}. \quad (3.33)$$

Here, notice that O_{10}^* is the point which is overlapped with O_{10} at first, but is on the surface of \mathbb{Q}_{00} and rotate with $\overrightarrow{OO_{00}}$.

Also, it is easy to calculate $\overrightarrow{OO_{10}^{**}}$, which is $\overrightarrow{OO_{10}^*}(0, l_0, 0)$ after two-step rotations, i.e.

$$\overrightarrow{OO_{10}^{**}} = \mathbf{R}_z(\theta_z) \cdot \mathbf{R}_y(\theta_y) \cdot \begin{bmatrix} 0 \\ l_0 \\ 0 \end{bmatrix} = \begin{bmatrix} -l_0 \sin \theta_z \\ l_0 \cos \theta_z \\ 0 \end{bmatrix}. \quad (3.34)$$

Therefore, combining Eq. (3.33) and 3.34, we have,

$$\overrightarrow{OO_{s10}} = \mathbf{R}_n(\theta_n) \cdot \overrightarrow{OO_{10}^{**}}. \quad (3.35)$$

Geometrically, Eq. (3.35) means that $\overrightarrow{OO_{s10}}$ is formed from $\overrightarrow{OO_{10}^{**}}$ rotating θ_n around \mathbf{n}_{PV} clockwise (view from the positive \mathbf{n}_{PV}). According to the definition of dot product and cross product, we have

$$\begin{cases} \overrightarrow{OO_{10}^{**}} \cdot \overrightarrow{OO_{s10}} = \cos \theta_n \\ \overrightarrow{OO_{10}^{**}} \times \overrightarrow{OO_{s10}} = \sin(-\theta_n) \mathbf{n}_{PV} \end{cases}. \quad (3.36)$$

Then it is easy to derive that

$$\theta_n = \begin{cases} -\arccos[2x_s y_s \sin \theta_z + (1 - 2y_s^2) \cos \theta_z] & \frac{z_s \sin \theta_z}{x_s} < 0 \\ \arccos[2x_s y_s \sin \theta_z + (1 - 2y_s^2) \cos \theta_z] & \frac{z_s \sin \theta_z}{x_s} \geq 0 \end{cases}, \quad (3.37)$$

where $\theta_n \in [-\pi, \pi]$.

To verify the above derivations and determine k_y and k_z , the same example data (see Table 2.1) and algorithms are applied as discussed previously. From the periodical contours of $G_{t,global}$, S_b , and P_{in} , we can conclude that the solutions can fulfill the optimum conditions. The optimum position nearest to the initial position is found, where $k_y = 1$ and $k_z = 0$ (Figure 3.10). Therefore, the optimum rotation angles for the three-DOF sun tracking are concluded as

$$\begin{cases} \theta_y = \pi - \arcsin(2x_s z_s), \\ \theta_z = \begin{cases} -\arccos\left(\frac{2x_s^2 - 1}{\cos \theta_y}\right), & x_s y_s \cos \theta_y < 0; \\ \arccos\left(\frac{2x_s^2 - 1}{\cos \theta_y}\right), & x_s y_s \cos \theta_y \geq 0, \end{cases} \\ \theta_n = \begin{cases} -\arccos[2x_s y_s \sin \theta_z + (1 - 2y_s^2) \cos \theta_z], & \frac{z_s \sin \theta_z}{x_s} < 0; \\ \arccos[2x_s y_s \sin \theta_z + (1 - 2y_s^2) \cos \theta_z], & \frac{z_s \sin \theta_z}{x_s} \geq 0. \end{cases} \end{cases} \quad (3.38)$$

3.3.3. VP-3-DOF SUN TRACKING

Besides the solutions mentioned above, we also found other solutions meeting the optimum conditions. However, those solutions share a common problem that they cannot avoid the shadows from walls and window frames, even without the shadows coming from the surrounding squares (see Supplementary Note 6 of Ref. [1]). Only the solution provided by Eq. (3.38) describes the shadows with the same shape as that of the illuminated area through an unshaded window. Therefore, this solution is the only one capable of avoiding shadows from walls and window frames.

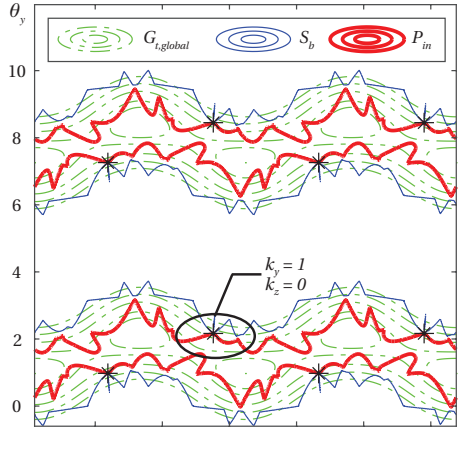


Figure 3.10: A periodic contour map of $G_{t,global}$ (green), S_b (blue), and P_{in} (red) on the squares as a function of θ_y , θ_z , and θ_n , where the value of θ_n is obtained by Eq. (3.37). The solution points are marked with stars, among which the one in the red circle is nearest to the initial position.

However, this solution for the three-DOF sun tracking still suffers from shading, when the pivots lie in the centre of the PV squares. Though the shape of shadows fulfills the requirement, the deviation of shadows caused by the fixed centres leads to interior glares and shadows on the PV squares from walls and window frames (Figure 3.11a). Fortunately, a trick is found to eliminate such a deviation by changing the position of the pivot according to the solar position. Specifically, the bottom left corner A of the target square is used as the pivot, when the solar azimuth A_s is less than the azimuth of the window. Similarly, the right bottom corner B is taken as the pivot, when A_s is greater than the azimuth of the window (Figure 3.11b). Mathematically, to switch the pivot from the centre to the corner A or B , translations are required before and after the rotations. Let $Q_0(x_{q0}, y_{q0}, z_{q0})$ be an arbitrary point on the target square in the initial position, and $Q(x_q, y_q, z_q)$ be the same point after the rotations. Also, we define two translations as $[0 \ -l_0/2 \ -l_0/2]^T$ and $[0 \ l_0/2 \ -l_0/2]^T$, which are the translations from O to A , and from O to B , respectively. Then, the position of Q after the mixed rotations and translations is obtained by

$$\begin{bmatrix} x_q \\ y_q \\ z_q \end{bmatrix} = \begin{cases} \mathbf{R}_{yzn}(\theta_y, \theta_z, \theta_n) \cdot \left(\begin{bmatrix} x_{q0} \\ y_{q0} \\ z_{q0} \end{bmatrix} - \begin{bmatrix} 0 \\ -l_0/2 \\ -l_0/2 \end{bmatrix} \right) + \begin{bmatrix} 0 \\ -l_0/2 \\ -l_0/2 \end{bmatrix}, & \theta_z \geq 0; \\ \mathbf{R}_{yzn}(\theta_y, \theta_z, \theta_n) \cdot \left(\begin{bmatrix} x_{q0} \\ y_{q0} \\ z_{q0} \end{bmatrix} - \begin{bmatrix} 0 \\ l_0/2 \\ -l_0/2 \end{bmatrix} \right) + \begin{bmatrix} 0 \\ l_0/2 \\ -l_0/2 \end{bmatrix}, & \theta_z < 0. \end{cases} \quad (3.39)$$

With Eq. (3.39), we can obtain the trajectories of the four corners of the target square. Such defined mixed rotations and translations can ensure that no shadow is on the PV

squares and no glare appears inside (Figure 3.11b). The perfect solution comes into effect with three-step rotations (see Eq. (3.38)) and an ingenious switch of pivots (see Eq. (3.39)). Therefore, we name this sun-tracking method as the variable-pivot-three-DOF (VP-3-DOF) sun tracking. Here we use the phrase “3-DOF” instead of “3-axis” because it is not necessary to actually have three axes in the physical structures as long as the corners of the target square move along the trajectories. Note that the pivots only need to switch one time a day when $\theta_z = 0$. The movement of the squares is continuous, as illustrated by the trajectories in Figure 3.11b. The visualization of the optimum VP-3-DOF sun tracking can be found in the Supplementary Video 1 of Ref. [1]. Therefore, we conclude that the VP-3-DOF sun tracking is able to achieve the maximum power generation and non-glare daylighting for this model.

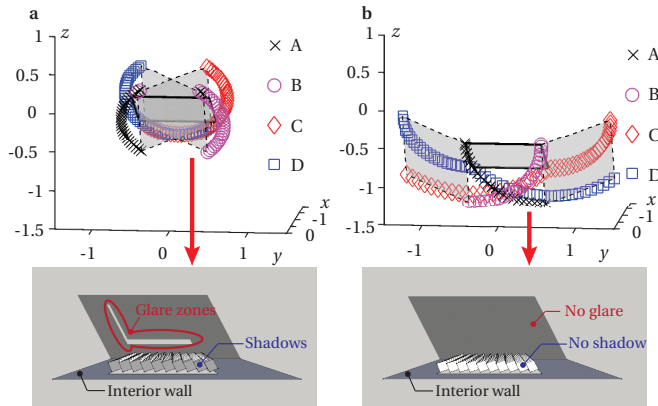


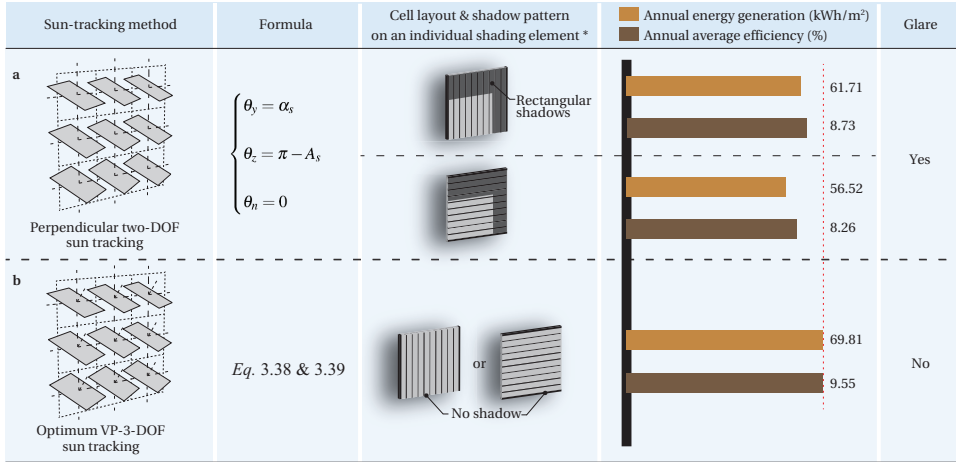
Figure 3.11: Optimum solutions to three-DOF sun tracking **a**, A schematic of the trajectories of a PV square with the optimum three-DOF sun tracking and the corresponding SketchUp simulation, where shadows are found on PV squares; and glare zones are found interior. The pivot is fixed in the centre of the PV square. **b**, A schematic of the trajectories of a PV square with the optimum variable-pivot-three-DOF sun tracking and the corresponding SketchUp simulation, where neither shadow nor glare is found. The pivot is variable from the corner A to B according to θ_z . Visualizations of 3-DOF and VP-3-DOF rotations are provided in Supplementary Video 1 of Ref. [1].

3.4. RESULTS

3.4.1. PHOTOVOLTAIC PERFORMANCE

ABOVE we succeeded in maximizing the power generation at a certain time instant with the VP-3-DOF sun tracking. Now we intend to verify that the VP-3-DOF sun tracking also benefits the annual energy generation and average module efficiency compared with conventional perpendicular two-DOF sun-tracking methods through simulation studies. Since the performance of the partially-shaded PV modules varies with the pattern of cell layouts, here we consider both layouts of vertical stripes and horizontal stripes. The method of calculating the shadows on the element with perpendicular two-DOF sun tracking has been introduced in the Supplementary Note 6 of Ref. [1].

Like in the previous chapter, by inputting a set of $G_{t,global}^{eq}$ for each solar cell in the



* Note that the number of solar cells on the individual shading element for illustration is not necessarily the same as the that for simulation.

Figure 3.12: Simulation results of four sun-tracking methods and two cell layouts using irradiation data of Shanghai. **a**, Perpendicular Two-DOF sun tracking. **b**, Optimum variable-pivot-three-DOF sun tracking. Note that in **a** we ignore the shadows from walls and window frames for simplified calculation. Therefore, the actual values of E_a and $\bar{\eta}_m$ in **c** shall be even less than that presented here. The sketch of sun-tracking method in **b** only presents the three-DOF rotations, instead of the variable pivot.

PV module, the simulation models generate hourly output power and module efficiency. Then the annual energy generation per unit area (E_a) and the annual average efficiency ($\bar{\eta}_m$) of the PV module can be calculated. The simulation results are obtained by using the climate data of Shanghai, as shown in Figure 3.12. It is obvious that the proposed optimum VP-3-DOF sun-tracking method performs better than the two-DOF counterpart in all the aspects of annual energy generation, annual average efficiency, and glare protection. In the example of Shanghai, with the VP-3-DOF sun tracking, E_a is improved by 13.12%; and $\bar{\eta}_m$ is improved by 9.39%. Therefore, we conclude that the optimum VP-3-DOF sun tracking is capable to gain the maximum annual energy generation and annual average efficiency, and also capable to protect glare from the sun.

To draw a general conclusion, E_a and $\bar{\eta}_m$ are calculated using the simulation results of the other eight cities in the world. As the average over the nine cities, E_a is improved by 27.40%; $\bar{\eta}_m$ is improved by 19.17% using our proposed optimum VP-3-DOF sun tracking (see Tables 3.1 and 3.2).

3.4.2. GLARE PROTECTION

Using the same method as in the previous chapter, the glare simulations are conducted in the position near the window of the reference office [8]. Figure 3.13 quantitatively and visually shows the simulation results based on the glare model mentioned above. Particularly, the proposed optimum VP-3-DOF sun tracking reveals imperceptible glare and 31% DGP. The results of point-in-time glare coincide with the theoretical derivations and

Table 3.1: Results of E_a calculated by the climate data of nine cities

City	E_a (kWh/m ²)			$\Delta E_a/E_a$ ***
	VP-3-DOF	Perp-V*	Perp-H**	
Shanghai	69.8083	61.7134	56.5245	13.12%
New York City	82.3466	61.9344	48.7999	32.96%
Tokyo	72.6332	58.9975	49.5441	23.11%
Beijing	84.5490	67.7503	55.4796	24.80%
London	61.6562	48.1851	41.3556	27.96%
Los Angeles	90.6252	63.9697	48.0345	41.67%
Toronto	75.7012	57.8710	47.7711	30.81%
Paris	56.9159	45.9986	39.3670	23.73%
Berlin	62.2552	48.8941	41.7071	27.33%
Average	72.9434	57.2571	47.6204	27.40%

*Perp-V indicates perpendicular two-DOF sun tracking with vertical cell layout.

**Perp-H indicates perpendicular two-DOF sun tracking with horizontal cell layout.

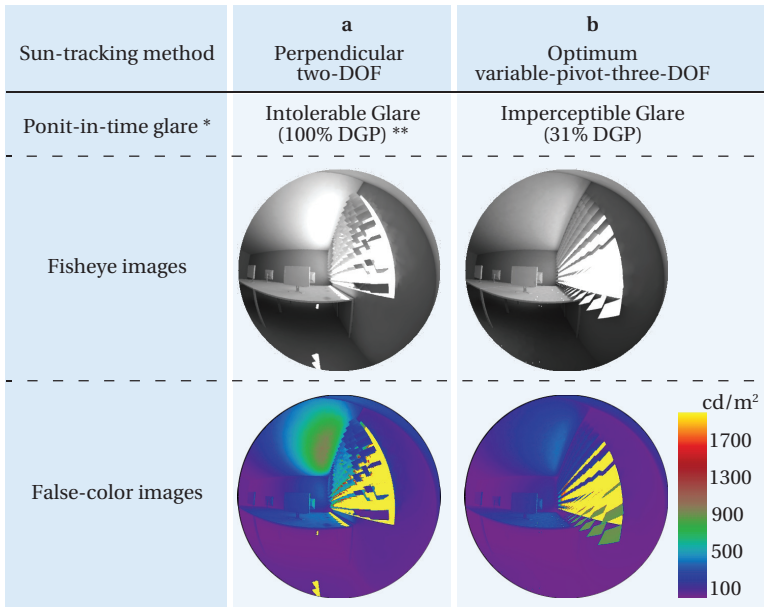
***In $\Delta E_a/E_a$, ΔE_a indicates the difference of E_a between VP-3-DOF and Perp-V; and E_a indicates the E_a of Perp-V.

Table 3.2: Results of $\bar{\eta}_m$ calculated by the climate data of nine cities

City	$\bar{\eta}_m$ (%)			$\Delta \bar{\eta}_m/\bar{\eta}_m$ *
	VP-3-DOF	Perp-V	Perp-H	
Shanghai	9.55	8.73	8.26	9.39%
New York City	9.60	7.70	6.66	24.68%
Tokyo	9.55	8.30	7.53	15.06%
Beijing	9.64	8.00	7.02	20.50%
London	9.39	8.07	7.56	16.36%
Los Angeles	9.66	7.10	5.85	36.06%
Toronto	9.54	7.81	7.03	22.15%
Paris	9.35	8.14	7.65	14.86%
Berlin	9.40	8.05	7.52	16.77%
Average	9.5200	7.9889	7.2311	19.17%

*In $\Delta \bar{\eta}_m/\bar{\eta}_m$, $\Delta \bar{\eta}_m$ indicates the difference of $\bar{\eta}_m$ between VP-3-DOF and Perp-V; and $\bar{\eta}_m$ indicates the $\bar{\eta}_m$ of Perp-V.

the shadow simulations by SketchUp.



* Simulation conditions: 11:00 AM, 20th March, 2017, clear sky, in the reference office, in Shanghai.

** Point-in-time glare is evaluated by discomfort glare rating (DGR) and daylight glare probability (DGP).

Figure 3.13: Simulation results of point-in-time glare by four sun-tracking methods.

3.5. DISCUSSION

3.5.1. VP-3-DOF SUN TRACKING

THE mechanical realization of the VP-3-DOF motion is out of the scope of the current study. Some recommendations to realize the VP-3-DOF motion are given as follows. Firstly, it is not necessary to have physical axes to achieve the rotation. The only requirement is to follow the trajectories provided by our mathematical model. Secondly, since it is an interior lightweight application, the use of fine translucent wires can be considered to actuate PV shading elements, similar to but more sophisticated than what the normal window blinds are using. Thirdly, electrical cables can be considered to be installed along the wires to interconnect the PV modules.

Besides vertical windows, the proposed VP-3-DOF sun tracking is also applicable to the horizontal sun roof. In terms of special scenarios, e.g. a glass greenhouse, the roof area is large and the incident sunlight need to be controlled. Compared with the case with vertical windows (Figure 3.14a), the optimum solution to the case with horizontal windows (Figure 3.14b) can be derived in a similar way. Detailed derivations and results are presented in the Supplementary Note 8 of Ref. [1]. A promising applications of the VP-3-DOF sun tracking is in a greenhouse with movable PV roof to utilize the sunlight for both food cultivation and electricity generation.

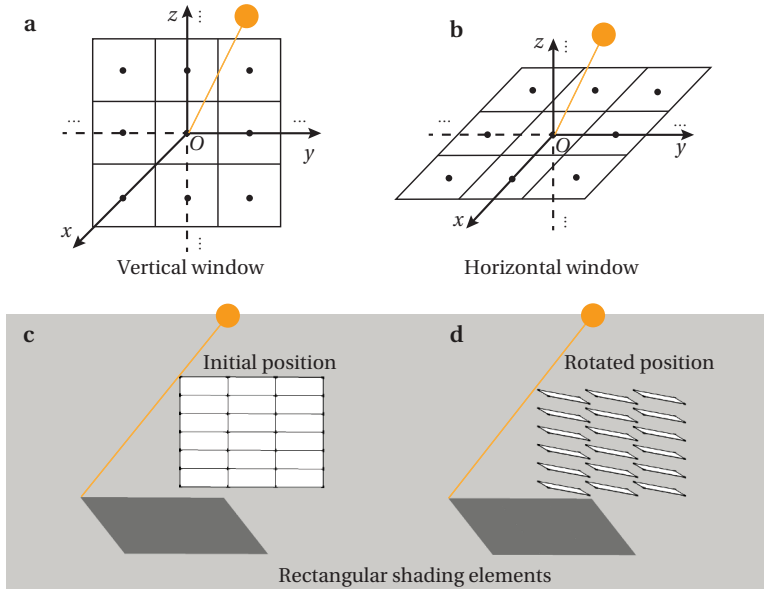


Figure 3.14: Extended application of VP-3-DOF sun tracking. **a**, The model of PV squares in the vertical window in the initial position. **b**, The model of PV squares in the horizontal window in the initial position. **c**, Rectangular PV shading elements in the initial position. The shadows are simulated by SketchUp. **d**, Rectangular PV shading elements in the rotated position. The simulated shadows are the same as that in the initial position.

Besides square PV shading elements, the rectangular PV shading elements can also apply to the VP-3-DOF sun tracking. It has been demonstrated by shadow simulations with SketchUp (Figure 3.14c & d).

3.5.2. LIMITATIONS OF THE CURRENT WORK

The proposed optimum sun-tracking methods have been developed based on an ideal interior model. However, they are not necessarily applicable to exterior applications, where the limitation of windows (see Assumption 1 in the previous chapter) does not exist. On the other hand, exterior BIPV applications require rigorous standards on wind resistance, snow load, etc. Furthermore, architects tend to focus on aesthetics instead of PV power generation in regards to the exterior architectural design. Therefore, further study is required before the proposed sun-tracking methods can be applied to the outdoor cases.

In this study, we have assumed that the window is mounted in a rarely-shaded high-rise building. However, in reality, high-rise buildings are usually built in congested urban areas, resulting in undesired shadows on the PV shading elements. As to the existing buildings, shadows from surrounding buildings can be simulated over the entire year. According to the shading conditions on the window area, case studies should be conducted to optimize the sun-tracking methods, cell layouts, and interconnections of the mini modules. As to new buildings, architects and urban planners should try to avoid severe shading on the vertical façade of the PV-integrated buildings. The optimum lo-

cations of buildings can also be obtained by the simulation of shadows over the entire year.

3.6. CONCLUSIONS

Buildings consume a large amount of energy every year, but also bear great potential of solar energy. The vertical window areas, which account for a large surface area of modern buildings, can potentially convert solar energy into electricity by active PV shading elements, which can meanwhile prevent against the sun glare. Conventional sun tracking sticks to the principle of minimizing the angle between the PV surface normal and the incident direction of the sunlight, aiming to obtain the maximum global irradiance on the PV surface. The novelty of this study is that we break through the conventional method and develop new sun-tracking methods optimized for the PV window shading elements.

In this chapter, we have investigated the performance of two-DOF and three-DOF sun tracking using our proposed irradiance model. The optimum variable-pivot-three-degree-of-freedom (VP-3-DOF) sun tracking enables the PV window to achieve the maximum power generation and non-glare daylighting at the same time. Compared with conventional perpendicular sun tracking, the proposed sun tracking methods improve the annual energy generation by 27.40% and the annual average efficiency by 19.17% as the average over nine cities in the world. Such module-level improvements are more pronounced than that triggered by new materials and process in most studies. Comparing the two proposed solutions in Chapters 2 and 3, the optimum one-DOF sun tracking with extended PV slats and particular cell layout requires simpler mechanical structure of rotations; while the optimum VP-3-DOF sun tracking requires less area of PV material and simpler design of cell layout.

Besides the benefits in energy generation, both solutions provide the building occupants with comfortable diffuse daylight and open exterior view. As an extended application, the optimum VP-3-DOF sun tracking for PV shading elements on horizontal glass roof of a greenhouse is capable to maximize the power generation, and also provides the crops with certain amount of diffuse daylight. An economic PV horticultural system can be built by applying the proposed sun-tracking method, which can increase the production of crops and reduce the energy consumption. Theoretically, the optimum variable-pivot-three-DOF sun-tracking method is applicable to any occasions requiring the maximum power generation and the access to the natural diffuse light.

REFERENCES

- [1] Y. Gao, J. Dong, O. Isabella, R. Santbergen, H. Tan, M. Zeman, and G. Zhang, *A photovoltaic window with sun-tracking shading elements towards maximum power generation and non-glare daylighting*, Applied Energy **228**, 1454 (2018).
- [2] D. Rossi, Z. Nagy, and A. Schlueter, *Adaptive distributed robotics for environmental performance, occupant comfort and architectural expression*, International Journal of Architectural Computing **10**, 341 (2012).
- [3] J. Hofer, A. Groenewolt, P. Jayathissa, Z. Nagy, and A. Schlueter, *Parametric analy-*

- sis and systems design of dynamic photovoltaic shading modules*, Energy Science & Engineering , 134 (2016).
- [4] P. Jayathissa, M. Luzzatto, J. Schmidli, J. Hofer, Z. Nagy, and A. Schlueter, *Optimising building net energy demand with dynamic BIPV shading*, Applied Energy **202**, 726 (2017).
- [5] T. Hong, K. Jeong, C. Ban, J. Oh, C. Koo, J. Kim, and M. Lee, *A preliminary study on the 2-axis hybrid solar tracking method for the smart photovoltaic blind*, Energy Procedia **88**, 484 (2016).
- [6] C. Koo, T. Hong, K. Jeong, C. Ban, and J. Oh, *Development of the smart photovoltaic system blind and its impact on net-zero energy solar buildings using technical-economic-political analyses*, Energy **124**, 382 (2017).
- [7] H. Mousazadeh, A. Keyhani, A. Javadi, H. Mobli, K. Abrinia, and A. Sharifi, *A review of principle and sun-tracking methods for maximizing solar systems output*, Renewable and Sustainable Energy Reviews **13**, 1800 (2009).
- [8] Y. Gao, J. Dong, O. Isabella, M. Zeman, and G. Q. Zhang, *Daylighting simulation and analysis of buildings with dynamic photovoltaic window shading elements*, in *Solid State Lighting: International Forum on Wide Bandgap Semiconductors China (SSLChina: IFWS), 2017 14th China International Forum on (IEEE, 2017)* pp. 52–55.

4

ENERGY PERFORMANCE OF BUILDINGS WITH PHOTOVOLTAIC WINDOW SHADES

Abstract

In previous chapters, PV windows have been studied towards optimum performances of power generation and sun glare protection. We have derived the formulas to compute the shade-free sun tracking (the optimum sun tracking in previous chapters) for a single-axis PV blind with an optimal design of cell layouts. The shade-free sun-tracking method has been proved to be capable of achieving the maximum power generation and non-glare daylighting. In this chapter, we focus on evaluating the contribution of this optimal sun-tracking method to the energy saving in buildings by comprehensively considering artificial lighting, heating and cooling. Via this comprehensive evaluation, the shade-free sun-tracking method is compared with three static tilt angles and the conventional perpendicular tracking method. The parametric model of the PV blind is integrated into the three-dimensional model of a reference office room. Simulations show that using the shade-free tracking method, the net energy consumption of the building, considering PV production, artificial lighting, heating and cooling, is reduced by 10.49%, compared to the perpendicular tracking method. With the shade-free tracking method, the PV blind generates more electricity than that consumed by artificial lighting.

Parts of this chapter have been published in the 14th China International Forum on Solid State Lighting (SSLChina), 52 (2017) [1]. Parts of this chapter have been submitted to Journal of Energy and Buildings.

4.1. INTRODUCTION

BESIDES electricity generation, PV windows can also adjust and control the amount of incident sunlight, thereby affecting the energy consumption of artificial lighting and air-conditioning inside the building environment. Two types of PV windows, static and dynamic, have been commonly used and studied. Static PV windows usually contain glazing-attached translucent PVs with certain transmittance or opaque PVs with certain spacing. Dynamic PV windows integrate opaque PVs with adjustable window treatments, e.g. blinds, shutters, etc.

As to a building with static PV windows, its energy performance can be affected by PV-window characteristics, such as the PV power conversion efficiency (PCE), the transmittance or spacing of solar cells, and the cell layout on the window glazing. Elarga et al. evaluated the energy performance of façade cavity integrated with semi-transparent PV modules. Results showed that such integrated PV system reduced the cooling energy demands of buildings [2]. Jovanovic et al. simulated the performance of PV modules combined with a Trombe wall. Results showed that an optimal tilt angle increased the electricity production of PV modules, which were suggested to be installed outside of the Trombe wall [3]. Schmid et al. simulated the net zero supplementary interior lighting powered by PV windows. Using separate opaque solar cells on a transparent glazing resulted in better performance than a transparent single-glazed window in terms of illuminance distribution and glare protection. An alternative approach, using a 30%-transparency thin-film PV window, performed even better in respect of glare protection [4]. Han et al. investigated the performance of a double-side PV façade through field measurement. Results indicated that it reduced the heat gain of the building in summer and generated extra electricity. The influence of the temperature on the conversion efficiency of see-through thin-film PV is negligible compared to considerable reduction of heat gain [5]. Zhang et al. studied the over all energy performance of a building with semi-transparent photovoltaic (STPV) modules by developing a comprehensive simulation model of thermal balance, daylighting and power generation. Results showed that STPV windows reduced the electricity consumption by 18% and 16% respectively compared to the clear single and double-pane glazings in Hong Kong [6]. Xu et al. investigated the overall energy performance of office buildings with spaced solar cells distributed on the windows. Results under the climatic conditions of central China indicated that the optimal PV cell coverage reduced the electricity consumption by 13% on average compared to the least favourable coverage ratio [7].

Compared to a static PV window, the dynamic counterpart, e.g. a PV blind, could flexibly adjust the incident sunlight by tuning the tilt angles of PV slats, consequently balancing the PV power generation and interior energy consumption. Kang et al. analyzed several parameters of a PV blind. Among a series of inclined angles (from 0° to 90° in 15° intervals), the maximum electricity production was obtained in the inclined angle of 75° . The optimal width of the PV module was half of the width of the blind to avoid PV shading effects. Moreover, the ventilation in the double-layer window façade decreased the temperature of the cavity, consequently improved the electricity production by 8.3% [8].

Kim et al. studied a combined system of a PV blind and dimmable LED lights. The PV modules (6% PCE) were attached to the blind slats. In the reference room, the slat angle

was kept at 0° . Meanwhile, in the adjacent test room, the slat angle was hourly controlled to be orthogonal to the profile angle of the sunlight. The LED lighting in both rooms was automatically controlled with the feedback of photosensors in order to maintain the illuminance level of the target working plane. Experimental results showed that the PV power generation in the test room was 32% more than that in the reference room; but the energy saving of LED lighting in the test room was 35% less than that in the reference room [9].

Bahr et al. assessed the design parameters of a PV-blind system based on a costs-benefits analysis. Two variables were considered: the ratio between the installation distance of adjacent slats to the module depth (1, 2, and 3), and the tilt angle (0° , 25° , and 60°). The profit rate of the PV blind system was calculated by considering heating and cooling loads, PV power generation with partial shading effects, daylighting and artificial lighting. Simulation results showed that the highest profit rate was obtained when the ratio was 2; and the tilt angle was 0° [10].

Mandalaki et al. investigated various typologies of PV shading systems in terms of energy efficiency and visual comfort conditions. The Brise-Soleil system was proved to be the most suitable typology to integrate PV modules. However, all typologies were assessed in a fixed position; and the tilt angle of blinds was not given [11].

Luo et al. compared the thermal performance of PV blind within a double skin façade (DSF) with that of conventional DSFs with and without shading blinds. Experimental results showed that the DSF PV blind can save 12.16% and 25.57% respectively in summer compared with those two counterparts [12].

Hu et al. conducted comparative studies on the BIPV Trombe wall systems in regard of electricity production and heating/cooling load reduction. Results showed that the PV blind-integrated Trombe wall system was superior to the glass-attached and mass wall-attached PV Trombe wall systems in terms of electricity saving and CO_2 emission reduction [13, 14].

Hong et al. investigated the design parameters of the PV blind by nonlinearity analysis. Three design variables were mainly considered, i.e. the orientation, the width of the PV panel (from 10 mm to 50 mm in 10 mm intervals), and the season. Results showed that the PV blind with 10 mm-width PV panels revealed the best performance in terms of electricity generation and saving-to-investment ratio at year 25 because the relatively smaller width alleviated the PV partial shading effects [15].

Park et al. developed a four-node-based finite element model ($\text{FEM}_{4\text{-node}}$) to predict the electricity generation of the PV blind. By this means, the economic performance of the PV blind can be comprehensively analyzed for practical applications [16]. Based on $\text{FEM}_{4\text{-node}}$, Oh and Koo et al. improved the prediction accuracy of the model by developing a nine-node-based finite element model ($\text{FEM}_{9\text{-node}}$) [17, 18].

Hong et al. proposed the bi-directional control method, which eliminated the partial shading problem of PV blinds. Compared with the uni-directional control method (PV panel remained as orthogonal to the profile angle of the sunlight), the bi-directional control improved the average illuminance of the room and generated comparative electricity [19]. In a following study, Hong et al. further evaluated the bi-directional control method in regard of lighting and thermal performance. Results showed that the energy consumption of lighting and heating system were reduced, but the cooling system con-

sumed more energy, compared with the uni-directional control method [20].

Koo et al. compared four type of PV blinds, i.e. amorphous silicon (a-Si) PV panels embedded in fixed blind, a-Si PV panels embedded in two-axis sun-tracking blind, copper-indium-gallium-selenide (CIGS) PV panels embedded in fixed blind, and CIGS PV panels embedded in two-axis sun-tracking blind. Simulation and analysis results showed that the two-axis CIGS PV blind performed better than other alternatives in terms of energy self-sufficiency rate and net present value at year 25 [21].

In Chapter 2, we have proposed a shade-free sun-tracking method (the optimum sun-tracking method) for single-axis PV blinds, installed inside the building. With further optimal design of the cell layout on the slats, the PV partial shading problem was properly solved. The proposed one-axis sun-tracking method and corresponding cell layout have been demonstrated to be capable of achieving the maximum PV power generation and non-glare daylighting. However, the influence of PV blinds on building energy performance was not estimated in terms of artificial lighting, heating and cooling.

In this work, we first introduce a typical built environment of a reference office room with an interior PV blind, whose tilt angle is tunable. Secondly, the model of slat-attached PV module containing series-connected solar cells is built considering the PV partial shading effects. Thirdly, artificial lighting design is conducted with commercially available luminaire in the reference office room. We assume that the lamps are accurately dimmable with sensors so that the lighting energy consumption can be compensated by daylighting, which is affected by the tilt angle of PV slats. Fourthly, the thermal model is implemented to evaluate the energy consumption of heating and cooling. Lastly, three static tilt angles and two sun-tracking methods of PV blinds are evaluated in terms of PV energy production, and energy consumption by artificial lighting, heating and cooling.

4.2. METHODS

IN this study, annual energy performance is calculated by building geometrical and mathematical models and implementing various softwares containing simulation engines and packages, as shown in Fig. 4.1. The three-dimensional (3D) model of a typical office room is built by Rhinoceros, which is a commercial computer-aided design (CAD) software [22]. The electricity output of PV blinds is simulated based on a single-diode PV model in MATLAB SimuLink [23], considering the PV partial shading effects. Two inputs of the PV model, equivalent global irradiance and cell temperature, are given as mathematical models. Daylighting and artificial lighting are simulated based on Radiance, which is a suite of programs for the analysis of lighting using hybrid deterministic/stochastic (Monte Carlo) ray tracing [24]. Energy consumptions by heating and cooling in the built environment are simulated based on EnergyPlus, a simulation engine containing many program modules for the calculation of heating and cooling energy demand [25]. In this study, simulation engines like Radiance and EnergyPlus are integrated in the Ladybug and Honeybee tools [26], which are free and open source environmental plugins for Grasshopper. Grasshopper, as a plugin of Rhinoceros, provides a parametric platform for graphical algorithm editing [27]. Fig. 4.1 shows the interconnected simulation platforms, engines, and softwares implemented in this study.

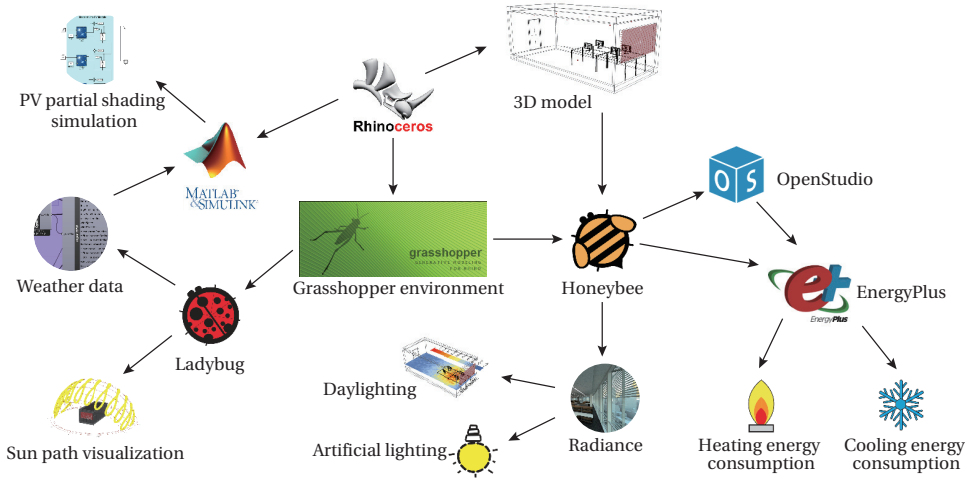


Figure 4.1: Simulation engines and tools used in this study.

4.2.1. 3D MODEL OF AN OFFICE ROOM

PV blinds mainly benefit the urban tall buildings, which hold a large area of windows and require a great amount of energy. To quantify the energy contribution of PV blinds, the CAD model of a typical office room is built by Rhinoceros [22]. We assume the office room is within a tall building located in Shanghai (31.40°N , 121.45°E). This office model is adapted from a reference office, which was proposed as a baseline for comparing different technologies, such as artificial lighting, daylighting, window treatment, etc. [28]. As shown in Fig. 4.2, the office room is designed in the shape of a shoebox, so that the impact of lighting and shading control is obvious. The south-facing window of the office room has a window-to-wall ratio (WWR) of 40%. PV blind is mounted on the interior side of the window glass. We assume that the slats of the PV blind rotate simultaneously, so that PV slats are parallel to each other and receive identical solar irradiance. The thickness of the PV-integrated slats is ignored in this model. For a PV blind with certain dimensions (w and l) and materials, its performance is mainly determined by the tilt angle (θ) of the slats (Fig. 4.2).

The dimensions of the office are shown in Figure 4.3; the reflectance of critical geometries in this model is listed in Table 4.1.

Table 4.1: Reflectance of critical geometries in the model of the reference office.

Geometry	Reflectance
Ceiling	0.80
Floor	0.20
Interior walls	0.50
Furnishings	0.50
Glazing	0.20
Door	0.50

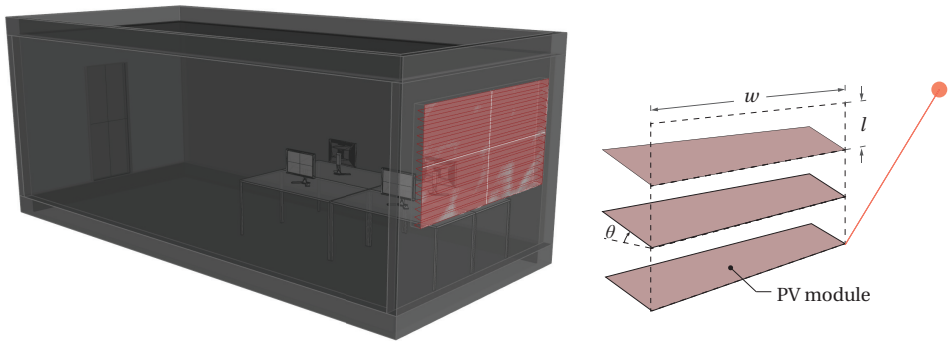


Figure 4.2: Perspective view of the office model with the PV blind.

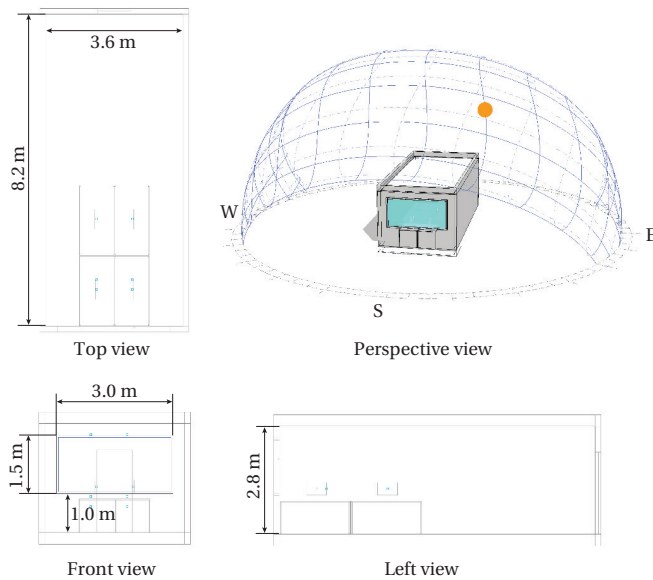


Figure 4.3: Dimensions of the reference office illustrated in four views: perspective, top, front, and left.

4.2.2. MODELS OF SOLAR CELL AND PV MODULE

An individual slat of the proposed PV blind contains several solar cells, which together form a PV mini-module. Our previous study has demonstrated that slat-integrated solar cells in the optimal layout of horizontal strips result in the maximum power generation of the single-axis PV blind [29]. Therefore, the horizontal-strip layout of solar cells is applied to the design of the mini-module in this study. Since internal shading could happen when the slats are in certain tilt angles, the PV module might suffer from PV partial shading effects, which affect the electrical performance of the PV blind. To precisely simulate the PV partial shading effects, each solar cell requires unique inputs of solar irradiance and cell temperature. The model of PV module is built by interconnecting 10 identical solar-cell models in series, as shown in Fig. 4.4. The single-diode model of a solar cell is used as a basic simulation unit. The equivalent circuit is also shown in Fig. 4.4, where the output current is described as

$$I = I_{light} - I_0 \left(\exp \left(\frac{V + R_s I}{A} \right) - 1 \right) - \frac{V + R_s I}{R_{sh}}, \quad (4.1)$$

where I_{light} is the light-generated current; I_0 is the diode saturation current; R_s is the series resistance; R_{sh} is the shunt resistance; $A = n_d k T_c / q$ is the modified ideality factor; n_d is the diode ideality factor; k is the Boltzmann constant ($1.3807 \times 10^{-23} J/K$); q is the electron charge ($1.6022 \times 10^{-19} C$); and T_c is the cell temperature. Detailed description of the single-diode model can be found in [30].

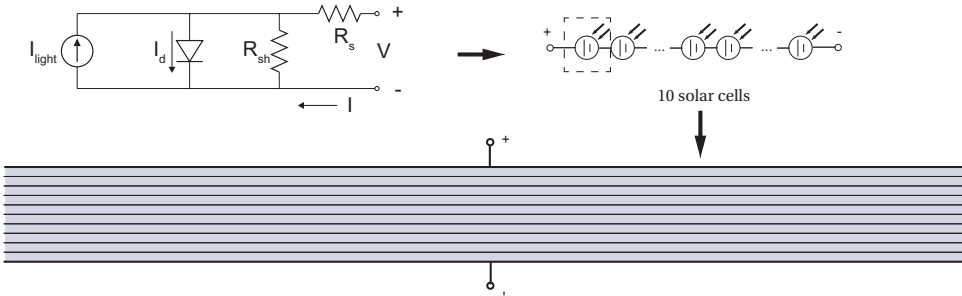


Figure 4.4: Models of solar cell and PV mini-module.

In this study, the PV model is configured according to a commercial thin film cadmium telluride (CdTe) module (First Solar Series 6TM, FS-6445). Detailed electrical specifications can be found in the data sheet of the product [31]. The PV model contains no bypass diode due to the thin film technology and special module dimensions. The simulation in terms of PV electricity generation is conducted in the environment of MATLAB SimuLink. Two types of inputs are necessary for the PV model, the solar irradiance on each cell and each cell's temperature.

4.2.3. INPUT PARAMETERS

In Chapter 2, a simplified model of solar irradiance was proposed and applied to the calculation of global irradiance on a tilt surface [29]. The global irradiance (G_{global}) on

the non-shading PV module has been derived as

$$G_{global} = I_e^{dir} (\sin \alpha_s \cos \theta - \cos \alpha_s \cos A_s \sin \theta) + G_{h,d}, \quad (4.2)$$

where I_e^{dir} is the direct normal irradiance of the sunlight; α_s and A_s are the solar altitude and azimuth respectively; and $G_{h,d}$ is the diffuse horizontal irradiance. Detailed explanation of each notation can be found in Chapter 2.

In the partial-shading conditions, solar cells on the mini-module receive different global irradiance. We assume that when the internal shading within the PV blind happens, the shading area receives no direct irradiance, but still receives diffuse irradiance. Here we simply treat this diffuse irradiance as $G_{h,d}$. For the cell in the partial shading position, its irradiance is contributed by both directly-illuminated global irradiance and diffuse irradiance. Thus, the equivalent global irradiance (G_{global}^{eq}) is used as the input of the cell model in partial shading,

$$G_{global}^{eq} = \left(1 - \frac{S_{shadow}^{cell}}{S_{cell}} \right) I_e^{dir} (\sin \alpha_s \cos \theta - \cos \alpha_s \cos A_s \sin \theta) + G_{h,d}, \quad (4.3)$$

where S_{cell} and S_{shadow}^{cell} are the area of an individual solar cell and the area of the shadow on the individual cell respectively.

The PV model also requires the input of the cell temperature (T_c), which could be affected by the environmental variables, such as ambient temperature (T_a), equivalent global irradiance (G_{global}^{eq}), wind speed, wind direction, and relative humidity. Since the PV blind is mounted interiorly, the influence of wind is ignored here. Also, the contribution of relative humidity to the cell temperature is ignored because it will not change with the tilt angle. Then, the simplified model of cell temperature is used:

$$T_c = 0.943 T_a + 0.028 G_{global}^{eq} + 4.3, \quad (4.4)$$

where the units of T_a and G_{global}^{eq} are respectively $^{\circ}C$ and W/m^2 . We use this model to estimate the temperature of solar cells which might be in shadows, though the model is originally developed for PV modules [32, 33].

4.2.4. TILT ANGLES AND SUN-TRACKING METHODS

The conventional sun tracking of PV systems aims to gain the maximum global irradiance on the PV module. For PV modules with single-axis sun tracking, the maximum global irradiance appears in the quasi-perpendicular sun-tracking method (Position D in Fig. 4.5, referred to as “perpendicular tracking method” in the following context) in no shading conditions [29]. However, for the case of PV blind, the maximum global irradiance might not necessarily result in the maximum power generation due to the partial shading effects. Our previous study has demonstrated that the shade-free tracking method (Position E in Fig. 4.5) results in the maximum power generation and non-glare daylighting [29]. In this study, three static tilt angles (0° (Position C), 15° (Position B), and 90° (Position A)) and two sun-tracking methods (Positions D and E) are chosen for the comparative analysis of the overall energy performance of the PV blind. To simplify the

calculation, the energy consumption of the sun-tracking system is ignored in this study. Detailed derivations of the tilt angles of the perpendicular and shade-free tracking methods can be found in Chapter 2 [29].

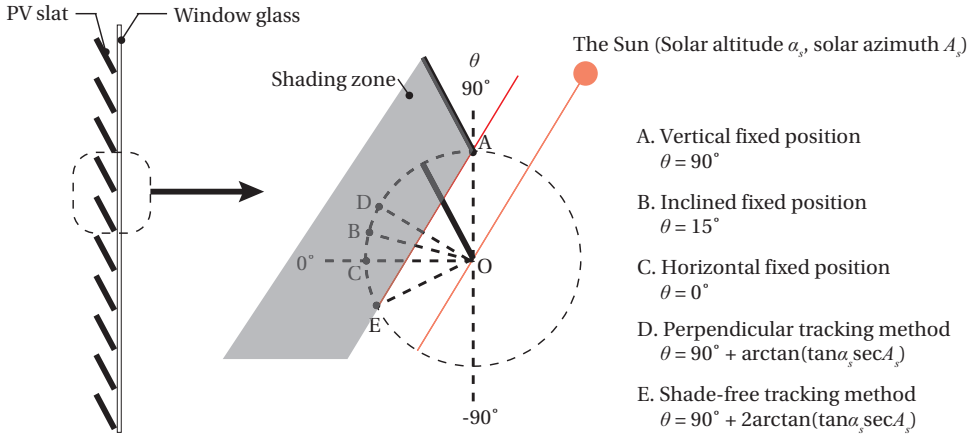


Figure 4.5: Cross-section diagram of three static tilt angles and two sun-tracking methods of PV slats.

4.2.5. DAYLIGHTING AND ARTIFICIAL LIGHTING

Regarding the PV blind in a fixed tilt angle, a static CAD model is sufficient for the simulation of interior daylighting for an entire year. However, situations are different with respect to sun-tracking PV blinds, whose tilt angle varies with the solar position. It means that a unique CAD model is required for each simulation time point over the entire year. Using a conventional simulation method would consume lots of time and efforts if the CAD models of PV blinds with various tilt angles were input manually. In this study, we use parametric modeling and simulation to solve this problem. Grasshopper is exactly such a parametric platform which is tightly integrated with Rhinoceros [22, 27]. Ladybug and Honeybee tools, as plugins of Grasshopper, are mainly used for the lighting and energy simulation in this study [26]. Ladybug uses the simplified irradiance model called GenCumulativeSky to generate a cumulative sky radiance distribution, which can accelerate the ray-tracing simulation by Radiance [34]. Honeybee visualizes the input parameters of Radiance, and enables parametric modeling by interconnecting lighting simulation blocks with Grasshopper components.

The illuminance on the target working plane contributed by daylighting varies with solar radiance, solar position, and the tilt angle of the PV slats. The daylighting simulation for an entire year (one-hour interval) can be run in a loop in the Grasshopper platform. The Grasshopper algorithm diagram for the loop simulation can be found in Appendix C.

In the daytime, the daylighting through the PV blind is sometimes not sufficient to meet the requirements of architectural standards of indoor illumination. That is when compensative artificial lighting is required during the day. For office environment, the standard average illuminance (\bar{G}_{sta}) on the target working plane (0.75 m height) is 500

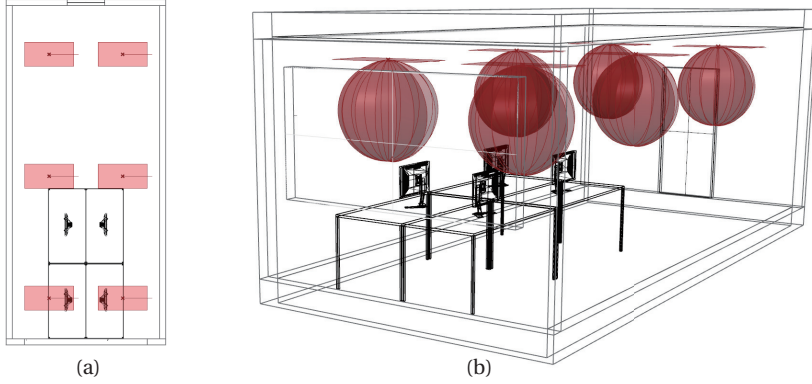


Figure 4.6: Interior artificial lighting design of the reference office room: (a) top view, and (b) perspective view.

lux [35]. At night, daylighting contributes zero to the indoor illumination, which is then entirely provided by artificial lighting. In this study, we assume that the office room is equipped with dimmable luminaire and smart lighting system, which is automatically and precisely controllable by the feedback signal of accurate light sensors. In fact, this feedback control functionality has already been realized in some commercial lighting systems. Theoretically, a relatively accurate illuminance distribution on the target working plane can be obtained by rationally distributing the light sensor [36]. To simplify the study, we only consider the average illuminance of the working plane, and ignore the influence of the illuminance contrast between the working plane and the background. We also assume that all luminaire are dimmed simultaneously. As shown in Fig. 4.6, six identical luminaire are mounted on the ceiling of the office room. The illuminance distribution in the room can be simulated by importing the IES file of the luminaire into Radiance in Honeybee. Detailed parameters of the chosen luminaire can be found in the product data sheet [37]. In respect of the energy consumption of artificial lighting, we assume that the illumination by daylighting and artificial lighting can be superimposed linearly. We also assume that the power consumption of six luminaire is proportional to the average illuminance. The human activities in the office determines the time to turn on/off the artificial lighting. The probability of lighting demand at a certain point of time ($\mathbb{P}_l(t)$) is given by the weekly schedule of the indoor lighting as shown in Fig. 4.7. The power consumption of artificial lighting at a certain time point ($P_l(t)$) can be estimated by

$$P_l(t) = \begin{cases} \left(1 - \frac{\bar{G}_{sun}}{\bar{G}_{sta}}\right) P_{sta} \mathbb{P}_l(t) & \bar{G}_{sun} < \bar{G}_{sta} \\ 0 & \bar{G}_{sun} \geq \bar{G}_{sta} \end{cases}, \quad (4.5)$$

where \bar{G}_{sun} is the average illuminance contributed by the daylighting; P_{sta} is the standard power consumption of artificial lighting, which can independently achieve the standard average illuminance on the target working plane.

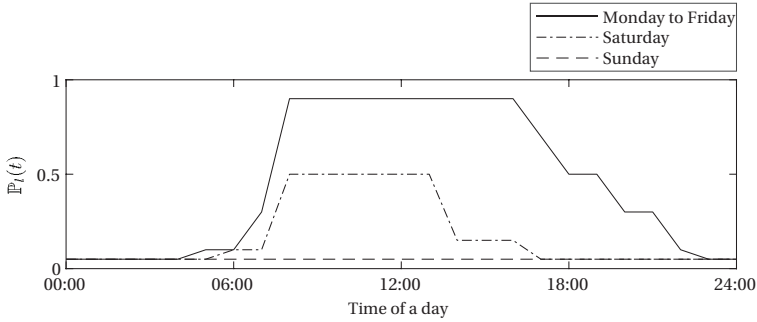


Figure 4.7: Weekly schedule of artificial lighting. $\mathbb{P}_l(t)$ is defined as the probability of lighting demand at a certain point of time

4.2.6. HEATING AND COOLING SYSTEM

The tilt angle of the PV blind affects the amount of incident sunlight, which changes the air temperature in the building environment, as it changes the daylighting mentioned above. In a commercial building, the room temperature is usually maintained within a certain range considering the human comfort. Therefore, the energy consumption by heating and cooling in the building varies with the tilt angle of the PV blind. The annual energy consumption by air-conditioning can be calculated by running a parametric simulation in Honeybee, using the EnergyPlus engine, which contains necessary valid models and default inputs. The weekly schedules of the maximum and minimum room temperature for a typical office environment are shown in Fig. 4.8 and 4.9. The Grasshopper algorithm diagram for the loop simulation of the annual energy consumption for heating and cooling can be found in Appendix C.

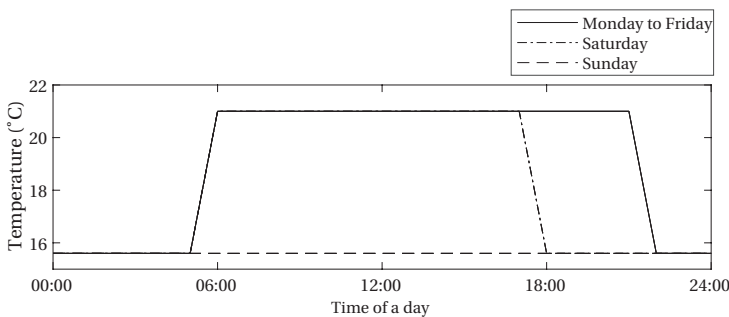


Figure 4.8: Weekly schedule of the minimum room temperature.

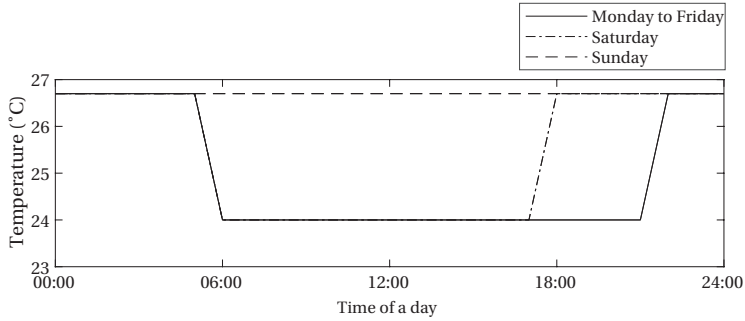


Figure 4.9: Weekly schedule of the maximum room temperature.

4.3. RESULTS

4.3.1. PV ELECTRICITY GENERATION

By inputting each cell's G_{global}^{eq} and T_c at a certain point of time into the model of the PV mini-module, the PV power generation is obtained, considering the PV partial shading effects. The power generation by the PV blind over an entire year is then obtained by running the MATLAB simulation in a loop. Simulation results under five positions are shown in Fig. 4.10. It is obvious that the vertical fixed position (Position A in Fig. 4.5) and the shade-free tracking method (Position E) reveal higher power generation compared to the other three positions. As explained in Chapter 2, the maximum PV power generation is achieved in the vertical fixed position and shade-free tracking method because the input power stays the maximum while no shading exists on the PV slats [29]. To quantitatively compare the PV power generation under five positions, accumulative annual power generation, i.e. the energy generation in the form of electricity, is calculated and shown in Fig. 4.11. Consistent with the results as shown in Fig. 4.10, the vertical fixed position and shade-free tracking method generate the maximum amount of electricity. However, the vertical fixed position turns the window into a wall, impeding the daylighting and blocking the view. Therefore, to obtain the maximum annual electricity generation by PV blind, the shade-free tracking method is a prime choice.

4.3.2. ENERGY CONSUMPTION BY ARTIFICIAL LIGHTING

The rated input power of an individual luminaire is 87 W. To obtain a standard average illuminance ($\bar{G}_{sta} = 500$ lux), the luminaire is dim to 72.63% of the rated input power when the daylighting contribution is zero (in the vertical fixed position or at night). Therefore, the standard power consumption of artificial lighting system (six luminaire) P_{sta} is 379 W. With P_{sta} , the illuminance distribution by artificial lighting on the target working plane is simulated by Radiance in Honeybee (Fig. 4.12). In this study, we calculate the illuminance on the working plane by daylighting and artificial lighting separately. First, the artificial lights are turned off. The daylighting contribution to the illuminance distribution on the working plane is simulated and the annual results (\bar{G}_{sta} for each time point) are obtained by running the Grasshopper algorithm in a loop. Second, by sub-

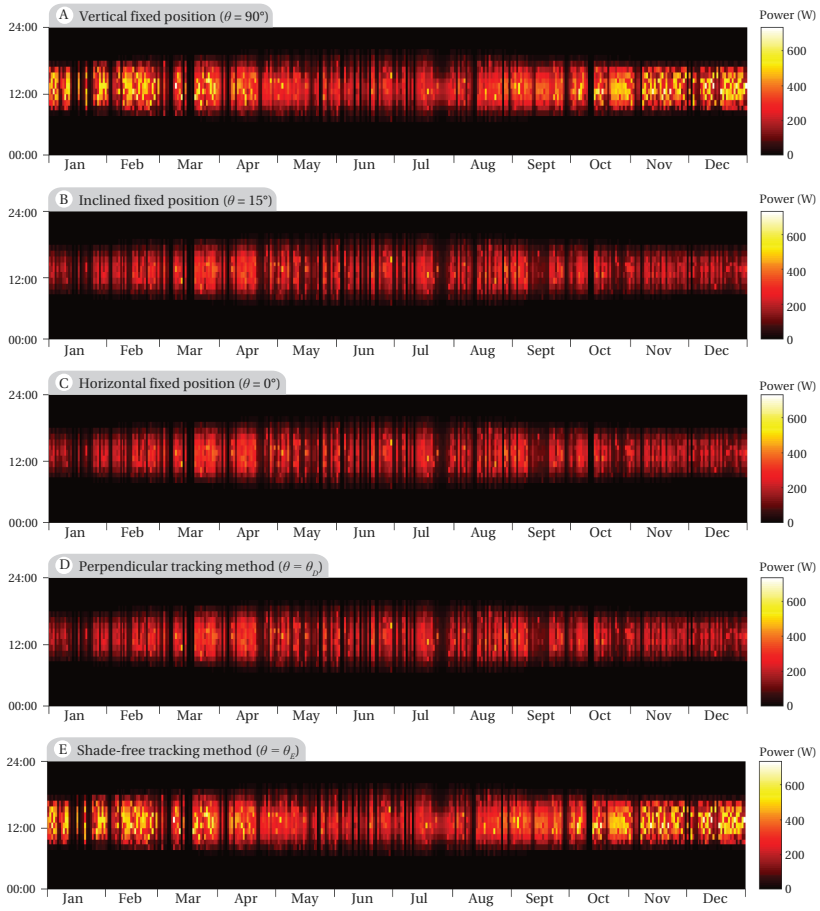


Figure 4.10: Power generation by PV blind under five considered positions (see Fig. 4.5) in one-hour time interval over the year.

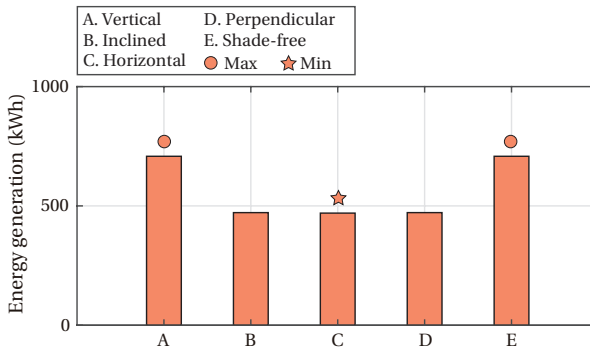


Figure 4.11: Annual electricity generation by the PV blind under five considered positions (see Fig. 4.5). The maximum and the minimum values are marked with solid circles and star respectively.

stituting \bar{G}_{sta} , \bar{G}_{sun} , P_{sta} , and $\mathbb{P}_l(t)$ into Eq. (4.5), the power consumption by artificial lighting at each point of time over an entire year is obtained, as shown in Fig. 4.13. It is obvious that the artificial lighting consumes more electricity in the vertical fixed position than the others, since the daylighting makes no contribution to the interior illumination in the vertical fixed position. In contrast, the horizontal fixed position and shade-free tracking method introduce more sunlight into the room and consume less electricity for artificial lighting compared to the other three positions. The annual electricity consumption is calculated by accumulating the power consumption over an entire year, as shown in Fig. 4.14. In terms of electric lights, the most energy-saving tilt angle of the PV slats appears in the horizontal fixed position. Considering both electricity generation by PV blind and electricity consumption by artificial lighting, the shade-free tracking method shows an obvious advantage over the other three fixed positions and one tracking method, and is the only method by which PV generates more electricity than that the lighting consumes (Fig. 4.15).

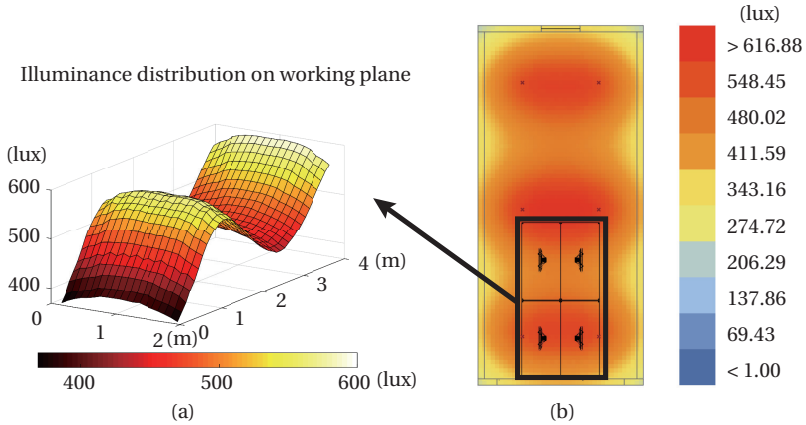


Figure 4.12: (a) Three-dimensional color map of illuminance distribution on the target working plane. (b) Two-dimensional color map of illuminance distribution of the reference office (same height as the working plane). Note that two color maps are illustrated by two different color bars from two different softwares.

4.3.3. ENERGY CONSUMPTION BY HEATING AND COOLING

By running the EnergyPlus simulation integrated with parametric models in a loop (Appendix C), the energy consumption by heating and cooling is obtained under five different positions of PV slats. The annual energy consumption by heating and cooling is then calculated as shown in Fig. 4.16. The vertical fixed position results in the maximum heating energy consumption and the minimum cooling energy consumption. The horizontal fixed position leads to the minimum heating energy consumption and the maximum cooling energy consumption. With respect to the combination of the energy consumption by heating and cooling, the shade-free tracking method consumes less energy than the others. But the difference from the most energy-consuming position (the inclined fixed position) is very small (within 0.44%). Detailed values of annual energy consumption by heating and cooling can be found in Table 4.2.

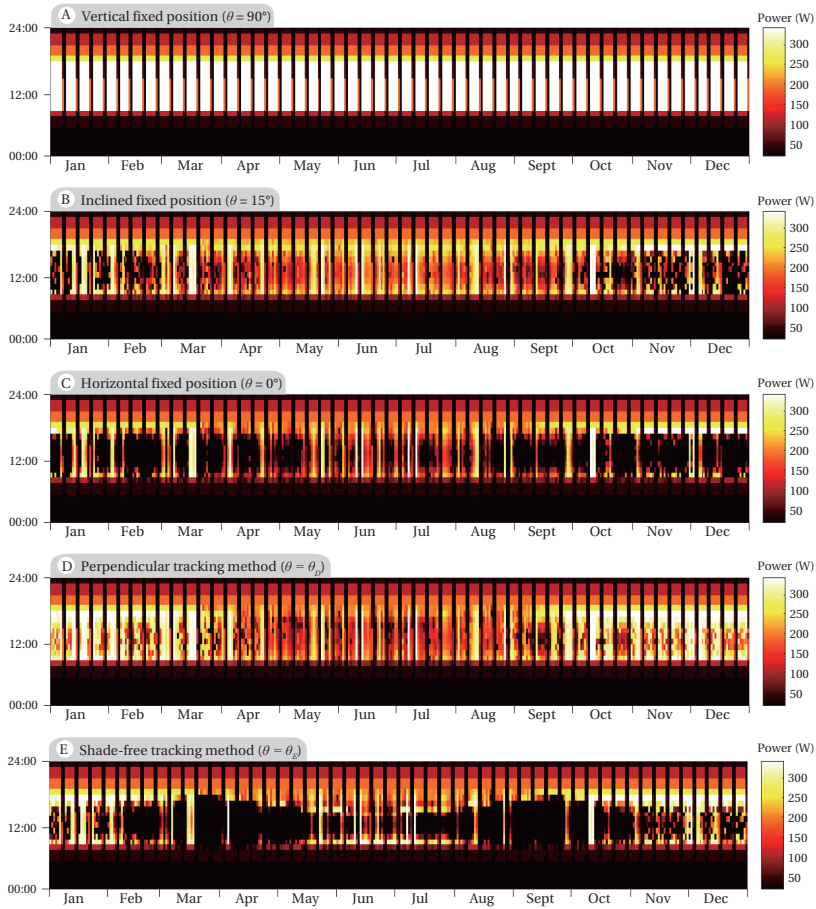


Figure 4.13: Power consumption by artificial lighting under five considered positions (see Fig. 4.5) in one-hour time interval over the year.

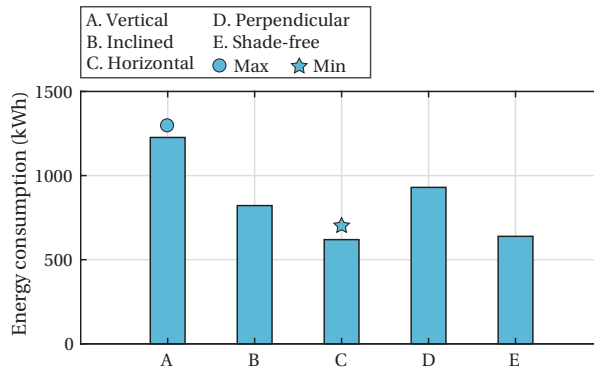


Figure 4.14: Annual electricity consumption by artificial lighting under five considered positions (see Fig. 4.5). The maximum and the minimum values are marked with solid circle and star respectively.

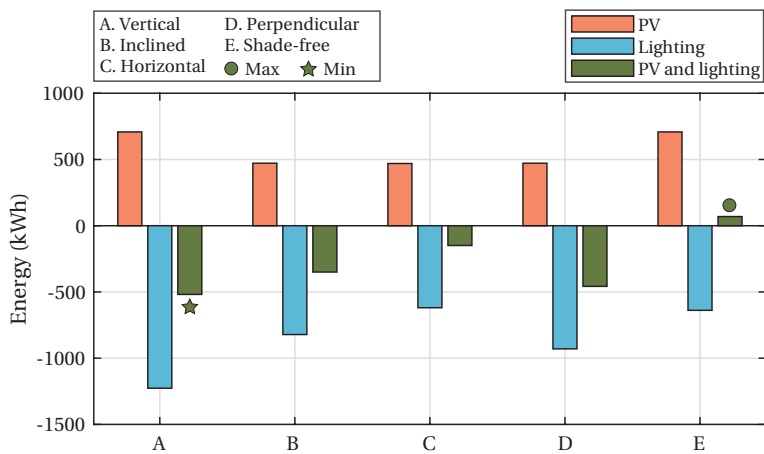


Figure 4.15: Annual electricity generation by PV blind (orange), annual energy consumption by artificial lighting (blue), and net annual energy generation/consumption by PV and lighting (green) under five considered positions (see Fig. 4.5). The maximum and the minimum values of the net energy generation/consumption are marked with solid circle and star respectively.

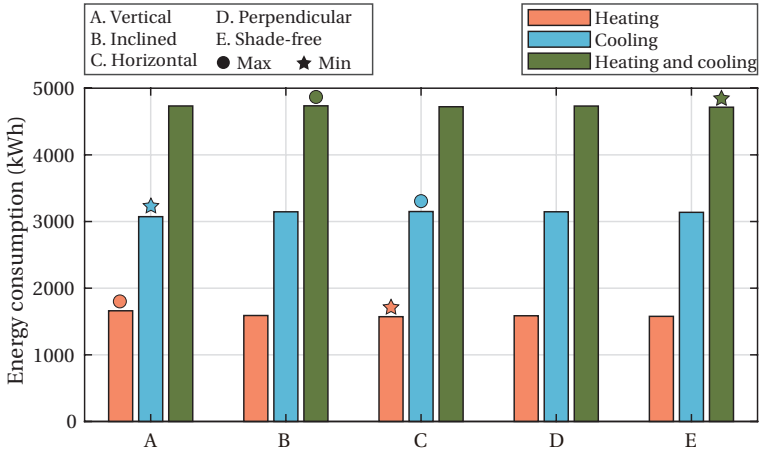


Figure 4.16: Annual electricity consumption by heating (orange), cooling (blue), and the combination of heating and cooling (green) under five considered positions (see Fig. 4.5). The maximum and the minimum values are marked with solid circles and stars respectively.

4.3.4. OVERALL ENERGY GENERATION AND CONSUMPTION

Given the aforementioned results, the overall net energy consumption can be easily calculated by considering the electricity generated by PV blind, the electricity consumed by artificial lighting, the energy consumption by heating and cooling. As shown in Fig. 4.17, the shade-free tracking method proves its superiority over others. Compared with the conventional perpendicular tracking method, the shade-free tracking method saves 10.49% energy. The horizontal fixed position (C) gives an annual energy consumption of 4871.54 kWh. The conventional perpendicular tracking method (D) increases this by 6.55% while the shade-free tracking method (E) reduces this by 4.63%. This shows that tracking can outperform the best fixed position, but only when the shade-free tracking scheme is used. Detailed values of overall net annual energy consumption can be found in Table 4.2.

Table 4.2: Overall annual energy consumption.

Energy consumption (kWh)	A	B	C	D	E	
Heating	1660.95	1589.96	1572.29	1586.25	1577.33	
Cooling	3072.86	3145.96	3149.84	3146.27	3137.78	
PV	-707.96	-471.84	-469.80	-471.88	-707.96	
Lighting	1226.59	821.58	619.21	929.79	638.79	
Overall	5252.45	5085.66	4871.54	5190.43	4645.95	
Energy saving by E		11.55%	8.65%	4.63%	10.49%	0.00%

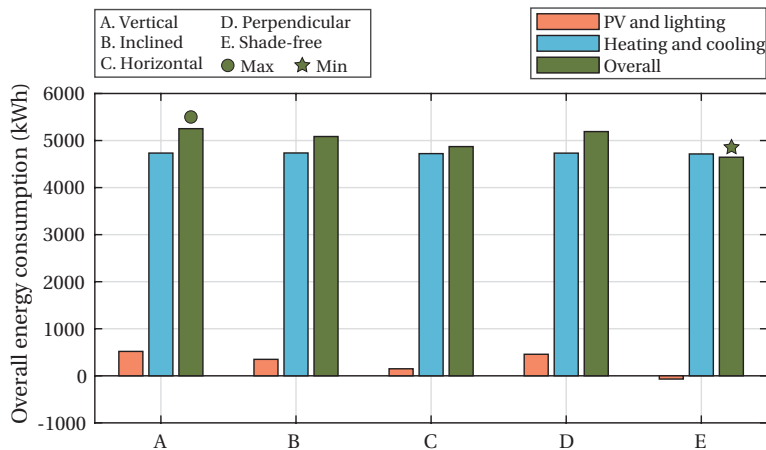


Figure 4.17: Net annual energy generation/consumption by PV and lighting (orange), annual electricity consumption by the combination of heating and cooling (blue), and overall net energy consumption considering PV generation, lighting, heating and cooling under five considered positions (see Fig. 4.5). The maximum and the minimum values are marked with solid circle and star respectively.

4.4. DISCUSSION

IN this study, the metropolis of Shanghai has been chosen as the location where the reference office building stands. The energy consumption by artificial lighting, heating and cooling are far more than the energy generated by PV blind. However, it is not necessarily the same for other cases due to the different solar radiation and climate conditions. Also, the shade-free tracking method has been demonstrated as the best tilt position for PV blind only when the office is located in Shanghai. As to other locations, further study is in need to draw a valid conclusion.

Besides locations, the architectural attributes, e.g. window-to-wall ratio (WWR), room dimensions, material reflectance, etc., can also affect the results of the simulations. Besides, we ignore the energy consumption of rotating the PV blind, which is actually much lower than that of lighting and air-conditioning systems, due to the light weight and low inertia of the PV blind. Therefore, we expect that the observed trends hold for a wider range of climate conditions, although the exact numbers might be different. This method can be used to evaluate any other cases provided with the required parameters. The evaluation of the comprehensive energy consumption and saving can hence be easily extended to the other scenarios.

For the case of this study, the PV blind is suitable to be integrated with artificial lighting system, since they present comparable amount of energy generation/consumption. Also, the PV blind outputs direct current (DC), which matches the requirement of solid-state lighting luminaire, e.g. LED lights.

4.5. CONCLUSIONS

IN this chapter, we have investigated the energy performance of a building-integrated PV blind in terms of PV electricity generation, electricity consumption by artificial lighting, and energy consumption by heating and cooling. Three static tilt angles and two sun-tracking methods have been analyzed and compared by building parametric models. Simulation results show that the shade-free tracking method is the most energy-saving operation scheme for the PV blind. The shade-free tracking method can reduce the net energy consumption by 10.49% compared with the conventional perpendicular tracking method; and by 4.63% compared with the horizontal fixed position. Among the five positions under evaluation, only by using the shade-free tracking method, the PV blind generates more electricity than that consumed by artificial lighting.

REFERENCES

- [1] Y. Gao, J. Dong, O. Isabella, M. Zeman, and G. Q. Zhang, *Daylighting simulation and analysis of buildings with dynamic photovoltaic window shading elements*, in *Solid State Lighting: International Forum on Wide Bandgap Semiconductors China (SSLChina: IFWS), 2017 14th China International Forum on (IEEE, 2017)* pp. 52–55.
- [2] H. Elarga, A. Zarrella, and M. De Carli, *Dynamic energy evaluation and glazing layers optimization of façade building with innovative integration of PV modules*, *Energy and Buildings* **111**, 468 (2016).
- [3] J. Jovanovic, X. Sun, S. Stevovic, and J. Chen, *Energy-efficiency gain by combination of PV modules and Trombe wall in the low-energy building design*, *Energy and Buildings* **152**, 568 (2017).
- [4] A. L. Schmid and L. K. S. Uehara, *Lighting performance of multifunctional PV windows: A numeric simulation to explain illuminance distribution and glare control in offices*, *Energy and Buildings* **154**, 590 (2017).
- [5] J. Han, L. Lu, J. Peng, and H. Yang, *Performance of ventilated double-sided PV façade compared with conventional clear glass façade*, *Energy and Buildings* **56**, 204 (2013).
- [6] W. Zhang, L. Lu, J. Peng, and A. Song, *Comparison of the overall energy performance of semi-transparent photovoltaic windows and common energy-efficient windows in Hong Kong*, *Energy and Buildings* **128**, 511 (2016).
- [7] S. Xu, W. Liao, J. Huang, and J. Kang, *Optimal PV cell coverage ratio for semi-transparent photovoltaics on office building façades in central China*, *Energy and Buildings* **77**, 130 (2014).
- [8] S. Kang, T. Hwang, and J. T. Kim, *Theoretical analysis of the blinds integrated photovoltaic modules*, *Energy and Buildings* **46**, 86 (2012).
- [9] S. H. Kim, I. T. Kim, A. S. Choi, and M. Sung, *Evaluation of optimized PV power generation and electrical lighting energy savings from the PV blind-integrated daylight responsive dimming system using LED lighting*, *Solar Energy* **107**, 746 (2014).

- [10] W. Bahr, *A comprehensive assessment methodology of the building integrated photovoltaic blind system*, Energy and Buildings **82**, 703 (2014).
- [11] M. Mandalaki, T. Tsoutsos, and N. Papamanolis, *Integrated PV in shading systems for Mediterranean countries: Balance between energy production and visual comfort*, Energy and Buildings **77**, 445 (2014).
- [12] Y. Luo, L. Zhang, X. Wang, L. Xie, Z. Liu, J. Wu, Y. Zhang, and X. He, *A comparative study on thermal performance evaluation of a new double skin façade system integrated with photovoltaic blinds*, Applied Energy **199**, 281 (2017).
- [13] Z. Hu, W. He, J. Ji, D. Hu, S. Lv, H. Chen, and Z. Shen, *Comparative study on the annual performance of three types of building integrated photovoltaic (BIPV) Trombe wall system*, Applied Energy **194**, 81 (2017).
- [14] Z. Hu, W. He, D. Hu, S. Lv, L. Wang, J. Ji, H. Chen, and J. Ma, *Design, construction and performance testing of a PV blind-integrated Trombe wall module*, Applied Energy **203**, 643 (2017).
- [15] T. Hong, C. Koo, J. Oh, and K. Jeong, *Nonlinearity analysis of the shading effect on the technical-economic performance of the building-integrated photovoltaic blind*, Applied Energy **194**, 467 (2017).
- [16] H. S. Park, C. Koo, T. Hong, J. Oh, and K. Jeong, *A finite element model for estimating the techno-economic performance of the building-integrated photovoltaic blind*, Applied Energy **179**, 211 (2016).
- [17] J. Oh, C. Koo, T. Hong, K. Jeong, and M. Lee, *An economic impact analysis of residential progressive electricity tariffs in implementing the building-integrated photovoltaic blind using an advanced finite element model*, Applied Energy **202**, 259 (2017).
- [18] C. Koo, T. Hong, J. Oh, and J.-K. Choi, *Improving the prediction performance of the finite element model for estimating the technical performance of the distributed generation of solar power system in a building façade*, Applied Energy **215**, 41 (2018).
- [19] S. Hong, A. S. Choi, and M. Sung, *Development and verification of a slat control method for a bi-directional PV blind*, Applied Energy **206**, 1321 (2017).
- [20] S. Hong, A. Choi, and M. Sung, *Impact of bi-directional PV blind control method on lighting, heating and cooling energy consumption in mock-up rooms*, Energy and Buildings **176**, 1 (2018).
- [21] C. Koo, T. Hong, K. Jeong, C. Ban, and J. Oh, *Development of the smart photovoltaic system blind and its impact on net-zero energy solar buildings using technical-economic-political analyses*, Energy **124**, 382 (2017).
- [22] *Rhinoceros*, <https://www.rhino3d.com>.
- [23] *MATLAB SimuLink*, <https://www.mathworks.com/products/simulink>.

- [24] *Radiance*, <https://www.radiance-online.org> .
- [25] U. S. DoE, *Energyplus engineering reference*, The reference to energyplus calculations (2018).
- [26] M. S. Roudsari, M. Pak, and A. Smith, *Ladybug: a parametric environmental plugin for grasshopper to help designers create an environmentally-conscious design*, in *Proceedings of the 13th international IBPSA conference held in Lyon, France Aug* (2013).
- [27] R. McNeel, *Grasshopper. Algorithmic modeling for Rhino*, (2017).
- [28] C. F. Reinhart, J. A. Jakubiec, and D. Ibarra, *Definition of A Reference Office For Standardized Evaluations of Dynamic Façade And Lighting Technologies*, 13th Conference of International Building Performance Simulation Association , 3645 (2013).
- [29] Y. Gao, J. Dong, O. Isabella, R. Santbergen, H. Tan, M. Zeman, and G. Zhang, *A photovoltaic window with sun-tracking shading elements towards maximum power generation and non-glare daylighting*, *Applied Energy* **228**, 1454 (2018).
- [30] A. Chouder, S. Silvestre, N. Sadaoui, and L. Rahmani, *Modeling and simulation of a grid connected PV system based on the evaluation of main PV module parameters*, *Simulation Modelling Practice and Theory* , 46.
- [31] *First Solar Series 6*, <http://www.firstsolar.com/Modules/Series-6> .
- [32] G. Tamizhmani, L. Ji, Y. Tang, L. Petacci, and C. Osterwald, *Photovoltaic Module Thermal / Wind Performance : Long -Term Monitoring and Model Development For Energy Rating*, NCPV and Solar Program Review Meeting , 936 (2003).
- [33] Y. Gao, J. Dong, O. Isabella, R. Santbergen, H. Tan, M. Zeman, and G. Zhang, *Modeling and analyses of energy performances of photovoltaic greenhouses with sun-tracking functionality*, *Applied Energy* **233-234**, 424 (2019).
- [34] D. Robinson and A. Stone, *Irradiation modelling made simple: the cumulative sky approach and its applications*, in *PLEA Conference* (2004) pp. 19–22.
- [35] M. Fontoynt, K. Ramanarivo, T. Soreze, G. Fernez, and K. G. Skov, *Economic feasibility of maximising daylighting of a standard office building with efficient electric lighting*, *Energy and Buildings* **110**, 435 (2016).
- [36] Y. Gao, Y. Lin, and Y. Sun, *A wireless sensor network based on the novel concept of an I-matrix to achieve high-precision lighting control*, *Building and Environment* **70**, 223 (2013).
- [37] *Philips CFI Arioso recessed perf*, <http://www.lightingproducts.signify.com/our-brands/daybrite/arioso-recessed-led.html> .

5

PHOTOVOLTAIC WINDOWS OF AGRICULTURAL GREENHOUSES

Abstract

In a broad sense, buildings serve not only human beings. Typical examples include glass greenhouses for plant cultivation, where incident sunlight can be controlled by dynamic photovoltaic (PV) windows on the roofs. PV windows in greenhouses offer more possibilities of energy production and microclimate control by adjusting the sun-tracking angles. In this work, we first build computer simulation models of typical greenhouses with high-density (1/2 roof area) and low-density (1/3 and 1/4 roof area) PV layouts. Then four special sun-tracking positions are found in the model of equivalent global irradiance. Simulation models are also built in terms of PV modules and interior irradiance. Simulations are conducted using the climate data of Delft, the Netherlands ($52.01^{\circ}N$, $4.36^{\circ}E$). Results show that high-density PVs under no-shading sun tracking generate 6.91% more energy than that under conventional (quasi-perpendicular) sun-tracking. Meanwhile, no-shading sun tracking allows more diffuse sunlight to enter the greenhouse mounted with high-density PV panels, resulting in 10.96% and 10.68% improvement on the annual average global irradiance and uniformity on the target plane compared to the fixed PV panels in the closed position. Regarding low-density PV layouts, which barely suffer from partial shading problems, quasi-perpendicular sun tracking improves the annual energy generation by 7.40% relative to the closed position. However, the average global irradiance reaches the minimum in this position because more sunlight is blocked by PVs. Meanwhile, the average uniformity of global irradiance reveals good (but not the best) performance, resulting in up to 9.80% (1/3 coverage) and 4.70% (1/4 coverage) improvement respectively compared to the closed position. The proposed methods and simulation results provide guidelines for the initial design and daily operation of PV greenhouses, aiming to balance the PV power generation and food production.

Parts of this chapter have been published in *Applied Energy* **233-234**, 424 (2019) [1].

5.1. INTRODUCTION TO AGRIVOLTAICS

RENEWABLE and clean energy, as the alternatives of fossil fuels, plays a critical role on alleviating the impacts of greenhouse-gas (GHG) emission on our environment [2]. As predicted by the International Energy Agency (IEA), renewable energy will share 30% of total world power generation in 2022, up from 24% in 2016, reaching over 8,000 TWh [3]. Among all the renewables, solar photovoltaic (PV) additions grew faster than the growth of any other source including coal, driven by sharp cost reductions and policy support [3]. By 2022, the global total solar PV capacity will reach 740-880 GW [3]. The huge PV capacity requires numerous PV panels and consequently a large area of land. For those regions where land resources are scarce, it is recommended to integrate PV panels with other forms of land utilization, such as buildings (BIPVs, i.e. Building Integrated Photovoltaics [4]), farmlands (agrivoltaics [5]), etc. The compound word “agrivoltaic” (agriculture and photovoltaics) refers to the association of PV power generation and agricultural activities on the same land area. This term was first invented and used in 2011 by Dupraz et al. [5]. But the concept of combining solar-energy conversion with plant cultivation was originally conceived as early as in 1981 [6]. After 37-year development, now typical modes of agrivoltaic systems include PV greenhouse, PV breeding, PV pumping, etc. [7]. Among them, PV greenhouse is one of the most common agrivoltaic systems due to the similarity with rooftop photovoltaic power stations. The comprehensive performance of PV greenhouse has been studied in Europe [8] and China [9]. Unlike residential buildings, however, agricultural greenhouses are built for the purpose of plant cultivation. Therefore, most research on PV greenhouse is mainly focusing on the optimal utilization of PV systems to produce both food and energy.

Agricultural greenhouse, usually equipped with transparent insulation materials, can protect the plants against hostile external environment and diseases, consequently lead to the production of plants with higher quality, and enable out-of-season cultivation. Compared with regular farmlands, greenhouse consumes more energy as the cost of creating moderate internal microclimate, such as solar irradiance, temperature, humidity, etc. Greenhouses in most regions of the world share a common problem of overheating during the summer and low temperature during the winter due to the seasonal air temperature and solar radiation. A practical solution is to install a sunshade device on the top of the greenhouse in order to control the amount of incident sunlight. Meanwhile, cooling and heating systems also help regulate the air temperature in the greenhouse. As photovoltaic industry booms, affordable PV panels can be used as the sunshade device, which blocks excess sunlight and also supply electricity to the electrical systems therein, e.g. artificial lighting, heating and cooling, irrigation, etc. A well-designed PV greenhouse can achieve the internal energy balance, i.e. the photovoltaic power generation is capable to cover the total energy consumption of daily operation, or even have extra electricity that can be sold to the electric power company. Such an ideal self-powered greenhouse can be called as “zero-energy greenhouse” [10].

The nature of PV greenhouse is to convert solar energy into the energy form that can be used by human, i.e. chemical energy (photosynthesis) and electric energy (photovoltaic effect). However, the intrinsic efficiency of the photosynthetic process is only around 3%, which is much lower than the conversion efficiency of typical commercial PV modules (around 20%). It means that the additional PV system will dramatically improve

the overall utilization rate of solar energy in the greenhouse. Dupraz et al. evaluated the land productivity with the indicator of Land Equivalent Ratio (LER). They found that the mixed system of crops (durum wheat) and PV panels (59% vertical projected cover of the ground) revealed the LER of 1.73, which means that 100 ha farm would produce as much electricity and food crops as a 173 ha farm with separate productions [5]. They also found that though the sun shade of PV panels reduced the wheat production, 57% reduction in sunlight availability resulted in only a 19% reduction in wheat yield. It means that the light efficiency of wheat crop is increased under the shade of PV panels [5].

In respect of PV greenhouse, a primary concern is whether the PV shading affects the growth of the plants. First of all, plants can be classified into sun and shade species based on their adaptability to the light intensity [11]. Therefore, partial shade caused by PV panels are not necessarily a disadvantage to the target plant depending on its light adaptability. For specific plants, common crops were investigated on the shading issue in some previous research. Cossu et al. observed a decreased annual yield of tomato in the testing PV greenhouse (50% coverage of the roof area, south), but a huge increase of income considering the PV power generation [8]. However, Urena et al. found no significant differences in commercial production, average weight, and flesh firmness of tomato comparing the greenhouse sections of 9.6% PV coverage with the control group (no PV coverage) [12]. The distinct results of those two studies on tomato yield might derive from the difference of PV coverage. Kadowaki et al. investigated the growth of hydroponically-cultivated Welsh onion in the PV greenhouse under the shadows casted by straight-line arranged PV-array (PV_s array, casting shadows on a specific area of the plants continuously) and checkerboard PV-array (PV_c array, casting shadows intermittently) respectively. Both the fresh weight and the dry-matter weight of Welsh onion cultivated under the PV_s array were significantly less than those in the control greenhouse; while the inhibitory effects under PV_c array were diminished. They concluded that geometrical arrangements of PV arrays drastically affected the growth of plants cultivated below the PV arrays [13]. Dupraz et al. estimated the wheat production under PV panels at full density (59% vertical projected coverage) and half density (29.5% vertical projected coverage) by using the generic STICS (Simulateur multiDisciplinaire pour les Cultures Standard) crop model. Simulation results showed that the reduction of sunlight caused by PV panels led to the reduction in wheat yield [5]. Marrou et al. studied the growth of four varieties of lettuces under two shade densities of PV panels (50% and 70% of the incoming radiation). They found that the lettuce yield was maintained because lettuce had the ability to adapt shading conditions and compensated the lack of light availability by a higher light harvesting capability [14]. In another research, Marrou et al. assessed the growth rate of three crops (lettuce, cucumber, and durum wheat) under full sun treatment (control) and two densities of PV panels as described in their former study. Results revealed that the growth rate was similar in all the treatments [15]. Valle et al. used sun trackers to balance the food and energy production in the combined PV panels and crops. Results show that dynamic agrivoltaic systems increase the electric production without competing with food [16]. Note that the last four research were conducted in the open field environment instead of the greenhouse. Based on the aforementioned relevant studies, PV panels in agricultural cultivation can affect the incident irradiance, soil temperature, air temperature, crop temperature, humidity, etc.

Considering the diversity of crops, it is hard to determine whether such shade effects are positive or not. In regard to the growth of tomato [8, 12] and wheat [5], reducing the shade degree helps alleviate the yield reduction. As to hydroponically-cultivated Welsh onion [13], increasing the uniformity of solar irradiance can benefit crop growth.

The incident light availability varies with the configuration of PV panels installed on the roof of the agricultural greenhouse. If the roof of the greenhouse is fully covered by PV panels, the crops cultivated therein may suffer from the lack of natural sunlight. Therefore, PV panels are usually mounted only on the south gable roof of the greenhouse, with a coverage rate less than or equal to 50%. However, farmers tend to cover the roof of greenhouse with PV panels in more than 50% coverage in order to earn more money, without considering the negative impacts on the agricultural production. Considering that, some national and European legislations force farmers to provide the proof of income from agricultural activity to receive the incentive tariff [17]. Therefore, it is necessary to find optimum arrangements of PV panels on the greenhouse roof.

In general, there are two types of PV greenhouses according to the sun-tracking abilities of the roof PV panels, i.e. fixed PV or dynamic ones. Greenhouse with fixed panels on the roof are mostly studied due to the low cost of installation and maintenance. Castellano et al. investigated a mono-pitched steel greenhouses entirely covered with PV panels (Figure 5.1a). A model was built to predict the shading effects inside the PV greenhouse [18]. Cossu et al. assessed the climate conditions inside a greenhouse in which 50% of the roof area was replaced with PV panels (Figure 5.1b). The roof PV system reduced the solar irradiance inside the greenhouse by 64%. In their work, the solar irradiance was distributed non-uniformly and varied seasonally, but usually followed a north-south gradient [8]. In another research, Cossu et al. compared south mounted PV greenhouse (Figure 5.1b) with both south and north mounted PV greenhouse (Figure 5.1c). They found that arrangement in Figure 5.1b resulted in higher power generation but also higher shading level. Meanwhile, arrangement in Figure 5.1c generated much less electricity but a more uniform internal shading [19]. Yano et al. [20] and Kadowaki et al. [13] conducted two similar studies by comparing straight-line (Figure 5.1d) and checkerboard (Figure 5.1e) PV arrays on the roof of a greenhouse. They found that both PV arrangements performed basically the same in terms of PV power generation. But checkerboard arrangement revealed better uniformity and consequently diminished the inhibitory effects of the PV shading on plants. Marucci et al. evaluated the dynamic PV greenhouse by the means of simulation [21] and field study [17, 22]. PV modules rotated around fixed axes to adjust the degree of shading inside the greenhouse. Also, highly reflective aluminum mirrors are used to enhance the PV power generation, as shown in Figure 5.1f. They suggested increasing the shading degree in the hot season. While during the season when the solar radiation is not adequate for plants, PV modules should rotate to allow more sunlight to enter the greenhouse. Trypanagnostopoulos et al. investigated the PV panels in north-south tracking arrangement (Figure 5.1g) and found that the north-south oriented rotating axis gave the higher electricity output than the east-west one did [23]. Obviously, dynamic PV greenhouses provide more possibilities than the fixed types in terms of power generation, light harvest, and heat insulation. However, existing studies on the dynamic PV greenhouse fail to derive the relationship between rotation angles and the solar position. In this study, PV power output and ir-

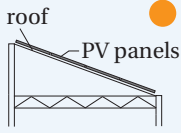
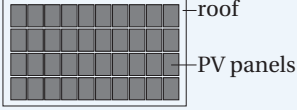
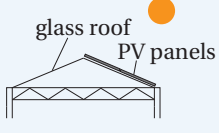
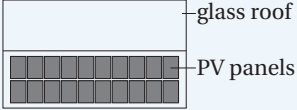
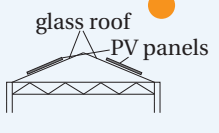
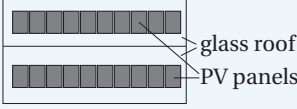
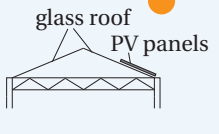
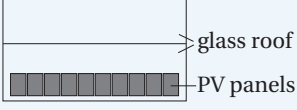
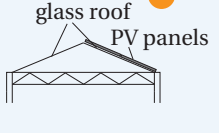
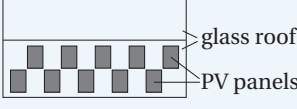
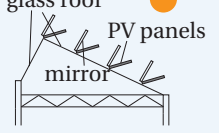
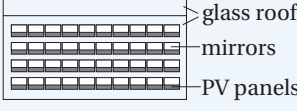
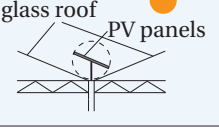
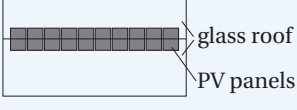
No.	Type	Left view	Top view
a ^[18]	Lean-to roof Fixed PV		
b ^[8, 19]	Gable roof Fixed PV		
c ^[19]	Gable roof Fixed PV		
d ^[13, 20]	Gable roof Fixed PV		
e ^[13, 20]	Gable roof Fixed PV		
f ^[17, 21, 22]	Saltbox roof Dynamic PV		
g ^[23]	Gable roof Dynamic PV		

Figure 5.1: Literature review on the PV layouts on the roofs of greenhouses.

radiance distribution are investigated under different sun-tracking methods, which are summarized as the functions of the solar position. Though the interior irradiance does not exclusively determine the production of crops, it could be used as the input for crop growth models that can further predict the effects on harvest yield of different crops.

To further improve the uniformity of incident sunlight, semi-transparent PV modules were integrated with greenhouses. PV modules were made to be transparent either regionally [24] or spectrally [25]. Though semi-transparent PV modules contribute to better uniformity of solar irradiance, they can hardly control the incident light as flexibly as the dynamic PV modules. Also, spectrally semi-transparent PV cannot necessarily match the spectra that various plants need during growth [26, 27].

Besides dynamic PV greenhouses, sun-tracking agrivoltaic systems in open-space farmland were also studied. Valle et al. built an open-space agrivoltaic prototype using one-axis orientable PV panels. Experimental results showed that the one-axis dynamic agrivoltaic system with the controlled tracking mode (aiming to alleviate the shading on the plants) can favour crop growth but at the expense of electric production [16]. Amaducci et al. simulated the performance of a dual-axis solar tracking agrivoltaic system built on suspended structures. They found that the solar tracking PV panels resulted in lower radiation but higher LER than the fixed PV panels [28]. The limitation of this agrivoltaic simulation platform is that it cannot precisely calculate the shadows on the PV panels and the consequent electricity production.

The innovations of this work is summarized as follows. (1) The overall performances of different sun-tracking methods are analyzed regarding different densities of PV layouts on the roof of the greenhouse. (2) Integrated models which consider the PV partial shading effects are established for the first time. Those models are capable to couple the general utilization of solar energy to the orientation of the roof-mounted PV panels. (3) The partial shading problems of high-density sun-tracking PV panels are solved by using innovative sun-tracking methods.

In this work, dynamic PV greenhouses were modeled, simulated and analyzed in order to find the proper sun-tracking method, which can balance the interior irradiance and PV generation. Firstly, geometric and mathematical models were built up for the simulations of PV power output and interior irradiance. Secondly, three types of PV layouts were analyzed according to the results at a given time instant and over the annual accumulation and average. The performance of four special sun-tracking positions was compared under different PV layouts. Lastly, proper sun-tracking methods for different types of PV layouts were discussed and concluded; and suggestions on dynamic PV greenhouses were also drawn.

5.2. METHODS

IN this study, sun-tracking mathematical models are developed and analyzed for PV panels on the roof of a greenhouse, effectively excluding the environmental interference, such as leaves falling onto the PV panels, human activities blocking the light sensors, etc. Those uncertainties are commonly found in an equivalent field study. Parametric three-dimensional models are visualized by Rhinoceros, a computer-aided design (CAD) software. Solar irradiance on the PV panels is derived and calculated based on the basic knowledge of photometry and solid analytical geometry. MATLAB SimuLink

is used to implement the simulation of the PV models, taking irradiance and module temperature as the inputs. Two plugins of Rhinoceros, Grasshopper [29] and DIVA [30], are used to evaluate the indoor daylighting. Regarding the annual performance of PV greenhouse, climate data such as solar irradiance, air temperature, wind speed, etc. is obtained from Meeonorm [31]. An overview of the modeling procedure is illustrated in Figure 5.2. The simulation platform is illustrated in Figure 5.3.

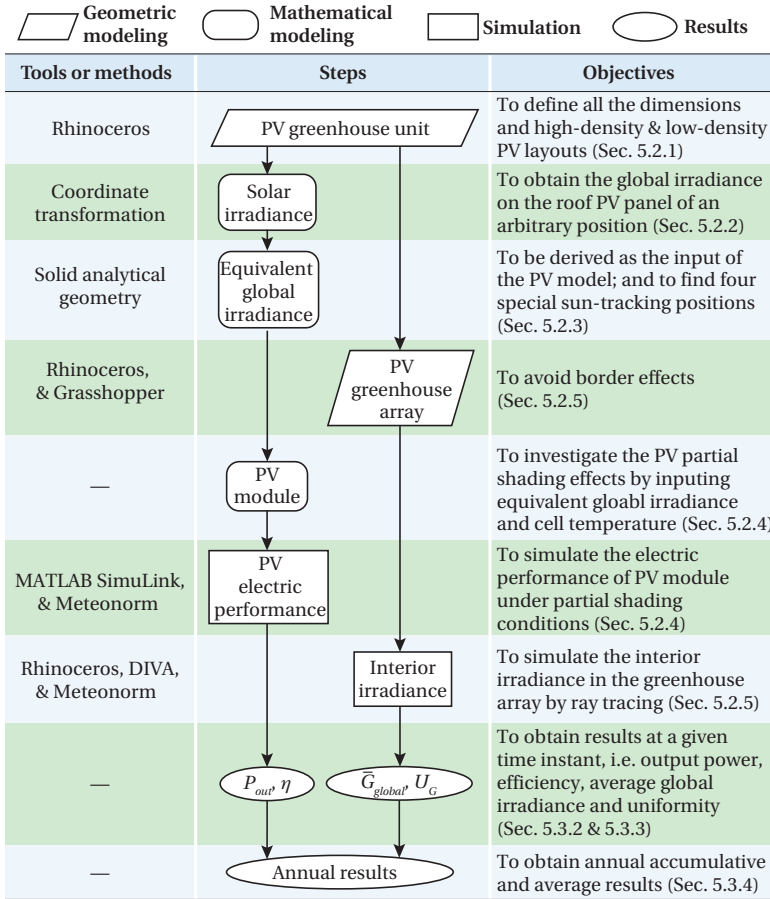


Figure 5.2: Technical routemap of this study and corresponding tools, methods, and objectives. Here geometric modeling indicates building three-dimensional models with CAD (computer-aided design) softwares.

5.2.1. GREENHOUSE MODEL

A typical steel-framed glass greenhouse usually presents a symmetrical gable roof. The pitched roof can enhance daylight harvest and prevent rainwater from stagnating on the roof. A large-scale greenhouse can be considered as the combination of a series of identical units of greenhouses. In this study, the appearance of a typical unit of the greenhouse

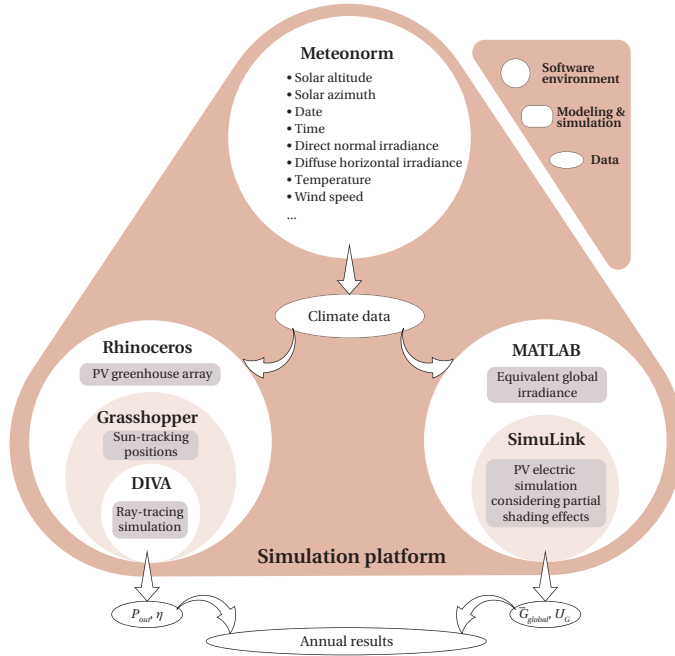


Figure 5.3: Simulation platform of this study.

(referred to as a unit for brevity in what follows) is illustrated in Figure 5.4. Note that the nomenclature in this chapter is independent of others. The geographical position of the greenhouse is determined by longitude (λ_{GH}) and latitude (ϕ_{GH}), and its orientation by the azimuth (A_{GH}). The size of the typical unit is determined by four parameters, i.e. length (l_{GH} , Figure 5.4a), height (h_{GH} , Figure 5.4c), roof width (w_r , Figure 5.4d), and roof inclination (α_r , Figure 5.4d). Other dimensions of the unit, such as the width (w_{GH} , Figure 5.4d), and the roof height (h_r , Figure 5.4d) can be derived from the given parameters (Eqs. (5.1) and (5.2)).

$$h_r = w_r \sin \alpha_r \quad (5.1)$$

$$w_{GH} = 2w_r \cos \alpha_r \quad (5.2)$$

Three-dimensional models of the unit are important to analyze the daylight harvest and power generation, and will be built in what follows. For simulations, we assign proper values to the aforementioned geometric parameters in Table 5.1, where the longitude and latitude represents the location of Delft, the Netherlands ($52.01^\circ N$, $4.36^\circ E$). The azimuth of the unit here indicates an east-west orientation, i.e. one of the roofs is south-facing. The height of the unit is given according to typical dimensions of Dutch greenhouses. The roof dimensions (l_{GH} and w_r) are set according to the dimensions of PV modules ($l_M = 1.5 m$, $w_M = 1 m$), so that the south roof can be exactly covered by two types of high density (HD) PV layouts (Figures 5.5a & b) and partially covered by two types of low density (LD) PV layouts (Figures 5.5c & d). In this study, each PV panel can rotate around one axis as shown in Figure 5.5. The position of the PV panel can be

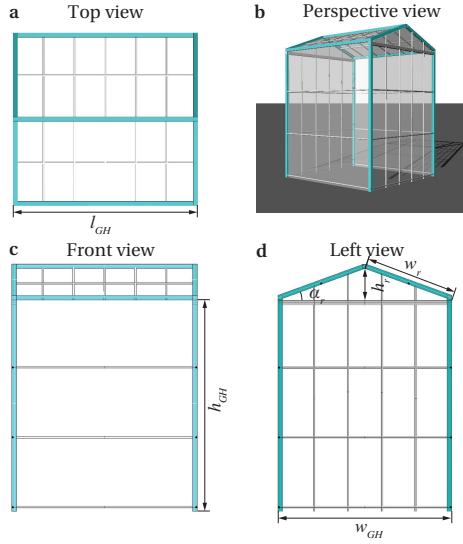


Figure 5.4: Model of the unit of a greenhouse and geometric parameters in **a**, top view, **b**, perspective view, **c**, front view, and **d**, left view.

Table 5.1: Parameters and values of the unit

λ_{GH}	ϕ_{GH}	A_{GH}	l_{GH}	h_{GH}	w_r	α_r	w_{GH}	h_r
$+4.36^\circ$	$+52.01^\circ$	π	6 m	4 m	3 m	20°	1.03 m	5.64 m

described by the normal of the PV surface (α_M, A_M), where the azimuth of the normal equals to that of the greenhouse (A_{GH}). Therefore, the rotation of PV modules is determined by α_M , which affects not only the irradiance on the PV surface, but also the irradiance entering into the greenhouse.

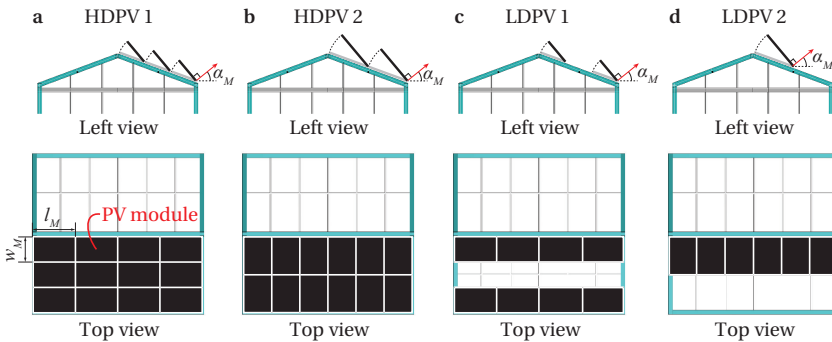


Figure 5.5: Left view and top view of four PV layouts on the roof of the unit, i.e. **a**, HDPV 1, **b**, HDPV 2, **c**, LDPV 1, and **d**, LDPV 2.

5.2.2. SOLAR IRRADIANCE MODEL

Solar irradiance is a critical factor for both PV power generation and plant cultivation. The global irradiance (G_{global}) contains direct and diffuse components. In a clear day, the direct normal irradiance (DNI, I_{dir}) usually contributes more than 90% of the global irradiance [32]. Since the diffuse proportion is small, here we will ignore the variation of the diffuse irradiance with the orientation of the PV panel, and simply use the diffuse horizontal irradiance ($G_{h,d}$) to represent the whole diffuse component. Therefore, the global irradiance on the PV surface is calculated by

$$G_{global} = I_{dir} \cos \gamma + G_{h,d}, \quad (5.3)$$

where γ is the angle between the incident direction of the sunlight and the normal of the PV surface. In this study, in order to calculate γ , we include the solar position (α_s, A_s) and the position of the PV module (α_M, A_M) in the same horizontal coordinate system (Figure 5.6a). Then we transform both positions from the horizontal coordinate system into Cartesian coordinate system for further derivations. The three-dimensional Cartesian coordinates are built so that the direction of A_M overlaps with x -axis (Figure 5.6b). In the Cartesian coordinates, the orientation of the PV module is denoted by a unit vector \mathbf{n}_M , i.e.

$$\mathbf{n}_M = \begin{bmatrix} x_M \\ y_M \\ z_M \end{bmatrix} = \begin{bmatrix} \cos \alpha_M \\ 0 \\ \sin \alpha_M \end{bmatrix}. \quad (5.4)$$

The difference between the two azimuth angles is denoted by ΔA , i.e.

$$\Delta A = A_M - A_s. \quad (5.5)$$

The solar position is denoted by a unit vector \mathbf{n}_s , which is derived by

$$\mathbf{n}_s = \begin{bmatrix} x_s \\ y_s \\ z_s \end{bmatrix} = \begin{bmatrix} \cos \alpha_s \cos \Delta A \\ \cos \alpha_s \sin \Delta A \\ \sin \alpha_s \end{bmatrix}. \quad (5.6)$$

Then, it is easy to derive $\cos \gamma$,

$$\cos \gamma = \mathbf{n}_M^T \cdot \mathbf{n}_s = x_s \cos \alpha_M + z_s \sin \alpha_M. \quad (5.7)$$

By substituting Eqs. (5.7) and (5.6) into Eq. (5.3), the global irradiance G_{global} is derived as

$$G_{global} = I_{dir} (\cos \alpha_s \cos \Delta A \cos \alpha_M + \sin \alpha_s \sin \alpha_M) + G_{h,d}. \quad (5.8)$$

5.2.3. EQUIVALENT IRRADIANCE UNDER PARTIAL DIFFUSE SHADOWS

Based on the PV layouts proposed in this study (Figure 5.5), it is possible to observe rectangular shadows on the PV modules during the rotation. In the shade area, direct normal irradiance is blocked. But there still exists part of the diffuse irradiance. Here, we simply treat the irradiance on the shading area as $G_{h,d}$, i.e. the diffuse horizontal irradiance. Regarding the PV module, the shading area is denoted as S_{shadow} . The input power on the PV module from the Sun is denoted as P_{in} . On the partially shaded PV module, the

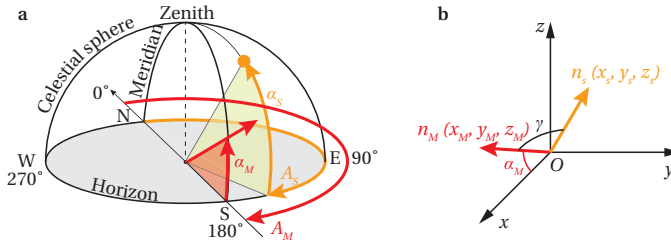


Figure 5.6: Definitions of solar position and PV-module position in **a**, horizontal coordinate system, and **b**, Cartesian coordinates.

global irradiance G_{global} in the illuminated area differs from that in the shade area, as long as DNI is not zero. To represent the irradiance level on the entire PV module, the equivalent irradiance (G_{module}^{eq}) is defined as the quotient of P_{in} divided by the area of PV module, and further derived by

$$\begin{aligned}
 G_{module}^{eq} &= \frac{P_{in}}{l_M w_M} \\
 &= \frac{I_{dir}(l_M w_M - S_{shadow}) \mathbf{n}_M^T \cdot \mathbf{n}_s + G_{h,d} l_M w_M}{l_M w_M} \\
 &= \left(1 - \frac{S_{shadow}}{l_M w_M}\right) I_{dir} (\cos \alpha_s \cos \Delta A \cos \alpha_M + \sin \alpha_s \sin \alpha_M) + G_{h,d}.
 \end{aligned} \tag{5.9}$$

Eq. (5.9) reveals that the shading area S_{shadow} plays an important role in the incident power of the PV module. Furthermore, partial shading affects the conversion efficiency (η) of the PV module. Therefore, it is critical to calculate the position of the rectangular shadow on the PV module for the evaluation of the PV input power and conversion efficiency.

In order to locate the position of the shadow, we simplify the PV modules as rectangular planes in the aforementioned Cartesian coordinates (Figure 5.7a). For HDPV 1 (Figure 5.5a), two PV modules are initially positioned in the closed state, where α_{M0} is derived as

$$\alpha_{M0} = \frac{\pi}{2} - \alpha_r. \tag{5.10}$$

In the Cartesian coordinates, two rectangular planes can rotate around their fixed axes. From the left view, it is obvious that two axes cross two important points, $O(0,0,0)$ and $O_1(w_M \sin \alpha_{M0}, 0, -w_M \cos \alpha_{M0})$, respectively. When the two planes rotate to an arbitrary position α_M , the point $Q_1(x_{q1}, y_{q1}, z_{q1})$ casts a shadow point $Q_{1s}(x_{q1s}, y_{q1s}, z_{q1s})$ according to the direction of \mathbf{n}_s (Figure 5.7b). The coordinates of Q_1 are derived as

$$\begin{bmatrix} x_{q1} \\ y_{q1} \\ z_{q1} \end{bmatrix} = w_M \begin{bmatrix} \sin \alpha_{M0} - \sin \alpha_M \\ 0 \\ \cos \alpha_M - \cos \alpha_{M0} \end{bmatrix}. \tag{5.11}$$

The point Q_{1s} determines the position of the shadow. In order to study the area of shadows, new coordinates $Ox'y'z'$ are built based on the tilt plane (Figure 5.7c). From coordinates $Oxyz$ to coordinates $Ox'y'z'$, a rotation matrix $\mathbf{R}_{C-C'}(\alpha_M)$ is required to achieve

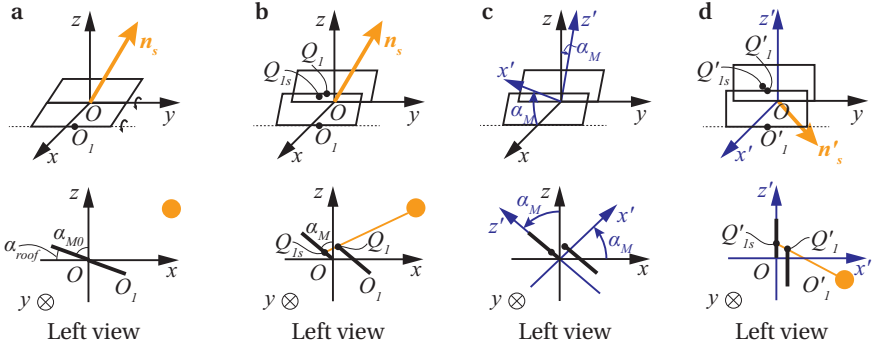


Figure 5.7: Coordinate transformation for derivations.

the transformation, i.e.

$$\mathbf{R}_{C-C'}(\alpha_M) = \begin{bmatrix} \cos \alpha_M & 0 & \sin \alpha_M \\ 0 & 1 & 0 \\ -\sin \alpha_M & 0 & \cos \alpha_M \end{bmatrix}. \quad (5.12)$$

In the new coordinates $Ox'y'z'$ as shown in Figure 5.7d, $\mathbf{n}'_M(x'_M, y'_M, z'_M)$, $\mathbf{n}'_s(x'_s, y'_s, z'_s)$ and $Q'_1(x'_{q1}, y'_{q1}, z'_{q1})$ are given respectively by

$$\mathbf{n}'_M = \begin{bmatrix} x'_M \\ y'_M \\ z'_M \end{bmatrix} = \begin{bmatrix} 1 \\ 0 \\ 0 \end{bmatrix}, \quad (5.13)$$

$$\mathbf{n}'_s = \begin{bmatrix} x'_s \\ y'_s \\ z'_s \end{bmatrix} = \mathbf{R}_{C-C'}(\alpha_M) \cdot \mathbf{n}_s = \begin{bmatrix} x_s \cos \alpha_M + z_s \sin \alpha_M \\ y_s \\ -x_s \sin \alpha_M + z_s \cos \alpha_M \end{bmatrix}, \quad (5.14)$$

$$\begin{aligned} \begin{bmatrix} x'_{q1} \\ y'_{q1} \\ z'_{q1} \end{bmatrix} &= \mathbf{R}_{C-C'}(\alpha_M) \cdot \begin{bmatrix} x_{q1} \\ y_{q1} \\ z_{q1} \end{bmatrix} \\ &= w_M \begin{bmatrix} \cos \alpha_M \sin \alpha_{M0} - \sin \alpha_M \cos \alpha_{M0} \\ 0 \\ 1 - \sin \alpha_M \sin \alpha_{M0} - \cos \alpha_M \cos \alpha_{M0} \end{bmatrix}. \end{aligned} \quad (5.15)$$

In the new coordinates $Ox'y'z'$, the surface of the target plane, where the shadow shows up, is $x' = 0$. The line $Q'_1Q'_{1s}$ can be defined as

$$\frac{x' - x'_{q1}}{x'_s} = \frac{y'}{y'_s} = \frac{z' - z'_{q1}}{z'_s} = \lambda_1, \quad (5.16)$$

where λ_1 is an arbitrary real number. Let $Q'_{1s}(x'_{q1s}, y'_{q1s}, z'_{q1s})$ denote the shadow point in the new coordinates. Since Q'_{1s} is both on the surface of the target plane ($x' = 0$) and

on the line $Q'_1 Q'_{1s}$, Q'_{1s} is the intersecting point, and defined by

$$\begin{cases} x'_{q1s} = 0 \\ \frac{x'_{q1s} - x'_{q1}}{x'_s} = \frac{y'_{q1s}}{y'_s} = \frac{z'_{q1s} - z'_{q1}}{z'_s} = \lambda_1 \end{cases}, \quad (5.17)$$

where the solution of $Q'_{1s}(x'_{q1s}, y'_{q1s}, z'_{q1s})$ can be easily found to be

$$\begin{cases} x'_{q1s} = 0 \\ y'_{q1s} = -\frac{y'_s}{x'_s} x'_{q1} \\ z'_{q1s} = -\frac{z'_s}{x'_s} x'_{q1} + z'_{q1} \end{cases}. \quad (5.18)$$

The coordinate z'_{q1s} can be used to calculate the area of the shadow, as long as the shadow exists. Before the calculation of shading area, boundary conditions needs to be confirmed. First of all, α_M should not exceed α_{M0} due to the physical limitation of the greenhouse roof (Figure 5.5). Secondly, the front side of the PV module has to face the Sun, i.e. the angle between \mathbf{n}'_s and \mathbf{n}'_M should not exceed $\pi/2$. Therefore, the rotation of the PV module is restricted by

$$\begin{cases} \alpha_M \leq \alpha_{M0} \\ \mathbf{n}'_s \cdot \mathbf{n}'_M \geq 0 \end{cases}, \quad (5.19)$$

which can be further written as

$$\arctan \frac{z'_s}{x'_s} - \frac{\pi}{2} \leq \alpha_M \leq \alpha_{M0}. \quad (5.20)$$

Within the range of (5.20), the condition that shadow exists on the target plane is

$$z'_{q1s} \geq 0. \quad (5.21)$$

By substituting Eqs. (5.14), (5.15) and (5.18) into (5.21), the range of α_M is derived as,

$$\alpha_M \geq 2 \arctan \frac{z'_s}{x'_s} - \alpha_{M0}. \quad (5.22)$$

By combining (5.20) and (5.22), the area of shadow on an individual PV module is derived as

$$S_{shadow} = \begin{cases} 0 & \alpha_{M0} < \alpha_p \\ \begin{cases} l_M z'_{q1s} & 2\alpha_p - \alpha_{M0} \leq \alpha_M \leq \alpha_{M0} \\ 0 & \alpha_p - \frac{\pi}{2} \leq \alpha_M < 2\alpha_p - \alpha_{M0} \end{cases} & \alpha_{M0} \geq \alpha_p \end{cases}, \quad (5.23)$$

where

$$\alpha_p = \arctan \frac{z'_s}{x'_s}. \quad (5.24)$$

By substituting Eq. (5.23) into Eq. (5.9), G_{module}^{eq} is finally given by

$$G_{module}^{eq} = \begin{cases} I_{dir}(x_s \cos \alpha_{M0} + z_s \sin \alpha_{M0}) & \alpha_{M0} < \alpha_p \\ \begin{cases} I_{dir}(x_s \cos \alpha_{M0} + z_s \sin \alpha_{M0}) & 2\alpha_p - \alpha_{M0} \leq \alpha_M \leq \alpha_{M0} \\ I_{dir}(x_s \cos \alpha_M + z_s \sin \alpha_M) & \alpha_p - \frac{\pi}{2} \leq \alpha_M < 2\alpha_p - \alpha_{M0} \end{cases} & \alpha_{M0} \geq \alpha_p \end{cases} \quad (5.25)$$

It is interesting to notice that when $\alpha_M \in [2\alpha_p - \alpha_{M0}, \alpha_{M0}]$, G_{module}^{eq} remains as a constant, which is independent of α_M . When the Sun is in the position where α_p is greater than α_{M0} , it means the PV panel will rotate inside the greenhouse to achieve intended sun tracking. Since the PV panel only has one axis and cannot go inside the glass roof, we let the α_M equals to α_{M0} in this situation (i.e. $\alpha_p > \alpha_{M0}$).

Several critical positions can be derived for further analysis as follows (Figure 5.8).

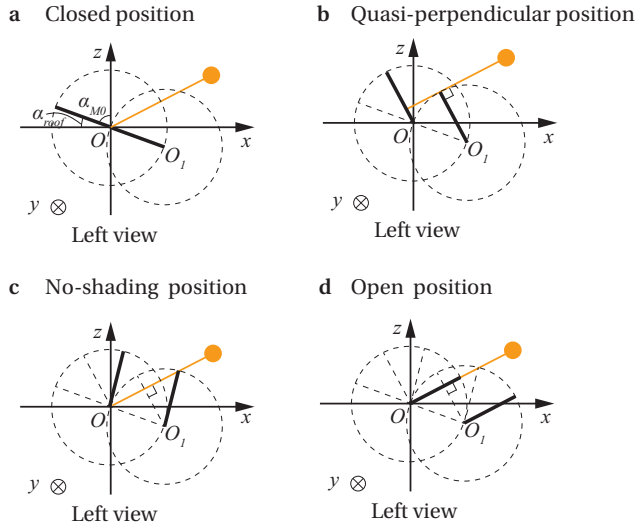


Figure 5.8: Left view of HDPV in four positions, i.e. **a**, closed position, **b**, quasi-perpendicular position, **c**, no-shading position, and **d**, open position.

- Closed position ($\alpha_M = \alpha_{M0}$)

When the PV modules stay in the closed position (Figure 5.8a), the PV panels are parallel with the greenhouse roof. Under this condition, the PV modules stay in the fixed position; and the sunlight barely penetrates the south roof, which is fully covered by PV modules.

- Quasi-perpendicular position ($\alpha_M = \alpha_p$)

To obtain the position where G_{global} reaches the maximum, Eqs. (5.3) and (5.7)

are further written as

$$\begin{aligned} G_{global} &= I_{dir}(x_s \cos \alpha_M + z_s \sin \alpha_M) + G_{h,d} \\ &= I_{dir} \sqrt{x_s^2 + z_s^2} \cos \left(\alpha_M - \arctan \frac{z_s}{x_s} \right) + G_{h,d}, \end{aligned} \quad (5.26)$$

where the maximum G_{global} is obtained when α_M equals to α_p . Here, the position of α_p is called the "quasi-perpendicular" position, because the sun ray is perpendicular to the PV module in the left view (Figure 5.8b). However, in the 3D space, the sun ray is not actually perpendicular to the PV module. Note that this position exists only when the condition $\alpha_{M0} \geq \alpha_p$ holds.

- No-shading position ($\alpha_M = 2\alpha_p - \alpha_{M0}$)

From Eq. (5.23), it is obvious that the position shown in Figure 5.8c ($\alpha_M = 2\alpha_p - \alpha_{M0}$) is where there happens to be no shadow on the target PV module. This position is important, because it minimizes the partial shading effects on PV power generation, and maintains a high G_{module}^{eq} (which will be demonstrated in later analysis). Note that this position exists only when the condition $\alpha_{M0} \geq \alpha_p$ holds.

- Open position ($\alpha_M = \alpha_p - \frac{\pi}{2}$)

In this position, the PV plane is parallel with the solar beam. Theoretically, the PV panels barely interact with direct solar irradiance; and the PV power generation is very low. We can simply treat this scenario as a greenhouse with no cover on the roof.

Aforementioned derivations are based on the layout of the high-density PV 1 (HDPV 1, Figure 5.5a). As to the layout of the high-density PV 2 (Figure 5.5b), similar models can be built. We will omit the details for brevity. Regarding the layout of the low-density PV 1 (LDPV 1, Figure 5.5c), there are possibilities that shadows are formed on the PV modules by the front row. Such shadows are mainly depending on the roof inclination (α_r). Since such shadows only exist when the solar altitude is very low and the solar radiation is weak, here we simply assume that there is no shading on the PV modules in LDPV 1. Apparently, there is also no shading on the PV modules in LDPV 2 (Figure 5.5d).

5.2.4. MODEL OF THE PV MODULE

To evaluate the PV performance under partial shading conditions, the model of PV module is built based on a commercially available PV module (Figure 5.9a). The PV module consists of 60 solar cells connected in series, parallel with three bypass diodes (Figure 5.9b). Bypass diodes allow current to pass around shaded or damaged cells in the PV module. Ideally there would be one bypass diode for each solar cell, but usually a group of series connected cells share one bypass diode for cost saving. The equivalent circuit of PV cell model is shown in Figure 5.9c. The I-V relationship of a PV cell is given by

$$I = I_L - I_0 \left(\exp \left(\frac{V + R_s I}{A} \right) - 1 \right) - \frac{V + R_s I}{R_{sh}}, \quad (5.27)$$

Table 5.2: Parameters of the selected PV module

Electrical data @ STC	TSM-315
Open Circuit Voltage - V_{OC} (V)	40.4
Short Circuit Current - I_{SC} (A)	9.88
Maximum Power Voltage - V_{MPP} (V)	33.3
Maximum Power Current - I_{MPP} (A)	9.46
Peak Power Watts - P_{MAX} (Wp)	315
Module Efficiency - η (%)	19.2
Temperature Coefficient of V_{OC} (%/K)	- 0.29
Temperature Coefficient of I_{SC} (%/K)	0.05

where I_L is the light-generated current; I_0 is the diode saturation current; $A = n_d k T / q$ is the modified ideality factor; n_d is the diode ideality factor; k is the Boltzmann constant ($1.3807 \times 10^{-23} J/K$); q is the electron charge ($1.6022 \times 10^{-19} C$); T is the cell temperature; R_s is the series resistance; and R_{sh} is the shunt resistance. Detailed model description can be found in [33].

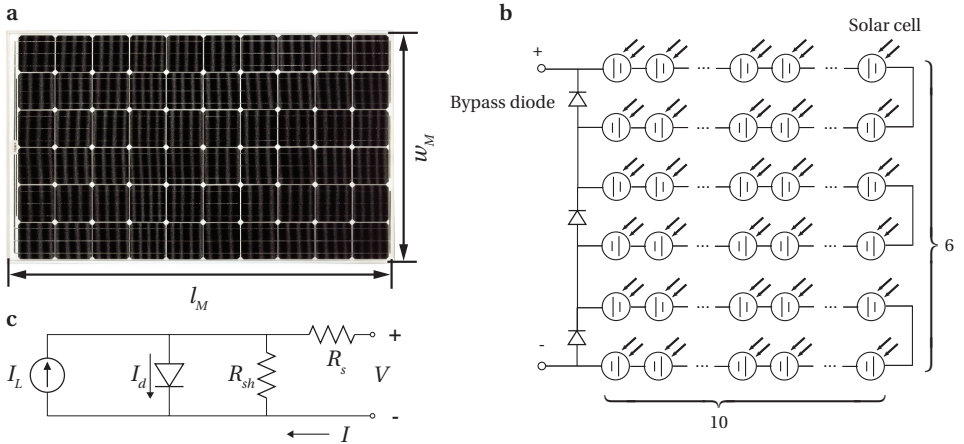


Figure 5.9: **a**, Dimensions of a PV module. **b**, Model of a PV module with three bypass diodes. **c**, Single-diode model of a PV cell.

In this study, the PV model is configured according to a Trina Solar product (TSM-DEG5(II)). This c-Si PV module product is as thin as 7.6 mm and specially recommended for greenhouse applications. Detailed electrical specifications can be found in Table 2. Note that here we simplify the dimensions of the PV module ($1.5 m \times 1 m$) to fit the roof of greenhouse model. The model of PV module is simulated in the environment of MATLAB SimuLink.

Two inputs, the equivalent global irradiance G_{module}^{eq} on the PV module and the module temperature, greatly affect the output of the model. As to the partial shading condition, the global irradiance and temperature on individual solar cells are not identical. Therefore, the inputs can be taken as 60 irradiance inputs and 60 temperature inputs

for each of the 60 solar cells. For the solar cells under the full shading condition, the input irradiance is $G_{h,d}$. For those fully exposed to the sunlight, the input irradiance is G_{global} (Eq. (5.8)). For those under the partial shading condition, the input irradiance is the equivalent global irradiance G_{cell}^{eq} , which can be calculated as Eq. (5.9) in the scale of a solar cell, i.e.,

$$G_{cell}^{eq} = \left(1 - \frac{S_{shadow}^{cell}}{S_{cell}}\right) I_{dir} (\cos \alpha_s \cos \Delta A \cos \alpha_M + \sin \alpha_s \sin \alpha_M) + G_{h,d}, \quad (5.28)$$

where S_{cell} is the area of an individual solar cell; and S_{shadow}^{cell} is the area of shadows on it. Eq. (5.28) covers the shading conditions of full shading (S_{shadow}^{cell} equals to S_{cell}) and fully exposed to sunlight (S_{shadow}^{cell} equals to 0).

The temperature of the PV module is affected by many environmental factors, such as ambient temperature (T_a), wind speed (v_{wind}), wind direction, equivalent global irradiance (G_{cell}^{eq}), relative humidity, etc. Here, to estimate the temperature on each solar cell, a simplified model is used:

$$T = 0.943 T_a + 0.028 G_{cell}^{eq} - 1.528 v_{wind} + 4.3, \quad (5.29)$$

where the units of T_a , G_{cell}^{eq} and v_{wind} are respectively $^{\circ}C$, W/m^2 , and m/s [34]. Though this model is originally developed to predict the temperature of the whole PV module, here it is used to estimate the cell temperature under different shading conditions [34].

5.2.5. MODEL OF THE PV GREENHOUSE ARRAY

Besides PV power generation, one of the most fundamental functions of PV greenhouse is plant cultivation, which requires proper intensity and distribution of irradiance. The light environment inside the greenhouse is more complicated than that on the PV panels. The irradiance on an interior plane is not only affected by the direct solar beam and sky diffuse irradiance, but also the multiple reflections and refractions from the complicated structures of the PV greenhouse. Therefore, instead of analytical modeling, ray tracing simulation is introduced to estimate the interior solar radiation by the tool DIVA, a Rhinoceros plugin [30]. One of the advantages about DIVA is that the ray tracing simulation can be conducted by defining material characteristics within the Rhinoceros environment, without the effort to export the greenhouse model into other optic softwares.

Based on the unit, a 9×9 greenhouse array is built for the ray tracing simulation (Figure 5.10a). The steel frame supports the greenhouse array; only the external façade contains glass. Material properties are assigned as in Table 3. Since the greenhouse array is the repetition of 81 units, we choose to study the target plane located in the central unit to avoid border effects (Figure 5.10b). In our simulation, the target plane was set at $0.5 m$ above the ground, which can be considered a representative height for greenhouse grown crops.

In this model of PV greenhouse array, dynamic PV panels are rotating according to the solar position. Therefore, it is difficult to model the PV panels for ray tracing simulation. Here, Grasshopper, an algorithmic modeling tool, is introduced to solve this

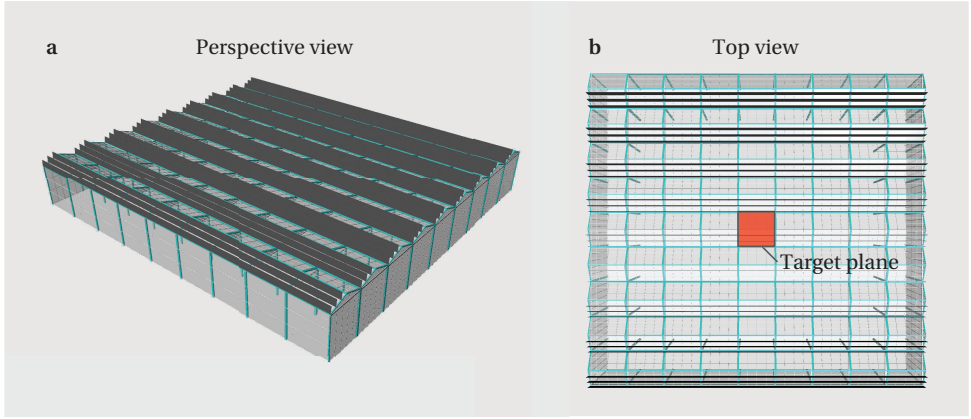


Figure 5.10: Model of the PV greenhouse array in **a**, perspective view, and **b**, top view, where the interior target plane (0.5 m high above the ground) is highlighted in red.

Table 5.3: Transmittance (T) and reflectance (R) of the materials in the greenhouse array

Glass (T)	Frames (R)	PV modules (R)	Ground (R)
88%	30%	30%	20%

problem [29]. Unlike RhinoScript, Grasshopper requires no knowledge of programming or scripting. Complicated algorithms can be achieved by interconnecting blocks in a graphical editor tightly integrated with Rhinoceros (see Appendix D). The information of location, date, and time is shared with DIVA, which contains the weather database of this location. The position of PV panels changes simultaneously when the number sliders of date and time are changed. By this means, ray tracing simulation can be conducted easily for any intended date and time.

Here, three indices (\mathbf{G}_{mat} , \bar{G}_{global} , and U_G) are used to evaluate the intensity and distribution of solar irradiance on the target plane. \mathbf{G}_{mat} is the matrix containing the global irradiance (G_{global}) at a grid of points, similar to the concept of *I-matrix* (illumination matrix) [35]. \mathbf{G}_{mat} is capable to describe the global information of the target plane, i.e.

$$\mathbf{G}_{mat} = \begin{bmatrix} G_{11} & \cdots & G_{1n} \\ \vdots & \ddots & \vdots \\ G_{m1} & \cdots & G_{mn} \end{bmatrix}, \quad (5.30)$$

where G_{ij} ($i = 1, 2, \dots, m$, $j = 1, 2, \dots, n$) represents the global irradiance of the corresponding point on the grid of the target plane. \bar{G}_{global} denotes the average global irradiance of the target plane, defined by

$$\bar{G}_{global} = \frac{\sum_{i=1}^m \sum_{j=1}^n G_{ij}}{mn}. \quad (5.31)$$

The uniformity of global irradiance on the target plane denoted by U_G can be written as

$$U_G = \frac{G_{global}^{min}}{\bar{G}_{global}}, \quad (5.32)$$

where G_{global}^{min} is the minimum value of the global irradiance on the target plane.

5.2.6. METHODS OF ANNUAL ACCUMULATIVE AND AVERAGE CALCULATION

Here we introduce the method of calculating the annual PV electricity production, the annual average global irradiance, and the annual average uniformity of global irradiance in a certain geographical location. Firstly, climate data is obtained from Meteonorm, such as solar altitude and azimuth, date and time, DNI, $G_{h,d}$, temperature, wind speed, etc. Secondly, the equivalent global irradiance G_{cell}^{eq} on each individual solar cell is calculated by Eq. (5.28). The temperature T of each individual solar cell is calculated by Eq. (5.29). Based on the model of PV module (Sec. 5.2.4), the power generation of the PV module in certain date and time can be simulated in MATLAB SimuLink by inputting G_{cell}^{eq} and T of each individual solar cell (60 cells in this case). Then the power output of one unit can be calculated according to different PV layouts and tilt angles. Lastly, the annual integral results of electricity production can be obtained by running a loop in MATLAB.

Regarding the ray-tracing simulation in DIVA, the Meteonorm data is firstly output as epw files. Then the irradiance matrix G_{mat} at a given time instant can be obtained from the model of the greenhouse array (Sec. 5.2.5). At the time instant, the average global irradiance \bar{G}_{global} of the target plane is obtained by Eq. (5.31); and the uniformity of the global irradiance is obtained by Eq. (5.32). Lastly, the annual average data are obtained by the simulation results of representative days of the year, i.e. the spring and autumnal equinox, and the summer and winter solstice.

5.3. RESULTS

5.3.1. PARTIAL SHADING EFFECTS ON PV MODULES

IN the aforementioned model of PV greenhouse, there could be rectangular shadows on the PV modules regarding the high-density PV (HDPV) layouts. Different HDPV layouts (Figures 5.5a & b) result in different shading patterns (Figure 5.11a & Figure 5.12a). Here, let I_{dir} be $1000 W/m^2$ (standard conditions), and $G_{h,d}$ be $100 W/m^2$. Let the sun ray be perpendicular to the PV module, i.e. γ equals to 0. The irradiance on the shading area is $100 W/m^2$; and on the direct-beam-illuminated area is $1100 W/m^2$. By simulating the model of PV module in MATLAB SimuLink, I-V curves and P-V curves with various lengths of shadow are obtained for HDPV 1 (Figures 5.11b & c) and HDPV 2 (Figures 5.12b & c). Meanwhile, the output power (P_{out}) and conversion efficiency (η) of the PV module are calculated for HDPV 1 (Figure 5.11d) and HDPV 2 (Figure 5.12d).

Results show that HDPV 1 performs better than HDPV 2 under rectangular shading conditions in terms of PV power generation. The poor behavior of PV module in HDPV 2 is mainly because the bypass diodes are not working when the shading percentages of three bypass circuits are equal (Figure 5.9b). Therefore, we will only consider HDPV 1 in the further analysis and discussion.

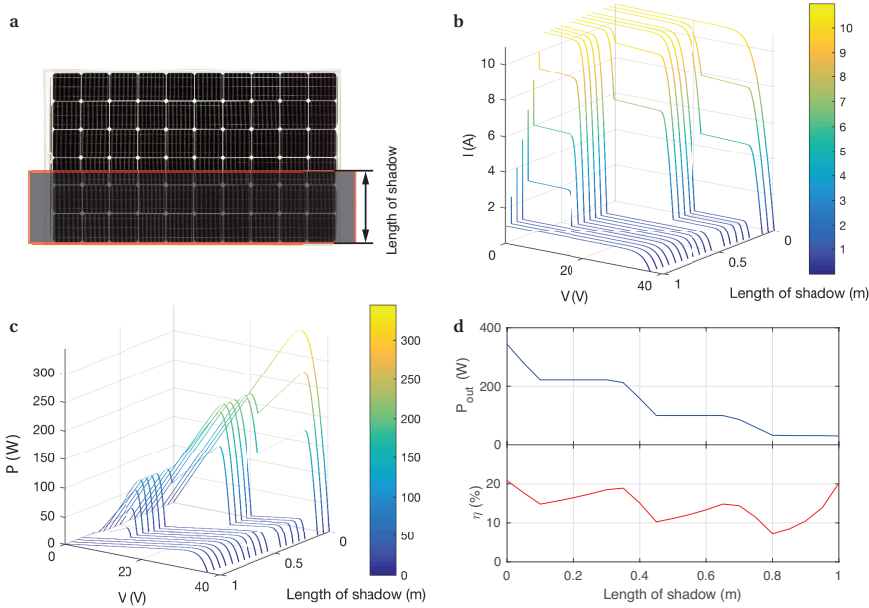


Figure 5.11: **a**, Shape and length of the shadow on the PV module of HDPV 1. **b**, I-V curves, **c**, P-V curves, **d**, output power, and conversion efficiency of the PV module of HDPV 1 changing with the length of shadows.

5.3.2. PV PERFORMANCE AT A GIVEN TIME INSTANT

As well known, the PV-generated energy is the integral of the output power over a certain period of time. Therefore, we first investigate the output power of the greenhouse dynamic PV at a given time instant. The location of the greenhouse is chosen as Delft, the Netherlands ($52.01^{\circ}N$, $4.36^{\circ}E$). The date is chosen as the spring equinox day (March 20th) and time as 10:00 am. In the equinox day, daytime and nighttime are of approximately equal duration; and the Sun appears in moderate positions in the sky. With the given location, date and time, the solar position is consequently determined. In this case, the solar altitude α_s is 0.47 rad and the solar azimuth A_s is 2.28 rad. Typical clear-sky conditions ($I_{dir} = 1000 \text{ W/m}^2$ and $G_{h,d} = 100 \text{ W/m}^2$) are used to study the solar radiation. According to the Meteornorm database [31], the ambient temperature (T_a) and wind speed (v_{wind}) are $4.3^{\circ}C$ and 5.4 m/s respectively. Following results at a given time instant are all based on such conditions, which will not be mentioned again.

In the proposed PV greenhouse model, the PV partial shading problem has to be considered, since it affects the output power of the PV module as proved above (Figures 5.11c & d). As to HDPV 1, PV modules in three different rows suffer from different shading conditions (Figure 5.13a). For convenience, modules are numbered as Module #1 and #2 according to their shading conditions. Apparently, Module #2 suffers from shading; and the shadows on it can be calculated by the shading model derived above. While Module #1 has no shading PV module in front of it. Meanwhile, the roof in front of Module #1 is made of transparent glass. Therefore, here we simply treat Module #1 as a

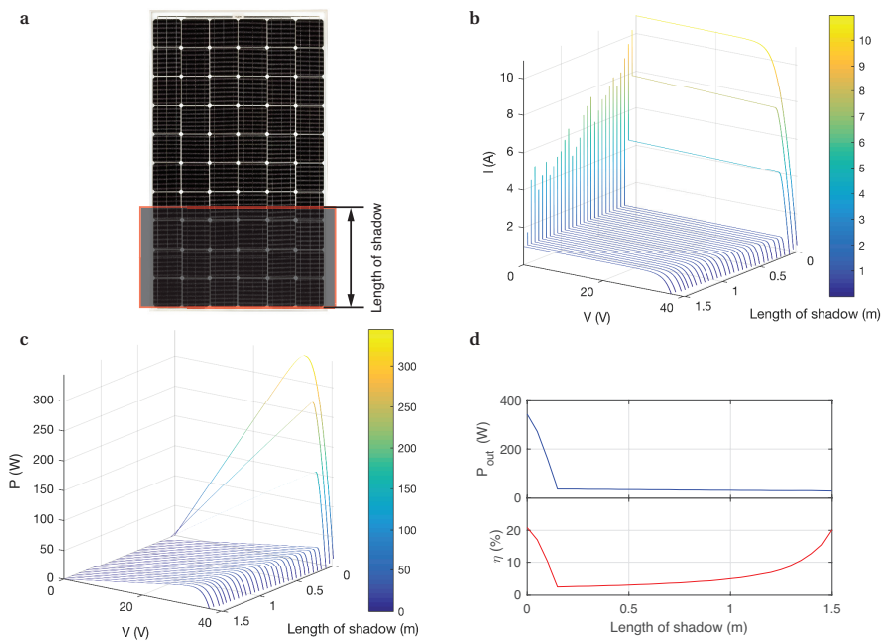


Figure 5.12: **a**, Shape and length of the shadow on the PV module of HDPV 2. **b**, I-V curves, **c**) P-V curves, **d**, output power, and conversion efficiency of the PV module of HDPV 2 changing with the length of shadows.

zero-shading PV module. According to different shading conditions, PV modules will be treated differently in regard of power generation. Note that an individual PV module is used to represent the performance of all the modules in the same row. We assume that different shading conditions only affect the performance of the individual PV module instead of the whole PV system. Border effects on the shading of PV modules are ignored here.

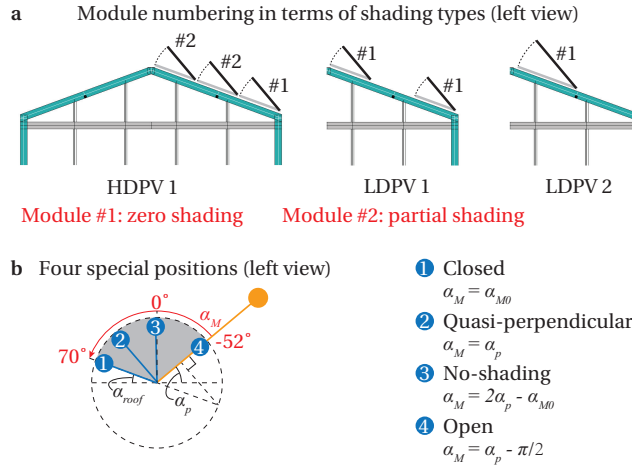


Figure 5.13: **a**, Left view of module numbering in term of shading types. **b**, Left view of four special sun-tracking positions and corresponding numbering.

With the given solar position, the range of module altitude is approximately between -52° and 70° according to Eq. (5.25), i.e. $\alpha_M \in [-0.91, 1.22]$ (Figure 5.13b). Four special positions are also illustrated and labeled in Figure 5.13b.

Based on the models of equivalent global irradiance (G_{cell}^{eq}), shadow length (z'_{q1s}) and PV module, simulations of PV power generation at different α_M are conducted in MATLAB SimuLink. Not surprisingly, Module #1 reveals different results compared to Module #2 due to different shading conditions (Figure 5.14). When α_M varies within its range, Module #1 exhibits smooth transitions in terms of I-V curves (Figure 5.14a) and P-V curves (Figure 5.14b). The peak output power appears where G_{global} reaches the maximum ($\alpha_M = \alpha_p$). In contrast, Module #2 produces fluctuating curves due to the partial shading conditions. The PV performance of Module #2 is apparently worse than that of Module #1 in respect of I-V curves (Figure 5.14c) and P-V curves (Figure 5.14d). Interestingly, the P-V curves of Module #2 are trimmed down significantly in the range of α_M where Module #1 performs the best.

To evaluate the overall results of PV performance in the unit, four indices of three layouts (HDPV 1, LDPV 1, LDPV 2) are calculated and compared, i.e. G_{global} (global irradiance of the area without shading), S_{shadow} (shadow area on Module #2), G_{module}^{eq} (equivalent global irradiance of HDPV 1), and P_{out} (output power of HDPV 1, LDPV 1, or LDPV 2). Results of four indices are aligned by α_M , with the maximum values marked by circles (Figure 5.15). Red lines with arrows indicate four special positions, corresponding

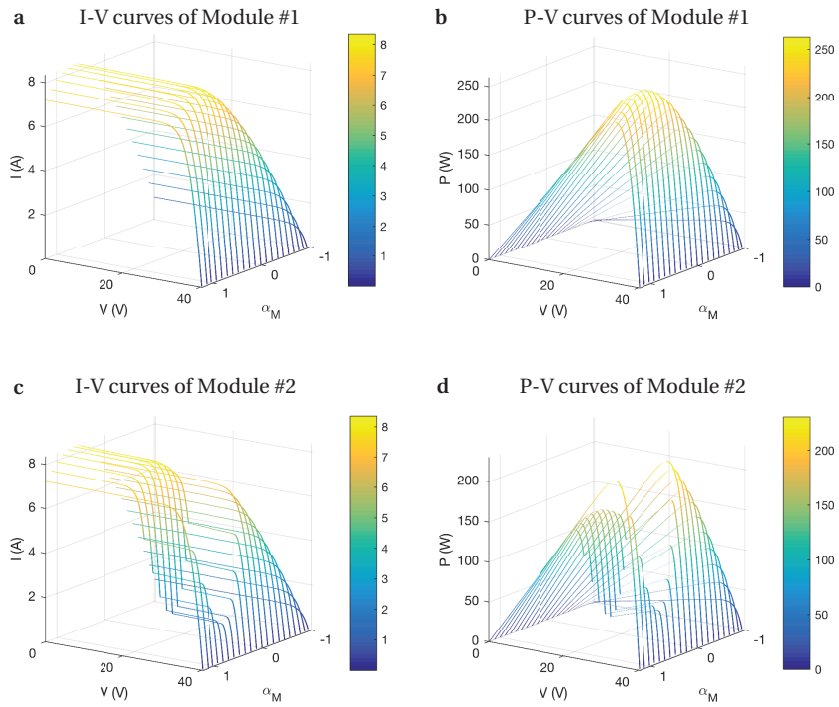


Figure 5.14: **a**, I-V and **b**, P-V curves of Module #1. **c**, I-V and **d** P-V curves of Module #2.

to those in Figure 5.13b. Regarding the zero-shading area, G_{global} reaches the maximum at the quasi-perpendicular position ($\alpha_M = \alpha_p$, i.e. position ②), as predicted by Eq. (5.26). However, in the very same position, S_{shadow} also reaches its peak, implying that shading problems offset part of the advantage of high global irradiance. As to G_{module}^{eq} , according to aforementioned theory (Eq. (5.25)), G_{module}^{eq} of Module #2 maintains as a constant when α_M varies from position ① to ③. However, the overall G_{module}^{eq} of HDPV 1 (12 PV panels) also counts the weight of Module #1 (1/3), resulting in the maximum G_{module}^{eq} in position ②. In other words, the overall input power of HDPV 1 peaks in position ②. However, the maximum input power cannot ensure the maximum output power due to PV partial shading effects. In this case, as to HDPV 1, the maximum P_{out} appears in position ① and ③, where G_{module}^{eq} maintains at a high level; and no shadow affects the PV conversion efficiency. Here, we can theoretically prove that values of G_{global} will always be equal in position of ① and ③ by substituting the boundary condition ($\alpha_M = 2\alpha_p - \alpha_{M0}$) into Eq. (5.8). It explains why P_{out} has two identical peaks. As to LDPV 1 and LDPV 2, both the maximum P_{out} points appear in position ②, where G_{global} reaches the maximum. Though LDPV layouts have higher overall efficiency due to no PV shading effects, HDPV 1 has more PV panels (12) than LDPV 1 (8) and LDPV 2 (6) in the same roof area of the unit. Therefore, we can conclude that under the given solar position, HDPV 1 in the closed position (①) and the no-shading position (③) perform equally best in terms of PV power generation.

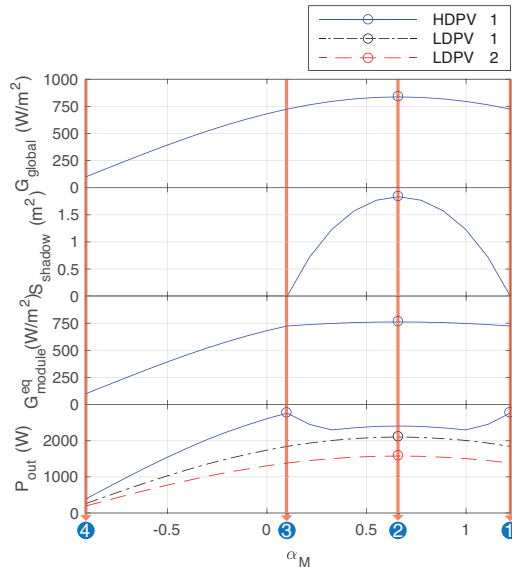


Figure 5.15: Results of three PV layouts at a given time instant in terms of G_{global} , S_{shadow} , G_{module}^{eq} , and P_{out} changing with α_M , with the maximum values marked by circles.

5.3.3. INTERIOR IRRADIANCE AT A GIVEN TIME INSTANT

Regarding HDPV 1, though PV modules in the closed position generate electric power as much as that in the no-shading position, the closed modules might result in relatively lower interior irradiance in the greenhouse due to the full coverage on the south roof. To test this hypothesis, the interior irradiance with PV modules under four special positions is simulated by the means of ray tracing. To avoid border effects, the center area of the PV greenhouse array is chosen as the target plane (red area), where interior irradiance can be affected by the changes of roof coverage (Figure 5.16). The area of the target plane is the same as the vertical projection area of the unit; the height of the target plane is 0.5 m . In the setting of the simulation, the target plane is divided into grid squares. It is like positioning an irradiance sensor in the center of each grid square. In this case, the grid interval is chosen as 0.1 m , resulting in 3,360 (60×56) elements in the \mathbf{G}_{mat} (Figure 5.16). By visualizing \mathbf{G}_{mat} of four special positions, colormaps are drawn as shown in Figure 5.17a-d. It is obvious that the open position reveals the maximum \bar{G}_{global} because it basically equals to no PV coverage. Compared with the open position, the other three positions reduce \bar{G}_{global} by different amounts, but increase U_G . The interior irradiance of LDPV 1 and LDPV 2 under three positions (not including the open position, which is basically the same for all PV layouts) are also visualized in Figure 5.18 and Figure 5.19.

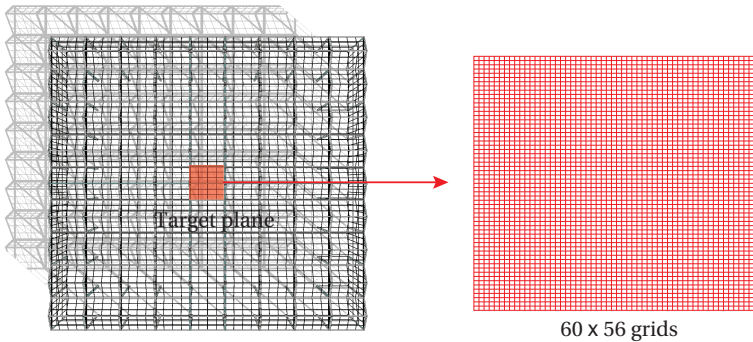


Figure 5.16: Top view of the target plane in the PV greenhouse array with shadows, and the grids on the target plane with 0.1 m interval.

Like Figure 5.15, results of \bar{G}_{global} and U_G of the target plane are aligned with that of P_{out} according to α_M (Figure 5.20). It is observed that for all the three PV layouts, with α_M decreasing, i.e. the PV modules rotating from the closed position (①) to the open position (④), \bar{G}_{global} increases gradually, and reaches the maximum in the open position. As to HDPV 1, U_G peaks in the no-shading position (③). U_G rises from ④ to ③, and maintains a high level from ③ to ①. As to LDPV 1 and LDPV 2, the maximum U_G locates somewhere near position ② and position ③ respectively.

Regarding HDPV 1, comparing the position ③ with ①, where the PV modules generate the same P_{out} , ③ is superior to ① in terms of both \bar{G}_{global} and U_G . It means that HDPV 1 in the no-shading position not only results in the maximum PV power generation, but also reveals better interior radiation than that in the closed position.

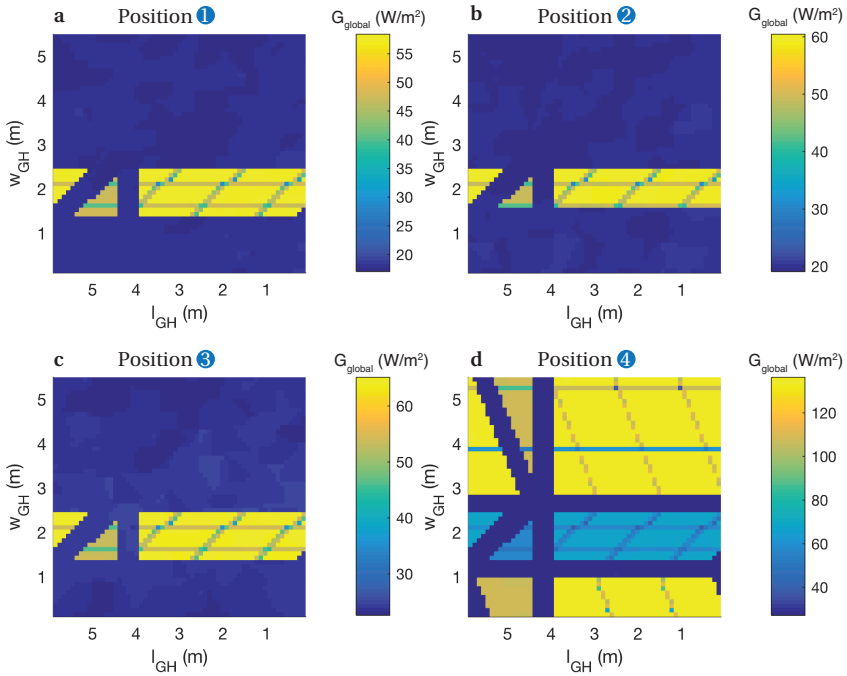


Figure 5.17: Color map of the global irradiance on the target plane with HDPV 1 in the sun-tracking positions of a ①, b ②, c ③, and d ④.

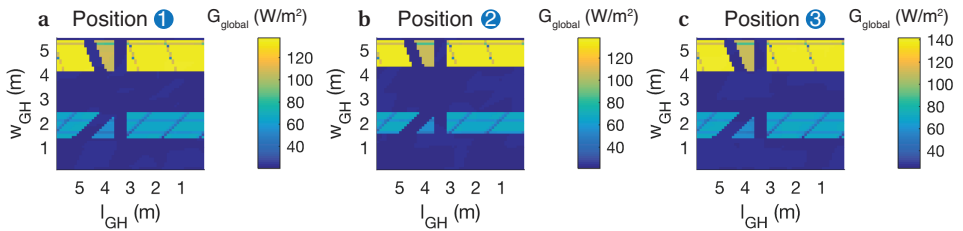


Figure 5.18: Color map of the global irradiance on the target plane with LDPV 1 in the sun-tracking positions of a ①, b ②, and c ③.

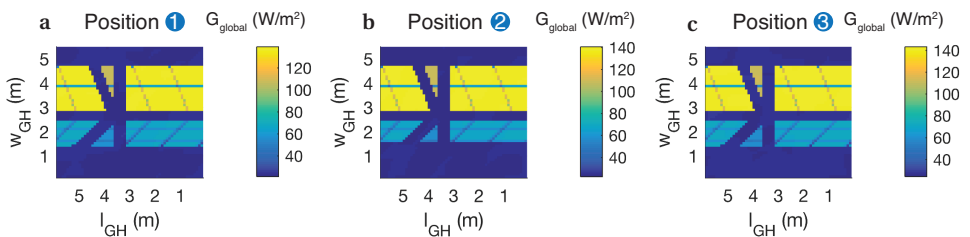


Figure 5.19: Color map of the global irradiance on the target plane with LDPV 2 in the sun-tracking positions of a ①, b ②, and c ③.

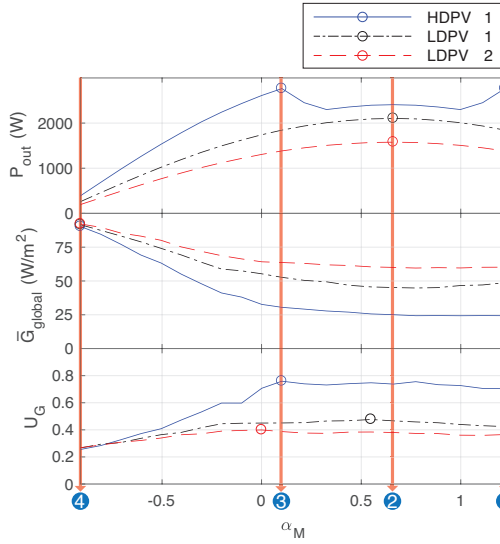


Figure 5.20: Results of three PV layouts at a given time instant in terms of P_{out} , \bar{G}_{global} , and U_G changing with α_M , with the maximum values marked by circles.

5.3.4. DAILY RESULTS IN HOURLY TIME STEP

As above, the PV output and interior irradiance are simulated on the scale of a time instant. In order to illustrate the trend of the concerned performance in a certain period of time, here we present hourly results of P_{out} , \bar{G}_{global} and \bar{U}_G in four representative days of the year, i.e. the spring equinox, the summer solstice, the autumnal equinox, and the winter solstice (Figures 5.21-5.23). Three types of PV layouts (HDPV 1, LDPV 1, and LDPV 2) and four special sun-tracking positions are compared and analyzed.

Regarding the output power of the unit, P_{out} decreases with the PV density. For HDPV 1, positions ① and ③ perform better than position ② due to the PV partial shading effects. While in LDPV 1 and LDPV 2, there is no shading on the PV panels. Therefore, position ② performs best in these cases. Note that, in cloudy days, DNI is low (even zero). In terms of PV power generation, there is no difference between various positions because of the equal $G_{h,d}$.

As to G_{global} , position ④ results in the highest G_{global} since it equals no PV coverage. Position ③ shows the second best results in most of cases. As to \bar{U}_G , position ④ results in the lowest uniformity in most of cases. Other three positions show close results, which require average results to compare.

5.3.5. ANNUAL ACCUMULATIVE AND AVERAGE RESULTS

From the hourly results above, it is hard to conclude the optimum sun-tracking strategy. To obtain convincing and straight results, the annual performance of the PV greenhouse is evaluated under the conditions of three PV layouts and four special sun-tracking positions. Here, three indices are employed to indicate the annual performance, i.e. the annual energy generation of the unit PV greenhouse, the annual average global irradi-

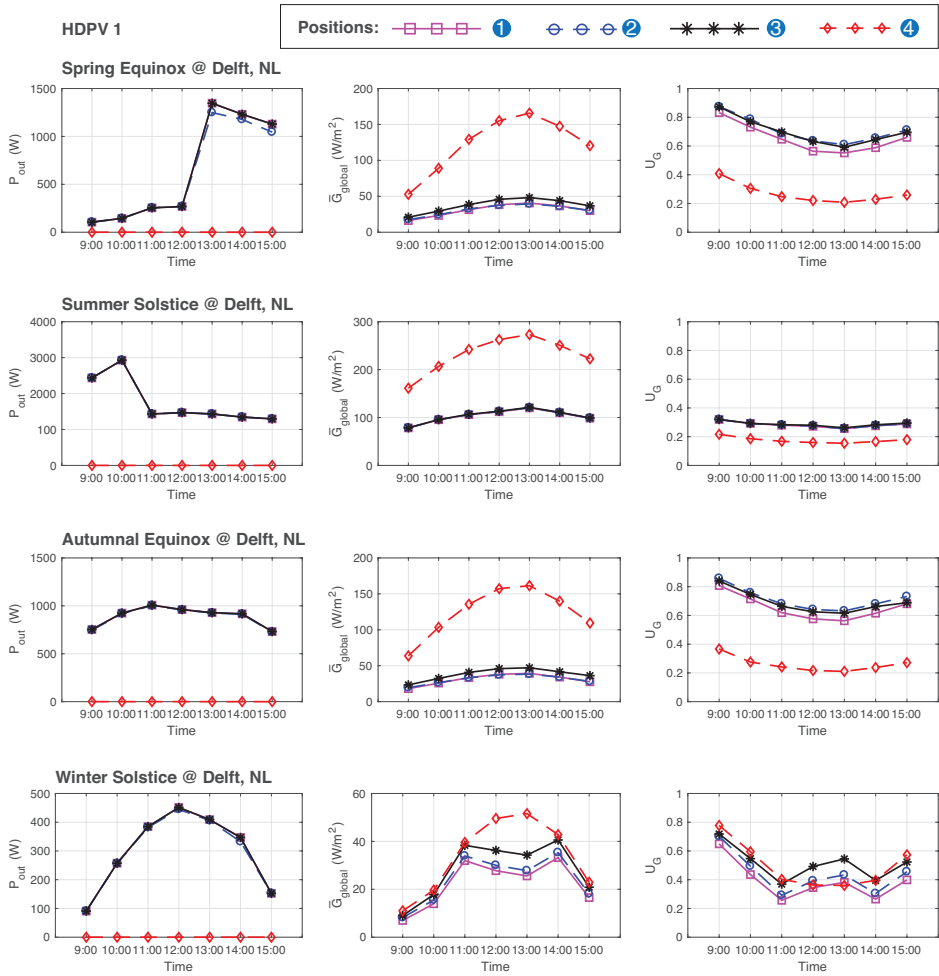


Figure 5.21: Hourly P_{out} , \bar{G}_{global} and \bar{U}_G of HDPV 1 in four special positions in four representative days of the year.

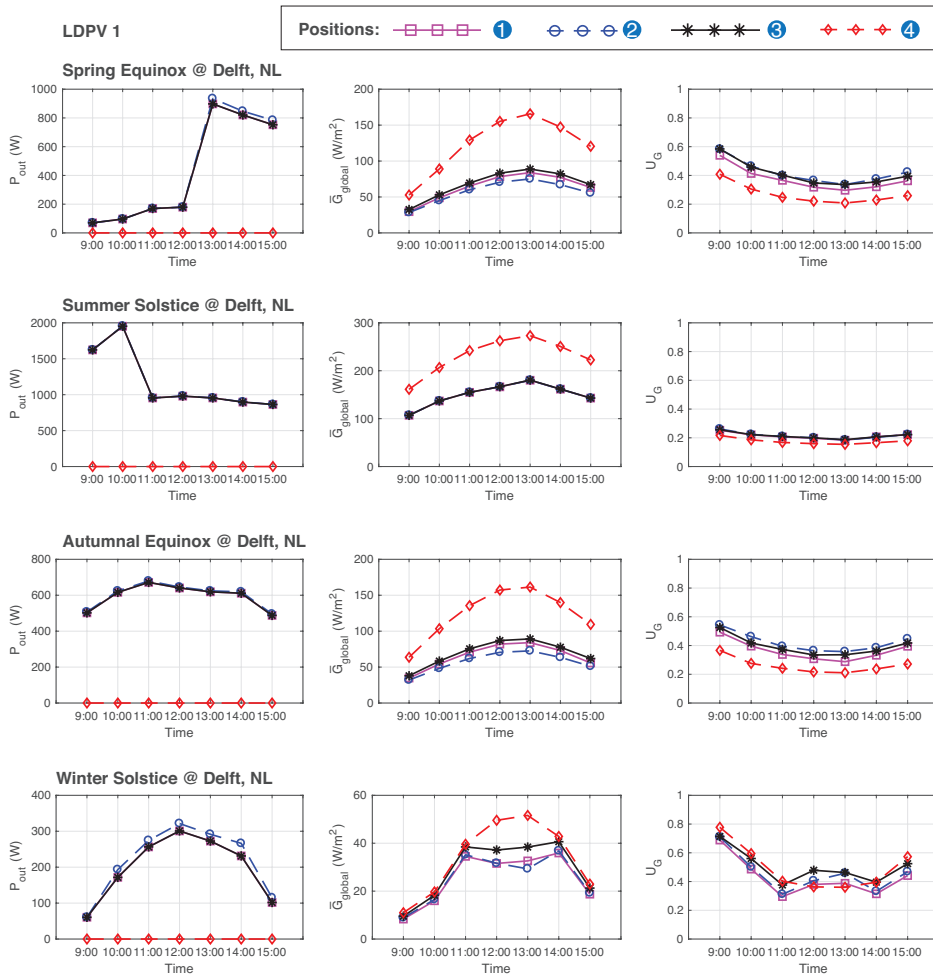


Figure 5.22: Hourly P_{out} , \bar{G}_{global} and \bar{U}_G of LDPV 1 in four special positions in four representative days of the year.

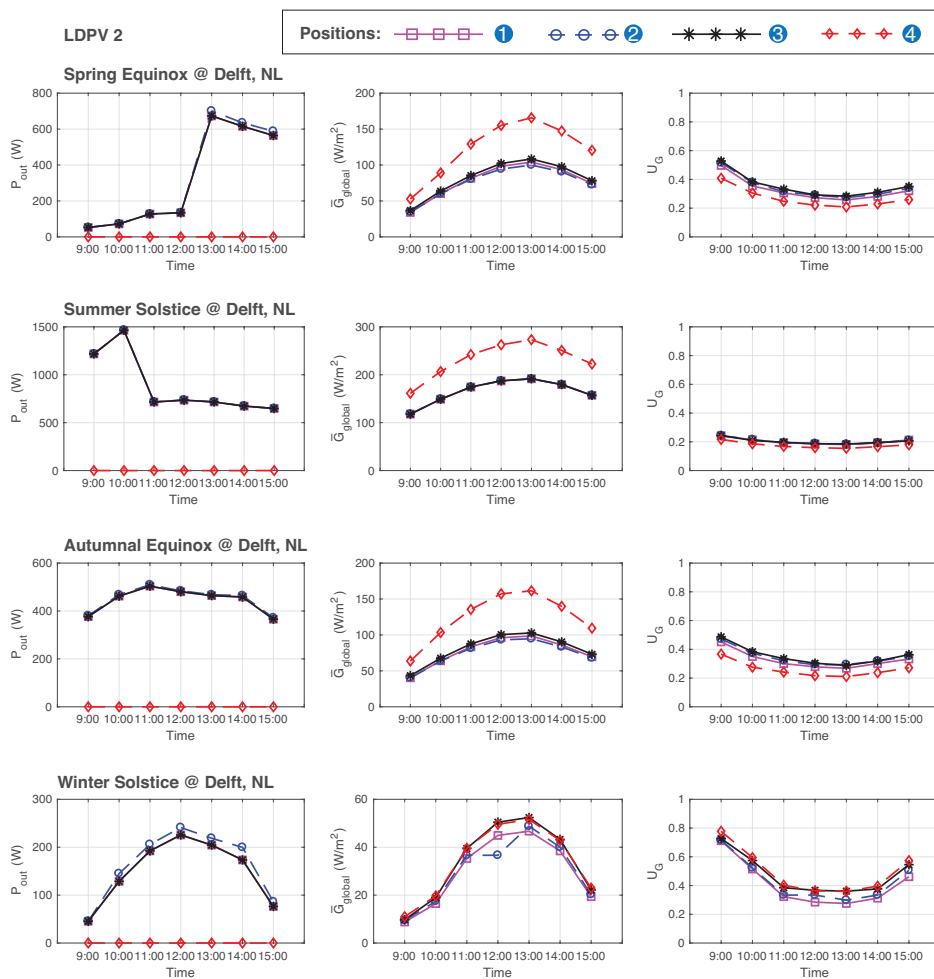


Figure 5.23: Hourly P_{out} , \bar{G}_{global} and \bar{U}_G of LDPV 2 in four special positions in four representative days of the year.

ance on the target plane, and the annual average uniformity of the global irradiance on the target plane (\bar{U}_G). Hourly climate data (9:00 - 15:00), including direct normal irradiance (I_{dir}), diffuse horizontal irradiance ($G_{h,d}$), ambient (air) temperature (T_a), wind speed (v_{wind}), is used to calculate the three indices. In an individual time interval, the electric energy generated by PV modules in the unit equals to the PV output power multiplied by the time duration (one hour). Then, the annual energy generation is calculated by the summation of 7×365 (2555) hourly energy values. Annual accumulative results of PV energy generation are shown in Figure 5.24. Consistent with the time-instant results, HDPV 1 outputs the maximum energy in position ① and ③; while LDPV 1 and LDPV 2 perform best in position ② in terms of the annual energy generation. As to position ④, we simply treat the open state as no PV coverage and consequently no PV energy generation.

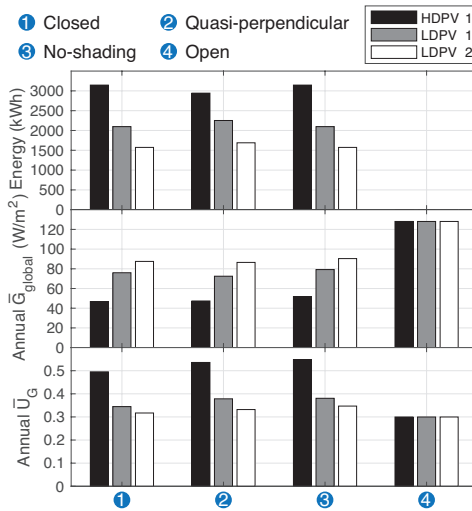


Figure 5.24: Results of three PV layouts in terms of annual accumulative energy, annual average global irradiance, and annual average uniformity of global irradiance on the target plane.

Figure 5.24 also shows the results of annual \bar{G}_{global} and \bar{U}_G on the target plane. The annual results of interior irradiance are the average values of four typical days of the year (March equinox, June solstice, September equinox, and December solstice). The reason of not using 365-day values is because precise ray-tracing simulations are time-consuming. It is obvious that for all the three PV layouts, the annual global irradiance reaches the maximum in the open position (④); while the annual uniformity of the global irradiance obtains the best results in position ③.

As to HDPV 1, the no-shading sun tracking (position ③) enables the unit PV greenhouse to increase the annual energy generation by 6.91% than the quasi-perpendicular sun tracking (position ②). Regarding interior irradiance, position ③ improves the annual \bar{G}_{global} and \bar{U}_G by 10.96% and 10.68% respectively compared with the closed position (①).

As to LDPV 1 and LDPV 2, the annual energy generation under quasi-perpendicular sun tracking (position ②) is increased by 7.40% and 7.40% respectively than that in the closed position (①). However, the annual \bar{G}_{global} in position ② shows the lowest values among all the four special positions. The annual \bar{U}_G maintains at a high levels in position ②, resulting in 9.80% and 4.70% increases respectively than that in the closed position (①).

5.4. DISCUSSION

5.4.1. BALANCING INTERIOR ILLUMINANCE AND PV GENERATION

DYNAMIC PV roofs can better control the incident light than the fixed ones. With respect to HDPV 1, the no-shading sun tracking results in the highest PV energy generation, the highest uniformity of global irradiance, and higher global irradiance than the closed (fixed) position. The PV panel position under no-shading sun tracking (position ③) can be easily calculated by the given solar position, i.e.

$$\alpha_M = 2 \arctan(\tan \alpha_s \sec \Delta A) - \alpha_{M0}. \quad (5.33)$$

As to LDPV 1 and LDPV 2, the PV generation performs best under the quasi-perpendicular sun tracking (position ②), i.e.

$$\alpha_M = \arctan(\tan \alpha_s \sec \Delta A). \quad (5.34)$$

5.4.2. OTHER IMPACT FACTORS

Besides light, other factors, such as air temperature, humidity, irrigation, the temperature and water contents of soil, etc., also affect the growth of crops. Though those factors relate to the sun-tracking schemes to a certain degree, it is difficult to estimate those factors without the knowledge of additional information. For instance, the thermal behavior is highly related to the solar radiation, but also affected by the local climate, ventilation systems, heating and cooling systems, etc. Therefore, further optimal design of PV layouts and sun-tracking schemes can be achieved when the details of PV greenhouses are given. In this study, we only consider the PV generation and the interior irradiance.

In this study, we mainly investigate the interior irradiance on the target plane in a PV greenhouse array, where border effects are ignored. However, for those greenhouses that only contains single row, border effects cannot be neglected any more. The impact of PV roof will be reduced, because the glass façades also contribute to the interior irradiance. Moreover, the shadows of PV roof will not exist inside the greenhouse when the solar altitude is very low. Therefore, conclusions in this study are not necessarily applicable to the single-row PV greenhouse.

The consumption of sun trackers are not considered here, because it heavily depends on the motors and the tracking intervals. When we discussed the PV partial shading problems in this study, the conventional PV module only has three bypass diodes (Figure 5.9b). However, some innovative PV product equips bypass diodes for every single solar cell in the PV module (e.g. AE SMP6-72). In this case, HDPV 1 and HDPV 2 suffer the same power reduction in the shading conditions. When such PV modules are used in PV greenhouse, conclusions of HDPV 1 also apply to HDPV 2.

5.4.3. IDEAL SIMULATION RESULTS

In our study, the sun-tracking theory is tested by ideal simulations. Compared with field study, the simulation results can reflect the average level of intended indices, because the climate data obtained from Meteonorm is the average over ten years. While field study can only test the results over a certain period of time (usually less than one year). Ideal simulations also avoid unexpected external interferences, e.g. random shading by leaves or animals, performance difference of the same batch PV modules, etc. As to the evaluation of interior irradiance, field study usually measures the irradiance of one or several points, which are not comparable to the 3,360 points in the ray-tracing simulation. Unless using some innovative image-processing technologies, field study can hardly obtain accurate \bar{G}_{global} and U_G . For further study on crop models, hourly irradiance data can be obtained for a certain period of time, e.g. a full growing season. Even though, further field study is still in need to verify the theory and conclusions in our study, especially with live plants. In the further field study, the mechanical rotation of PV panels can be realized by installing one-axis sun trackers at the back of PV panels, without affecting the solar irradiance on the PV panel and in the greenhouse.

5.4.4. RESTRICTIONS OF THE CURRENT WORK

Though the proposed modeling and simulation scheme (Figure 5.3) is capable of performing the intended simulations, there are still margins to further improve the results, dependent on the availability of the simulation tools and some related models. In this work, Meteonorm outputs climate data with the minimum time interval of one hour. Other data sources or real-time measurements can also be used in the models. Regarding DIVA, its current version does not support the loop function over a period of time. The ray-tracing simulations of the greenhouse array have to be run manually in the current work. As to the model of the PV module, two inputs, i.e. global irradiance and module temperature, are considered in the electrical performance of the PV module. However, in reality, relative humidity (RH) can affect not only the module temperature, but also the incident irradiance. Besides, water vapour particles may enter the solar cell enclosure and consequently affect the performance of the PV module. More accurate PV models considering RH shall be further investigated in the future.

Generally, the energy performance of a PV greenhouse contains not only PV electricity production and interior irradiance, but also the thermal behavior, plant production, and electricity consumption. The model can be made even more comprehensive by including e.g. Computational Fluid Dynamics (CFD) models [36] and crop models [5].

5.5. CONCLUSIONS

IN this work, we have investigated the energy performance of PV greenhouses under three PV layouts and four special sun-tracking positions. The PV layout should be determined at the initial stage of the greenhouse design according to the light preference of crops. The high-density PV (HDPV) layout is capable to form more uniform interior irradiance and generate more electricity; while low-density PV (LDPV) layouts enable higher global irradiance in the greenhouse. Four sun-tracking methods (closed, quasi-perpendicular sun tracking, no-shading, and open) are proposed to regulate the

daily operation of the PV greenhouse with determined PV layouts. Dynamic positions of PV modules by different sun-tracking methods are derived as the functions of the solar positions. With respect to HDPV 1, the no-shading sun tracking can achieve the highest annual energy generation and annual average uniformity of interior global irradiance among others. Compared to conventional (quasi-perpendicular) sun-tracking method, no-shading sun tracking generate 6.91% more electricity under the layout of HDPV 1. Meanwhile, annual average global irradiance and uniformity are improved by 10.96% and 10.68% respectively compared to the fixed PV panels in the closed position. As to LDPV 1 and LDPV 2, the best performance of electricity production is obtained by the quasi-perpendicular sun tracking, which leads to the lowest interior global irradiance and relatively high irradiance uniformity. Compared to the closed position, the annual generation is increased by 7.40% under quasi-perpendicular sun tracking. Meanwhile, annual average uniformity of global irradiance are increased by 9.80% (LDPV 1) and 4.70% (LDPV 2).

REFERENCES

- [1] Y. Gao, J. Dong, O. Isabella, R. Santbergen, H. Tan, M. Zeman, and G. Zhang, *Modeling and analyses of energy performances of photovoltaic greenhouses with sun-tracking functionality*, Applied Energy **233-234**, 424 (2019).
- [2] B. Obama, *The irreversible momentum of clean energy*, Science **355**, 126 (2017).
- [3] IEA, *Renewables 2017*, Tech. Rep. 42 (2017).
- [4] M. Ritzen, Z. Vroon, and C. Geurts, *Building integrated photovoltaics*, Photovoltaic Solar Energy: From Fundamentals to Applications , 579 (2017).
- [5] C. Dupraz, H. Marrou, G. Talbot, L. Dufour, A. Nogier, and Y. Ferard, *Combining solar photovoltaic panels and food crops for optimising land use: Towards new agrivoltaic schemes*, Renewable Energy **36**, 2725 (2011).
- [6] A. Goetzberger and A. Zastrow, *On the Coexistence of Solar-Energy Conversion and Plant Cultivation*, (1981).
- [7] J. Xue, *Photovoltaic agriculture - New opportunity for photovoltaic applications in China*, Renewable and Sustainable Energy Reviews **73**, 1 (2017).
- [8] M. Cossu, L. Murgia, L. Ledda, P. A. Deligios, A. Sirigu, F. Chessa, and A. Pazzona, *Solar radiation distribution inside a greenhouse with south-oriented photovoltaic roofs and effects on crop productivity*, Applied Energy **133**, 89 (2014).
- [9] C. Li, H. Wang, H. Miao, and B. Ye, *The economic and social performance of integrated photovoltaic and agricultural greenhouses systems : Case study in China*, Applied Energy **190**, 204 (2017).
- [10] I. Sartori, A. Napolitano, and K. Voss, *Net zero energy buildings: A consistent definition framework*, Energy and Buildings **48**, 220 (2012).

- [11] N. K. Boardman, *Comparative Photosynthesis of Sun and Shade Plants*, Annual Review of Plant Physiology **28**, 355 (1977).
- [12] R. Urena, J. Perez, M. Perez, A. Carreno, A. J. Callejon, and F. J. Vazquez, *Experiences on the Integration of Thin Film Photovoltaic Modules in a Mediterranean Greenhouse*, in *XVIIth World Congress of the International Commission of Agricultural and Biosystems Engineering (CIGR)* (2010) pp. 1–7.
- [13] M. Kadowaki, A. Yano, F. Ishizu, T. Tanaka, and S. Noda, *Effects of greenhouse photovoltaic array shading on Welsh onion growth*, Biosystems Engineering **111**, 290 (2012).
- [14] H. Marrou, J. Wery, L. Dufour, and C. Dupraz, *Productivity and radiation use efficiency of lettuces grown in the partial shade of photovoltaic panels*, European Journal of Agronomy **44**, 54 (2013).
- [15] H. Marrou, L. Guilioni, L. Dufour, C. Dupraz, and J. Wery, *Microclimate under agri-voltaic systems : Is crop growth rate affected in the partial shade of solar panels ?* Agricultural and Forest Meteorology **177**, 117 (2013).
- [16] B. Valle, T. Simonneau, F. Sourd, P. Pechier, P. Hamard, T. Frisson, M. Ryckewaert, and A. Christophe, *Increasing the total productivity of a land by combining mobile photovoltaic panels and food crops*, Applied Energy **206**, 1495 (2017).
- [17] A. Marucci and A. Cappuccini, *Dynamic photovoltaic greenhouse: Energy efficiency in clear sky conditions*, Applied Energy **170**, 362 (2016).
- [18] S. Castellano, P. Santamaria, and F. Serio, *Solar radiation distribution inside a monospan greenhouse with the roof entirely covered by photovoltaic panels*, Journal of Agricultural Engineering **47**, 1 (2016).
- [19] M. Cossu, L. Murgia, M. Caria, and A. Pazzona, *Economic feasibility study of semi-transparent photovoltaic technology integrated on greenhouse covering structures*, International Conference Ragusa SHWA2010 , 648 (2010).
- [20] A. Yano, M. Kadowaki, A. Furue, N. Tamaki, T. Tanaka, E. Hiraki, Y. Kato, F. Ishizu, and S. Noda, *Shading and electrical features of a photovoltaic array mounted inside the roof of an east-west oriented greenhouse*, Biosystems Engineering **106**, 367 (2010).
- [21] A. Marucci, D. Monarca, M. Cecchini, A. Colantoni, and A. Cappuccini, *Analysis of internal shading degree to a prototype of dynamics photovoltaic greenhouse through simulation software*, Journal of Agricultural Engineering **46**, 144 (2015).
- [22] A. Marucci and A. Cappuccini, *Dynamic photovoltaic greenhouse: Energy balance in completely clear sky condition during the hot period*, Energy **102**, 302 (2016).
- [23] G. Trypanagnostopoulos, A. Kavga, Souliotis, and Y. Tripanagnostopoulos, *Greenhouse performance results for roof installed photovoltaics*, Renewable Energy **111**, 724 (2017).

- [24] M. Cossu, A. Yano, Z. Li, M. Onoe, H. Nakamura, T. Matsumoto, and J. Nakata, *Advances on the semi-transparent modules based on micro solar cells: First integration in a greenhouse system*, Applied Energy **162**, 1042 (2016).
- [25] F. Yang, Y. Zhang, Y. Hao, Y. Cui, W. Wang, T. Ji, F. Shi, and B. Wei, *Visibly transparent organic photovoltaic with improved transparency and absorption based on tandem photonic crystal for greenhouse application*, Applied Optics **54**, 10232 (2015).
- [26] R. Croce and H. Van Amerongen, *Natural strategies for photosynthetic light harvesting*, Nature Chemical Biology **10**, 492 (2014).
- [27] G. D. Massa, H. H. Kim, R. M. Wheeler, and C. A. Mitchell, *Plant productivity in response to LED lighting*, HortScience **43**, 1951 (2008).
- [28] S. Amaducci, X. Yin, and M. Colauzzi, *Agrivoltaic systems to optimise land use for electric energy production*, Applied Energy **220**, 545 (2018).
- [29] K. Lagios, J. Niemasz, and C. F. Reinhart, *Animated Building Performance Simulation (ABPS) - Linking Rhinoceros/Grasshopper With Radiance/Daysim*, SimBuild 2010, 321 (321).
- [30] J. A. Jakubiec and C. F. Reinhart, *DIVA 2.0: Integrating daylight and thermal simulations using rhinoceros 3D, DAYSIM and EnergyPlus*, Proceedings of Building Simulation 2011: 12th Conference of International Building Performance Simulation Association, 2202 (2011), arXiv:arXiv:1011.1669v3.
- [31] J. Remund and S. Kunz, *METEONORM: Global meteorological database for solar energy and applied climatology* (Meteotest, 1997).
- [32] A. Smets, K. Jäger, O. Isabella, R. van Swaaij, and M. Zeman, *Solar Energy: The Physics and Engineering of Photovoltaic Conversion, Technologies and Systems* (UIT Cambridge, 2016) p. 488.
- [33] A. Chouder, S. Silvestre, N. Sadaoui, and L. Rahmani, *Modeling and simulation of a grid connected PV system based on the evaluation of main PV module parameters*, Simulation Modelling Practice and Theory **20**, 46 (2012).
- [34] G. Tamizhmani, L. Ji, Y. Tang, L. Petacci, and C. Osterwald, *Photovoltaic Module Thermal / Wind Performance : Long -Term Monitoring and Model Development For Energy Rating*, NCPV and Solar Program Review Meeting, 936 (2003).
- [35] Y. Gao, Y. Lin, and Y. Sun, *A wireless sensor network based on the novel concept of an I-matrix to achieve high-precision lighting control*, Building and Environment **70**, 223 (2013).
- [36] T. Boulard, J. C. Roy, J. B. Pouillard, H. Fatnassi, and A. Grisey, *Modelling of micrometeorology, canopy transpiration and photosynthesis in a closed greenhouse using computational fluid dynamics*, Biosystems Engineering **158**, 110 (2017).

6

TRANSPARENCY-TUNABLE PHOTOVOLTAIC WINDOWS

Abstract

Previous chapters mainly focus on the modeling and optimization of PV windows with sun-tracking elements. In this chapter, a PV-powered transmittance-tunable device is introduced as an alternative of PV windows. This work comprises two main parts, one of which is the method of designing and fabricating semi-transparent thin-film amorphous silicon solar cells. The other is the control of the PV windows by polymer dispersed liquid crystal (PDLC) films. Using an optical model, GenPro4, we provide with a simulation method to optimize the configuration of such solar cells. For a single-junction amorphous silicon solar cell, the optimized thickness of the absorber layer is obtained at 170 nm to realize a target average transmittance of 20% in the visible range of the sunlight spectrum. Measurement results show that an average transmittance of 20.04% is achieved with the conversion efficiency of 6.94%. Additionally attached to a PDLC film, the transmittance of the PV window can be further controlled. The prototype of a house model has been built to demonstrate the feasibility of such a combination.

Parts of this chapter have been published in the IEEE 44th Photovoltaic Specialist Conference (PVSC), 2605 (2017) [1].

6.1. INTRODUCTION TO SEMI-TRANSPARENT SOLAR CELL

SEMI-TRANSPARENT photovoltaics (STPVs) are drawing more and more attention due to the prospect of PV applications integrated with architecture, agriculture, automobile, etc. [2, 3]. STPVs not only contribute to the reduction of greenhouse gas emission, but also to the esthetic design of PV systems because of the colorful and translucent appearance [4]. Comparing with other promising candidates for STPV (such as Perovskite [5], organic photovoltaics [6], etc.), thin-film silicon technology reveals its advantages in the respect of stability, abundant raw material, capability of mass production and very large area deposition [7]. Currently, commercially available STPV products applying thin-film silicon technology vary in module efficiency, transmittance, and color appearance [4]. Customized modules can be installed as the windows in buildings [2], the envelope of glass greenhouse [3], and even automotive sunroof and windows [6]. One of the challenges for promoting this technology is to improve the efficiency of energy conversion while preserving the transparency of target surfaces.

Unlike conventional opaque solar cells, the back contact in semi-transparent solar cells acts as only a conductive layer, instead of a back reflector. To achieve desired transparency, most previous research was conducted by replacing the metal back contact with transparent back contact (TBC) and tuning the thickness of certain layers based on existing structures of opaque solar cells. However, experimental results of those research were presented by different criteria on the transparency of STPV, such as the average transmittance over a certain spectral band, the transmittance at a certain wavelength, etc. Therefore, here relevant literatures are reviewed individually without concluding the best candidate among them. Yeop Myong et al. invented and investigated three approaches to fabricating proper back contacts for colored semi-transparent PV modules, i.e. TBC type with green color, hybrid type with additional laser-scribed patterns and blue encapsulating film, and opaque back contact (OBC) type with additional laser-scribed patterns. Module-level values of average total transmittance in the wavelength range of 360-750 nm (T_{365_750}) and the nominal conversion efficiency (η) were shown in TBC type ($T_{365_750} = 14.0\%$, $\eta = 5.6\%$), hybrid type ($T_{365_750} = 30\%$, $\eta = 3.5\%$), and OBC type ($T_{365_750} = 10\%$, $\eta = 6.4\%$), respectively [4]. Lim et al. conducted a series of experiments to obtain the optimal thickness of transparent conductive oxide (TCO) [8], high-bandgap (HB) n/i-interface layers [9], and p-Si layer [10], respectively. In [8], the thickness of TCO was taken as the variable, and hydrogenated amorphous silicon (a-Si:H) with TCO thickness of 300 nm exhibited an outstanding performance ($T_{400_800} = 21.6\%$, $\eta = 5.6\%$). In [9], HB layers were introduced to decrease shunt loss and increase carrier collection. Among all HB-layer structures, the cell fabricated with triple HB layers showed the best optoelectronic performance ($T_{400_800} = 23.6\%$, $\eta = 6.9\%$). In [10], the thin p-Si layer was employed to obtain high transparency and high current density while a buffer layer was used to enhance, which was reduced by the thin p-Si layer. The best performance ($T_{500_800} = 30.7\%$, $\eta = 5.36\%$) was found when the thickness of p-Si layer was 7.5 nm and the thickness of buffer layer was 0.5 nm. Lee et al. investigated ultra-thin intrinsic a-Si/organic hybrid structures which are able to produce transmissive or reflective colors (red, green, and blue). It was claimed that the power efficiency of the hybrid cell was obtained up to 3%. Transmission spectra were plotted in curves, without calculating the values of average transmittances [11].

Previous research shares a common problem that the variable thicknesses of target layers were chosen manually based on the experience of researchers. The interval of chosen variables cannot be too small since fabricating cell samples costs time and efforts. Therefore, precise simulation plays an important role in optimizing the configurations and structures of semi-transparent solar cells quickly. However, details of simulation methods were rarely mentioned in previous research. In this study, GenPro4, an optical model developed at the PVMD group, is applied to the design and optimization of semi-transparent single-junction a-Si:H solar cells [12, 13]. GenPro4 represents the solar cell as a multilayer structure and calculates the fraction of incident light absorbed in each layer, taking into account scattering of light at the interfaces. Such model and its previous versions have been validated for a wide variety of wafer-based and thin-film solar cells [12–15]. The photocurrent density associated to the absorptance in the absorbing i-layer, to the reflection and to the transmittance of the solar cell can be accurately calculated with proper input data, such as surface morphologies, layers thickness and refractive indexes. GenPro4 supports our efforts in fabricating, testing and measuring solar cells with various configurations to obtain solar cells with balanced optical and electrical performance.

In this work, an optimization method is proposed to design and fabricate semi-transparent solar cells. At first, the device structure was modified based on the structure of a state-of-the-art opaque solar cell. Then, GenPro4 was deployed to optimize the thickness of the target i-layer to obtain desired transmittance. According to the simulation results, a sample was fabricated and measured to compare with our estimation. Conclusions were drawn at the end, along with necessary analysis and discussion.

6.2. SEMI-TRANSPARENT AMORPHOUS SILICON SOLAR CELL

6.2.1. DESIGN AND OPTIMIZATION

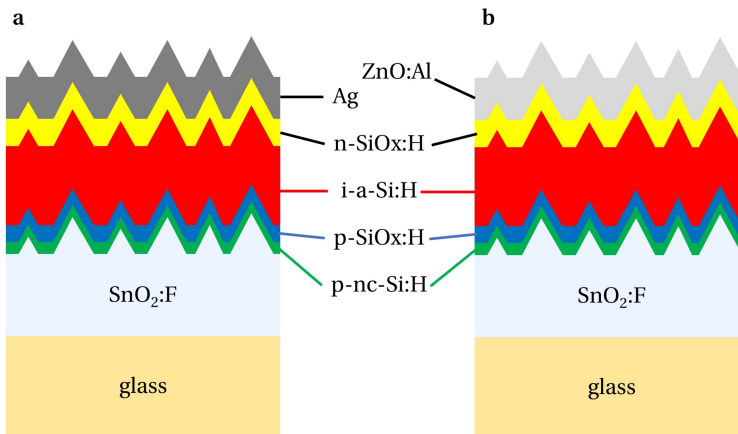


Figure 6.1: Schematic structures of single-junction a-Si:H solar cells with **a** Ag and **b** ZnO:Al as back contact, respectively. The direction of light incidence is from bottom to top.

STATE-OF-THE-ART opaque single-junction a-Si:H cells have a device structure as shown in Figure 6.1a. To obtain a semi-transparent structure, the Ag back reflector is replaced with ZnO:Al transparent conductive oxide (TCO), which enables the transmittance of un-absorbed light through the solar cell, as shown in Figure 6.1b. Since GenPro4 is a purely optical model, which does not consider the electrical characteristics of the solar cell, we assume that the open circuit voltage (V_{OC}) and the fill factor (FF) maintain typical values when we adjust the thickness of each layer within reasonable ranges. With GenPro4, the implied photocurrent can be calculated quickly as a function of the thickness of absorber layer. In this way, we can possibly estimate the conversion efficiency of the solar cell in terms of simulation variables, i.e. the thickness of crucial layers. Theoretically, the thickness of all the seven layers should be taken as input variables. However, relatively thin layers, such as p-layer and n-layer, contribute to a relatively small portion of light absorption, but have critical impact on electrical characteristics. Therefore, the thickness of p-nc-Si:H, p-SiO_x:H, and n-SiO_x:H is kept constant in the optical simulation. Meanwhile, the thickness of glass and fluorine-doped tin oxide (SnO₂:F) is determined by the nanotextured Asahi-VU substrate, and the thickness of ZnO:Al is chosen to be 300 nm, ensuring both high transmittance and sufficiently low sheet resistance. Thus, the variable layers are narrowed down to the i-layer only.

To estimate the conversion efficiency (η) of the cell, we assume that V_{OC} stays at 0.85 V, and FF at 0.7. The implied short circuit current density (J_{SC}) can be obtained from the optical simulation. Then, as the power input (P_{in}) is the standard 100 mW/cm², $\eta = J_{SC}V_{OC}FF/P_{in}$. Figure 6.2 presents the efficiency and transmittance with varying thickness of i-layer from 50 to 500 nm. As both curves reveal distinct trends, a trade-off must be made to achieve decent efficiency and satisfying transmittance, which is set at 20% for STPV applications [16]. The corresponding thickness of the i-layer is in this way determined.

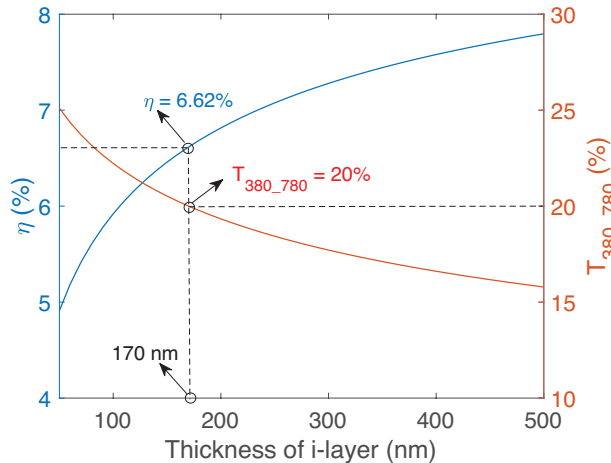


Figure 6.2: The estimated efficiency (η) and the average transmittance between 380 nm and 780 nm (T_{380_780}) of the semi-transparent a-Si:H solar cell as a function of the thickness of i-layer.

The detailed structure of semi-transparent device is shown in Table 6.2. Owing to GenPro4 model, experiments with layer thickness as variables can be avoided. Also, GenPro4 can generate the reflectance, absorptance and transmittance of each layer at different wavelength as shown in Figure 6.3. The average transmittance of the solar cell is calculated according to the transmitted spectrum in the wavelength between 380 and 780 nm. The simulation tool can also help us investigating the optical contribution of each layer for further improvement.

Table 6.1: Layers of semi-transparent solar cell with optimal thickness.

Layer	Thickness (nm)
glass	7×10^5
SnO ₂ :F	700
p-nc-Si:H	4
p-SiO _x :H	15
i-a-Si:H	170
n-SiO _x :H	30
AZO	300

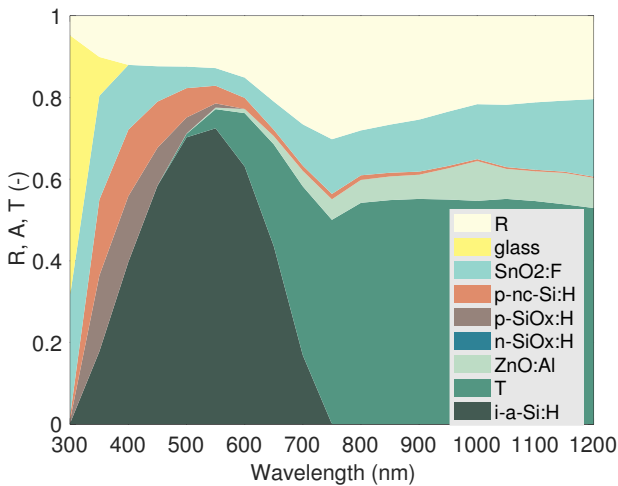


Figure 6.3: Area plot of reflectance, absorptance and transmittance of each layer at different wavelength.

6.2.2. EXPERIMENTAL PROCESS AND RESULTS

STPV cells were fabricated on Asahi-VU type substrates, which are glass coated with nano-textured SnO₂:F serving as front TCO and light-scattering surface. The solar cells use a-Si:H as the absorber and have a structure of glass/700 nm SnO₂:F /4 nm p-nc-Si:H/20 nm p-SiO_x:H/170 nm i-a-Si:H/60 nm n-SiO_x:H/300 nm ZnO:Al. The thin-film silicon alloy materials were deposited in a multi-chamber system using plasma-enhanced chem-



Figure 6.4: Semi-transparent cell sample viewed at the rear with the window as background.

ical vapor deposition (PECVD) at radio frequency (RF) of 13.56 MHz. ZnO:Al is used as the rear transparent electrode and was deposited by RF magnetron sputtering with a shadow mask, which also defines the area of the solar cells. The semi-transparent sample fabricated as above is presented in Figure 6.4, in which the rear of the cell is facing the camera with the window as background. The performance of the solar cells was examined by current-voltage (I-V) and external quantum efficiency (EQE) measurements. In specific, I-V measurement was conducted under AM1.5G solar spectrum with an irradiance of 1000 W/m^2 with a dual-lamp continuous solar simulator (WACOM WXS-90S-L2, class AAA) at a controlled sample temperature of 25°C . The sample was tested in open rear configuration (i.e. no reflective chuck). The EQE measurement was performed using an in-house system. V_{OC} and FF were determined by the I-V measurement. J_{SC} was obtained by weighting the measured EQE with the AM1.5G solar spectrum. Table 6.2 presents the measured parameters comparing with those obtained from the optical simulation. It turns out that the best measured efficiency is 0.32% higher than the simulation results due to the underestimation of J_{SC} .

Table 6.2: Solar cell parameters from simulation and measurement.

Parameters	Simulation	Measurement
V_{oc} (V)	0.85	0.83
J_{sc} (mA/cm^2)	11.13	13.24
FF	0.70	0.63
η (%)	6.62	6.94

The reflectance and transmittance of the sample are also measured with a Lambda 950 spectrophotometer. Measurement and simulation results are shown in Figure 6.5. The measured reflectance is lower than that in simulation in the range between 300 to 660 nm. On the other hand, the measured transmittance fits well with the simulation data. It means that more light is absorbed by the solar cell than expected, which could explain why J_{SC} is higher than the estimated data. This abnormal results might come from several reasons. First, the thickness of some layer(s) in the fabricated solar cell may be different from that in simulation. The different thickness leads to more absorption and less reflection. Second, there might be deviation during the measurement of reflectance and transmittance. As for the transmittance, the measurement result is 20.04%, which is close to the desired value 20%.

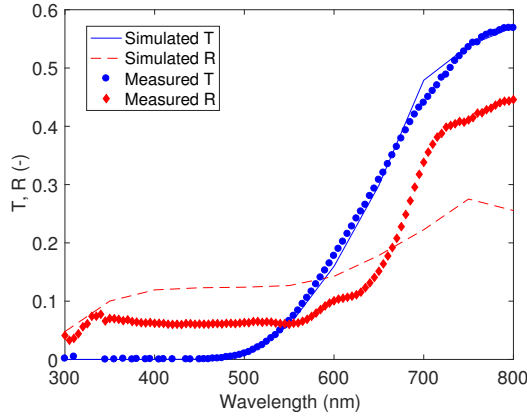


Figure 6.5: Transmittance and reflectance of the solar cell obtained by measurement and simulation.

6.3. PDLC FILM

6.3.1. WORKING PRINCIPLE

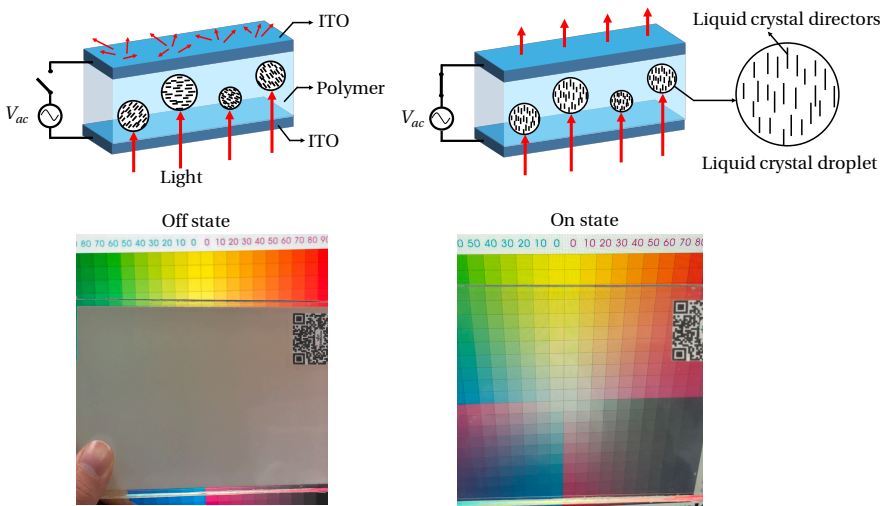


Figure 6.6: Working principle of PDLC film.

A Polymer-dispersed liquid-crystal (PDLC) film is a sandwiched structure which can switch from opaque to transparent state in a second. The liquid mix of polymer and liquid crystals is placed between two layers of glass or plastic that include a thin layer of TCO (transparent conductive oxides). The working principle is illustrated in Figure 6.6. Without applied voltage, the liquid crystal directors are randomly arranged in the droplets, resulting in scattered light (off state). Once an AC voltage is applied to the elec-

trodes, the electric field causes the directors to align, allowing light to pass through (on state). The short response time and great optical performance make PDLC a promising candidate for smart window.

A PDLC product purchased from *InnoGlass* has been used in this study. Critical parameters are listed in Table 6.3.

Table 6.3: Key parameters of PDLC film. *Haze refers to the average haze in the wavelength range of visible light. The numbers are from the product data sheet.

Parameters	Values
Size (cm ²)	10 × 10
V_{on} (V _{AC})	65
I_{on} (mA)	1.90
P (mW/cm ²)	1.24
f (Hz)	50 - 60
Haze* (off)	80
Haze* (on)	2

6.3.2. EXPERIMENTAL PERFORMANCE

To understand the optical and electrical properties of PDLC film, the spectral transmittance has been measured by applying varied AC voltage. Figure 6.7 shows that the transmittance of PDLC film is continuously tunable from 0 to 65 VAC.

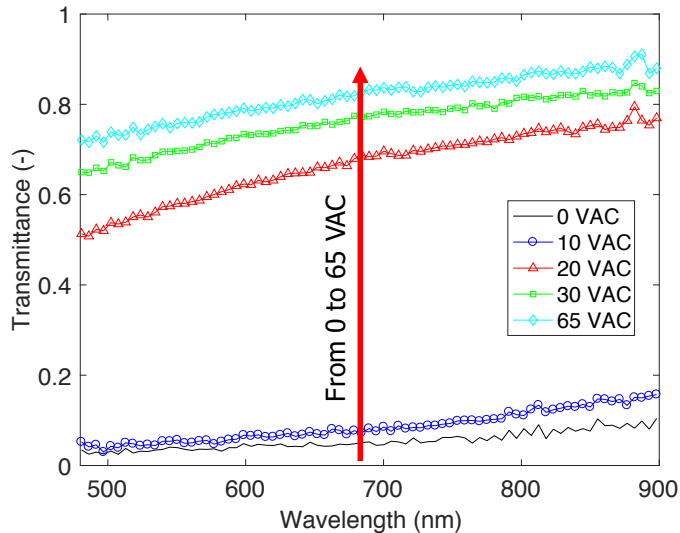


Figure 6.7: Measured spectral transmittance of PDLC film.

Theoretically several photovoltaic materials with different bandgaps can be stacked onto each other in order to fully absorb light with different wavelengths. Such tandem

cells are called multi-junction solar cells. Commonly, we build a multi-layer structure aiming to achieve an efficiency as high as possible. But in this case, part of the visible light requires passing through windows. Therefore, our design should weaken the absorption of visible wavelengths and enhance that of infrared (IR) and ultraviolet (UV) light. However, it means lower efficiency for solar cells to let considerable portion of sunlight pass through. Then the layer design becomes a trade-off between transmittance and efficiency. The minimum acceptable efficiency is determined by the basic energy demand of the PDLC films, with a power consumption around 5-12 W/m².

Let's assume that the PDLC film works 8 hours/day with a power consumption of 10 W/m². Considering the system loss of 20%, the PV source has to deliver the energy of 0.08 kWh/m². In Delft (52.01° N, 4.36° E), the annual solar irradiation is 999kWh/m², and average daily irradiation is 2.7 kWh/m² [17]. If the influence of tilt angle could be ignored, the minimum acceptable efficiency is calculated by

$$\eta = \frac{0.08kWh/m^2}{2.7kWh/m^2} = 3.0\% \tag{6.1}$$

It means that the PV film with efficiency above 3% is sufficient to power the PDLC film with the same area under above assumptions. As mentioned above, we have fabricated the semi-transparent solar cell with 6.94% efficiency, which is sufficient to power the PDLC film.

Figure 6.8 illustrates the structure of a STPV-PDLC tandem device. Figure 6.9 shows the appearance of the tandem device in off and on states.

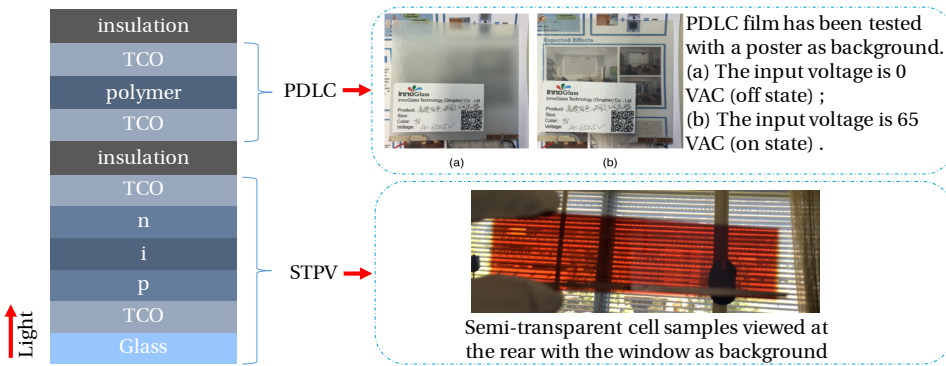


Figure 6.8: Schematic structure of a STPV-PDLC tandem device.

6.4. PROTOTYPE

To demonstrate the feasibility of the tandem structure, a prototype house model has been built. The PDLC here is powered by a battery through a mini inverter. The extra energy generated by the STPV can also supply electricity for LED lights.

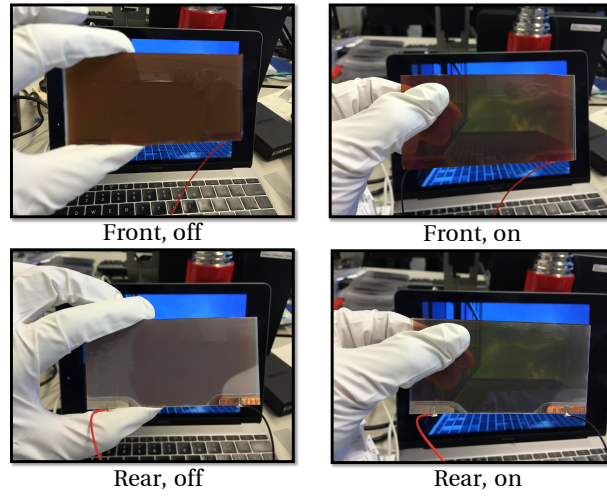


Figure 6.9: Appearance of the STPV-PDLC tandem device in off and on states in front and rear views.

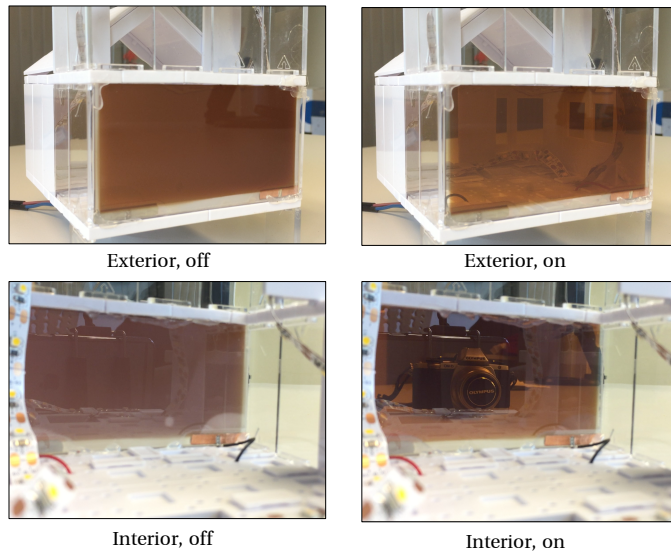


Figure 6.10: A prototype house model with the STPV-PDLC tandem device.

6.5. DISCUSSION AND CONCLUSION

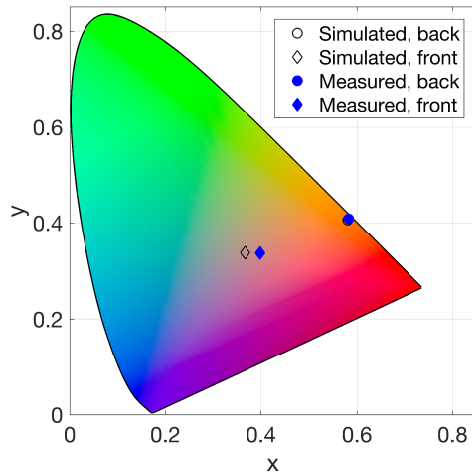


Figure 6.11: Color appearances of the semi-transparent solar cell marked in the CIE 1931 color space chromaticity diagram. Circles represent the color appearance viewed from the side of the back contact, i.e. inside the window, and diamonds represent the color appearance viewed from the side of the front glass, i.e. outside the window. Hollow markers represent simulated results, and solid markers represent measured results.

The optical model GenPro4 was applied to the optimization of STPV cells based on thin-film silicon technology. The simulation method was proven to be able to find out the optimal thickness of the variable layer according to the target transmittance of solar cells. A sample cell was fabricated accordingly and measured in experimental environment. Results show that proposed method can deliver precise estimation of transmittance. Electrical parameters are estimated by empirical data, whose accuracy cannot be ensured. The optimal semi-transparent cell sample shows competitive optoelectronic performance ($T_{380_780} = 20.04\%$, $\eta = 6.94\%$) comparing with the results in previous research. Literature review on semi-transparent solar cells reveals that it is difficult to evaluate the optoelectronic performance since various criteria were used in the results. Here we suggest that three types of transmittance should be calculated based on the transmittance spectrum, i.e. average transmittance over a certain spectral band, energy-weighted transmittance, and vision-weighted transmittance. Details on the transmittance calculations shall be discussed in the future to standardize the evaluation method of semi-transparent solar cells, which benefits both research and industrial community.

Further research on STPV can also be conducted by the proposed method. One of the critical parameters of semi-transparent solar cells is, for instance, the color appearance, which can be calculated according to the transmission and reflection spectra obtained by GenPro4 [18]. Figure 6.11 presents the color appearances of the semi-transparent solar cell viewed from both front and back sides. The xy coordinates of simulated and measured colors are marked in the CIE 1931 color space chromaticity diagram. It's obvious that the back color obtained from simulation is basically overlapped with the simulated

result, which is calculated depending on the spectral transmission yielded by GenPro4. It implies that tedious experimental process can be replaced with GenPro4 modeling by varying materials and tuning the thickness of each layer in order to obtain the desired color appearance. The simulated front color drifts from the measured one due to the deviation of spectral reflectance.

Also, optical characteristics under different light sources or acting on the angle of incidence and polarization can be simulated in GenPro4 by replacing the source files. For example, the color appearance at night can be obtained by replacing the standard solar light source files with indoor LED light source files while reversing the sequence of layers. The design process of STPV cell can therefore be dramatically accelerated by the proposed optimization method.

REFERENCES

- [1] Y. Gao, F. T. Si, O. Isabella, R. Santbergen, G. Yang, J. Dong, G. Zhang, and M. Zeman, *Performance Optimization of Semi-Transparent Thin-Film Amorphous Silicon Solar Cells*, in *2017 IEEE 44th Photovoltaic Specialist Conference (PVSC) (2017)* pp. 2605–2609.
- [2] G. Quesada, D. Rousse, Y. Dutil, M. Badache, and S. Hallé, *A comprehensive review of solar facades. Transparent and translucent solar facades*, *Renewable and Sustainable Energy Reviews* **16**, 2643 (2012).
- [3] A. Yano, M. Onoe, and J. Nakata, *Prototype semi-transparent photovoltaic modules for greenhouse roof applications*, *Biosystems Engineering* **122**, 62 (2014).
- [4] S. Yeop Myong and S. Won Jeon, *Design of esthetic color for thin-film silicon semi-transparent photovoltaic modules*, *Solar Energy Materials and Solar Cells* **143**, 442 (2015).
- [5] K.-T. Lee, L. Guo, and H. Park, *Neutral- and Multi-Colored Semitransparent Perovskite Solar Cells*, *Molecules* **21**, 475 (2016).
- [6] K.-S. Chen, J.-F. Salinas, H.-L. Yip, L. Huo, J. Hou, and A. K.-Y. Jen, *Semi-transparent polymer solar cells with 6% PCE, 25% average visible transmittance and a color rendering index close to 100 for power generating window applications*, *Energy & Environmental Science* **5**, 9551 (2012).
- [7] F.-J. Haug and C. Ballif, *Light management in thin film silicon solar cells*, *Energy Environ. Sci.* **8**, 824 (2015).
- [8] J. W. Lim, S. H. Lee, D. J. Lee, Y. J. Lee, and S. J. Yun, *Performances of amorphous silicon and silicon germanium semi-transparent solar cells*, *Thin Solid Films* **547**, 212 (2013).
- [9] J. Wook Lim, M. Shin, D. J. Lee, S. Hyun Lee, and S. Jin Yun, *Highly transparent amorphous silicon solar cells fabricated using thin absorber and high-bandgap-energy n/i-interface layers*, *Solar Energy Materials and Solar Cells* **128**, 301 (2014).

- [10] J. W. Lim, D. J. Lee, and S. J. Yun, *Semi-Transparent Amorphous Silicon Solar Cells Using a Thin p-Si Layer and a Buffer Layer*, ECS Solid State Letters **2**, Q47 (2013).
- [11] J. Y. Lee, K. T. Lee, S. Seo, and L. J. Guo, *Ultra-thin intrinsic amorphous silicon/organic hybrid structure for decorative photovoltaic applications*, 2014 IEEE 40th Photovoltaic Specialist Conference, PVSC 2014, 956 (2014).
- [12] M. Zeman, O. Isabella, S. Solntsev, and K. Jäger, *Modelling of thin-film silicon solar cells*, Solar Energy Materials and Solar Cells **119**, 94 (2013).
- [13] R. Santbergen, T. Meguro, T. Suezaki, G. Koizumi, K. Yamamoto, and M. Zeman, *GenPro4 Optical Model for Solar Cell Simulation and Its Application to Multijunction Solar Cells*, IEEE Journal of Photovoltaics **7**, 919 (2017).
- [14] R. Santbergen and R. J. C. van Zolingen, *The absorption factor of crystalline silicon PV cells: A numerical and experimental study*, Solar Energy Materials and Solar Cells **92**, 432 (2008).
- [15] A. Ingenito, O. Isabella, S. Solntsev, and M. Zeman, *Accurate opto-electrical modeling of multi-crystalline silicon wafer-based solar cells*, Solar Energy Materials and Solar Cells **123**, 17 (2014).
- [16] C. Y. Tsai and C. Y. Tsai, *Development of tandem amorphous/microcrystalline silicon thin-film large-area see-through color solar panels with reflective layer and 4-step laser scribing for building-integrated photovoltaic applications*, Journal of Nanomaterials **2014** (2014), 10.1155/2014/809261.
- [17] A. Smets, K. Jäger, O. Isabella, R. van Swaaij, and M. Zeman, *Solar Energy: The Physics and Engineering of Photovoltaic Conversion, Technologies and Systems* (UIT Cambridge, 2016) p. 488.
- [18] R. W. G. Hunt and M. R. Pointer, *A colour-appearance transform for the CIE 1931 standard colorimetric observer*, Color Research & Application **10**, 165 (1985).

7

CONCLUSIONS AND PERSPECTIVES

7.1. ANSWER THE QUESTIONS

BY far, the five research questions proposed in Section 1.4 have been answered in Chapter 2 – 6. Concise answers are listed as follows.

1. How to generate electricity in the window area of buildings by integrating photovoltaic applications?
A: Two solutions have been proposed and investigated within this dissertation, (1) integrating opaque PV solar cells with window shading elements (e.g. one-axis PV blinds), and (2) attaching semi-transparent photovoltaic solar film to the window glass (Chapter 1).
2. What is the optimal sun-tracking position for the interior PV shading elements to achieve the maximum power generation and non-glare daylighting, and what is the optimal layout of solar cells on the slat of PV blinds?
A: Regarding one-axis PV blinds, the optimum sun-tracking position is given by $\theta_y = 2 \arctan(z_s/x_s)$; and the optimal layout of solar cells is illustrated in Figure 2.9d (Chapter 2). As to PV windows with three-DOF shading elements, the optimum sun-tracking position has been described by Eq. (3.38) and (3.39); and there is no limitation to the cell layout (Chapter 3).
3. How to balance the overall annual energy performance of buildings integrated with PV blinds in terms of PV power generation, artificial lighting, heating and cooling?
A: By using the sun-tracking methods in the aforementioned answer, the optimal overall energy performance can be achieved compared to the counterparts (Chapter 4).
4. How is the PV performance across the full range of rotation angles in the greenhouses with high-density and low-density PV layouts, and how is the corresponding interior irradiance distribution?

A: Across the full range of rotation angles of the PV panels attached to the Dutch greenhouse (Figure 5.4), four special positions (Figure 5.13) have been found. Apparently, open position results in the minimum power generation and the maximum interior solar irradiance. No-shading sun tracking can achieve the highest annual energy generation in high-density PV greenhouses; and conventional (quasi-perpendicular) sun tracking leads to the highest annual energy generation in low-density PV greenhouses. The closed position usually results in the highest irradiance uniformity, but the lowest global irradiance (Chapter 5).

5. How to fabricate semi-transparent thin-film amorphous silicon (a-Si) solar cell, and how to control the transmittance of the semi-transparent PV window?

A: By replacing the metal back contact with TCO (transparent conductive oxides) and reducing the thickness of i-layer, a semi-transparent a-Si solar cell is fabricated. The transmittance of the semi-transparent PV window can be controlled by an attached PDLC film (Chapter 6).

7.2. CONCLUSIONS

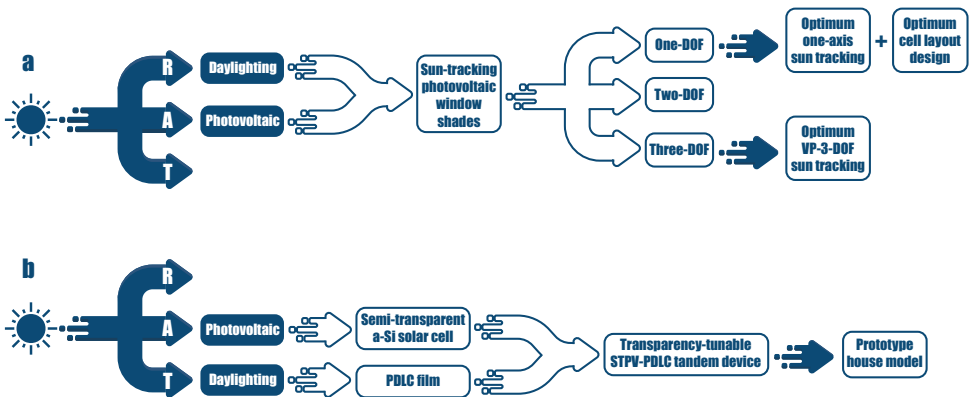


Figure 7.1: Two types of PV windows: **a**, window shading elements integrated with opaque solar cells, and **b**, window glass integrated with semi-transparent solar cells (Here R, A, and T represents the reflection, absorption, and transmission of the sunlight at the PV-attached surface).

PHOTOVOLTAIC windows have to be capable to allow sunlight to partially enter the building, otherwise windows become walls. That is the main difference between photovoltaic windows and photovoltaic façades. In this dissertation, two types of PV windows have been discussed: window shading elements integrated with opaque solar cells, and window glass integrated with semi-transparent solar cells. One of the main differences between the two types of PV windows is how they contribute to the daylighting of the interior environment, as shown in Figure 7.1. Regarding the first type, i.e., opaque PV shading elements, indoor daylighting mainly comes from the diffused sunlight reflected from the PV shading elements, since the optimum sun tracking aims to avoid direct sunlight, which might cause glare (Figure 7.1a). In contrast, semi-transparent PV windows enable indoor daylighting by transmitted sunlight through semi-transparent

solar cells, which could be regulated by PDLC films (Figure 7.1b).

According to the degree of freedom (DOF), mechanical structures of PV shading elements fall into three categories: one-DOF, two-DOF, and three-DOF (Figure 7.1a). In this dissertation, the one-DOF PV shading elements, i.e. PV blinds, have been proven to be capable to achieve the maximum power generation and non-glare daylighting by the optimum sun-tracking method and particular design of cell layout. Compared to conventional conventional quasi-perpendicular sun tracking, the proposed one-DOF sun-tracking method improves the annual energy generation by 12.00% and the annual average efficiency by 8.52% (Chapter 2). This sun-tracking method can also result in the best building energy performance of a typical office room, considering the PV electricity generation, artificial lighting consumption, and heating and cooling consumption (Chapter 4). Similar sun-tracking methods can be applied to the one-DOF PV modules installed on the pitched roof of a glass greenhouse. Compared to conventional (quasi-perpendicular) sun-tracking method, the proposed no-shading sun tracking generate 6.91% more electricity under the high-density PV layout (HDPV 1). Meanwhile, annual average global irradiance and uniformity are improved by 10.96% and 10.68% respectively compared to the fixed PV panels in the closed position (Chapter 5).

PV shading elements with two DOFs have been mathematically proven to be not able to gain either maximum power generation or non-glare daylighting under the strict assumptions. With one additional DOF, we have derived the optimum rotation angles of the variable-pivot-three-degree-of-freedom (VP-3-DOF) sun-tracking elements and demonstrate that the optimum VP-3-DOF sun tracking can achieve the aforementioned goals. Compared to conventional perpendicular sun tracking, the optimum VP-3-DOF sun tracking improves the annual electricity generation and average module efficiency by 27.40% and 19.17% respectively. In contrast with one-DOF PV blinds, VP-3-DOF sun tracking requires less PV materials, but more sophisticated mechanical structures (Chapter 3).

For the second type of PV windows (Figure 7.1b), in this dissertation we focus on the design and fabrication of semi-transparent thin-film amorphous silicon solar cells. Using an optical model, GenPro4, we provide with a simulation method to optimize the configuration of such solar cells. The optimized thickness of the absorber layer is obtained at 170 nm to realize a target average transmittance of 20% in the visible range of the sunlight spectrum. Measurement results show that an average transmittance of 20.04% has been achieved with the conversion efficiency of 6.94%. The transmittance of the PV window can be further controlled by additionally attaching a polymer dispersed liquid crystal (PDLC) film. The prototype of a house model has been built to demonstrate the feasibility of the tandem concept (Chapter 6).

7.3. PERSPECTIVES

THE nature of PV windows is to turn the undesirable part of sunlight into useful electricity energy. Two main challenges are how to define “undesirable” and how to fabricate cost-effective solar cells. In this dissertation, we mainly focus on improving the power conversion efficiency of PV window while considering other variables, such as building energy, human factors in lighting, etc. Further attention shall be paid to the following aspects.

1. **Mechanical structure and control system.** The sun tracking of PV shading elements is driven by motors and transmission devices. With respect to one-DOF PV blinds, commercial window blinds can provide sufficient examples of mechanical design. However, three-DOF window shading elements have been rarely found due to the sophisticated mechanical structure. Further development of three-DOF rotation device is necessary for the application of VP-3-DOF sun tracking. Meanwhile, the power consumption of the motor is critical for commercial products, but has been ignored in the theoretical calculation in this dissertation. As the cost of light sensors decreases, interior irradiance sensors and exterior illuminance sensors can be included in the closed-loop control system to track the solar direction and regulate the incident daylight.
2. **Electrical and optical performance.** High-quality and low-cost solar cells are critical to semi-transparent PV windows. Here, “high-quality” refers to high power conversion efficiency (PCE), reasonable transmittance, and desirable color rendering index (CRI). To gain high quality and low cost, other promising PV materials besides silicon should be investigated, such as organic photovoltaic (OPV), perovskite, etc. For a certain configuration of solar cell, increasing the PCE would probably decrease the transmittance. How to balance the PCE and transmittance of PV windows for optimal overall energy performance would be an important topic.
3. **Electrochromic materials and devices.** Current PDLC products aim at high-end market due to the high prices. Existing electrochromic materials and devices are not ready for large-scale application because of many factors, such as performance, cost, market, etc. In the future, low-cost and low-power electrochromic materials and products need to be developed. For cheaper devices, low-cost transparent conductive layers shall be used to replace the expensive ITO, e.g. Ag nanowire.
4. **Bi-facial effects of semi-transparent solar cells and modules.** Semi-transparent solar cells are naturally bi-facial solar cells, which require different test methods from conventional opaque solar cells. The measurement of semi-transparent solar cells should be standardized in both academic and industrial communities. In real applications, how to evaluate the electricity production of semi-transparent solar cells considering the incident light from both sides should be addressed.

Based on the conclusions of this dissertation, suggestions are made for architects who work on photovoltaic-related building design or reconstruction. First and foremost, photovoltaics disfavor shadows, which imply less solar radiation and greater possibilities of current-mismatching problems. For planned buildings, the location and orientation shall be chosen carefully so that shading from surrounding buildings and plants is minimum. The sunward façade can be designed to appear a tilt angle if possible in order to increase the solar irradiation. Irregular geometrical shell shall be carefully designed to avoid internal shading. In respect to existing buildings, shading evaluation shall be carried out before PV design and installation. Space between PV modules shall be fully considered to avoid shading.

The orientation of the PV module determines the amount of solar irradiance on it,

and consequently affects its electrical performance, especially the current. When PV modules are connected in series, the circuit current is limited by the lowest one. This current mismatching problem shall be considered for those PV applications on complex geometrical façade and curved roofs, or those with advanced sun-tracking algorithms. Besides orientation, different color appearances of PV modules could also lead to current mismatching. As mentioned in Chapter 1, PV manufactures nowadays can provide with colorful and even white PV products for BIPV applications. When PV modules with different colors are mixedly mounted on the same façade, they will most likely deliver different current. Therefore, electrical circuit design shall be considered besides aesthetic appearance.

PV windows are not limited to building applications. Theoretically, any occasion that requires light transmittance and power supply is the potential carrier. For example, electric vehicles, aircrafts, billboards, and even mobile phones (Figure 7.2). Applications of PV windows could be beyond imagination.



Figure 7.2: Possible applications of photovoltaic windows.

NOMENCLATURE

ABBREVIATIONS

PV	Photovoltaic
PCE	Power conversion efficiency
LCOE	Levelized cost of electricity
c-Si	Crystalline silicon
GaAs	Gallium arsenide
a-Si	Amorphous silicon
CdTe	Cadmium telluride
CIGS	Copper indium gallium (di)selenide
QD	Quantum dot
IEA	International Energy Agency
BIPV	Building-integrated photovoltaic
ZEB	Zero energy building
EHA	Equivalent horizontal area
DOF	Degree of freedom
VP-3-DOF	Variable-pivot-three-DOF
DSF	Double skin façade
FEM _{4-node}	Four-node-based finite element model
FEM _{9-node}	Nine-node-based finite element model
DNI	Direct normal irradiance
UGR	Unified glare rating
DGP	Discomfort glare probability
DC	Direct-current
AC	Alternating-current
ASE	Adaptive solar envelope
STPV	Semi-transparent photovoltaic
3D	Three-dimensional
CAD	Computer-aided design
WWR	Window-to-wall ratio
GHG	Greenhouse-gas
LER	Land Equivalent Ratio
STICS	Simulateur mulTIdisciplinaire pour les Cultures Standard
HD	High density
LD	Low density
HDPV	High-density photovoltaic
LDPV	Low-density photovoltaic

PDLC	Polymer dispersed liquid crystal
TBC	Transparent back contact
OBC	Opaque back contact
TCO	Transparent conductive oxide
HB	High-bandgap
PECVD	Plasma-enhanced chemical vapor deposition
RF	Radio frequency
I-V	Current-voltage
EQE	External quantum efficiency
IR	Infrared
UV	Ultraviolet
OPV	Organic photovoltaic

NOTATIONS

Notations for Chapter 1	
$R_{v/h}$	Ratio of the annual solar energy received on the sunward (e.g. equator-facing for temperate zones) vertical unit area to that received on the horizontal unit area
$G_{v,global}$	Global irradiance on a vertical plane
$G_{h,global}$	Global irradiance on a horizontal plane

Notations for Chapter 2	
$G_{v,global}$	Global irradiance on a vertical plane
$G_{h,global}$	Global irradiance on a horizontal plane
$G_{t,global}$	Global irradiance on a tilt plane
I_e^{dir}	Direct normal irradiance (DNI)
γ	Angle between the PV surface normal and the incident direction of the sunlight
$G_{h,d}$	Diffuse irradiance on a horizontal plane
R_d	Diffuse transposition factor
$G_{t,ground}$	Ground-reflected irradiance on a tilt plane
$G_{t,beam}$	Direct irradiance on a tilt plane
$G_{t,d}$	Diffuse irradiance on a tilt plane
P_{in}	Input power of PV modules
S_b	Direct-beam-illuminated PV area
S_{b0}	Direct-beam-illuminated PV area on the individual shading element
S_b^i	Direct-beam-illuminated PV area on the individual solar cell
η_m	Efficiency of a PV module
P_{out}	Output power of PV modules
E	Energy generated by PV modules
t	Time
w	Width of the PV window

l	Length of the PV window
α_s	Solar altitude
A_s	Solar azimuth
\mathbf{n}_s	Unit vector (x_s, y_s, z_s) indicating the solar position in Cartesian coordinate system
α_{PV}	Altitude of the normal of the PV surface
A_{PV}	Azimuth of the normal of the PV surface
\mathbf{n}_{PV}	Orientation of the rotated PV surface in the Cartesian coordinate system, i.e. (x_n, y_n, z_n)
\mathbf{n}_{PV0}	Initial orientation of the PV surface in the Cartesian coordinate system, i.e. $(1, 0, 0)$
\mathbf{R}	Rotation matrix
S_{PV}	Total area of PV surface
S_{PV}^i	Area of PV surface on the individual solar cell
l_0	Vertical length of an individual shading element
l_{ts1}	Length of the triangular shadow on the PV slat
l_{ts2}	Length of the triangular shadow on the PV slat
I	Current of the equivalent circuit of solar cell
I_{ph}	Light-induced current
I_{o1}	Reverse saturation current of diode 1
I_{o2}	Reverse saturation current of diode 2
V	Voltage across the solar cell electrical ports
$V_{T1,2}$	thermal voltage of the PV module having N_s cells connected in series
N_s	Number of solar cells connected in series
R_s	Series resistance
R_p	Parallel resistance
a_1	Quality factors (or emission coefficients) of diode 1
a_2	Quality factors (or emission coefficients) of diode 2
k	Boltzmann constant, i.e. $1.3807 \times 10^{-23} J/K$
q	Electron charge, i.e. $1.6022 \times 10^{-19} C$
T	Temperature of the p-n junction
$L_{s,t}$	Luminance in the direction connecting the observer with each source
L_b	Background luminance
$\omega_{s,t}$	Solid angle subtending the source from the position of the observer
P_i	Guth position index, expressing the dependence of perceived discomfort glare on the position of the source i with respect to the observer
E_v	Vertical eye illuminance
$G_{t,global}^{eq}$	Equivalent global irradiance of partially shaded PV panel
$\mathbf{R}_y(\theta_y)$	Rotation matrix for the rotation around y -axis by the angle of θ_y
O	Origin of the Cartesian coordinates, i.e. $(0, 0, 0)$
E_a	Annual energy generation
$\bar{\eta}_m$	Annual average efficiency of the PV module
R_{w/l_0}	Ratio of the width (w) to the side length (l_0) of the slat
l_{tri}	Side length of the triangular shadow caused by walls and window frames
w'	Width of the extended horizontal slats

Notations for Chapter 3	
$\mathbf{R}_y(\theta_y)$	Rotation matrix for the rotation around y -axis by the angle of θ_y
$\mathbf{R}_z(\theta_z)$	Rotation matrix for the rotation around z -axis by the angle of θ_z
$\mathbf{R}_n(\theta_n)$	Rotation matrix for the rotation around \mathbf{n}_{PV} by the angle of θ_n
$G_{t,global}$	Global irradiance on a tilt plane
I_e^{dir}	Direct normal irradiance (DNI)
\mathbf{n}_{PV}	Orientation of the rotated PV surface in the Cartesian coordinate system, i.e. (x_n, y_n, z_n)
\mathbf{n}_{PV0}	Initial orientation of the PV surface in the Cartesian coordinate system, i.e. $(1, 0, 0)$
$G_{h,d}$	Diffuse irradiance on a horizontal plane
S_b	Direct-beam-illuminated PV area
S_{b0}	Direct-beam-illuminated PV area on the individual shading element
l_0	Vertical length of an individual shading element
w_0	Horizontal length of individual shading element, equal to l_0 in the case of a square shading element
n_l	Number of horizontal rows of square shading elements
n_w	Number of vertical columns of square shading elements
Q_{ij}	Square with the number of ij
O	Centre of the square; origin of the Cartesian coordinates, i.e. $(0, 0, 0)$
O_{ij}	Centre of Q_{ij}
O_{sij}	Imaginary shadow point of O_{ij} on the surface of the target square casted by the sunlight in the original Cartesian coordinates $Oxyz$, i.e. $(x_{O_{sij}}, y_{O_{sij}}, z_{O_{sij}})$
$Q_{Aij}, Q_{Bij}, Q_{Cij}$	Four corners of Q_{ij}
Q_{Dij}	Target square
Q_{00}	Target square
$\mathbf{R}_{zy,C-C'}(\theta_z, \theta_y)$	Rotation matrix from the original Cartesian coordinates $Oxyz$ to the new Cartesian coordinates $Ox'y'z'$ for the two DOFs
O'_{ij}	Transformed O_{ij} in the new Cartesian coordinates, i.e. $(x'_{O_{ij}}, y'_{O_{ij}}, z'_{O_{ij}})$
O'_{sij}	Transformed O_{sij} in the new Cartesian coordinates, i.e. $(x'_{O_{sij}}, y'_{O_{sij}}, z'_{O_{sij}})$
\mathbb{T}_{sur}^{k1}	A set defined in 3.5
\mathbb{T}_{sqsh}	Union of the total \mathbb{T}_{sur}^{k1}
Q_{rec}	Rectangle $Q_A Q_B Q_C Q_D$, denoted as $(y'_{qA}, z'_{qA}, y'_{qC}, z'_{qC})$
$k1$	Number of \mathbb{T}_{sur}^{k1}
$k2$	Number of the elements in \mathbb{T}_{sqsh}
k_{temp}	A temporary variable
$k3$	Number of rectangles
S_{PV0}	PV area on an individual shading element
S_{sh0}	Shading area on an individual shading element

\mathbb{T}_{recsh}	A set of k_2 rectangular shadows on the target square
$\mathbf{R}_{nzy, C-C'}(\theta_n, \theta_z, \theta_y)$	Rotation matrix from the original Cartesian coordinates $Oxyz$ to the new Cartesian coordinates $Ox'y'z'$ for the three DOFs
d	Distance from a point to a line
$\mathbf{R}_x(\theta_x)$	Rotation matrix for the rotation around x -axis by the angle of θ_x
k_x	Integer parameter for the periodic solutions of θ_x
$\mathbf{R}_{yzn}(\theta_y, \theta_z, \theta_n)$	Rotation matrix for three-phase rotations around y -axis, z -axis, and \mathbf{n}_{PV} by the angle $\theta_y, \theta_z,$ and θ_n respectively.

Notations for Chapter 4	
w	Width of the PV slat
l	Length of the PV slat
θ	Tilt angle
I	Current of the equivalent circuit of solar cell
V	Voltage across the solar cell electrical ports
I_{light}	Light-generated current
I_d	Diode saturation current
R_s	Series resistance
R_{sh}	Shunt resistance
A	Modified ideality factor
n_d	Diode ideality factor
k	Boltzmann constant, i.e. $1.3807 \times 10^{-23} J/K$
q	Electron charge, i.e. $1.6022 \times 10^{-19} C$
T_c	Cell temperature
G_{global}	Global irradiance on the non-shading PV module
I_e^{dir}	Direct normal irradiance (DNI)
α_s	Solar altitude
A_s	Solar azimuth
$G_{h,d}$	Diffuse horizontal irradiance
G_{global}^{eq}	Equivalent global irradiance on a partial shading solar cell
S_{cell}	Area of an individual solar cell
S_{shadow}^{cell}	Area of the shadow on an individual solar cell
T_a	Ambient temperature
\bar{G}_{sta}	Standard average illuminance on the target working plane (0.75 m height)
\bar{G}_{sun}	Average illuminance contributed by the daylighting on the target working plane (0.75 m height)
$P_l(t)$	Power consumption of artificial lighting at a certain time point
P_{sta}	Standard power consumption of artificial lighting
$\mathbb{P}_l(t)$	Probability of lighting demand at a certain point of time

Notations for Chapter 5

λ_{GH}	Longitude of the greenhouse
ϕ_{GH}	Latitude of the greenhouse
A_{GH}	Azimuth of the greenhouse
l_{GH}	Length of the greenhouse
h_{GH}	Height of the greenhouse
w_r	Roof width
α_r	Roof inclination
w_{GH}	Width of the greenhouse
h_r	Roof height
α_s	Solar altitude
A_s	Solar azimuth
α_M	Altitude of the normal of the PV module
A_M	Azimuth of the normal of the PV module
α_{M0}	Altitude of the normal of the PV module in the closed state
G_{global}	Global irradiance on the PV module
I_e^{dir}	Direct normal irradiance (DNI)
$G_{h,d}$	Diffuse horizontal irradiance
γ	Angle between the incident direction of the sunlight and the normal of the PV module
\mathbf{n}_M	Unit vector (x_M, y_M, z_M) , indicating the position of the PV module in the Cartesian coordinates $Oxyz$
ΔA	Difference between the azimuth of the PV module and the solar azimuth
\mathbf{n}_s	Unit vector (x_s, y_s, z_s) , indicating the solar position in the Cartesian coordinates $Oxyz$
S_{shadow}	Shading area on the PV module
l_M	Length of the PV module
w_M	Width of the PV module
P_{in}	Input power on the PV module from the Sun
G_{module}^{eq}	Equivalent irradiance on the whole area of the PV module
G_{cell}^{eq}	Equivalent irradiance on the individual solar cell
S_{cell}	Area of the individual solar cell
S_{shadow}^{cell}	Shading area on the individual solar cell
η	Conversion efficiency of the PV module
O	Origin of the Cartesian coordinates $Oxyz$, i.e. $(0, 0, 0)$
O_1	Point in the rotation axis of one of the PV modules in the Cartesian coordinates $Oxyz$
Q_1	Point on the PV module in the Cartesian coordinates $Oxyz$, i.e. (x_{q1}, y_{q1}, z_{q1})
Q_{1s}	Shadow of Q_1 on the PV module in the Cartesian coordinates $Oxyz$, i.e. $(x_{q1s}, y_{q1s}, z_{q1s})$
$\mathbf{R}_{C-C'}(\alpha_M)$	Rotation matrix, enabling the rotation of α_M around the y -axis from the original Cartesian coordinates $Oxyz$ to the new Cartesian coordinates $Ox'y'z'$

\mathbf{n}'_M	Unit vector (x'_M, y'_M, z'_M) , indicating the position of the PV module in the new Cartesian coordinates $Ox'yz'$
\mathbf{n}'_s	Unit vector (x'_s, y'_s, z'_s) , indicating the solar position in the new Cartesian coordinates $Ox'yz'$
Q'_1	Point on the PV module in the new Cartesian coordinates $Ox'yz'$, i.e. $(x'_{q1}, y'_{q1}, z'_{q1})$
Q'_{1s}	Shadow of Q'_1 on the PV module in the new Cartesian coordinates $Ox'yz'$, i.e. $(x'_{q1s}, y'_{q1s}, z'_{q1s})$
λ_1	An arbitrary real number
α_p	Altitude of the normal of the PV module in the quasi-perpendicular position
I	Current of the equivalent circuit of single diode model
V	Voltage of the equivalent circuit of single diode model
I_L	Light-generated current
I_0	Diode saturation current
A	Modified ideality factor
n_d	Diode ideality factor
k	Boltzmann constant, i.e. $1.3807 \times 10^{-23} J/K$
q	Electron charge, i.e. $1.6022 \times 10^{-19} C$
T	Cell temperature
R_s	Series resistance
R_{sh}	Shunt resistance
T_a	Ambient temperature
v_{wind}	Wind speed
V_{OC}	Open circuit voltage
I_{SC}	Short circuit current
\mathbf{G}_{mat}	Matrix of global irradiance at a grid of points on the target plane
G_{ij}	Global irradiance of the corresponding point (i, j) on the grid of the target plane
G_{global}^{min}	Minimum value of the global irradiance on the target plane
\bar{G}_{global}	Average global irradiance on the target plane in the PV greenhouse
U_G	Uniformity of global irradiance on the target plane in the PV greenhouse
\bar{U}_G	Annual average uniformity of global irradiance on the target plane in the PV greenhouse

Notations for Chapter 6

V_{OC}	Open circuit voltage
FF	Fill factor
η	Power conversion efficiency
J_{SC}	Short circuit current density
P_{in}	Input power

APPENDIX B

Pseudocode algorithms for Chapter 3.

Algorithm 1 Find squares contributing to the shadows on the target square by f_{sqsh}

```
1: function  $f_{sqsh}(Q_{ij})$ 
2:   for  $k_1 = 1, 2, 3, \dots$  do
3:     for all  $Q_{ij} \in \mathbb{T}_{sur}^{k_1}$  do
4:       if  $(|y'_{sOij}| < l_0) \& (|z'_{sOij}| < l_0) \& (x'_{Oij} > 0)$  then
5:          $Q_{ij} \in \mathbb{T}_{sqsh}^{k_1}$ 
6:       else
7:          $Q_{ij} \notin \mathbb{T}_{sqsh}^{k_1}$ 
8:       end if
9:     end for
10:    if  $\mathbb{T}_{sqsh}^{k_1} = \emptyset$  then
11:      End Loop  $k_1$ 
12:       $k_1 \leftarrow k_1 - 1$ 
13:    else
14:      Continue Loop  $k_1$ 
15:    end if
16:  end for
17:   $\mathbb{T}_{sqsh} \leftarrow \mathbb{T}_{sqsh}^1 \cup \mathbb{T}_{sqsh}^2 \cup \dots \cup \mathbb{T}_{sqsh}^{k_1}$ 
18:   $k_2 \leftarrow \#\mathbb{T}_{sqsh}$ 
19:  return  $\mathbb{T}_{sqsh}$  and  $k_2$ 
20: end function
```

Algorithm 2 Find the overlapped rectangle of k_3 rectangles by $f_{ov}^{k_3}$

```

1: function  $f_{ov}^2(Q_{rec1}, Q_{rec2})$ 
2:    $Q_{rec0} \leftarrow (0, 0, 0, 0)$ 
3:   if  $(y'_{qA1} < y'_{qC1}) \& (y'_{qA2} < y'_{qC1}) \& (z'_{qA1} < z'_{qC1}) \& (z'_{qA2} < z'_{qC1})$  then
4:     if  $y'_{qA1} \geq y'_{qA2}$  then
5:        $y'_{qA3} \leftarrow y'_{qA1}$ 
6:     else
7:        $y'_{qA3} \leftarrow y'_{qA2}$ 
8:     end if
9:     if  $y'_{qC1} \leq y'_{qC2}$  then
10:       $y'_{qC3} \leftarrow y'_{qC1}$ 
11:    else
12:       $y'_{qC3} \leftarrow y'_{qC2}$ 
13:    end if
14:    if  $z'_{qA1} \geq z'_{qA2}$  then
15:       $z'_{qA3} \leftarrow z'_{qA1}$ 
16:    else
17:       $z'_{qA3} \leftarrow z'_{qA2}$ 
18:    end if
19:    if  $z'_{qC1} \leq z'_{qC2}$  then
20:       $z'_{qC3} \leftarrow z'_{qC1}$ 
21:    else
22:       $z'_{qC3} \leftarrow z'_{qC2}$ 
23:    end if
24:     $Q_{rec3} \leftarrow (y'_{qA3}, z'_{qA3}, y'_{qC3}, z'_{qC3})$ 
25:  else
26:     $Q_{rec3} \leftarrow Q_{rec0}$ 
27:  end if
28:  return  $Q_{rec3}$ 
29: end function
30:
31: function  $f_{ov}^{k_3}(Q_{rec1}, \dots, Q_{rec k_3})$ 
32:    $Q_{rec12} \leftarrow f_{ov}^2(Q_{rec1}, Q_{rec2})$ 
33:    $Q_{rec123} \leftarrow f_{ov}^2(Q_{rec12}, Q_{rec3})$ 
34:   ...
35:    $Q_{rec1\dots k_3} \leftarrow f_{ov}^2(Q_{rec1\dots(k_3-1)}, Q_{rec k_3})$ 
36:  return  $Q_{rec1\dots k_3}$ 
37: end function

```

Algorithm 3 Calculate the area of a rectangle by f_s

```

1: function  $f_s(Q_{rec}(y'_{qA}, z'_{qA}, y'_{qC}, z'_{qC}))$ 
2:    $S \leftarrow (y'_{qC} - y'_{qA})(z'_{qC} - z'_{qA})$ 
3: return  $S$ 
4: end function

```

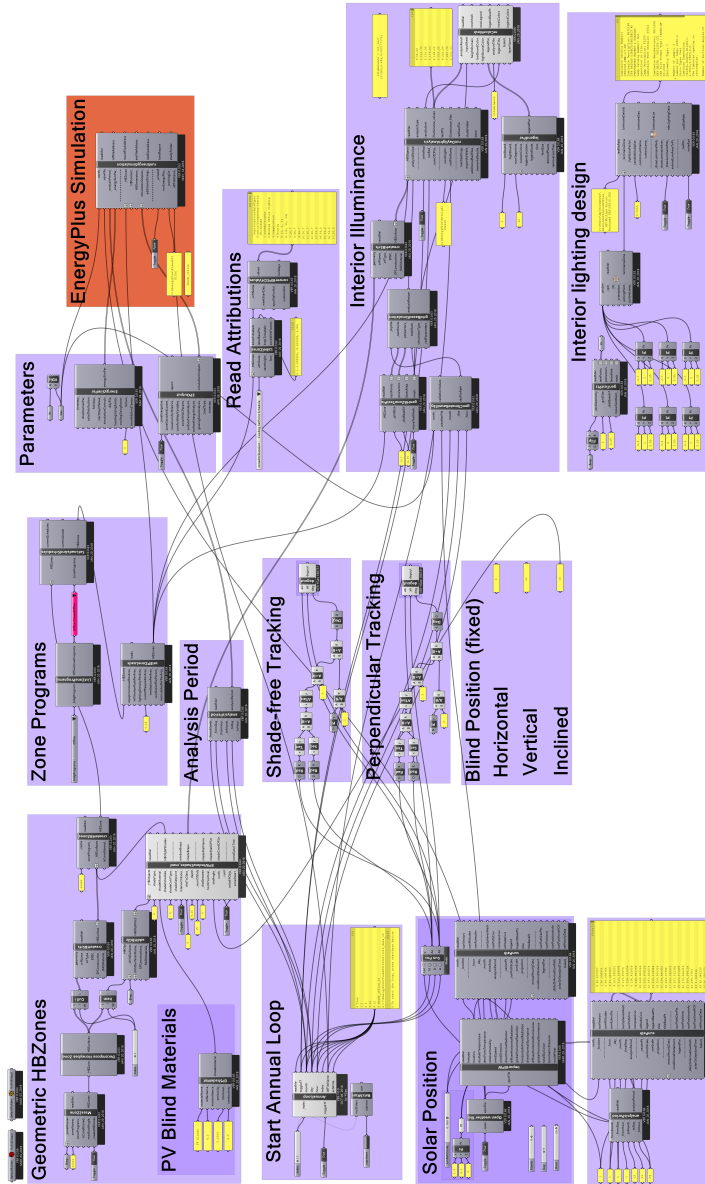
Algorithm 4 Calculate the total area of shadows on the target square

```

1: if  $n'_s \cdot n'_{pV} \leq 0$  then
2:    $S_{sh0} \leftarrow S_{pV0}$ 
3: else
4:   Find  $k_2$  squares (as a set of  $\mathbb{T}_{sqsh}$ ) contributing to the shadows on the target square
   by  $f_{sqsh}$ 
5:   Find  $k_2$  rectangular shadows on the target square by  $f_{ov}^2$  and denote as a set of
    $\mathbb{T}_{recsh}$ 
6:   Find calculate the area of  $k_2$  rectangular shadows on the target square by  $f_s$ ,  $S_{k2} \leftarrow$ 
    $S_{rec1} + \dots + S_{reck2}$ 
7:   Find  $C_{k2}^2$  overlapped rectangles from  $\mathbb{T}_{recsh}$  by  $f_{ov}^2$  and calculate the sum of their
   area  $S_{C_{k2}^2} \leftarrow S_{rec1rec2} + \dots + S_{rec1reck2}$ 
8:   Find  $C_{k2}^3$  overlapped rectangles from  $\mathbb{T}_{recsh}$  by  $f_{ov}^3$  and calculate the sum of their
   area  $S_{C_{k2}^3} \leftarrow S_{rec1rec2rec3} + \dots + S_{rec1rec2reck2}$ 
9:   ...
10:  Find  $C_{k2}^{k2}$ , i.e., 1 overlapped rectangle from  $\mathbb{T}_{recsh}$  by  $f_{ov}^{k2}$  and calculate its area
    $S_{C_{k2}^{k2}} \leftarrow S_{rec1\dots reck2}$ 
11:  Calculate the total area of shadows on the target square  $S_{sh0} \leftarrow S_{k2} - S_{C_{k2}^2} + S_{C_{k2}^3} -$ 
    $S_{C_{k2}^4} + \dots$ 
12: end if
13: return  $S_{sh0}$ 

```

APPENDIX C



SUMMARY

Human beings consume enormous amounts of energy worldwide. More than a third of global energy consumption is attributable to the building sector. As a renewable and clean energy source, photovoltaic (PV) solar power generation is envisioned as one of the most promising solutions to the global energy crisis. Window-integrated PV has been predicted to become the largest part of the building-integrated PV (BIPV) market. This dissertation has contributed to the developments of building-integrated PV windows in the aspects of optimal power generation, incident irradiance and illuminance.

This dissertation is structured in seven distinct chapters. In **Chapter 1**, a brief introduction to solar energy, photovoltaics, and building-integrated PV windows in general is given. This chapter leads the following Chapters 2-6, each containing an independent research topic.

In **Chapter 2**, a mathematical model of solar irradiance and a geometrical model of a reference office are built, which are also useful in Chapter 3 and 4. Additionally, one-axis PV blinds are modeled and an optimal sun-tracking angle has been found to achieve both maximum power generation and non-glare daylighting. The optimal design of cell layout is also proposed to avoid shading from window frames.

In **Chapter 3**, PV shading elements with extra degree of freedoms (DOF) have been modeled and analyzed in a similar way as in Chapter 2. Two-DOF PV shading elements have been proved to be the same as one-axis PV blinds with respect to optimal sun-tracking positions. PV shading elements with three-DOF sun-tracking abilities are demonstrated capable to meet all the requirements, i.e. gaining the maximum power generation, protecting from glare, and avoid shadows from the window frame. A corresponding variable-pivot three DOF (VP-3-DOF) sun-tracking algorithm is given in the form of an analytical solution.

In **Chapter 4**, the overall energy performance of the reference office with one-axis PV blinds is analyzed over an entire year. Photovoltaic power generation and power consumption by artificial lighting, heating and cooling have been fully considered.

In **Chapter 5**, PV windows are applied to the skylight in Dutch greenhouses. Unlike vertically-mounted PV windows mentioned above, the greenhouse PV panels are installed on a pitched roof to regulate the sunlight for plants, instead of humankind. PV layouts in high and low densities are evaluated under four special sun-tracking positions with regard to power generation and interior irradiance. Simulation results provide guidelines to balance the PV power generation and food production in greenhouses.

In **Chapter 6**, semi-transparent devices are fabricated to demonstrate the PV windows. The incident sunlight can be tuned with PDLC films to form self-powered photoelectrochromic devices.

Chapter 7 concludes the insights throughout the dissertation. In addition, an outlook is given on PV windows.

SAMENVATTING

De mensheid verbruikt wereldwijd enorme hoeveelheden energie. Meer dan één derde van het wereldwijde energieverbruik is toe te schrijven aan gebouwen. Fotovoltaïsche zonnestroom is een hernieuwbare en schone energiebron die wordt gezien als één van de meest veelbelovende oplossingen voor het wereldwijde energieprobleem. Men verwacht dat raam-geïntegreerde zonnestroom het grootste deel van de gebouw-geïntegreerde zonnestroommarkt zal gaan uitmaken. Dit proefschrift draagt bij aan de ontwikkeling van gebouw-geïntegreerde zonnestroomramen.

Dit proefschrift is ingedeeld in zeven hoofdstukken. Hoofdstuk 1 geeft een korte inleiding over zonne-energie en gebouw-geïntegreerde zonnestroomramen. Dit hoofdstuk is de inleiding tot de hoofdstukken 2 tot en met 6, die elk een eigen onderzoeksonderwerp beschrijven.

In hoofdstuk 2 worden een wiskundig model van zonnestraling en een geometrisch model van een kantoorgebouw ontwikkeld. Deze modellen worden ook gebruikt in hoofdstukken 3 en 4. Daarnaast worden zonnestroomjaloezieën, die draaibaar zijn om één as, gemodelleerd en geanalyseerd. Het blijkt dat de draaihoek die de stroomopwekking maximaliseert ook een maximum aan niet-verblindend daglicht binnenlaat. Verder worden de posities van de zonnecellen geoptimaliseerd om schaduwwerking van het raamkozijn te voorkomen.

In hoofdstuk 3 worden zonnestroomelementen met extra vrijheidsgraden gemodelleerd en geanalyseerd. Elementen met twee vrijheidsgraden blijken de zon even goed te volgen als zonnestroomjaloezieën die draaibaar zijn om één as. Ook worden stroomopwekkende zonweringselementen met drie vrijheidsgraden beschouwd. Deze voldoen aan alle vereisten, namelijk het maximaliseren van stroomopbrengst, het tegenhouden van verblindend zonlicht en het voorkomen van schaduwwerking van het raamkozijn. De draaihoeken voor het optimaal meebewegen met de zon zijn uitgedrukt in wiskundige formules.

In hoofdstuk 4 wordt de energiehuishouding van een kantoorgebouw met draaibare zonnestroomjaloezieën gedurende een heel jaar geanalyseerd. De fotovoltaïsche energieopwekking en het energieverbruik door verlichting, verwarming en koeling zijn meegenomen in de analyse.

Hoofdstuk 5 beschouwt zonnestroomramen toegepast in de daken van Nederlandse kassen. Deze ramen worden op het schuine dak van de kas geïnstalleerd en naast het opwekken van zonnestroom reguleren ze ook het zonlicht voor de planten in de kas. De energieopbrengst en de instraling van zonlicht in de kas zijn door middel van simulaties geëvalueerd voor zowel een lage als een hoge dichtheid van geïntegreerde zonnecellen onder vier mogelijke draaihoeken. De resultaten van de simulaties bieden richtlijnen om de energieopwekking en voedselproductie in kas tegen elkaar af te wegen.

In hoofdstuk 6 worden schaalmodellen van semitransparante zonnestroomramen

gefabriceerd die elektrisch schakelbare PDLC-films bevatten. Deze reguleren het doorgelaten zonlicht automatisch, met door het raam zelf opgewekte zonnestroom.

Hoofdstuk 7 vat de inzichten van het proefschrift samen. Daarnaast wordt een toekomstbeeld van zonnestroomramen geschetst.

ACKNOWLEDGEMENTS

THE train is approaching the terminal. Flashbacks are flooding my mind at the end of the four-year journey. It is my honor and privilege to board the *TU Delft Express*, sitting in the cabin of *solar energy*, with the opportunities to enjoy the beautiful scientific view through, of course, *a photovoltaic window*. In this journey, we have also become the beautiful view for the passengers on parallel tracks as our exciting results published. This could never happen without the full support and concerted efforts of all crew members, to whom I owe my deepest gratitude.

Prof. dr. Miro Zeman, the conductor of the train, deserves the very first of my great appreciation. My adventure started in October of 2014, when nobody can certainly tell where this PV-window project is heading and how it ends. As my promotor, Prof. dr. Miro Zeman indicated the possible direction of my study and encouraged me to go for it. Miro, thank you for being such an excellent group leader and creating the collaborative and warm PVMD family. Working with all the talented peers in this group, I can easily find everything I need to do world-class science. I still remember the night in an old-fashioned Dutch restaurant, where you gave a remarkable speech mentioning that how you started this group many years ago. Your constant passion and strong belief in building a more sustainable world inspire us to explore the photovoltaic technologies for all humankind. Thank you for extending my stay in Delft so that I can accomplish the PV-window demonstration. Thank you for supporting me to attend the IEEE Photovoltaic Specialists Conference in Washington D.C. Nearly before my graduation, you are honored as a Knight of the Order of the Dutch Lion in Delft. I feel so honored and so lucky to be one of your students. Thank you for all the help and freedom you have provided, making this journey comfortable and fulfilling.

Prof. dr. Kouchi Zhang, as my co-promotor, is the man who offered me the ticket at the very beginning of this journey. When I was applying for this PhD position, Prof. dr. Kouchi Zhang decided to have me on board immediately after receiving my CV. Kouchi, thank you for always believing in me and having faith in my abilities. It is your efforts that make this joint program happen and work. Your diligence, motivation, and extraordinary stamina impress me and urge me to become a better man. Besides working, together we go hiking, boating, and dining in your beautiful house. Thank you for enrolling me in this joint program and creating so many great memories.

My daily-supervisors, Dr. Olindo Isabella and Dr. Jianfei Dong have always been by my side, answering my questions in detail and providing prompt help. Jianfei, thank you for your innumerable long phone conversations at nights, discussing my working progress and plan. Thank you for revising my manuscripts word by word and giving valuable advice on how to publish a decent journal paper. Thank you for providing your cozy apartment and making my stay in Delft much easier. Especially thank you for letting your baby daughter be the youngest female model in my photography collection. Your sincere care and generous help benefit me in every aspect of my life. Olindo, you are

such a hard-working man that sometimes I feel like an Italian and you are a Chinese (no offense). You start working so early in the morning and reply my email no matter it is midnight or holiday. Thank you for helping me prepare the slides for the 33rd PVSEC-26 in Singapore. Those insightful discussions in that afternoon somehow lead to our subsequent publications. Thank you for revising my posters over and over again until they look perfect. Also thank you for reading through the thesis draft and giving me very detailed corrections on language and typos. To me, you are a diligent scientist, a responsible supervisor, and more than a good friend. Amazingly, we met in Nanjing two years later and had a lot of fun beyond science. I am so glad to hear that you have become the head of the PVMD group. Olindo, Jianfei, Kouchi, and Miro, thank you for all your cooperative efforts as my fancy mentoring team. Being guided by four wise men is like being raised by four caring parents, making me feel like a spoiled child in the scientific world.

I would also like to express my grateful thanks to the other committee members of my thesis defense, Prof. dr. Angèle Reinders, Prof. dr.-ing Tillmann Klein, Prof. dr. Arthur Weeber, and Prof. dr. ir. Willem van Driel. Thank you for all your comments and suggestions on my draft thesis. Your critical review has been a valuable contribution for improving the quality of this dissertation.

My study and research at Delft University of Technology cannot be accomplished without the help of other members in the Photovoltaic Materials and Devices (PVMD) Group. Prof. dr. Arno Smets, thank you for treating us with beers and snacks in the /pub, where we had the most important weekly evaluation and shared opinions on work and life. Dr. Rudi Santbergen, thank you for creating the great GenPro4 package and showing me the simulation tricks which dramatically accelerate my calculation. Thank you for helping Olindo and me present our poster in the EU PVSEC 2017 in Amsterdam. Also thank you for spending your time helping me translate the propositions and summary into Dutch. Dr. Fai Tong Si, thank you for contributing your ideas to my project and helping me fabricate a lot of samples. Dr. Guangtao Yang, Johan Blanker, and Gianluca Limodio, you three are the best office mates ever. Guangtao, you are always ready to help me out with work problems. I am so happy to be invited to party with your lovely family in Chinese and Dutch holidays. Johan, thank you for translating hundreds of Dutch letters and forecasting the uncertain Dutch weather for me. Gianluca, you are so nice to include me in every football game, in one of which China scored two historic goals vs Italy & the Netherlands. I should especially thank our technicians, Stefaan Heirman, and Martijn Tijssen. Your kind support and superb expertise finally result in a functional demonstration system. I would also like to express my gratitude to our secretary, Ilona van der Wenden, for solving my problems in regard of VISA, accommodation, reimbursement, etc. My memories of the PVMD group are incomplete without any of you, Dr. R.A.C.M.M. van Swaaij, Dr. Ravi Vasudevan, Dr. Andrea Ingenito, Paula Perez Rodriguez, Nasim Rezaei, Robin Vismara, and Yilei Tian. Besides your scientific insights, I always remember my first group meeting, the frisbee city league, the spikeball o'clock, and the special pool night. Thank you all for jointly creating the excellent environment where I can access to the up-to-date technologies and apply them to my project with a light heart.

In Delft, I also met a group of talent scholars and sincere friends. They are Dr. Jia

Wei, Dr. Jing Zhang, Dr. Pan Liu, Dr. Rene Poelma, Dr. Huaiyu Ye, Dr. Mingzhi Dong, Dr. Jianlin Huang, Dr. Guangjun Lv, Dr. Bo Sun, Dr. Pengfei Sun, Dr. Xueming Li, Manjunath R. Venkatesh, Boyao Zhang, Hengqian (Daniel) Yi, and Hao Zhang. Thanks a lot for your precious advice on career and life. The conversations we had at lunch break alleviated the suffering caused by Dutch food.

This joint project cannot happen without the financial support of the State Key Laboratory of Solid State Lighting, China Advanced Semiconductors Industry and Innovation Alliance and TU Delft Beijing Research Center. I must express my gratitude to the initiators and executors of the laboratory, Ling Wu, Jun Ruan, Xiang Zhou, Mingming Wang, Weiqiao Yang, and Jingkan Xiong. I would also like to express my appreciation to my colleagues, Dr. Jiajie Fan, Dr. Cheng Qian, Dr. Yang Liu, Haining Wu, Hongyu Tang, and other staff, for helping me build the experimental set-up and assist with patent applications.

I wish to express my sincere appreciation to Prof. dr. Hairen Tan, who kindly included me in the perovskite-startup group and granted me the freedom to experiment ideas. Your generous support towards my project provided a smooth transition to my postdoctoral career. I would also like to thank the other group members at Nanjing University, Prof. dr. Jia Zhu, Ke Xiao, Pengchen Zhu, Shuai Gu, Renxing Lin, Qiaolei Han, Xin Luo and Jin Wen. We had great time discussing the amazing progress of perovskite technology and playing badminton doubles.

My study on PV windows would be impossible without the initial help of my advisors back in Fudan University, Prof. dr. Yaojie Sun, and Prof. dr. Yandan Lin. Thank you for imparting your knowledge on photovoltaic solar energy and human factors in lighting during my master's study. I would also like to thank all the teachers in my life. Together, your contributions to my knowledge and habits make me who I am today.

In this journey, I never feel lonely thanks to the company of all my good friends, Yu (Ottmar) Wu, Mengdi (Gary) Dong, Jiannan (Ryan) Ren, Tong Cui, Hao Jin, Biyu Wang, Yueqi (Niki) Wang, Liang Di, Tao (Tony) Yan, Jingjing (Candice) Qiu, Zhuoer Li, and Lin Bo. Thank you for encouraging me in my tough times and sharing my joys after every achievement. I am also thankful to my uncle Prof. dr. Laijun Zhao, and his wife, my aunt Yuling Zhang, for taking care of my life in Shanghai for many years and advising on my career whenever I had doubts.

Words are barely able to express my deepest gratitude to my parents, Wanjun Gao, and Lixia Qi. But here I will try my best anyway. I feel so lucky to have you as my parents, who instill me with an optimistic attitude and strong will. You provide me with the conditions to receive the world's best education despite your tight budget, asking nothing for return but my health and happiness. The best I could possibly give you back is the full love in my heart, and a poem, "*In the mid-April, / a baby is raised. / Like grass owes the Sun, / the love is never repaid.*"

最深的感谢献给我的父母，感谢你们对我无私的爱和无条件的支持。
谁言寸草心，报得三春晖。

LIST OF PUBLICATIONS

JOURNAL PUBLICATIONS

1. **Y. Gao**, J. Dong, O. Isabella, R. Santbergen, H. Tan, M. Zeman, and G.Q. Zhang, *Modeling and analyses of energy performances of photovoltaic greenhouses with sun-tracking functionality*, Applied Energy **233–234**, 424 (2019).
2. **Y. Gao**, J. Dong, O. Isabella, R. Santbergen, H. Tan, M. Zeman, and G.Q. Zhang, *A photovoltaic window with sun-tracking shading elements towards maximum power generation and non-glare daylighting*, Applied Energy **228**, 1454 (2018).
3. **Y. Gao**, J. Dong, O. Isabella, R. Santbergen, H. Tan, M. Zeman, and G.Q. Zhang, *Annual energy performance of building-integrated sun-tracking PV blinds*, Energy and Buildings. (Under review)
4. **Y. Gao**, J. Dong, O. Isabella, H. Tan, M. Zeman, and G.Q. Zhang, *Transmittance-controllable neutral-color perovskite solar cells for smart windows*. (In preparation)
5. Y. Ouyang, Y. Li, P. Zhu, Q. Li, **Y. Gao**, J. Tong, L. Shi, Q. Zhou, C. Ling, Q. Chen, Z. Deng, H. Tan, W. Deng, and J. Wang, *Photo-oxidative Degradation of Methylammonium Lead Iodide Perovskite: Mechanism and Protection*, Journal of Materials Chemistry A, 2019.
6. **Y. Gao**, J. Dong, Y. Sun, Y. Lin, and R. Zhang, *PV arc-fault feature extraction and detection based on bayesian support vector machines*, International Journal of Smart Grid and Clean Energy **4**, 283 (2015).
7. **Y. Gao**, Y. Lin, and Y. Sun, *A wireless sensor network based on the novel concept of an I-matrix to achieve high-precision lighting control*, Building and Environment **70**, 223 (2013).

CONFERENCE CONTRIBUTIONS

1. **Y. Gao**, J. Dong, O. Isabella, M. Zeman, and G.Q. Zhang, *Daylighting simulation and analysis of buildings with dynamic photovoltaic window shading elements*, in 2017 14th China International Forum on Solid State Lighting: International Forum on Wide Bandgap Semiconductors China (SSLChina: IFWS), Beijing, China, pp. 52–55, Nov 2017.
2. **Y. Gao**, F. T. Si, O. Isabella, R. Santbergen, G. Yang, G.Q. Zhang, and M. Zeman, *Transmittance-tunable photovoltaic window based on thin-film solar cells and polymer dispersed liquid crystal films*, in the 34th European Photovoltaic Solar Energy Conference and Exhibition (EU PVSEC 2017), Amsterdam, The Netherlands, Sep 2017.
3. **Y. Gao**, F. T. Si, O. Isabella, R. Santbergen, G. Yang, J. Dong, G.Q. Zhang, and M. Zeman, *Performance optimization of semi-transparent thin-film amorphous silicon solar cells*, in the 44th international 2017 IEEE Photovoltaic Specialists Conference (PVSC-44), Washington D.C., USA, pp. 2605–2609, Jun 2017.

4. D. Wang, Y. Sun, Y. Lin, and **Y. Gao**, *Analysis of light environment under solar panels and crop layout*, in the 44th international 2017 IEEE Photovoltaic Specialists Conference (PVSC-44), Washington D.C., USA, pp. 2048–2053, Jun 2017.
5. **Y. Gao**, J. Dong, O. Isabella, M. Zeman, and G.Q. Zhang, *A rapid method of estimating the solar irradiance spectra with potential lighting applications*, in 2016 13th China International Forum on Solid State Lighting (SSLCHINA 2016), Beijing, China, pp. 90–93, Nov 2016.
6. **Y. Gao**, O. Isabella, J. Dong, R. Santbergen, G.Q. Zhang, and M. Zeman, *Solar tracking issues and partial shading effects of an ideal interior photovoltaic shading model*, in the 33rd (PVSEC-26), Singapore, Oct 2016.
7. **Y. Gao**, H. Wu, J. Dong, and G.Q. Zhang, *Constrained optimization of multi-color LED light sources for color temperature control*, in 2015 12th China International Forum on Solid State Lighting (SSLCHINA 2015), Shenzhen, China, pp. 102–105, Nov 2015.
8. **Y. Gao**, J. Zhang, Y. Lin, and Y. Sun, *An innovative photovoltaic DC arc fault detection method through multiple criteria algorithm based on a new arc initiation method*, in the 2014 IEEE 40th Photovoltaic Specialist Conference (PVSC-40), Denver, Colorado, USA, pp. 3188–3192, Sep 2014.
9. Y. Lin, **Y. Gao**, Y. Sun, S. Zhang, and W. Wang, *An automatic evaluation system for the photometric performance of vehicle headlamps using image processing algorithms*, in the 2014 International Conference on Mechatronics and Electronic Engineering (MCE 2014), Shenyang, China, pp. 599–604, Sep 2014.
10. **Y. Gao**, Y. Sun, and Y. Lin, *A fast measurement method for light distribution of vehicle headlamps*, in the 2nd International Forum on Automotive Lighting (IFAL), Shanghai, China, pp. 78–83, Jun 2014.
11. **Y. Gao**, Y. Sun, and Y. Lin, *A novel wireless lighting control strategy using RBF neural networks and genetic algorithm*, in Computational Intelligence and Cybernetics (CYBERNET-ICSCOM), 2013 IEEE International Conference, Yogyakarta, Indonesia, pp. 62–66, Dec 2013.

PATENTS

1. **Y. Gao**, J. Dong, and G.Q. Zhang, *A photovoltaic desk for the correction of sitting position*, China, CN201621445088.9, Nov 2017.
2. **Y. Gao**, J. Dong, and G.Q. Zhang, *A photovoltaic mobile power for charging mobile devices*, China, CN201621444147.0, Aug 2017.
3. **Y. Gao**, J. Dong, and G.Q. Zhang, *A photovoltaic window blind for power generation and glare protection*, China, CN201621446331.9, Aug 2017.
4. **Y. Gao**, J. Dong, and G.Q. Zhang, *A photovoltaic mobile phone protection shell*, China, CN2016-21445390.4, Aug 2017.
5. Y. Sun, **Y. Gao**, Y. Lin, L. Ma, Y. Wu, *A DC arc fault detection method based on multiple criteria in PV systems*, China, CN201310155965.3, May 2013.

6. Y. Sun, Y. Lin, Y. Wu, J. Qiu, **Y. Gao**, *A method for a detection and protection circuit to control desaturation in a T-shaped three-level inverter*, China, CN201210499056.7, Nov 2012.
7. Y. Lin, M. Dong, **Y. Gao**, *A novel kind of automobile wheel integrated with LED display systems*, China, ZL201220572090.8, Nov 2012.

CURRICULUM VITÆ

Yuan GAO

16-04-1988 Born in Jinzhou, China.

EDUCATION

- 2007–2011 Bachelor of Engineering (B.E.) in Electrical Engineering & Automation
Fudan University, Shanghai, China
Thesis: A Rapid Illumination Detecting Method Based on
Data Reconstruction Algorithms
- 2011–2014 Master of Science (M.Sc.) in Photoelectric System & Control Technology
Fudan University, Shanghai, China
Thesis: Research on the Detectable Characteristics of DC
Arc Fault in PV Systems and the Safety Strategy of
Arc Fire Prevention
Supervisors: Prof. dr. Yaojie Sun, Prof. dr. Yandan Lin
- 2014–2018 Doctor of Philosophy (Ph.D.) in Electrical Sustainable Energy
Delft University of Technology, Delft, the Netherlands
Thesis: PV Windows: Theories, Devices and Applications
Promotor: Prof. dr. Miro Zeman
Co-Promotor: Prof. dr. G.Q. Zhang
Supervisors: Dr. Olindo Isabella, Dr. Jianfei Dong

WORK EXPERIENCE

- 2014–2018 Algorithm Engineer
State Key Laboratory of Solid State Lighting, Changzhou, China
- 2018 Research Assistant
Nanjing University, Nanjing, China

PROJECTS

- 2012–2013 Major Science and Technology Projects on Manufacturing Large Aircraft
This project is mainly conducted at Fudan University:
- Proposing a novel concept of I-matrix for precise lighting control with distributed sensors in the cockpit
 - Building the CAD model of the cockpit in DIALux and simulating the lighting scenarios
 - Realizing the data reconstruction and sensor optimization with RBF neural networks and genetic algorithms
- 2013–2014 Fast Measurement Project for Light Distribution of Vehicle Headlamps
This project is mainly conducted at Fudan University, cooperating with Shanghai Motor Vehicle Inspection Certification and Tech Innovation Center:
- Conducting research on standards and regulations on the photometric performance of vehicle headlamps
 - Designing and conducting field experiments cooperating with the Institute of Motor Vehicle Lamp Inspection in Shanghai Motor Vehicle Inspection Center
 - Using the concept of I-matrix in image processing to obtain the info of light distribution on the 25m screen
 - Realizing the automatic recognition and aiming of cutting-off line with edge detection algorithms
- 2013–2014 National Natural Science Foundation of China
This project is mainly conducted at Fudan University:
- Studying DC-arc discharge characteristics in PV systems
 - Searching for fast arc fault pattern recognition algorithms to identify DC-arc fault signal characterization and to achieve strong robustness
 - Proposing solutions to the DC-arc fault protection in PV systems

2014–2018

Photovoltaic Windows for Sustainable Built Environment

This project is mainly conducted in the PVMD Group, Delft University of Technology, collaborating with China State Key Laboratory of Solid State Lighting and Nanjing University:

- PV shades: Optimization of sun-tracking methods and cell layouts of the photovoltaic shades to achieve the maximum power generation considering the partial shading effects
- Semi-transparent solar cells: Design and optimization of thin-film amorphous silicon solar cells, design and fabrication of neutral color perovskite solar cells, and integration with PDLC films
- Building energy performance: Simulation of the annual energy performance of reference buildings integrated with photovoltaic windows, including PV shades and semi-transparent PV windows